Multi-Objective Optimization for Joint Inversion of Geodetic Data

Séverine Furst

THÈSE POUR OBTENIR LE GRADE DE DOCTEUR DE L'UNIVERSITE DE MONTPELLIER

En Mathématiques et Modélisation

École doctorale I2S

Unité de recherche Géosciences Montpellier

et Institut Montpelliérain Alexander Grothendieck

Multi-Objective Optimization for Joint Inversion of Geodetic Data

Présentée par Séverine Furst

Le 1er octobre 2018

Sous la direction de Bijan Mohammadi

et Jean Chéry

Devant le jury composé de

Riad Hassani, Professeur, Sofia-Antipolis	Rapporteur
Luis Rivera, Professeur, EOST	Rapporteur
Christel Tiberi, Chargée de recherche, GM	Examinateur
Virginie Pinel, Chargée de recherche, ISTerre	Examinateur
Dominique Dubucq, Géophysicien, Total	Invité
Michel Peyret, Ingénieur de Recherche, GM	Invité
Bijan Mohammadi, Professeur, IMAG	Directeur
Jean Chéry, Directeur de Recherche, GM	Co-directeur

UNIVERSITÉ DE MONTPELLIER

The power of imagination makes us infinite.

John Muir

Remerciements

Il y a cinq ans je faisais un stage d'été en pétrophysique à Aberdeen en Écosse. Je n'imaginais pas qu'aujourd'hui (14 juillet 2018), je serais à quelques jours de déposer ce manuscrit de thèse. J'ai su relativement tôt que je voulais étudier les géosciences, mais cet attrait pour la recherche s'est vraiment révélé en Nouvelle-Zélande pendant mon stage de master. Ensuite, il a fallu trouver un projet de thèse. La première épreuve du doctorant à proprement parler. Réaliser une thèse de doctorat demande de l'investissement personnel, professionnel et intellectuel dès lors que l'on décide d'en faire une. Ce n'est pas tout d'être passionnée par un thème, il faut aussi vouloir apprendre. Et pas seulement apprendre à chercher, mais aussi apprendre à être chercheur: accepter les critiques et les conseils, prendre du recul, s'interroger, partager ses travaux même inachevés, poser des questions, prendre des décisions, collaborer, échanger et communiquer. Cette liste n'est certainement pas exhaustive, mais elle donne un aperçu de ce que j'ai pu développer en plus des nouvelles connaissances en géophysique, au cours de ces trois dernières années. L'ensemble de ce travail n'aurait pas été possible sans l'intervention d'un grand nombre de personnes.

Je souhaite à présent les en remercier.

Je tiens tout d'abord à remercier Jean Chéry, Bijan Mohammadi et Michel Peyret qui ont participé à l'encadrement de ma thèse. L'encadrement d'une thèse est un point essentiel pour la bonne réussite du projet. Malgré des habitudes de travail différentes entre nous quatre, des idées souvent difficiles à exprimer et des ambitions de travail toujours plus grandes, j'ai eu la chance d'avoir une équipe d'encadrement présente, motivée, impliquée et soucieuse. Je voudrais remercier plus particulièrement Jean Chéry pour ses conseils professionnels et personnels, sa patience, la confiance qu'il a su m'accorder ainsi que toutes les sorties spéléo auxquelles j'ai pu participer, le vélo et l'appartement. Je souhaite également remercier Frédéric Masson (EOST) de nous avoir mis en contact et de m'avoir permis de réaliser ce projet de thèse.

Je tiens à remercier Luis Rivera et Riad Hassani d'avoir rapporter cette thèse. Je remercie également Christel Tiberi et Virginie Pinel d'avoir acceptde faire partie de mon jury de thèse. Les questions soulevés ont permis d'apprhender avec un oeil critique ce travail et ainsi, de me rendre compte de l'étendue des applications et de l'intérêt de mon travail pour la communauté scientifique.

Ces travaux de thèse ont pu être possibles grâce à la conviction et la motivation d'Antoine Jacques (Total S.A.) pour développer de nouvelles méthodologies de surveillance et d'exploitation en utilisant la géodésie. Je le remercie d'avoir convaincu la compagnie Total S.A. de financer cette thèse en collaboration avec le LabEx NUMEV (n° ANR-10-LABX-20). En outre, je remercie également les collègues de Total S.A., d'Aquitaine Electronique et de Drillstar Industries qui participaient aux réunions d'avancement de thèse en apportant des connaissances sur le domaine, en soulevant des questions et donnant des avis constructifs. Merci à Renaud Briand (Aquitaine Electronique) pour son intérêt et son implication dans ce travail. Un grand merci aussi à Kyle Anderson et à l'équipe de l'USGS Menlo Park (Californie) pour leur accueil durant l'été 2017, leur soutien et leur partage de connaissances en déformation volcanique. Je souhaite remercier les collègues du laboratoire Géosciences Montpellier pour leurs conseils, leurs discussions et les échanges scientifiques et personnels. Je tiens à remercier Nicolas Saby et l'équipe de l'IREM pour cette belle expérience de communication scientifique auprès des lycéens.

Mais que seraient trois années de thèse sans les collègues doctorants? Que ce soit dans le même bureau, au café, autour d'une bière dans un bar, au Pota'GM, sur le terrain, dans les conférences, en montagne, ils représentent une part majeure de cette joie de vivre et de travail durant ces trois années à Montpellier. Merci à Anaïs (Bébé) Maréchal, Robin Kurtz (la Robinette) & Fredou, Romain Leroux-Mallouf, Bárbara Dressel, Sven Philit, Manon Dubois, Manon Genti, La Gaine, Alizia Tarayoun & Oswald Malcles, Sofía Escario, Enora Tourneur, Rémi Caillibotte & Alexandre Cugerone, Matthieu Plasman, Pierre Malié et tous les copains de Ma Thèse en 180s. Benou, le BG du Larzac, c'était un plaisir de grimper avec toi, de te provoquer, j'ai apprécié ta bonne humeur et tes répliques. Otta, on a failli commencer une coloc au tout début, puis on a eu la flemme, mais il y a toujours eu cette complicité entre nous qui fait que tu sois venue chez moi ce printemps! Avec Anitax, on a profité de tellement de soirées toutes les trois. Merci pour votre sourire, vos accents, vos expressions, votre naturel, votre présence. Sam mon co-bureau qui me supporte depuis le début, je te remercie pour ta présence et ton soutien. Cyp, grand maître du jeu, merci pour tous les moments de partages et les folles soirées. Laure, Max (le vieux) et Bowie, la fameuse canicrèche cette année, merci pour votre soutien et vos plaisanteries, l'escalade et les soirées. Max (le jeune), Tim et Agathe, merci de m'avoir motivée à sortir grimper quelques fois en falaise ou à la salle ces dernières semaines. Loïs, pour tout le temps que tu as passé sur Youtube et sur les sites de comparaison de matériel ainsi que ta motivation à nous emmener dans des aventures uniques. Ils ne sont pas tous doctorants (ou docteurs), mais nous nous connaissons depuis les années à l'EOST (voire plus) et nous avons continué à partager ensemble et nous nous soutenons aujourd'hui encore. Merci à Flo, Fanny & Jerem, Nico, Jeannette & Vaval, Aubé & Gugu, le Patron & sa femme, Matthias, Paulo, Marion et Baptiste.

S'il n'est pas toujours facile de faire une thèse, il est encore plus difficile de comprendre le ressenti et les impressions d'un doctorant quand on ne l'a pas vécu soi-même. Je voudrais remercier donc très chaleureusement mes parents, ma soeur et mon frère pour leur admiration, leur soutien, leur fierté et leur confiance en moi. Aussi loin qu'ils étaient, ils me permettaient de tester mes convictions et de totalement déconnecter afin de mieux recommencer.

Julie, Roulie, la mère Muel, Princess, peu importe comment je t'appelle tu as été pour moi un pilier, une personne avec qui j'ai tant partagé émotionnellement et personnellement et à qui je pouvais me plaindre parce que je savais qu'en retour tu faisais pareil. On a pris 2 chemins différents, on ne vit pas la même chose, mais on se comprend et on s'admire. Sylvain, nos chemins se sont croisés quelques fois depuis que je suis à Montpellier jusqu'à ce que tu t'installes dans le bureau à l'automne dernier. Parachuté avec deux thésards en dernière année, tu as été une bouffée d'innocence, de fraîcheur et bonne humeur pour moi. Ta présence, ton soutien et ton admiration m'ont été très précieux cette année.

Les Soun! Une coloc qui s'est improvisée mais qui représente ma seconde famille, qu'on soit tous ensembles ou éparpillés aux quatre coins de la Terre. Lisouille, j'adore te faire pleurer de rire, découvrir ce que tu aimes manger, aller boire des mojitos, faire des jeux et chanter des chansons Disney avec toi. Audrey, tu m'as fait découvrir en première tout mon potentiel d'escalade, de rando, d'alpi, de ski, mais tu as surtout été une oreille bienveillante et une boule d'énergie rayonnant de bonheur et ma moitié. Oli, nous avons partagé tellement d'expériences personnelles et professionnelles, toujours prêt à aider ou à partir pour l'aventure, présent en toutes circonstances, ta persévérance, ta force et ton intelligence font partie des qualités pour lesquelles tu es un modèle pour moi. Merci à mon petit Pistou qui m'a fait garder la tête sur les épaules.

Merci à tous d'être tels que vous êtes et de m'avoir soutenue dans cette aventure.

Table of Content

Chapter 1

Introduction

The flat Earth model is one of the conceptions of Earth's shape as a plane or disk (Figure 1.1a). Many ancient cultures believed to the flat Earth theory and nowadays (in 2018) some societies yet support the idea of a flat Earth. However, the first evidence for the spherical shape of the Earth was provided around 330 BC by Aristotle, ancient Greek philosopher and scientist. Later around 240 BC, another Greek philosopher Eratosthenes was able to estimate the Earth's circumference at 250 000 stadia, about 40 000 km (compared to the present-day value of 40 075.017 km at the equator, WGS-84) by comparing altitude elevations of the mid-day sun at two places (Syenes and Alexandria, Egypt) a known North-South distance apart. Although Earth looks perfectly spherical from space (Figure 1.1b), its circumference and diameter differ at the poles from the equator. Because Earth rotates, this sphere is distorted by the centrifugal force. This force causes objects to move outward from their center of gravity (*e.g.* the same force pushes outward the bend the occupants of a car). The centrifugal force is greatest at the equator which creates a outward bulge and therefore implies a larger radius of the Earth at the equator (6 378 km instead of 6 356 km at the poles). Instead of being a true sphere, the Earth is flattened at the poles : its shape is an oblate spheroid or ellipsoid, with a larger circumference and radius at the equator.

The Earth's shape is commonly represented on maps, projecting a 3-dimension object in 2-dimensions. Topography is then used to measure and represent the Earth in terms of horizontal coordinate system (*e.g.* latitude, longitude) and altitude. The altitude defines the vertical distance between the mean sea level and a point at the Earth's surface. Another description of the Earth is given by its geopotential field, associated to the variations of gravitational acceleration, caused by mass excess or deficit at depth (Figure 1.1c). As Gauss described it, the geoid is the "mathematical figure of the Earth" which corresponds to the location of a given gravity potential value (gravity equipotential). It represents the shape that would take the surface of the oceans under the only influences of Earth's gravity and rotation (*e.g.* without ocean motions, atmospheric loads and astronomical tides). Everywhere on this surface, plumb lines would point perpendicular and a water level would be parallel to the geoid. This smooth but asymmetric surface is the directly linked to the uneven distribution of mass within and on the Earth's surface.

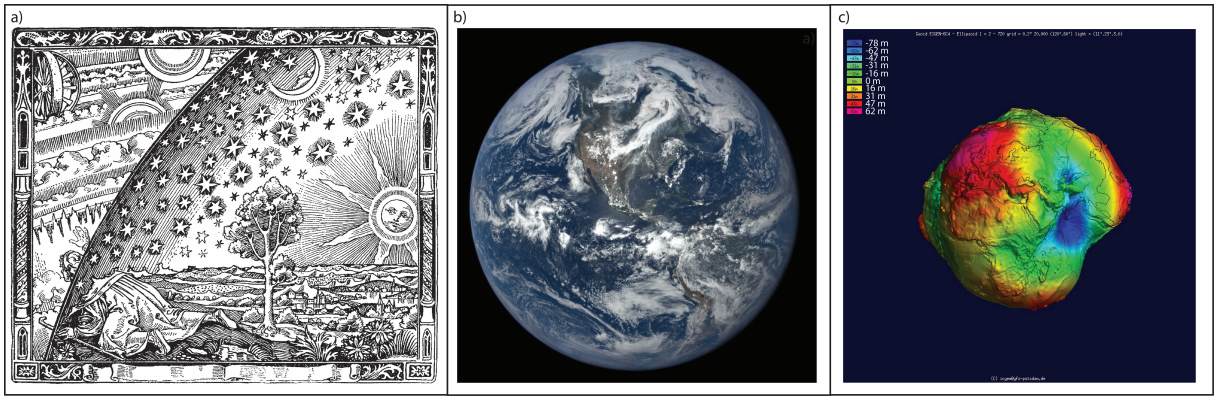

Figure 1.1: *Different representations of the Earth. a) Medieval cosmology representing the flat Earth bounded by a solid and opaque sky, or firmament on the Flammarion engraving (Flammarion, 1888). b) View of the Earth from space (NASA). c) 3D representation of the Geoid undulations with ×20 000 vertical exaggeration (International Centre for Global Earth Models).*

This latter model gives a physical representation of Earth's shape. But the surface can also be locally affected by different deformation processes depending on the forces applied to the Earth's parts. Solid bodies like rocks can deform when sufficiently large forces are applied. The ability of a rock to handle the stress depends on its elastic and plastic properties. Because rocks are constantly subjected to stresses due to thermal and geodynamical processes, the Earth's shape keeps changing since its formation. Melted rocks arise along rift zones and cool down to create new oceanic floor, mountains rise from subduction or collision of two tectonic plates and are being eroded, trenches form along subduction zones in deep oceans, volcanoes inflate and deflate with deep magma movements... Along with these natural processes, anthropogenic activities modify the shape the Earth at different space and time scales. Indeed, surface displacements can also be induced by the extraction or the storage of resources (*e.g.* salt, ore, oil, gas).

These permanent changes of the Earth's surface are measured using instruments and techniques developed for geodetic purposes. At the crossroads of astronomy, geophysics and oceanography, geodesy aims at precisely defining the shape, dimensions and gravity field of the Earth and its time evolution (Helmert, 1880). The geodetic devices used for deformation monitoring depend on the application, the chosen method, and the preferred measurement intervals in space and time. Among the various geodetic instruments, levelling has been used for almost two centuries to determine the height differences of a chosen point with respect to the given datum, which is generally the mean sea level. In 2018, this one dimensional measurement of the surface displacement is completed by other geodetic measurements recorded by instruments with different time and space resolutions including GNSS, InSAR and tiltmeters. Indeed, technological advances of the past 30 years permit to develop these geodetic devices in order to measure more precisely and accurately deformations of the Earth's surface from the meter level down to the nanometer level. Thanks to these complementary tools, the characterization of the Earth's shape can now be described in 3 dimensions. Using up to date geodetic instruments, changes of Earth's surface induced by deep processes are precisely measured. This deep strain is caused by

numerous factors (*e.g.* incoming magma, extracting resources, fluids flow, creeping, rheological variations) leading to the deformation of the source and its surrounding medium up to the surface. Therefore, using surface, aerial and satellite observations, we attempt in this work to explain the surface deformation linked to the strain at depth. The processes affecting the source can be elastic or anelastic, and they cause the volume of the source to increase or decrease.

In this thesis, our goal is to quantify the deep strain from the knowledge of surface motions. Because we are not explicitly seeking for the origin of the deformation, the physical problem is formalized as a numerical formulation using analytical (or numerical) models depending on the geometry of the source and the mechanical properties of the medium. In a first kind of models, we assume that horizontal variations of interseismic velocities are due to variations of lateral rigidities of lithospheric plates, considering a numerical representation of lithospheric plate. For the second kind of models, we used analytical models of spherical sources (Mogi, 1958) and planar dislocations (Okada, 1992) in order to simulate deformations observed at the surface induced by volume variations. The ground displacements can be observed in volcanic systems, salt mining and unconventional reservoirs by various geodetic instruments and techniques. In this work, we explicitly consider GPS, tiltmeters, levelling surveys and InSAR interferograms. Linking these observations to an assumed physical process is permitted using a dedicated inverse strategy. By doing so, we aim at retrieving the parameters defining the process that produces modelled data explaining at best the observed ones. Testing in an optimal way as many values parameters as necessary, we build a function that estimates the similarity between modelled and observed data, named the functional or cost function. This latter should converge towards zero when the optimal parameters set is found. However, due to imperfect data measurements, the functional never reaches this value. Moreover, due to the possibly ill-posed nature of the inverse problem, the functional can display several minima. There are many different methodologies of optimization used to minimize the functional depending on the complexity of the physical problem, the considered data, the level of desired precision or the computational capacities. In this work, we choose a global optimization strategy to escape from local minima developed by Mohammadi and Saïac (2003) which allows us to consider physical problems of different complexities and various data types at low computational cost. Therefore, this work aims at jointly inverting various geodetic data using a global optimization approach to recover the best model and instrument parameters.

Among the motivations of this work, the long term monitoring of geological systems remains challenging and persuaded us to develop an integrated methodology that could be used to determine both instrumental and strain source parameters in various domains (such as interseismic plate deformation, volcanic deformation, salt mining and hydraulic fracturation in unconventional extraction of oil & gas reservoirs). Another motivation was to implement an adapted inversion strategy for tilt data. Indeed, surface displacements induced by extraction of oil & gas in unconventional reservoirs are nano- to micrometric and only tiltmeters are sensitive enough to measure them. Therefore, this thesis is part of the MIRZA project that focuses on building small drifting tiltmeters (see Chapter 3). As a specific work parckage of the project, the work presented here allows to model the

instrumental drift of tiltmeters along with volumetric variations of deep fractures. Applied to volcanic system or salt extraction, the joint inversion of multiple geodetic dataset would permit to precisely determine the strain source along with long-term drift of tiltmeters.

Figure 1.2 compiles 25 of the most recurrent words in this manuscript, highlighting the preponderance of the data which can be real observations, synthetics data or modeled data. This gives an insight of the different subjects that are approached in my thesis. This manuscript is structured as follows: after briefly reviewing the inverse problems in geodesy (Chapter 2), I present the key issues associated to geodetic reservoirs deformation (Chapter 3) that brought us to develop our methodology (Chapter 4) demonstrated using different levels of complexity. This approach is firstly used to determine the lateral rigidity of the lithosphere using interseismic velocities measured in the Western United States (Chapter 5). Then, we invert time series of synthetic tilt data to retrieve volume variations of a spherical source and a tensile fracture (Chapter 6). Finally, a full joint inversion of GPS, tilt, InSAR and levelling data is performed using our approach (Chapter 7). At last, I summarize the contributions of the methodology and the remaining issues, leading to improvements and future applications (Chapter 8).

Figure 1.2: *Cluster of the most recurrent words in this manuscript (built using Voyant Tools developed by Sinclair and Rockwell, 2014).*

Chapter 2

Literature review : a glance of inverse problems in geodesy

Résumé

On assimile souvent un protocole de chimie à une recette de cuisine, mais on peut faire un rapprochement similaire entre la mise au point d'une recette de cuisine et le problème inverse en géophysique. Par exemple si je cherche à reproduire ce muffin si délicieux de la boulangerie, je vais commencer par choisir un ensemble d'ingrédients de base. Mais il manque les quantités exactes pour obtenir le muffin souhaité. Une méthode pour les trouver serait de cuisiner autant de muffins qu'il me sera nécessaire en testant des quantités différentes jusqu'à finalement ne plus goûter aucune différence avec le muffin souhaité. En faisant cela, je minimise l'écart, la différence, entre mon muffin et celui de la boulangerie. Une fois les bonnes quantités trouvées, j'ai résolu ce que l'on appelle un problème inverse: à partir du résultat (le muffin), j'ai relié mon modèle (les ingrédients) à mes inconnues (les quantités) en utilisant ma recette.

Ce genre d'approche est couramment utilisée en géophysique avec, à la place du muffin, des données mesurées par des instruments à la surface. Ces données sont le résultat de phénomènes physiques en profondeur (quantités des ingrédients). Pour relier le tout, les équations régissant mon modèle tiennent lieu de recette de cuisine.

Je présente dans ce chapitre un bref état de l'art sur le problème inverse en géodésie. J'aborde tout particulièrement les notions qui seront employées tout au long de ce manuscrit qui concernent les différents modèles directs (la recette), les données géodésiques (le muffin) et les méthodes d'optimisation utilisées pour les relier.

2.1 The muffin recipe

After gathering all the ingredients to bake muffins for dessert, you need to follow your recipe to mix them in the right quantities to eventually obtain delicious muffins.

But now, imagine you want to replicate the muffins you just bought. You know the ingredients that are commonly used in muffins' recipes, but you need to identify the quantities that will best reproduce the muffins. You need to bake as many muffins as necessary varying the quantities until you cannot taste or see any difference with the good muffin. So you are trying to minimize the distance separating your trial muffin from the target muffin, such as

$$J = \|\text{trial muffin} - \text{target muffin}\|$$

Solving the ingredient-recipe mystery is more commonly called an inverse problem : I have the result (the muffins) and I want to find the unknowns (the quantities) from the chosen recipe producing the muffin. And switching back to geophysics, we usually record data at the surface (the muffins) that we try to explain the origin (the ingredients quantities) using a conceptual model (the recipe).

The following sections review the forward models (the recipe), the data (the muffins) used for inverse problems in geodesy and give a brief overview of different methodologies to approach inverse problems.

2.2 Forward models

When it comes to build a strategy to retrieve characteristics of a physical system, we need to choose the forward model that links the observations to the parameters we are looking for. But to understand how such problem is solved, it is necessary to identify forward models that are used through the inversion. Forward, because they give the general response to a given set of parameters by applying theoretical models. In the case of geodetic strain, they allow to link source characteristics (location, size, orientation, internal stress or strain) to the surface deformation of the crust in response to rheological processes.

Forward models can be divided into two categories: analytical and numerical. The former ones allow the calculation of displacements, tilts, strain or stress induced by a source at depth using mathematical relations solving the constitutive equations of the problem as a whole. Widely used because of their low computational cost, they are limited to simple geometries and rheological assumptions. On the opposite, numerical models are based on spatial discretization of the source, its surrounding medium and the topography. For such cases, the forward model accounts for a more precise description of the geophysical properties of the medium. Nevertheless, this gain is much more expensive computationally than analytical simulations.

In this section, I present some of the analytical and numerical models that are used in this study or considered for further improvements.

2.2.1. Analytical models

2.2.1.1. Spherical source

The so-called *Mogi model* is the simplest and probably the most used analytical solution for a pressurized source in a homogeneous elastic half-space. Named after the scientist, Kiyoo Mogi, that first applied it to a geophysical problem (Mogi, 1958), it considers a spherical source embedded in an ideal semi-infinite uniform elastic body. This source is defined by its radius a, centered at a depth z_s beneath the free surface at $z = 0$ (Figure 2.1). A uniform internal pressure P is applied to the boundary of the spherical source. The system is described by four variables, including the cartesian coordinates of the point source ($\vec{x} = x_s, y_s, z_s$) and pressure (P) (Mogi, 1958). The approximation of a point source stands as long as the depth of the source is at least three times the radius of the source (Battaglia et al., 2013b). This model predicts 3-D surface displacement $\vec{u} = (u_x, u_y, u_z)$ pointing in the direction from the source to the observation point (unit vector $\vec{n}_1$, Figure 2.1) such as,

$$\vec{u}(a, R, P, \vec{n}_1) = \frac{(1-\nu)Pa^3}{\mu R^2}\vec{n}_1 \tag{2.1}$$

with $\vec{n}_1$ the unit vector in the direction defined by the source and the observational point. $R = \sqrt{(x-x_s)^2 + (y-y_s)^2 + (-z_s)^2}$ is the distance between the observation point at the surface $(x, y, 0)$. ν and μ are respectively the Poisson's ratio and shear modulus.

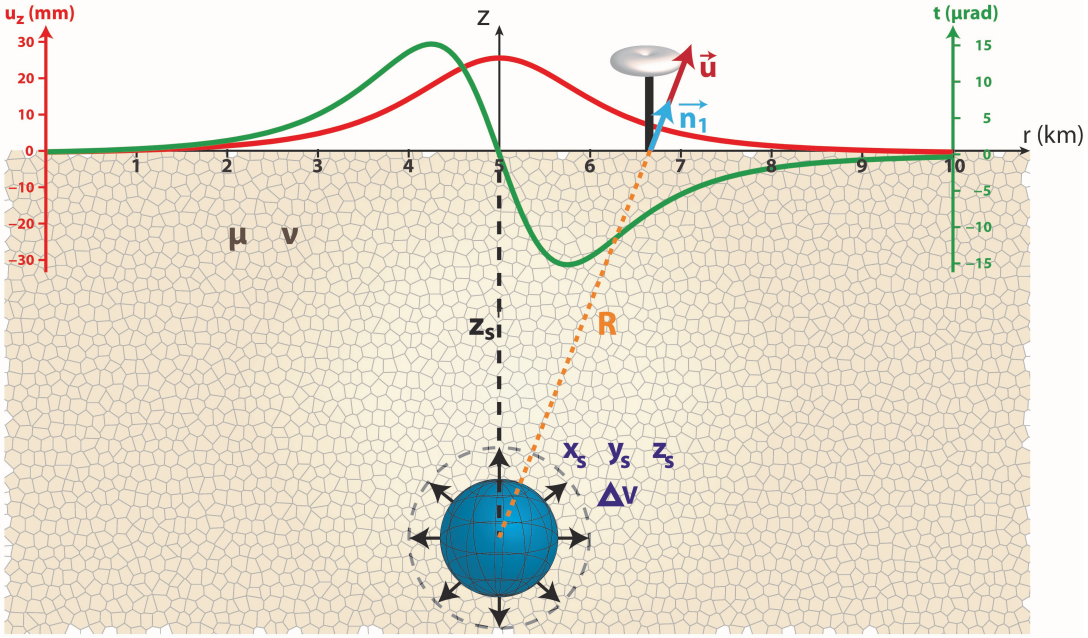

Figure 2.1: *Representation of an isotropic volume variation $\Delta V = 250\ 000\ m^3$ embedded in a homogeneous and elastic half space at 1500 m deep (after Mogi, 1958). The spherical source should be small relatively to its depth ($|z_s| \gg a$). The displacement $\vec{u}$ is pointing in the direction $\vec{n}_1$ while the tilt $\vec{t}$ is the spatial gradient of u_z. The red curve represents the vertical displacement (in mm) for such configuration and the green curve represents the values of tilt (in μrad).*

The volumetric change ΔV associated with the deformation can be introduced in Eq. (2.1) using the definition of ΔV,

$$\Delta V = \frac{\pi}{\mu} P a^3 \tag{2.2}$$

which leads to,

$$\vec{u}(R, \Delta V, \vec{n}_1) = \frac{1-\nu}{\pi R^2} \Delta V \vec{n}_1 \tag{2.3}$$

Therefore, the surface deformation can be derived using either the volume variation of the source ΔV or the associated radius a combined with the pressure P. The quantity Pa^3 is the "strength" of the singularity and therefore the cavity radius a and the pressure change P are inseparable. The radius a of the source is often unknown for geophysical applications and the volume change of the point source is more commonly estimated rather than pressure changes (Mossop and Segall, 1999). The displacements produced by volume or pressure changes can be measured using GPS, InSAR or levelling (described in the next section).

The components of the ground tilt vector are given by the horizontal derivatives of the vertical displacement $\vec{u}_z$ such as $\vec{t} = -\nabla u_z$,

$$\vec{t}(z_s, r, R, \Delta V, \vec{n}_2) = \frac{1-\nu}{\pi} \Delta V \frac{3 z_s \, r}{R^5} \vec{n}_2 \tag{2.4}$$

with $\vec{n}_2$ the unit vector included in the plane tangent to the surface deformation pointing in the direction of minimal deformation. $r = \sqrt{(x-x_s)^2 + (y-y_s)^2}$ is the distance between the projection at the surface of the source and the observation point (Figure 2.1). If the ground subsides, $\vec{n}_2$ points towards the center of the subsidence. On the contrary, during an uplift (Figure 2.1) $\vec{n}_2$ points outwards the maximum uplift. Commonly used in volcano deformation when observed data are sparse or showing axial symmetry, the Mogi's model is also employed as a test model before implementing more sophisticated models (Bonafede and Ferrari, 2009). The main advantage of this forward model is the small number of parameters involved, allowing rapid computation (Nunnari et al., 2005). However, one needs to consider the limitations to the applicability of this model:

1. The sources must be deep compared to their radius.
2. The stress field becomes singular in the neighborhood of the source.
3. At this level of approximation, the size of the cavity cannot be estimated separately from the pressure change.
4. When considering high negative pressure change, Eq. (2.2) shows that it can lead to a negative final volume. Yet it is physically impossible obtaining such final volume.

Considering higher-order in the Taylor expansion to the stress and displacement fields leads to the formulation given by McTigue (1987) for shallow sources and non-singular stress field in the vicinity of the source. Starting from Eq. (2.1) the analytical solution given by McTigue (1987) can be written in its factorized form as,

$$\vec{u}(a, z_s, r, R, \Delta V, \vec{n}_1) = \frac{(1-\nu) P a^3}{\mu R^2} \left\{ 1 - \left(\frac{a}{z_s}\right)^3 \left[\frac{1}{2} \frac{(1+\nu)}{7-5\nu} - \frac{15}{4} \frac{(2-\nu)}{7-5\nu} \frac{z_s^2}{R} \right] \right\} \vec{n}_1 \tag{2.5}$$

Let's call $M = 1 - \left(\frac{a}{z_s}\right)^3 \left[\frac{1}{2}\frac{(1+\nu)}{7-5\nu} - \frac{15}{4}\frac{(2-\nu)}{7-5\nu}\frac{z_s^2}{R}\right]$. By considering a higher order term in the expression of the volume change,

$$\Delta V = \pi a^3 \frac{P}{\mu}\left[1 + \left(\frac{a}{z_s}\right)^4\right] \tag{2.6}$$

we can write an equivalent expression of Eq. (2.5) in terms of the change in volume of the body,

$$\vec{u}(a, z_s, r, R, \Delta V, \vec{n}_1) = \frac{(1-\nu)}{\pi R^2}\Delta V\left[1 + \left(\frac{a}{z_s}\right)^4\right]^{-1} M\ \vec{n}_1 \tag{2.7}$$

This form eventually allows to search for all three parameters ΔV, a and z_s.

If $\left(\frac{a}{z_s}\right)^3 << 1$, Eq. (2.5) and Eq. (2.7) reduce to the Mogi solution for a deep dilatation source. Indeed, if we consider a source radius $a = \frac{z_s}{2}$ the correction to the *Mogi model* (second term in Eq. (2.7)) is only 12.5%. Thus, if the accuracy of the geodetic survey is lower than 12.5% or if site effects produced by shallow heterogeneities and topography affect by less than 12.5% the geodetic signal, then the Mogi's assumptions are sufficient (Battaglia et al., 2013a).

Ground tilt equations are finally derived from Eq. (2.7)

$$\vec{t}(a, z_s, r, R, \Delta V, \vec{n}_2) = \frac{(1-\nu)}{\pi}\Delta V\left[1 + \left(\frac{a}{z_s}\right)^4\right]^{-1} M\frac{3z_s.r}{R^5}\vec{n}_2 \tag{2.8}$$

If one wants to explain a lack of axial symmetry of geodetic data, models of cylindrical (Yukutake and Tachinaka, 1967) and spheroidal (Davis, 1986a; Yang et al., 1988; Cervelli, 2013) sources have been explicitly written to account for more complex source geometries. For instance, one can use an elongated spheroid (Yang et al., 1988) to model a conduit under a constant pressure. Also, Camacho et al. (2011) propose an analytical approach to consider source with a free geometry. They approximate the source by an aggregation of elementary point sources, producing displacements and tilts that are the sum of individual sources. Ronchin et al. (2017) propose another approach considering numerical models (see next section).

This study focuses on modeling geological reservoirs such as hydrocarbons, salt and volcanoes. These geological systems are deforming under a large variety of source processes. Besides using spheroidal or elongated sources for salt caves or magmatic chambers, it could be appropriate to model dikes or fractures. Therefore another model is useful: the rectangular dislocation model.

2.2.1.2. Planar dislocations

The analytical solution for the surface and internal displacements, strains and tilts due to a strike-slip, dip-slip and tensile dislocation in a half-space has been given by Okada (1992):

$$u_i = \frac{1}{F}\int\int_S \Delta u_j\left[\lambda\delta_{jk}\frac{\partial u_i^n}{\partial\zeta^n} + \mu\left(\frac{\partial u_i^j}{\partial\zeta^k} + \frac{\partial u_i^k}{\partial\zeta^j}\right)\right] n_k dS \tag{2.9}$$

where $u_i = (u_1, u_2, u_3)$ are the 3 components of the displacement vector $\vec{u}$ at the observation point induced by a dislocation $\Delta u_j = (\zeta_1, \zeta_2, \zeta_3)$ of a magnitude F across the surface S. $n_k = (n_1, n_2, n_3)$ is the normal vector to the surface S. u_i^j is the i^{th} component of the displacement at the observation point due to a force F in the j^{th} direction. λ and μ are respectively the Lamé's first parameter and the shear modulus. This general expression leads to a complex system of equations entirely described in Okada (1992). The geometry is illustrated in Figure 2.2 for the specific case of surface deformation induced by a planar dislocation. Similarly to the *Mogi model* or *McTigue model*, the half-space is homogeneous, isotropic, elastic and assumes no topography. Here the source is a planar facet, characterized by its length (L), width (W), depth (z_s) and dislocation type (strike ζ_1, dip ζ_2 or tensile ζ_3) (Figure 2.2). Because of its complex analytical expression, the tilt vector is numerically calculated as $-\nabla u_3$.

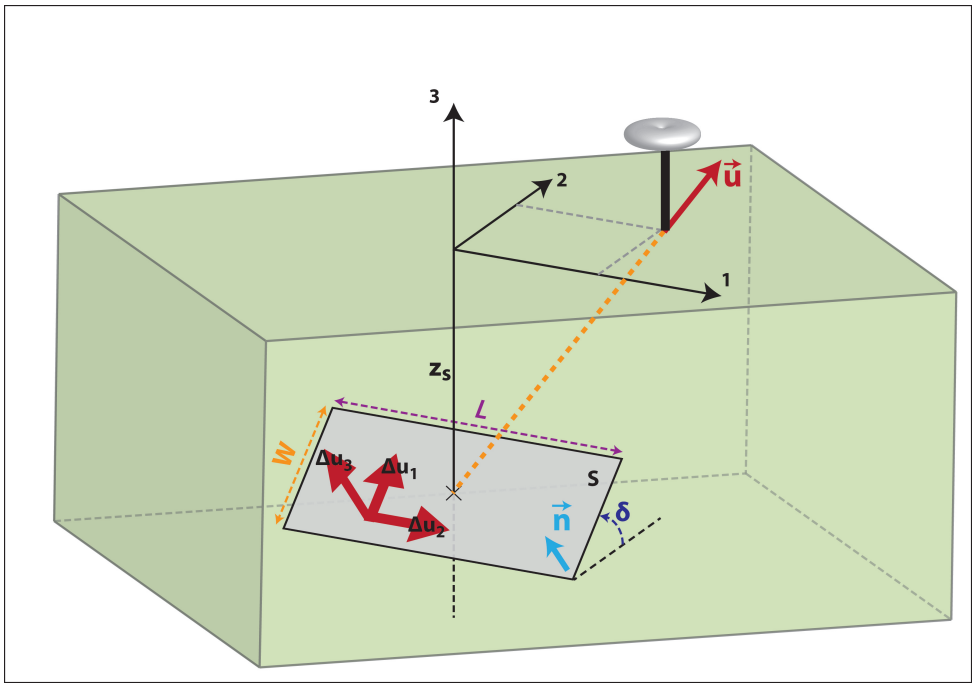

Figure 2.2: *Representation of a dislocation in a homogeneous and elastic half space (Okada, 1992). The red arrows stand for the dislocation types 1) dip-slip, 2) strike-slip and 3) tensile. The planar dislocation is located at a depth z_s, has a width W, a length L and a dip δ.*

2.2.2. Numerical models

The use of analytical models implies that the geometry of the source as well as the characteristics of the medium remain simple. In the presence of complex structures numerical models like finite elements, finite differences or boundary elements are needed. Based on the source and medium discretization, they allow for the simulation of the deformation associated to one or several sources of any geometry and heterogeneous medium (*e.g.* non flat topography, anelastic rheology).

When finite elements are used, the solution of governing differential equations of analytical models are approximated by decomposing the domain into blocks of either identical

or various size and applying constitutive equations and stress balance to individual elements or nodes of the mesh (*e.g.* Dieterich and Decker, 1975; Dragoni and Magnanensi, 1989; Ooi and Yang, 2010; Anderson et al., 2015). If the domain of interest is large compared to the size of the source, implementing an adaptive mesh makes sense. In order to capture strain gradients, the mesh size should be finer near the source and coarser in the far field. One can also use an adaptive mesh depending on the surface distribution of the dataset.

The boundary element method transforms the volume problem into a surface problem thanks to an integration of the stress balance equations. This may lead to a reduction of computational time. Therefore such models are also widely used by the geophysical community (*e.g.* Cayol and Cornet, 1997; Peltier et al., 2007; Maerten, 2010; Li et al., 2015; Weng, 2015).

Although this thesis will mainly consider analytical models, we also used a numerical model of a lithospheric plate in Chapter 5.

2.3 Geodetic observations

The Earth's surface is shaped by numerous geological processes among which plate tectonics and volcanism create the most obvious surface deformation features. Geodesy focuses on the representation of the shape of the Earth based on various measurements of surface displacement and gravitational field in a three-dimensional time-varying space. Space and terrestrial techniques are used in geodesy to study these geodynamical phenomena, using continuously recording instruments or repeat surveys.

Measuring surface deformation is handled by several surveying techniques, continuous or repeated (Global Navigation Satellite System, Interferometric Synthetic Aperture Radar, levelling, gravimetry, tiltmeters, strainmeters, Electronic Distance Measurement, photography, photogrammetry, water-level gauging, lava lake-level...). I briefly describe hereafter five of these techniques: Global Navigation Satellite System (GNSS), Interferometric Synthetic Aperture Radar (InSAR), tilt, levelling and gravimetric surveys.

2.3.1. Global Navigation Satellite System

A Global Navigation Satellite System is achieved by a constellation of 18 to 30 satellites put in Medium Earth Orbit (between 19 000 and 23 000 km above sea level, Hager et al., 1991). There are currently four operational GNSSs: the Global Positioning System (GPS) from the United States, the Russian GLONASS and the European Union's GALILEO which should be fully operational by 2020 just like the Chinese COMPASS. GNSS is used to provide positioning in the inertial reference frame of the Earth. The system uses receivers spread on the surface to measure the transmitting time of signals from GNSS satellites. When at least four satellites are used (Figure 2.3), data post-processing allows to compute the spatial coordinates of the receiver and its time evolution. The measure of the receiver's position is a 3-components values generally given with a daily accuracy of 1 mm (Hager et al., 1991) with respect to a reference frame named International Terrestrial Reference Frame (ITRF).

Therefore, GNSS networks provide with 3-D displacements and velocities vectors with a wide range of sampling rates with respect to the ITRF. As far as possible, network are used to continuously record time series (typical sampling rate of 1 to 30 s) but episodic observations or campaigns are also conducted to improve spatial density.

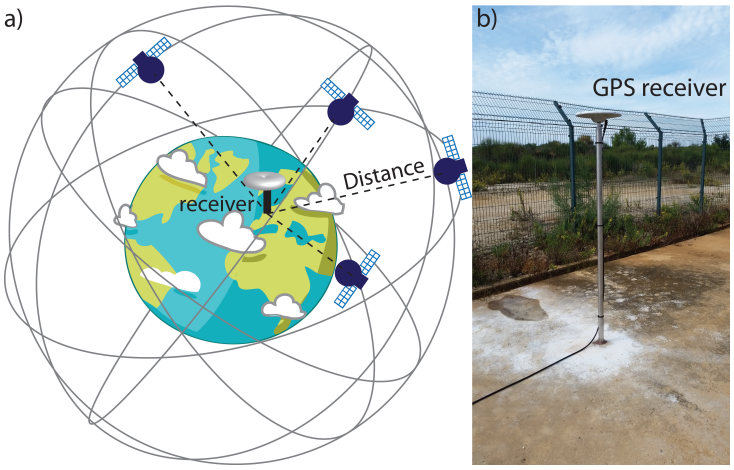

Figure 2.3: *a) Principle of acquisition of GNSS data with at least 4 satellites to compute position of the receiver and time. b) GPS receiver antenna on the brine extraction site of Vauvert (Gard, France).*

2.3.2. Interferometric Synthetic Aperture Radar

Satellite radar orbiting at 800 km uses electromagnetic radiation at microwave frequencies pointing to the side rather than straight down the targets. So the arrival path of the radar signal is oblique to the surface being imaged (Figure 2.4). Conversely to real aperture radar, synthetic aperture radar (SAR) is based on the Doppler effect. Indeed, as Wiley (1965) first noticed, a large antenna aperture can be synthesized using the frequency spread in the echo signal produced by the Doppler effect. This enables a decametric ground resolution.

Imaging the Earth's surface using radar systems is based on the spatial reflectivity information from illuminated targets. Those targets need to be relatively invariant with time so they are not blurred and can be followed through time.

Each pixel in a SAR image contains information about amplitude and phase, corresponding respectively to the intensity of the returned radar energy and to a fraction of complete wavelength (variations of phase). The measure of the Earth's deformation can be derived from the recorded phase by forming an interferogram. To do so, one subtracts two images recorded over the same area at different times. The resulting phase-difference fringes are proportional to the change in the distance between the ground and the satellite. This process is repeated with tens or even hundreds of images from the same area to improve the phase change resolution and to follow up the deformation through time (Massonnet and Feigl, 1998; Richards, 2007).

Numerous missions include satellite imaging radar systems (ERS1 & 2, ENVISAT, SENTINEL-1, TERRASAR-X, COSMO-SKYMED, RADARSAT, TANDEM-X, JERS1, ALOS) with different orbit repeat cycles, from 6 to 46 days.

The spatial coverage of InSAR technique is much better than the discrete sampling of other geodetic techniques and is capable of imaging day and night. By using microwaves (like GNSS), it has cloud-penetrating capabilities due to very low atmospheric absorption at typical radar wavelengths. However, vegetation or snow cover are usually obstacles that may affect the measure of ground deformation by decreasing the correlation between successive images. Also, a long repeat time is a limitation to precise measures of ground deformation for rapid events because of slow ground modifications. Finally, only the deformation in the Line-Of-Sight direction of the satellite (Figure 2.4) is displayed by interferograms. When corrected from topographic phase change, this component (u_{LOS}) of the deformation is measured with an accuracy of a few mm. With standard InSAR treatment, tt is important to note that unlike GPS, a full 3-D ground displacement cannot be achieved with InSAR.

Practically, standard InSAR faces major limitations among which decorrelation associated with vegetation coverage, atmospheric biases due to tropospheric condition changes, or sensitivity to local Digital Elevation Model (DEM) errors. One way to cope with this, is to adopt a Multi-Temporal InSAR approach (MT-InSAR) which processes time-series of radar images (e.g. Ferretti et al., 2000; Berardino et al., 2002; Hooper et al., 2004). The objective of such techniques is twofold. First, they select pixels (generally called Permanent or Persistent Scatterers (PS)) that have a steady backscattering behavior over the whole time-series. Then, they invert the ground deformation component of the interferometric phase by discriminating it from other sources of phase delay (turbulent atmospheric effect or DEM error), based on their spatio-temporal signature. This leads to individual time-series of ground position for each PS from which mean velocities are generally derived.

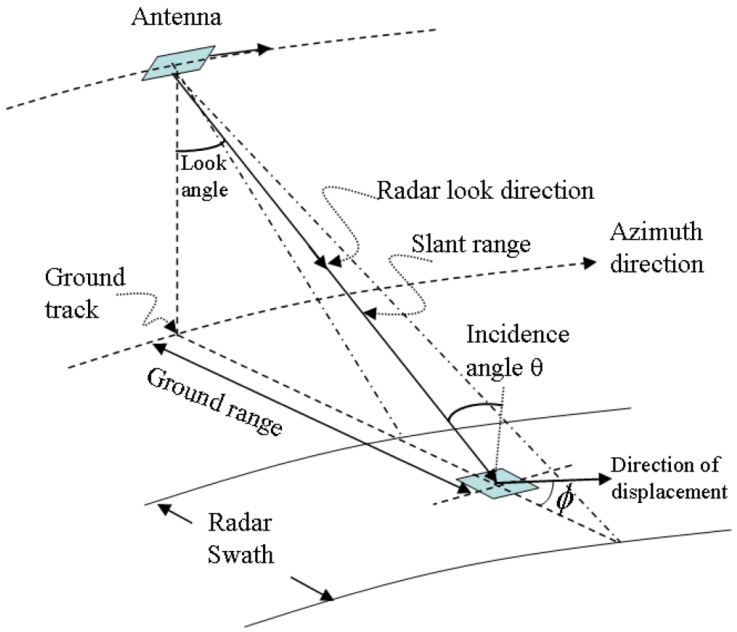

Figure 2.4: *Geometric model of a SAR system. Slant range is the length between the antenna and ground pixel while ground range is the distance between the ground track and the ground pixel (from Zhou et al., 2009).*

2.3.3. Tilt monitoring

Measuring crustal tilt consists in estimating the temporal variations of rigid body rotation with respect to the vertical plumb line (Figure 2.5). Thus, without using any dedicated instruments, the tilt can be derived from other data (z-derivative of surface displacement recorded by GPS), or instruments (seismometers, pendulum) or methods (levelling) that are sensitive to ground tilt. Otherwise, we can distinguish between simple and folded pendulums, liquid level systems (long-based tiltmeters) or bubble tiltmeters (similar to a very high resolution carpenter's level). A comprehensive review of tiltmeters is provided by Agnew (1986). When installed within a few meters of the surface, tiltmeters are plagued with ground tilt such as differential thermal expansion of near-surface materials, rainfall and pumping effects. For instance, thermal effect or wind at the surface produce locally a millirad signal on the surface while hydrology and earth tides create amplitude ranging from 0.1 to 10 μrad.

In order to minimize these effects and to record crustal and reservoirs deformation, borehole tiltmeters are installed at depth ranging from few meters to several tens of meters (Harrison and Herbst, 1977; Ricco et al., 2018). These highly sensitive instruments (up to 5 nrad of resolution, equivalent to 5 mm over 1000 km) measure temporal variations of the orientation of their body with respect to the local gravity vector. The data are continuously recorded in a standalone mode, no sophisticated processing is needed unlike GPS or InSAR, apart from extracting the signal induced by terrestrial and oceanic tides (Wyatt et al., 1982). Therefore, tilt data can be transfered and analyzed in nearly real time which can be convenient to survey rapid surface deformation during volcanic unrest for instance.

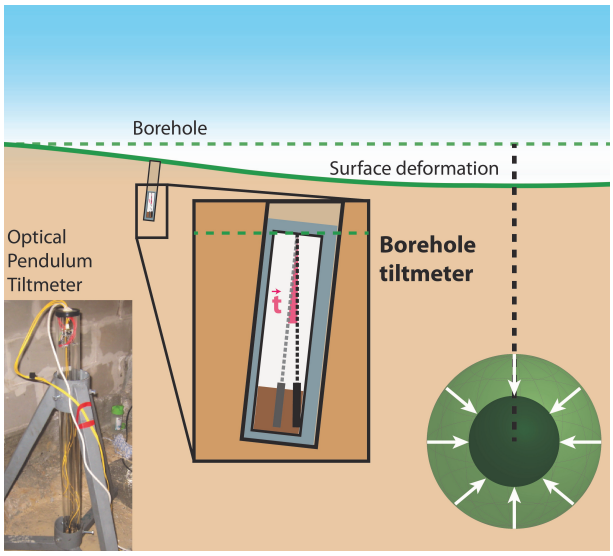

Figure 2.5: *Measuring surface deformation induced by a decrease of spherical volume using borehole tiltmeter and picture of a prototype of optical pendulum tiltmeter (Chawah et al., 2015a).*

2.3.4. Levelling surveys

Even if levelling is a low-tech geodetic approach, it remains one of the most accurate to measure vertical height changes over kilometric baselines. Before the advance of satellite geodesy, this method was the only one providing millimetric precision of the vertical motion (Jouanne et al., 1995, 1998; Nocquet et al., 2016). Differential levelling is commonly used to complete circuits, lines or networks within a network of permanent benchmarks. By repeated surveys, one can measure the height changes as a function of time. It features a digital or optical level and one or two levelling rods (Figure 2.6). Starting from a point of known or assumed elevation (BM1), several stable points are chosen along a line or circuit to reach a final location (BM2). The level is then set up in such way that backsight (BS) reading on the bench mark as well as foresight (FS) reading the next point are both allowed. The instrument is then shifted to some other position in forward direction (Figure 2.6). The measure issued from levelling surveys is then relative to an initial point which is used to adjust different profiles containing the same point (Jouanne et al., 1995, 1998; Nocquet et al., 2016).

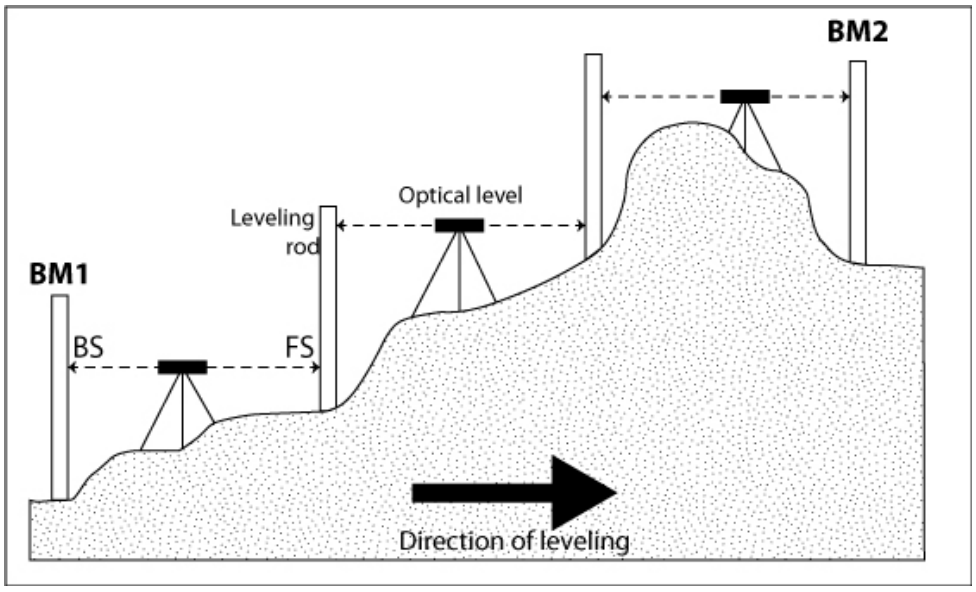

Figure 2.6: *Sketch of differential levelling procedure. The height differences between datum point (BM1) and another benchmark (BM2) are estimated by accumulating differences between foresight (FS) and backsight (BS) readings on a levelling rod.*

Bossler (1984) reports the different configurations and their resolutions, ranging from 0.1 to 1 mm per km. The accuracy of the method is dependent of several factors; combination of equipment, field procedures, survey characteristics (double-run sections, circuits) and type of corrections (rod scale, rod temperature, level collimation, refraction, astronomic, orthometric, gravimetric). For high precision surveys, the elevation accuracy ranges from 0.5 to 2 mm per $\sqrt{\text{km}}$ (Bossler, 1984). It is important to notice that the error on the measurements is increasing with the distance like a Brownian noise. This error is markedly different from the one occurring on GPS, which displays a different error to baseline relation.

2.3.5. Gravimetric surveys

In some cases, ground deformation is significant enough to be detectable by gravimeters as these instruments are sensitive to changes in the subsurface distribution of mass. Conversely, mass can change without surface deformation (Jacob et al., 2008; Fores et al., 2017). Therefore, gravimetric and surface measurements bring complementary information about physical processes occurring underground. Similarly to GPS stations, gravimeters can be used as continuous stations or during surveys. Combining both methods provides a better spatial and temporal coverage.

Free-fall gravimeters such as Micro-g Lacoste FG5 (Sasagawa et al., 1995) provide precise co-measurements of the time t and the falling distance d of a free-falling corner cube in a vacuum chamber, giving the local value of the gravity g with an accuracy of 1 to 2 μGal (knowing that the gravity $g = 981\ 000\ 000\ \mu$Gal). FG5 and A10 instruments (Micro-g) are the most affordable and transportable absolute gravimeters for geodetic studies.

Relative gravimeters can measure the difference in the acceleration due to gravity at different locations or times. Supraconductive gravimeters are the most precise of the relative gravimeters, but they cannot be easily moved. For field surveys and uneven environments, spring-based gravimeters (Figure 2.7) have been developed such as the widely used Lacoste & Romberg CG-5 (accuracy of 5 μGal). Because its sensor is a mechanical spring, these instruments provide a measure evolving with the aging of the spring. In survey mode, the instrumental drift can be corrected by measuring at the exact same place a few times a day knowing the time varying gravity of this specific site.

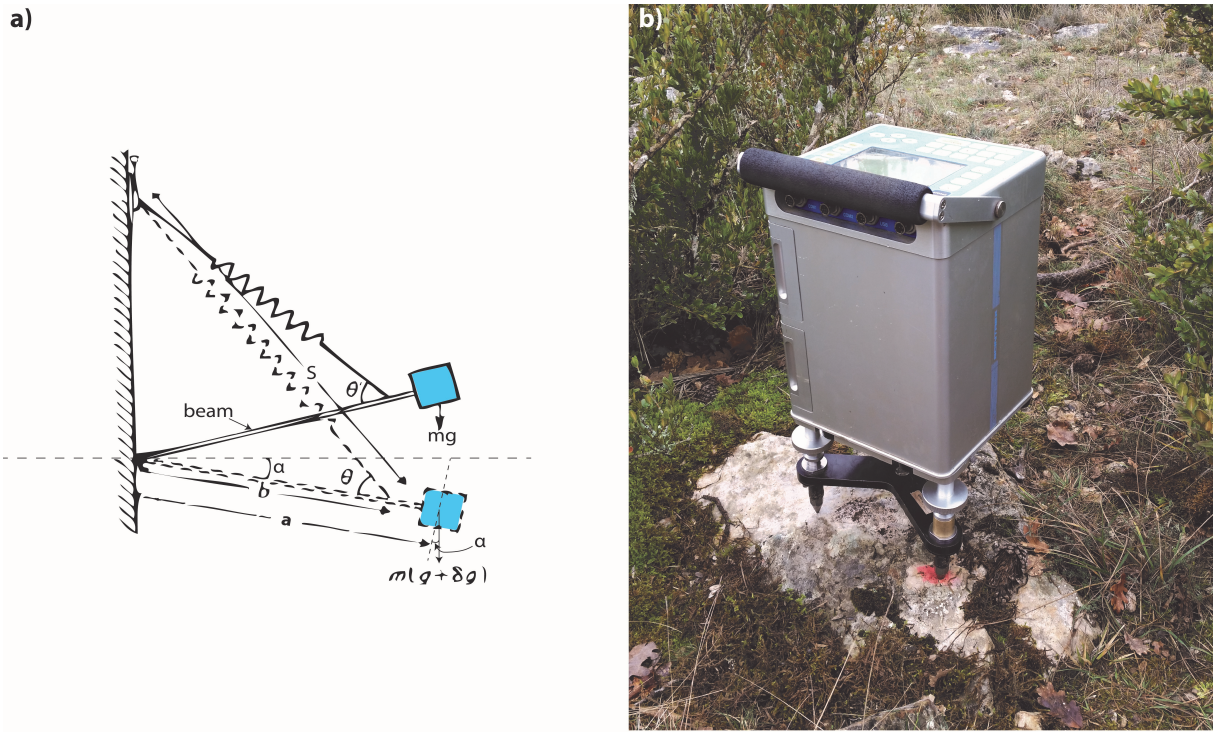

Figure 2.7: *a) Principle of spring-base gravimeter. b) The CG5 relative gravimeter from Lacoste & Romberg.*

2.4 Solving inverse problems

When the parameters of a model are known, the physical theories allow us to predict the resulting measurements (e.g ground displacement or tilt). This is called the forward problem. By contrast, the inverse problem aims at inferring the parameters of a given model using the observations. This implies that an inverse problem does not necessarily have a unique solution contrary to the forward problem which generally gives a unique solution for one set of parameters. The core of this work is about the optimization of inverse problems in geodesy. By inverse problems, we mean the process of estimating the parameters producing surface observations. Optimization refers to the process of minimization or maximization of a cost function by finding the best set of parameters in a defined domain.

2.4.1. Some background about inversion theory

The inverse problem consists in finding an optimal set of model parameters p explaining the observations d^* (Tarantola, 2004) such as,

$$d^* = G(p) \tag{2.10}$$

where G represents the governing equation relating the model parameters p to the observed data d^*. The operator G can be linear or non-linear depending on the complexity of the relation between the model parameters and the observations. Each component of the parameter p can be seen as one degree of freedom of the system while each equation introduced in G is a constraint for one degree of freedom.

By considering a linear problem, Eq. (2.10) reduces to:

$$d^* = Gp \tag{2.11}$$

Ideally, solving an inverse problem consists in inverting the matrix G to directly infer the parameter from the observations. Eq. (2.11) becomes

$$p = G^{-1}d \tag{2.12}$$

where d is the modelled data. Because G is usually not invertible, this latter relation cannot be directly applied.

To solve the inverse problem, one needs to compare the predicted data (d) from the model to the observations (d^*). The comparison is made through the functional hereafter named J, a function that measures the fit between modeled and observed data. Minimizing this difference is the goal an optimization algorithm. For noise-free data and a valid forward model of the phenomenon, the fit should be perfect. A common objective function (or functional) is often characterized by the L-2 norm of the misfit between the observations and predicted data.

$$J = \|d^* - d\|_2^2 \tag{2.13}$$

Inverse problems are typically ill posed, as opposed to the well-posed problems more typical when modeling physical situations where the model parameters or material properties are known. Jacques Hadamard first introduced the concept of a well-posed problem

which is characterized by three conditions: existence, uniqueness, and stability of the solution or solutions (Hadamard, 1902). Figure 2.8 represents geometric views of those conditions depending on the convexity of the functional. If the functional admits a solution for the given parameters, the optimal case would be that the solution is unique and stable (Figure 2.8a). However, it is not usually the case. The stability refers to whether the solution is substantially changed when the perturbations are introduced in the optimal state. For instance, the noise affecting the data may produce arbitrarily large errors in the solutions. The solution is said non-unique when multiple sets of parameters give the same minimum value of the functional (Figure 2.8b). Because real data contains noise and sometimes more complex signals (*e.g.* drift), inverse problem in geophysics are more likely to have no exact solution (Figure 2.8c) or even local minima (Figure 2.8d). Thus the smallest value of the functional within a given range is a local minimum as long as the entire domain of the functional has not been analyzed. If a minimum is also the smallest value of the entire domain, then it refers to the global minimum of the function. This latter value is the goal of an inverse problem that can be solved using different approaches (see Section 2.4.2.).

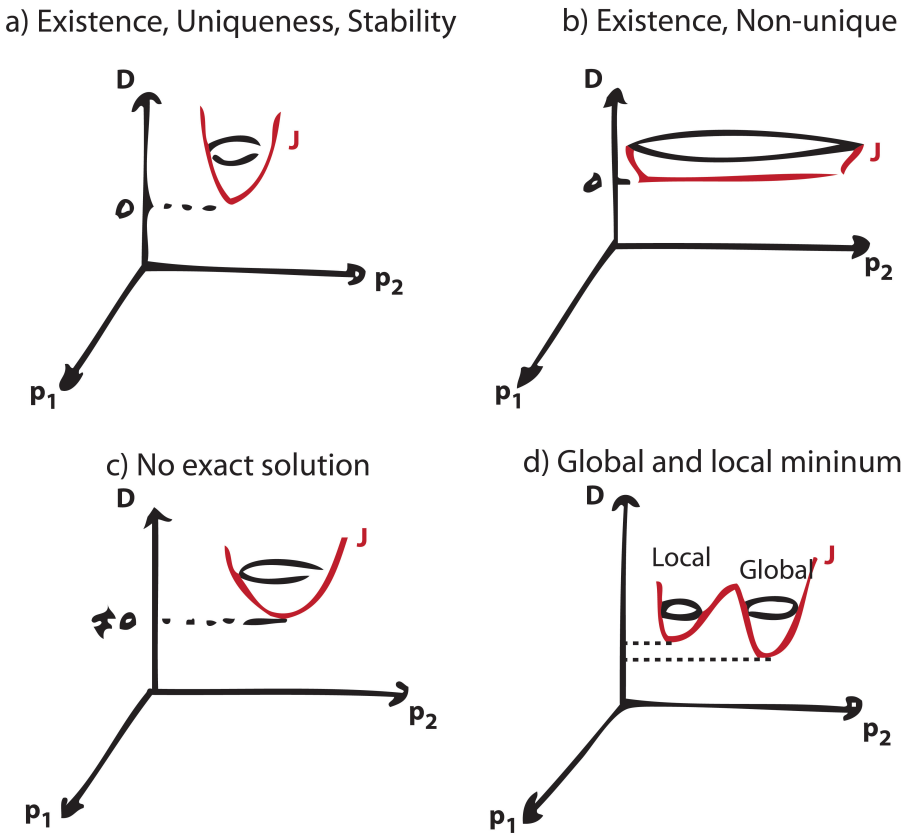

Figure 2.8: *Geometric views of different behaviours of the functional J with D the quadratic distance between the observed and predicted data and p_1 and p_2 are model parameters. a) A well-posed problem according to Hadamard's definition (Hadamard, 1902), b) the problem converges towards 0 but is non-unique, c) J has a unique minimum but the solution is not exact it does not fully explain the data and d) non-convex J admitting local and global minima, which is usually the case in geophysical inverse problems.*

When inverting geodetic data, we are exploring a functional with an unknown behavior including data uncertainties and a specific parametrization. In most geodetic inverse problem, a limited number of observations describe a finite number of unknown parameters, leading to an ill-conditioned problem. Therefore such problems are not well posed in the sense of Hadamard, but one can develop methodology of optimization that tends to approach Hadamard's conditions: if a global minimum exists (even if it is non-null), the inversion process should find it with respect to the data uncertainties and all additional signals. If more unknowns p than available equations are considered, the system is underdetermined : there are not enough constraints restricting the degrees of freedom. In such case, G (from Eq. (2.11)) is not invertible and the solution p provided by the inversion is non-unique. Uniqueness of the solution can be targeted considering *a priori* constraints at different steps of the optimization: either during the process (*e.g.* a Tikhonov regularization introduces additional information to solve ill-posed problems or to prevent overfitting) or once the minimization is completed. This ensures smoother and more stable results.

In the following studies, we could implement both approaches, depending on the *a priori* information. To minimize the objective function, different algorithms can be considered.

2.4.2. Optimization algorithms

Optimization algorithms aim at resolving an inverse problem by minimizing a functional involving a parameter set. The choice among different classes of algorithms is dictated by the available knowledge of the functional and also by computational issues. In most cases, only local minima are determined and reaching the global minimum is not guaranteed. In Chapter 4, I detail the algorithm allowing us to approach the global minimum of a general functional. But first, I give an overview of stochastic algorithms and gradient descent algorithms.

2.4.2.1. Stochastic optimization

Such methods of optimization generate and use random variables, from random functionals to random constraints. For instance, Markov Chain Monte Carlo methods (MCMC) are a class of computational algorithms that calculates an approximated numerical solution based on repeated random sampling. Monte Carlo methods rely on an objective function which is used in the forward problem to calculate the difference between modelled and observed data. A probability density function is associated to these values of the objective function to determine the optimal set of parameters. At the end there are as much objective functions as random sampling, defining the probability of the parameter set to give the smallest objective function. Even if the random search process is potentially inefficient and therefore slow, it converges towards an optimum. They allow the simulation of systems with multiple coupled degrees of freedom. Sambridge and Mosegaard (2002) gives an exhaustive review of the widespread use of Monte Carlo methods in geophysics. They are commonly used in inversions applied to fault characterization (*e.g.* Yabuki and Matsu'ura, 1992; Minson et al., 2014), reservoir characterization (*e.g.* Hesse and Stadler, 2014; Maerten et al., 2016, magmatic systems characterization (*e.g.* Fukushima et al., 2000; Obrizzo et al., 2004; Segall, 2013; Anderson and Poland, 2016).

2.4.2.2. Gradient-based algorithms

The lost hiker. *The philosophy of the approach can be explained using a simple analogy. Let's imagine a hiker trapped by a heavy fog in the mountain and trying to get down, i.e. trying to reach the valley (the minima). Therefore, the value of the function J is the current altitude of the hiker. Due to the fog, the path is almost invisible except in the immediate vicinity of the hiker. Hence he must use the local information to find the direction of the valley. The most obvious way to do so is to look at the steepness of the hill at its current position and heads toward the direction of the steepest descent. In this analogy, the hiker stands for the algorithm which explores the sequence of parameter settings symbolized by the path. The steepness of the hill represents the local slope at the current point, i.e. the gradient of the functional.*

A gradient descent is a first-order iterative optimization algorithm (considering the first derivative only of a Taylor development) also known as steepest descent. It aims at finding the minimum of a functional generating a series of parameters allowing to approach the target at best. The search direction is defined by the gradient of this functional at the current point. The local minimum is thus iteratively determined by estimating the gradient then moving to the next point in the direction of the negative gradient. The value of the step ρ used to move to the next value can be constant at each iteration or several ρ can be tested to find the one giving the smallest value. Starting from a fixed initial value x_0, the algorithm seeks the nearest local minimum of a function by stepping from the current stage x_i to the new one x_{i+1} by minimizing the local downhill gradient $-\rho\nabla J(x_i)$.

Gradient descent strategy is working in spaces of any dimensions, even in infinite-dimensional ones. The gradient descent can take many iterations to compute a local minimum with a required accuracy, if the curvature in different directions is very different for the given functional. Methods based on Newton's method and inversion of the Hessian using conjugate gradient techniques can be better alternatives (Nocedal and Wright, 1999). Generally, such methods consider the second order of a Taylor development and converge in fewer iterations, but the cost of each iteration is higher.

Gradient-based algorithms are probably not the most common algorithms to retrieve model parameters but numerous geophysical applications can be found in the literature for electromagnetic (*e.g.* Cockett et al., 2015) or gravity (*e.g.* Qin et al., 2016; Zhaohai, 2016) data inversions. In this work, I use a methodology of inversion based on the steepest gradient descent method.

2.4.2.3. Semi-deterministic approach

We previously distinguished deterministic approaches, which involve no degree of randomness, from stochastic approaches based on a random sampling of the parametrization space. The present work is based on the development of a semi-deterministic approach, meaning that we consider a deterministic approach with some degree of randomness (Ivorra, 2006). The algorithm later described in Chapter 4 is based on a steepest gradient descent to seek local minima from an initial set of parameters. But a mix of gradient descent and stochastic approach is superimposed to the gradient method to expand the search by randomly choosing new sets of initial parameters. This allows to cover a wider domain of the functional and eventually to converge towards the global minimum.

2.4.3. Integrating multiple geodetic data

When inverting data of different natures, various terminologies are used including joint inversion, data fusion or data assimilation. Because the differences between those process are sometimes not well stated, I define here what I call joint inversion, data fusion and data assimilation.

Joint inversion can be achieved if all the different data are linked to a common physical model. This forward model describes the state of a system at a given time. For example, analyzing surface deformation observation, requires joint inversion strategies to invert multiple types of data with cross parameter constraints (*e.g.* Colombo et al., 2007; Palano et al., 2008; Segall et al., 2013; Geirsson et al., 2014). The objective function for this joint inversion problem can be formulated following the theory explained in Tarantola (2004) by simply summing the squared data misfit normalized by their covariances. A weighting factor can also be introduced to scale each data type contribution.

Alternatively, when speaking of data fusion or data assimilation, one combines heterogeneous data. More specifically, data assimilation uses new data to improve the definition of the model deduced from previous observations. At each time interval, the previous state of the model is considered to produce the best solution. Firstly developed and mainly used for meteorology (*e.g.* Wilgan et al., 2015) or hydrology forecasting (*e.g.* Alvarado-Montero et al., 2017), geophysical applications of data assimilation can also be found (*e.g.* Wilschut et al., 2011; Hesse and Stadler, 2014; Zhan and Gregg, 2017).

The goal of this work is to assemble different kinds of data using a single forward model in order to describe the evolution of a time dependent system. Based on the previous definitions, we present in this manuscript a methodology of joint inversion of time-dependent geodetic data. The corresponding methodology is described in Chapter 4.

Chapter 3

Challenges of geodetic inverse problem: a common methodology for mining, oil and gas and volcanic strain?

Résumé

La déformation du sol a lieu à des échelles spatiales et temporelles très variées. Dans ce travail, nous nous intéressons aux mouvements au sein des réservoirs géologiques. Nous appellons réservoir géologique, un lieu oú sont accumulées des réserves, qu'elles soient minérales, liquides, solides ou gazeuses. La variation de ces réserves, d'origine naturelle ou induite par l'activité humaine, est la cause des déformations. Nous considérons dans ce manuscrit les réservoirs (1) volcaniques, (2) miniers et (3) pétroliers (huile et gaz). En effet, ces trois types de réservoirs sont particulièrement bien instrumentés et étudiés d'un point de vue géodésique du fait des risques qui y sont associés ainsi que la gestion de leur exploitation. Nous présentons des exemples concrets de ces 3 réservoirs afin de discuter des enjeux qui leurs sont associés:

1. ***Volcanique**: le système magmatique du Kīlauea (Hawaï);*
2. ***Minier**: le comportement des cavités salines (extraction et lessivage) à Vauvert (France);*
3. ***Réservoirs pétroliers non-conventionel**: l'extraction de gaz en Argentine (par Total S.A)*

Au cours de ma thèse, j'ai eu l'occasion de m'impliquer dans l'étude de ces différents réservoirs. En collaboration avec Kyle Anderson de l'USGS, j'ai traité et inversé les données de tilt et de GPS issues de l'éruption de 2011 du Kīlauea. En outre, j'ai également contribué à l'installation d'instruments sur le site de Vauvert. Enfin, j'ai participé aux réflexions concernant le design d'un site pilote en Argentine qui vise à installer un réseau de inclinomètres pour la surveillance de l'extraction de gaz. Je prévois de réaliser une modélisation de ce design avec les outils développés dans la thèse.

Je présente dans ce chapitre les différentes caractéristiques de chacun de ces réservoirs et la déformation de surface qui leur est associée. Une revue des enjeux de la modélisation, me conduit à proposer une méthodologie d'optimisation commune à ces 3 systèmes.

3.1 Introduction to geologic deformation sources

The geodetic techniques (described in Chapter 2) provide a time-space record of the surface deformation above various kinds of reservoirs among which volcanoes are probably the most monitored and studied because of their high associated hazards and/or risks (Fernández et al., 2017). Some sites like Kīlauea or Etna volcanoes are widely instrumented thanks to their readily access, recurring activity (at human time-scale) and research centers means. Geological reservoirs such as salt mines also host some geodetic instruments or surveys, due to legal obligations asking for the monitoring of the induced deformation at the surface. For confidentiality reasons, dataset containing several types of data are more seldom for oil and gas unconventional reservoirs, though several tilt and InSAR surveys have been conducted on various plays to control the fracking process and its consequences (Castillo et al., 1997; Olson et al., 1997; Warpinski et al., 1997; Fisher and Warpinski, 2011; Warpinski, 2014; Jha et al., 2008; Zhou et al., 2015; Caffagni and Bokelmann, 2016). For this reason, publications including inversions of multiple datasets on Oil & Gas reservoirs are yet uncommon.

We develop a methodology to answer issues for those three types of reservoirs that I describe hereafter.

1. **Volcanic systems**. Widely monitored by geodetic systems along with other sismological and geophysical instruments and geochemical measurements, volcanoes provide one of the best examples of large surface displacement. The main source of this deformation, the volume change of magma in the magmatic chamber, is often treated like a point source (Mogi or McTigue models, *e.g.* Segall, 2010; Lingyun et al., 2013) while dikes propagation is usually modelled by a planar dislocation (Okada's model, *e.g.* Fukushima et al., 2005; Lundgren et al., 2013). The case of Kīlauea Volcano is particularly studied thanks to its extended geodetic network and the accessibility of both site and data (`https://volcanoes.usgs.gov/volcanoes/kilauea/`).

2. **Salt mining**. Mining activities are commonly subjected to monitoring due to the surface deformation induced by this industry. Because of its long term subsidence history, geographic location and the numerous available data, the salt exploitation of Vauvert (Gard, France) is particularly interesting (Godano et al., 2012). Previous studies (Raucoules et al., 2003, 2004) have highlighted a quasi-perfect spherical bowl of subsidence in Vauvert. As a result, we assume that the extraction of salt from deep layers can be assimilated to point sources in this case. Indeed, a dozen of wells are continuously extracting the salt under the form of brine from lower saliferous layer at a depth ranging from 2000 to 3000 m.

3. **Unconventional reservoirs**. During the exploration stage, oil and gas companies conduct geophysical surveys (seismic reflexion/refraction, borehole seismic, well logging) to estimate the potential of conventional and unconventional Oil & Gas reservoirs. While extracting the resource, they can also monitor this extraction using repeated surveys or continuous measurements. These methodologies have provided stable and reliable results but they remain expensive and limited. As the process of

fracking can be considered as a sum of many planar dislocations (Okada's model, Astakhov et al., 2012; Warpinski, 2014), we could give a first approximation of the induced deformation at the surface with a spatially optimized geodetic network and using an appropriate mechanical model.

During my thesis I was partially involved in the study of the aformentioned geological systems. In particular, I treated in collaboration with Kyle Anderson from USGS (Menlo Park, USA) GPS and tilt data from the 2011 Kamoamoa eruption Kilauea Volcano and inverted them considering a Mogi source. Furthermore, I contributed to install three GPS stations and one tiltmeter on the extraction site of Vauvert. Further work has to be done on the application of the inverse method on these three sites, representing important perspectives of the present work. In a near future, I plan to design the experimental site on Total S.A. exploitation in Argentine. In collaboration with Aquitaine Electronique, an array of 20 optical tiltmeters is planned to be deployed on the field to monitor the different steps of gas extraction. In this chapter, I describe these three geological reservoirs along with their actual methodological challenges in order to conclude on the relevance for a common methodology for inverting geodetic data.

3.2 Volcano deformation modeling

3.2.1. From surveys to monitoring

In the early years of volcano studies (before the 20^{th} century), scientists were conducting surveys and short-lived expeditions on volcanoes, usually as a response to major eruptions. The concept of volcano monitoring which consists in studying volcanoes before, during and after eruptions, was introduced by the volcanologist Thomas A. Jaggar, Jr. when founding the Hawaiian Volcano Observatory in 1912. Nowadays (in 2018), 79 observatories are continuously monitoring hundreds of volcanoes over the planet.

3.2.2. Deformation sources

On its way to the surface, the magma modifies the surrounding rocks and fluids creating cracks, conduits and underground reservoirs. This induces a pressure change in the medium, which is reflected on the surface by displacements that may progressively reshape the volcano. Inflation of the surface occurs when magma accumulates in reservoirs or fractures while deflation is observed whenever the magma eventually erupts emptying the reservoirs and conduits. Shape variations due to inflation and deflation are determined by ground-deformation measurements such as GPS velocities (*e.g.*: Fukushima et al., 2005; Peltier et al., 2009), InSAR displacements (*e.g.*: Yun et al., 2006), levelling (*e.g.*: Obrizzo et al., 2004), tilt (*e.g.*: Anderson et al., 2010; Gambino et al., 2014), strain (*e.g.*: Sturkell et al., 2013) or gravimetry data (*e.g.*: Poland and Carbone, 2016). The analytical models presented in Chapter 2 allow to approximate such deformation. For instance, the volumetric changes undergone by a reservoir when magma fills it or erupts are usually modelled by spherical sources (Mogi, 1958; McTigue, 1987). Besides isotropic sources, other analytical models have been developed to account for more sophisticated

source geometries and mechanical models yet tractable using analytical modelling. Among those models, prolate spheroid (Yang et al., 1988), ellipsoid (Davis, 1986b), spherical source embedded in a viscoelastic shell (Dragoni and Magnanensi, 1989) and open and closed pipe (Bonaccorso and Davis, 1999) can be used to model more complex sources requiring more parameters. Also, magma traveling through the medium can create cracks or reactivate preexisting fractures. The resulting dikes of sills can therefore be modelled like the opening of planar dislocations (Okada, 1992) or even penny shaped cracks (Fialko et al., 2001). All those analytical models can be combined to build a complex model of deformation, under the assumption of flat topography and homogeneous medium.

3.2.3. Plumbing system of Kīlauea, Hawaii

Kīlauea volcano is located on the island of Hawaii, on the southeastern slope of the largest active volcano on Earth, Mauna Loa volcano. Topographically, Kīlauea appears as only a bulge on the flank of Mauna Loa (Figure 3.1). Long thought as a satellite crater of Mauna Loa, Kīlauea appears to have its own magma-plumbing system (Tilling et al., 2010).

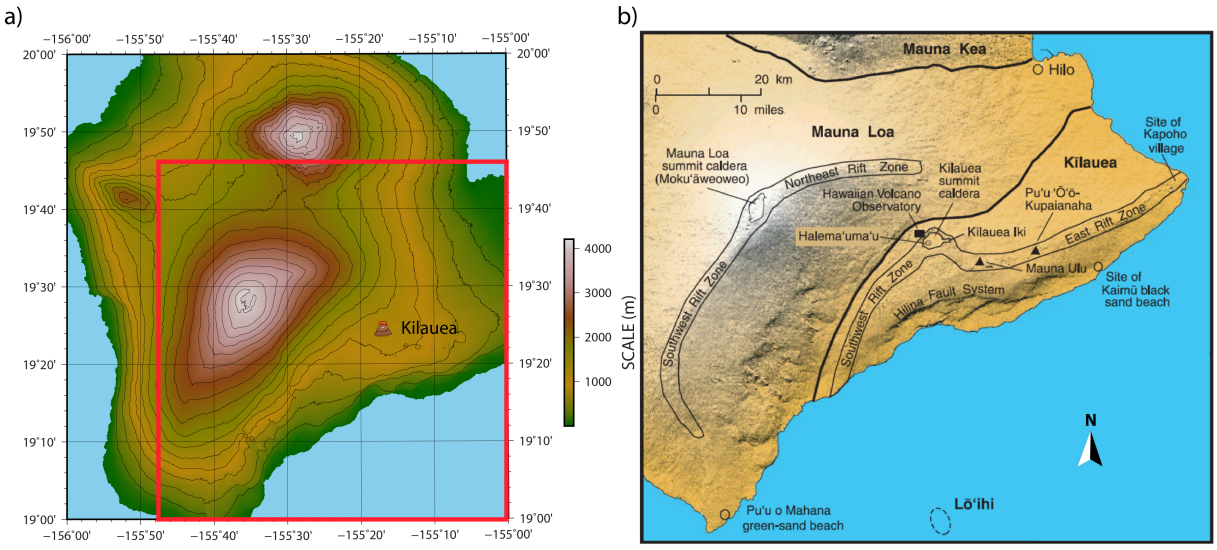

Figure 3.1: *a) Topographic map of the Island of Hawaii and focus on the South-East part of the island, on Mauna Loa and Kīlauea volcanoes. b) Volcanic activities are gathered within Kīlauea summit caldera (Halema'uma'u lava lake) and Southwest and East Rift Zones (SRZ and ERZ) where Mauna Ulu and Pu'u 'Ō'ō are craters of Kīlauea. The Hawaiian Volcano Observatory is located on the border of the summit crater.*

Volcanic activity at Kīlauea is known to be continuous along the East Rift Zone (Figure 3.1) since 1983, with some peaks of more violent activity such as the ongoing eruption (started on the 2^{nd} of May 2018). The magma supplies to the lower East Rift Zone generating one of the most significant eruption of the past few years with multiple fissure eruptions, and even explosive eruption of ash punctually occurring at the summit crater. This intense volcanic activity is monitored by a complete geodetic network (Figure 3.2)

including GPS stations and surveys, levelling routes, tiltmeters, strainmeters and InSAR studies (Tilling et al., 2010).

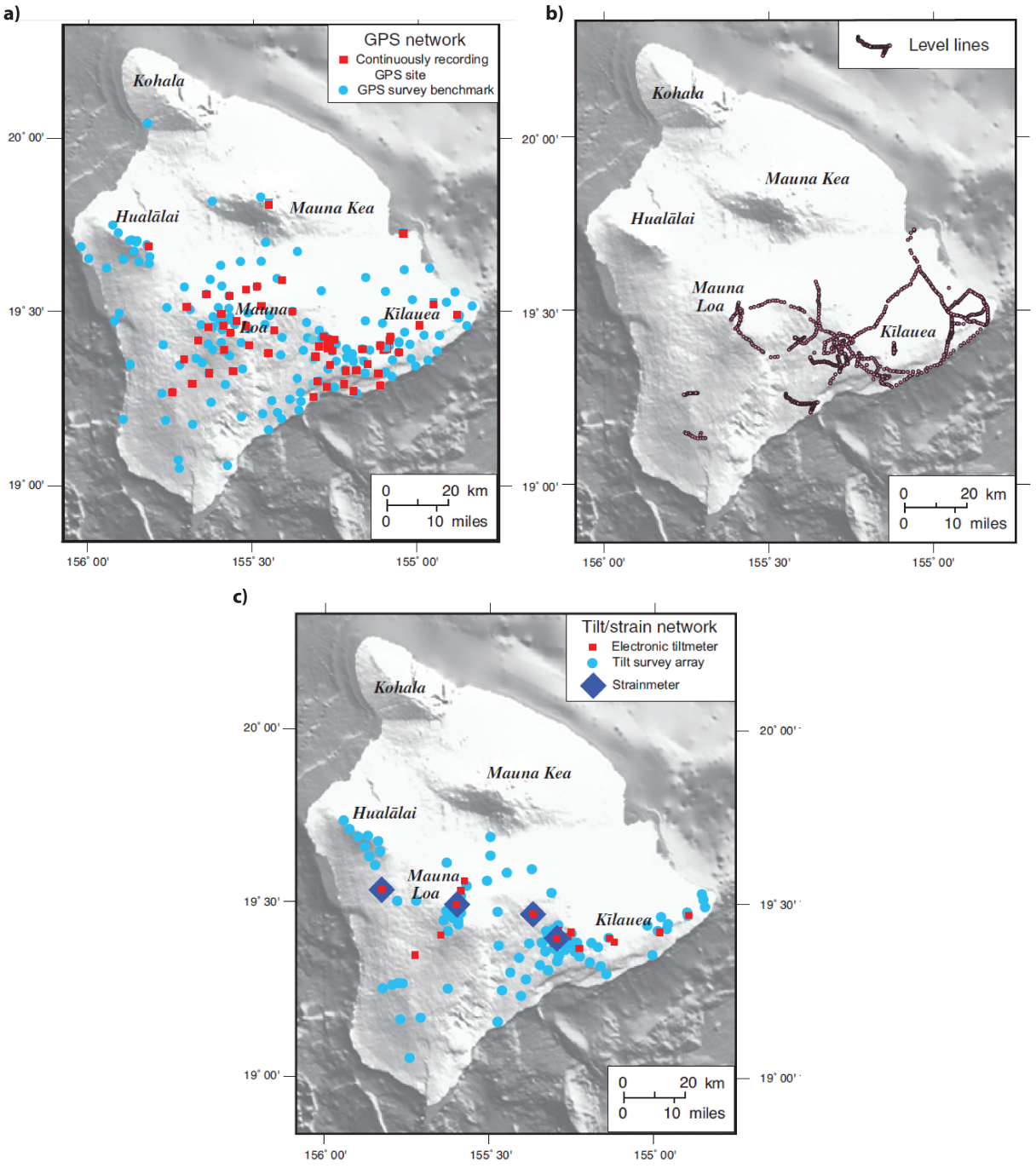

Figure 3.2: *Geodetic network of Hawaii with a) Continuous GPS stations (red squares) and survey benchmarks (blue dots), b) levelling lines and c) electronic tiltmeters (red squares), tilt survey arrays (blue dots) and strainmeters (blue diamonds) (from Tilling et al., 2010).*

Because I partly processed and analyzed data associated to the 2011 Kamoamoa eruption (4-9th March 2011), I display on Figure 3.3, GPS and tilt data from the summit station of the Kilauea (UWEV and UWE respectively). With a daily sampling, the three components of GPS record events of low frequency while tiltmeter measure high frequency events (one data per minute). Figure 3.3 illustrates the typical order of magnitude of displacements occurring on volcanoes (from several cm up to several tens of cm for strong eruptions). For instance, the slow inflation of the caldera started almost 4 months prior to the rapid deflation of 9.3 cm measured by the GPS. The tilt signal associated to this event is as large as 71.6 μrad. On Figure 3.3b, higher frequency events (typically Deflation-Inflation events) can be detected with tiltmeters.

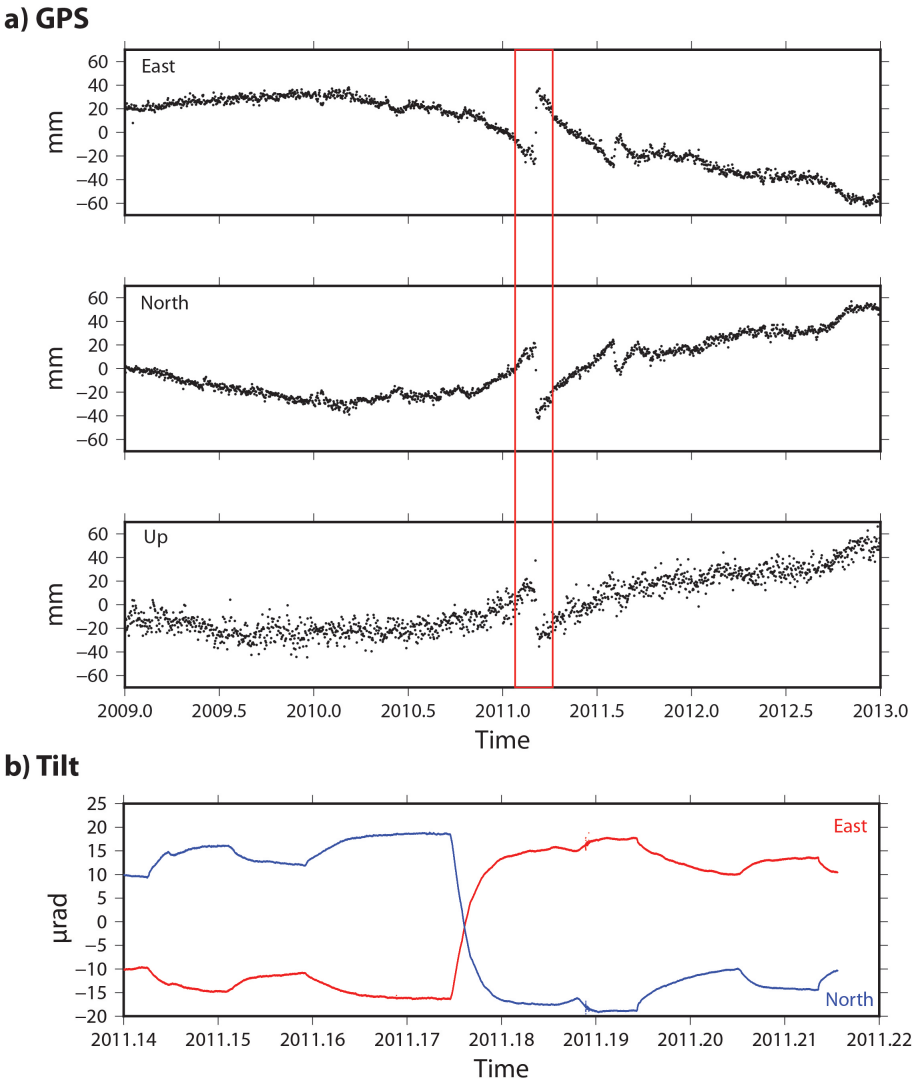

Figure 3.3: *a) Summit GPS (UWEV station) signal from 2009 to 2013 (from top to bottom: East, North and Up components). The red rectangles indicates the interval considered for the display of tilt data. b) Plot east-west (red) and north-south (blue) tilt from summit tiltmeter (UWE station) from February 20th 2011 through 20th March 2011. The Kamoamoa eruption occurred on the 4th of March.*

Apart from this specific event, the continuous activity of Kīlauea consists in short and long-term trends of summit inflation and deflation, rift zone opening, slow slip events, intrusions, formation of new eruptive vents, and other volcanic and tectonic changes. Let's now focus on deflation-inflation (DI) events occurring over periods of hours to days (rapid and cyclic summit inflation and deflation). Because they are one of the most common signals measured by geodetic network (GPS, InSAR, strain and tilt) they can be used to specify the shallow magmatic plumbing of the volcano as they are also strongly correlated to levels of lava lake from both the summit crater and Pu'u'Ō'ō crater (slightly shifted in time due to its location, Figure 3.1). For the 2011 Kamoamoa eruption (Figure 3.3), these changes in levels of lava lake were studied using gravimetric data (Poland and Carbone, 2016).

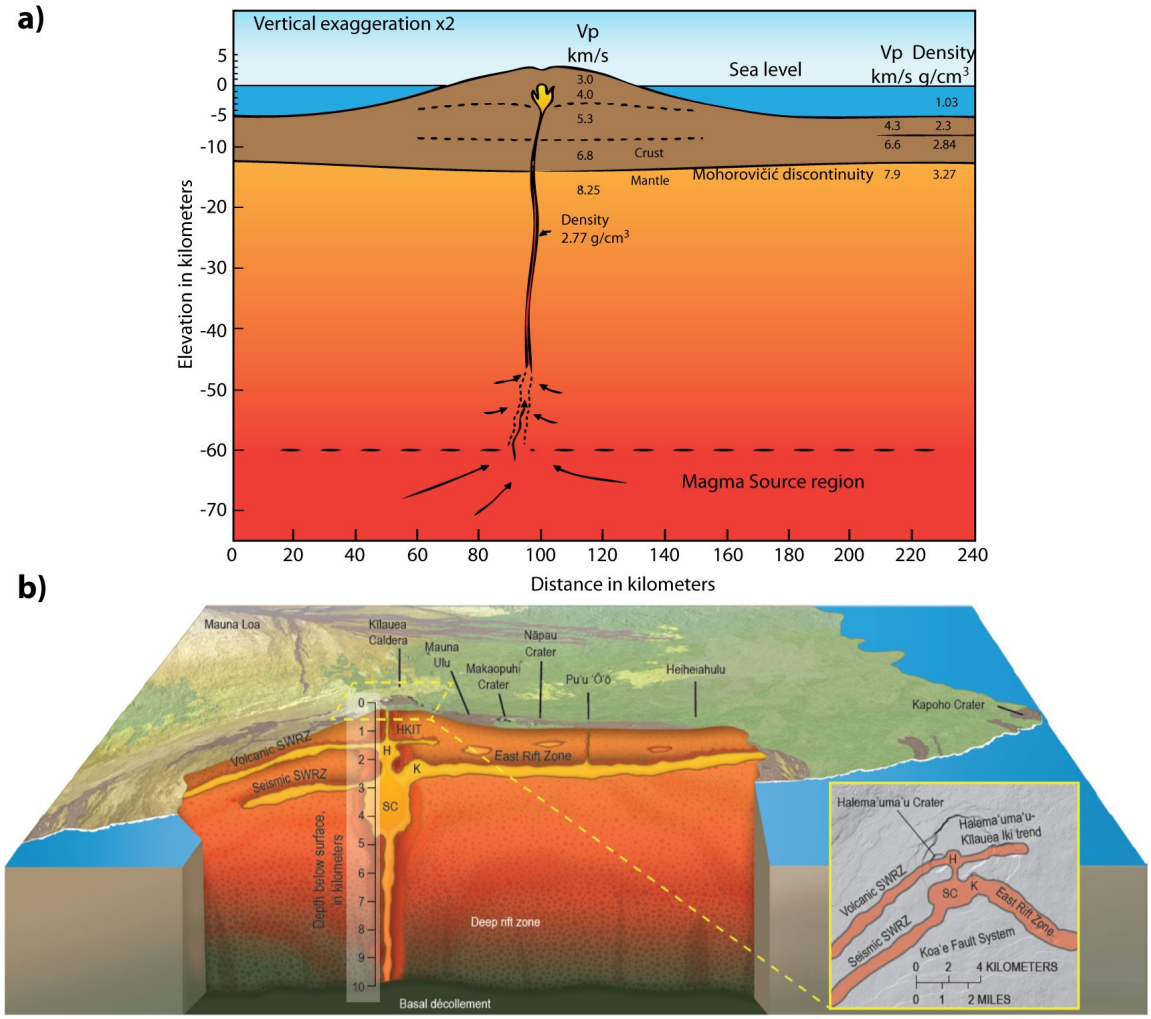

Figure 3.4: *Interpretations of magmatic plumbing system of Kīlauea Volcano as a) Eaton and Murata (1960) first suggested and b) proposed by Poland et al. (2014)*

The scientific community has long been interested in the magmatic plumbing system of Kīlauea. Following the model anatomy for the volcano proposed by Eaton and Murata (1960) and later refined by Tilling and Dvorak (1993), the magma uprising from the mantle underneath Kīlauea was stored in a shallow reservoir near the summit caldera (at

few kilometers depth, Figure 3.4a). From there, the magma can either erupt in the caldera or create fissure eruptions in the East or Southwest Rift Zones. Nowadays, numerous studies aim at defining the plumbing system of the Kīlauea (Zurek, 2007; Lundgren et al., 2013; Poland et al., 2014; Anderson et al., 2015; Orr et al., 2015; Zhai and Shirzaei, 2016) using geodetic data and sometimes geochemical data. They agree on the complexity of the system which includes a deep reservoir between 3 to 5 km deep feeding a shallower reservoir about 1.5 km deep (Figure 3.4b). Nevertheless, few studies has yet jointly inverted more than two data types. Therefore, the geometry (size and shape) of the summit magma storage reservoir as well as the connections between the magmatic chambers and the volcanic activities in rifting zones remain poorly constrained.

Because the volcanic activity of Kīlauea is monitored by such complete geodetic network (Figure 3.2), the following studies could be relevant for the characterization of the magma plumbing system:

1. **Joint inversion of geodetic data.** The evolution of volume changes over time could be modelled using long time series of various data types.

2. **Tilt inversion during Deflation-Inflation events.** Deflation-Inflation events are particularly well recorded on the summit tilt network because of the high sensitivity and temporal resolution of borehole tiltmeters. If one can estimate the long-term drift of those instruments, the source of Deflation-Inflation events could be more accurately described. In turn, this would probably improve the knowledge of plumbing system.

3.3 Salt mining and induced strain

3.3.1. About the salt

Rock salt (halite) is a sedimentary rock formed by the evaporation of sea water under specific conditions at different geological times. These layers of salt are generally covered by rock formations. They are located underground or inside mountains, though some can also be found on the surface in desert regions. The buried layers of salt can be mined for chemistry or hydrocarbons storage. They mainly contain crystals of sodium chlorite (NaCl), but can also include impurities such as clay, anhydrite or calcite. The rocksalt is particularly resistant to isotropic compression but creeps under lithostatic pressure with a typical viscosity ranging from 10^{17} to 10^{20} Pa.s (van Keken et al., 1993). Variations of composition and conditions of crystallization of the salt influence the creeping velocity by a factor from 1 to 20, as well as its water-solubility.

3.3.2. Deep rock salt reservoirs: case of Vauvert (France)

The deep salt deposit of Vauvert (Gard, France) has been discovered during the 1952-1962 oil survey conducted by ELF (Valette, 1991). Since 1972, the company *KemOne* (previously *ELF ATOCHEM-Saline de Vauvert*) is extracting the salt from deep reservoirs (2500-3000 m) in the form of a solution saturated in salt, the brine. The salt deposit

of Vauvert belongs to one of the on-shore half-graben of the extensional Camargue basin, located in the Gulf of Lion passive margin (southern France). This graben results from the Oligo-Aquitanian rifting of the margin during the Mediterranean Sea expansion. This distensive phase spreads from -30 to -15 My and affects the rim of the Alpine belt (Pyrenees, Languedoc, Gulf of Lion, Camargue, Valentinois, Bresse, Rhine plain). The NE-SW oriented basins are controlled by the SE-dipping Nîmes normal fault (Figure 3.5).

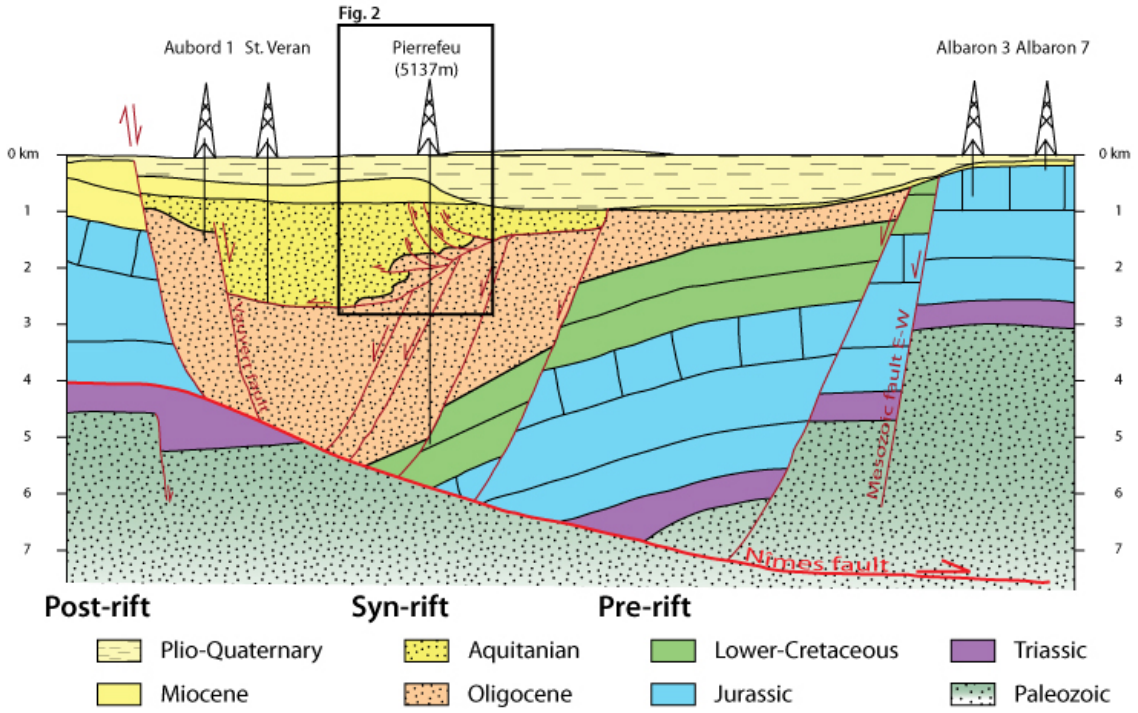

Figure 3.5: *Geological cross-section (NW-SE) across the Camargue Basin. The site of brine exploitation is delimited by the black rectangle (from Valette and Benedicto, 1995).*

Camargue basin contains up to 4000 m of syn-rift sediments which overly a substratum of carbonates from Lower Cretaceous (-130 My). The rapid Oligo-Aquitanian sedimentation formed a succession of continental to lagunal series generally found between 900 and 4900 m deep (Figure 3.6):

1. The **Clay series** gathers 2 sub-series: the *"gray series"* (2000 m-thick of deposit of clay, sand, limestone, marl, conglomerate and lignite) and the *"red series"* (200 m of clay and gypsiferous marls with several intercalations of marl and sand of palustrine environment);

2. The **Saliferous series** (900 m-thick) with four formations: the infra-saliferous, the lower saliferous, the intermediate marl and the upper saliferous formations;

3. The **Marine clay series** range from 800 to 1500 m-thick and correspond to three sequences of Aquitanian deposits, mainly composed of clay with insertion of limestones, sandstones or bench of dolomite.

During the Miocene crustal spreading, syn-rift sediments were covered by transgressive Burdigalian marine sediments and coastal molasses before being uplifted and eroded during the Messinian event (from 5.96 to 5.33 million years ago). The whole formation was finally overlaid by one last stage of sedimentation occurring during the Pliocene. This geological description is described in Valette and Benedicto (1995).

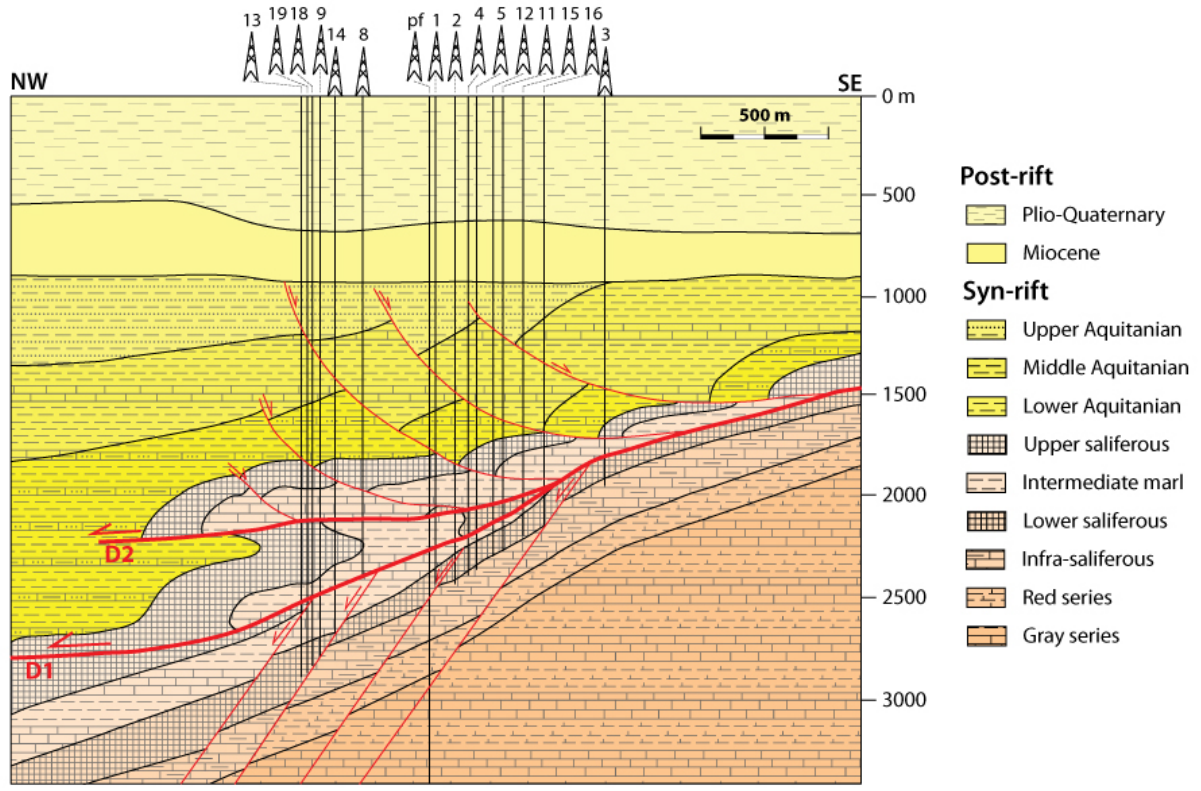

Figure 3.6: *Geological structural scheme of the concerned area, Vauvert (from Valette and Benedicto, 1995).*

3.3.3. Extraction and induced deformation

In-situ leaching (ISL), also called solution mining is either used to create caverns in the rock salt layer for gas storage or to recover the salt in the form of brine that is then transformed into chlorine and caustic soda. This process works by artificially dissolving minerals occurring naturally in a solid state. When the extraction of salt aims at storing hydrocarbons, only one well is drilled (Figure 3.7a). Water is then injected in the central part of the tube (or in the annulus) and dissolves the salt on its way up (or down). Brine is produced by the annulus (or in the central part).

If the extraction aims at recovering the salt for further transformation, two to more wells can be hydraulically connected in the salt layer by initial or induced fracturation of the medium. A configuration of two wells is defined as doublet and occasionally, triplet can also be used. Water is injected in one well and brine produced in the other well (or wells)(Figure 3.7b). To increase the productivity of doublets, water can be alternatively injected in one and the other well (Valette, 1991).

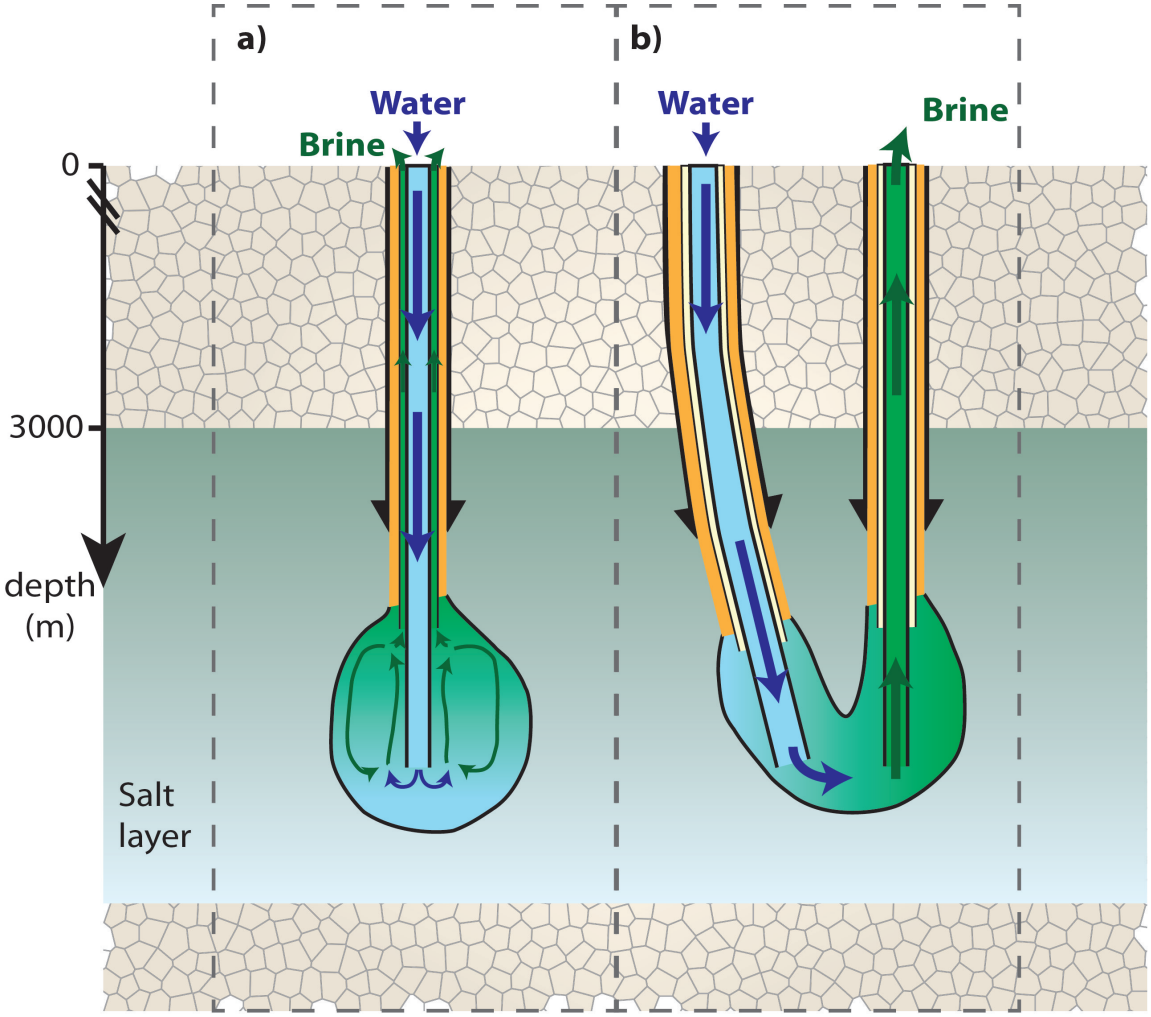

Figure 3.7: *Solution mining a) for the creation of cavities in the rock salt layer to store hydrocarbons or b) for the recovery of brine used in the chemical industry.*

In few cases, additional hydraulic fracturation is necessary to reconnect doublets (1) because the complexity of the salt layer (fracture, insoluble sublayers) may damage the well or (2) as a result of cavern growth along the well decreasing the strain on the tube and leading to the end of the tube to break. In both cases, the well is sealed by a plug and extraction is translated upward in the salt layer.

When the quality of the extracted brine does not conform to the expectations, the brine is used to complement another depleted brine until the doublet is sealed at the surface. In such case, due to salt creeping an increase in pressure will be observed at the well head. When this surface pressure reaches the lithostatic pressure of the cavern, it must be released to insure security of the exploitation and integrity of the well. After a rapid decrease in pressure, the well is drained during several years (up to several decades). The pressure of the residual brine at depth induces the creep of the salt until the cavern closure (Bérest et al., 2001).

At the salt exploitation of Vauvert, 43 wells (doublets or triplets with two wells under

construction) were directly drilled in the salt layer to dissolve the anhydrite (Figure 3.9a). Among those wells, 14 are extracting brine, two are being drained and the others are abandoned. For the active sets, water is injected in one well at a pressure of 95 bars, while the second extract the brine at 2 bars. The underground circulation of fluid is allowed by the fracturation created to connect the wells. This brine is then concentrated and stored in a basin before being carried to Fos-sur-Mer, 70 km South-East of Vauvert. In 2017, up to 1 million of tons of brine were extracted from about 4 active doublets (two as backup doublets). The brine is then used in the chemical industry to produce chlorine and caustic soda.

Let's look at the extraction with numbers (Figure 3.8). Considering that the brine has a salt content of 250 to 310 kg/m^3 and rock salt has a volumetric mass of 2160 kg/m^3, the creation of a cavity of one cubic meter of salt produces around between 7 to 8.5 m^3 of brine. Because part of the injected water replaces the salt downhole, more than 8.5 m^3 of injected water is necessary to produce the above quantity of brine. Using these parameters and considering as an illustration 712 days of data between January 7th 2015 until December 12th 2016, the doublets PA36-37 of the site of Vauvert produced 1.85 million of cubic meters of brine, corresponding to 538 000 tons of salt. Such amount of salt extracted from the layer produces a cavity of nearly 250 000 m^3 corresponding to a radius of a spherical cavity of 39 m.

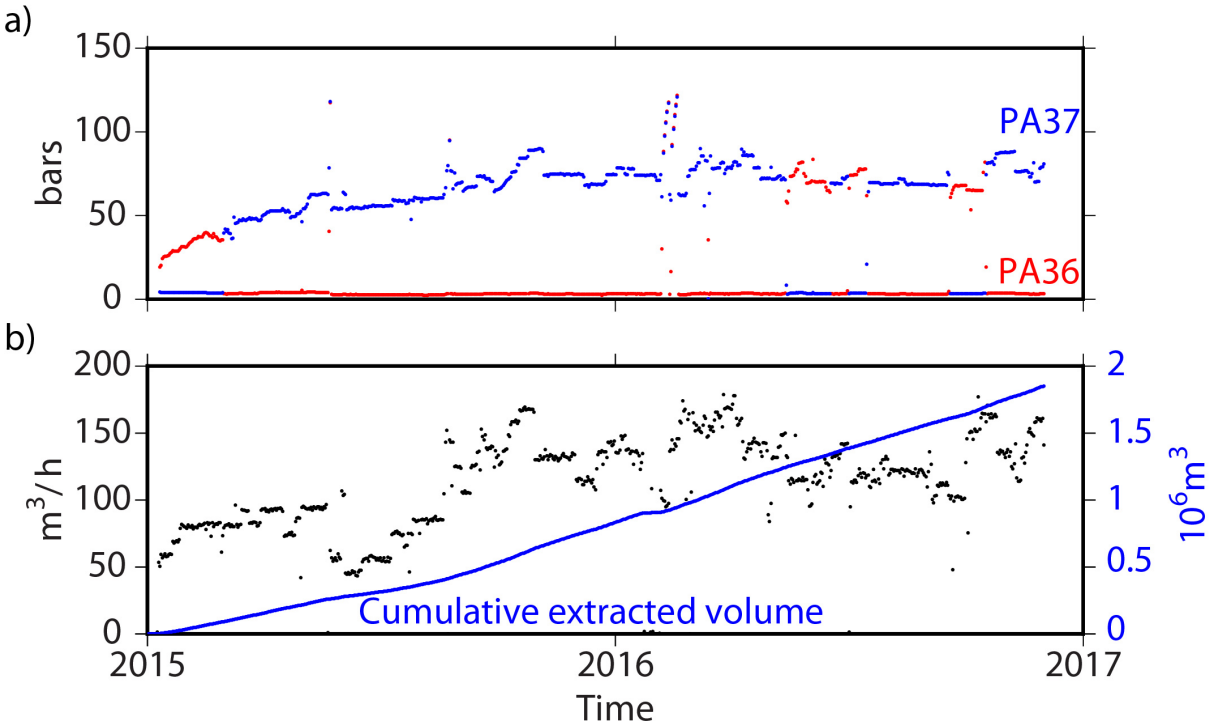

Figure 3.8: *a) Pressure at the two wells of the doublets from January 7th 2015 (start of the activity at this doublets) until November 27th 2016. High pressures are associated to the injection well, while low pressure are linked to the production well. b) Production flow of extracted brine at doublets PA36-37 and cumulative extracted volume of brine (blue curve). Data are provided by KemOne company.*

Even if those cavities are filled with brine, the difference in density between rock salt and brine produces a change in stress equilibrium that leads to elastic and visco-elastic deformation of the surrounding medium (Bérest and Brouard, 2003; Bérest et al., 2006; Berest et al., 2012). At the surface, a bowl of subsidence attests this deep deformation (Raucoules et al., 2003).

Modelling the surface deformation of such exploitation could be appropriate not only to predict the evolution of subsidence but also to understand the potential connections between wells or with secondary reservoirs with the goal of improving the brine productivity. In particular, the large amount of available data in the salt exploitation in Vauvert could be jointly inverted to precisely constrain the model. As for the choice of the model, the process of extracting the salt can be approximated by elastic deformations when short period of time are considered. More complex models can be envisaged to approach the real behaviour of the salt:

- A linear elastic forward model with very low values of the elastic parameter as for a damage approach (such as implemented by Got et al., 2017 based on Kachanov, 1958).
- Visco-elastoplastic models suitable for the salt behaviour such as Lemaître-Menzel-Schreiner model (Vouille et al., 1984) Northon-Hoff model (Norton, 1929) or Munson-Dawson model (Munson and Dawson, 1984).

3.3.4. Monitoring the deformation

Because of the large volumes of extracted salt, the surface deformation needs to be monitored to prevent the potential damages to infrastructures of nearby cities. This monitoring is mandatory for mining activities like salt extraction in Vauvert. Therefore, the site is monitored since 1996 (Figure 3.9a), first performed only by IGN (Institut Géographique National, Figure 3.9b) using levelling surveys. In 2009, the company Fugro-Geoid yearly deploys three temporary GPS stations, to which we added four permanent stations (one in 2015 and three in 2016). Besides GPS stations, the company achieved InSAR studies from ENVISAT and SENTINEL-1 images (PhD thesis of Samuel Doucet in preparation at Géosciences Montpellier) and gravimetric surveys (relative and absolute) in collaboration with the research laboratory Géosciences Montpellier. Finally, in February 2018 we installed a Halliburton borehole tiltmeter next to one GPS station. Data are continuously processed and these different geodetic surveys globally agree to state that the subsidence above the exploitation reaches about 2 cm/yr as already shown by previous studies (Raucoules et al., 2003).

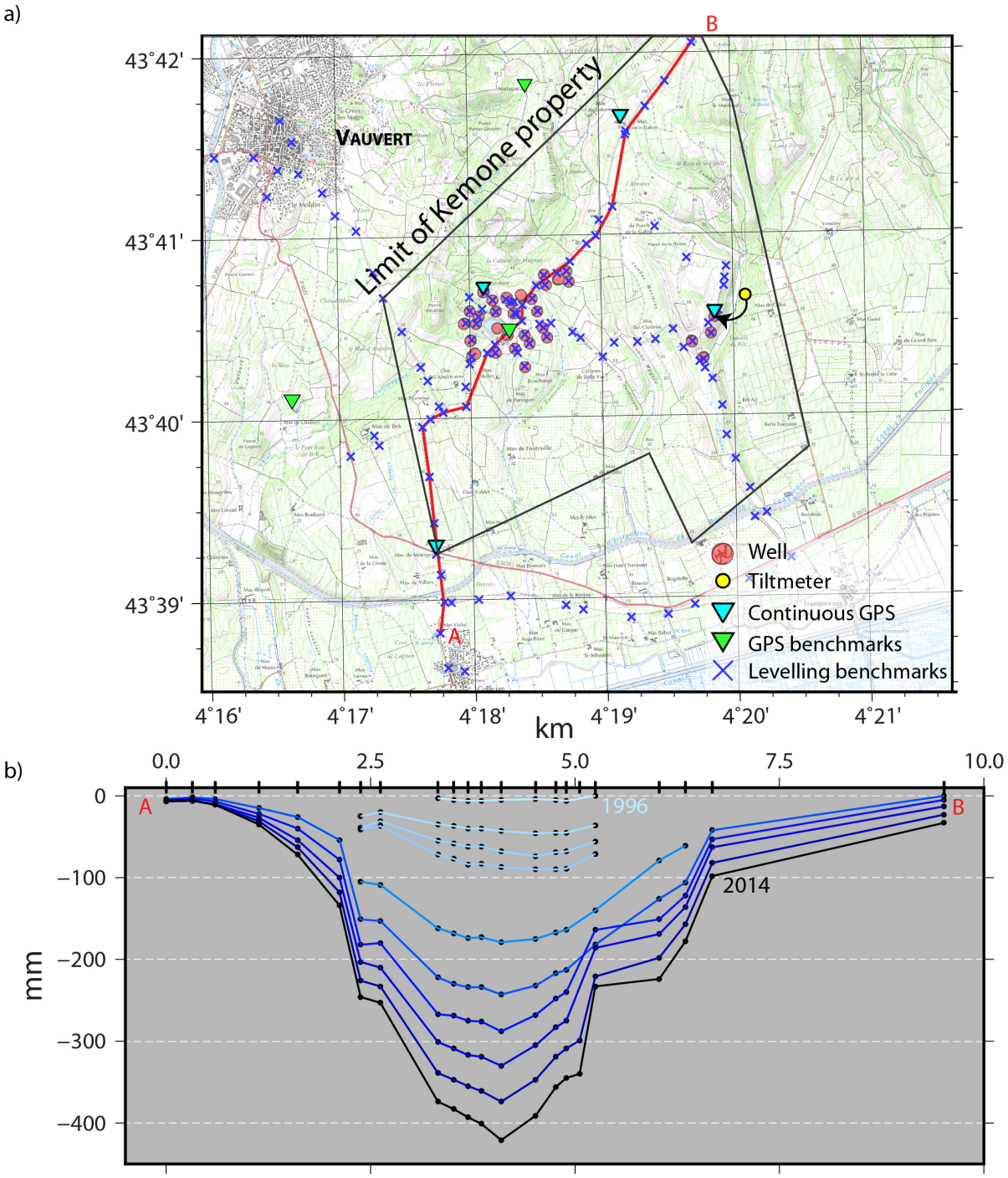

Figure 3.9: *a) Geodetic network of the salt exploitation in Vauvert. Wellheads are represented by red circles, GPS by inverted triangles (blue for permanent and green for survey benchmarks), levelling benchmarks are identified by blue crosses and the tiltmeter is marked by a yellow dot with an arrow indicating its exact location. b) Levelling data along the A-B profile (red line on a) performed by IGN (Institut Géographique National) from 1996 to 2014. Here only one year out of two is displayed to lighten the graph.*

3.4 Deformation monitoring of unconventional reservoirs

3.4.1. About the fracking controversy

Hydraulic fracturing is a technique commonly used to improve reservoir connection in geothermal power plants, salt reservoirs and Oil & Gas fields. Invented in the 40's, this technique is now widely used in non-conventional reservoirs thanks to increase of the fuel price and the rapid progress in extraction techniques. Those compact shale reservoirs present such low permeability (between 4.93×10^{-20} and 1.97×10^{-20} m^2) that conventional methods (oil and gas wells) are inefficient to extract the resource. Therefore, unconventional methods are developed, such as hydraulic fracturation (fracking), to produce oil and/or gas from the reservoir. It is used to create a large and complex network of fractures which connects the production wells with the greatest possible volume of reservoir rocks. Due to the scarcity of conventional reservoirs, those unconventional techniques become necessary to reach more reservoirs and increase productivity but is highly controversial. Indeed, scientific studies and citizen actions report the negative impacts of the fracking activity on the environment and local communities. Among the negative impacts of unconventional extraction (Jackson et al., 2014; Mayer, 2016; Meng, 2017), one may cite:

- the use of large quantities of water injected in the reservoirs which also contain chemicals;
- the post-treatment of this fluid;
- the management of the chemicals;
- the seismic hazards induced by the injection of pressurized water;
- the risk of ground and aquifer pollution due to gas or fluids leaks.

Rarely, the process of fracking might generate earthquakes detectable by the population, such as the magnitude 4.4 event in British Columbia (Canada, 2014). Nevertheless, events of such magnitude remain isolated while smaller events, called microseisms are commonly induced by hydraulic fracturation. This activity is accurately monitored to identify faults and fractures (Wessels et al., 2011) allowing to characterize the fracking process in the vicinity of the well (Le Calvez et al., 2016). In this section, I present the technique of hydraulic fracturation from a geodesist point of view, focusing on the surface deformation and leaving the controversy as an open question.

A vertical well is drilled reaching the thin layer ($\sim$ 200 m thick) containing the desired resource (here the methane). Fractures are generated at multiple intervals of the horizontal section of well drilled in the reservoir. To do so, perforating guns are used to perforate the casing, cement and rock to connect the reservoir to the well. Then, fractures are created by a well constrained injection of high-pressure fluids mainly composed by water and proppant (typically sand) but also containing some chemical additives to improve fluid stimulation. Under the pressure of about 68 MPa or 9880 psi (Antoine Jacques, Total

S.A.), fractures are created in the reservoir rock. The proppant remains in the fractures keeping them open when the pressure is relieved, thus permitting to fluids or gas to flow from the reservoir to the exploitation well. At the end of hydraulic fracturing process, a Stimulated Reservoir Volume (SRV) is created (about 10 000 m^3, Zoback, 2007). The stimulation segment of the well is then isolated using a specific plug and the process of fracking is repeated. Once the entire horizontal section of the well has been stimulated, the production begins, recovering first the injected water and then oil or gas (Figure 3.10).

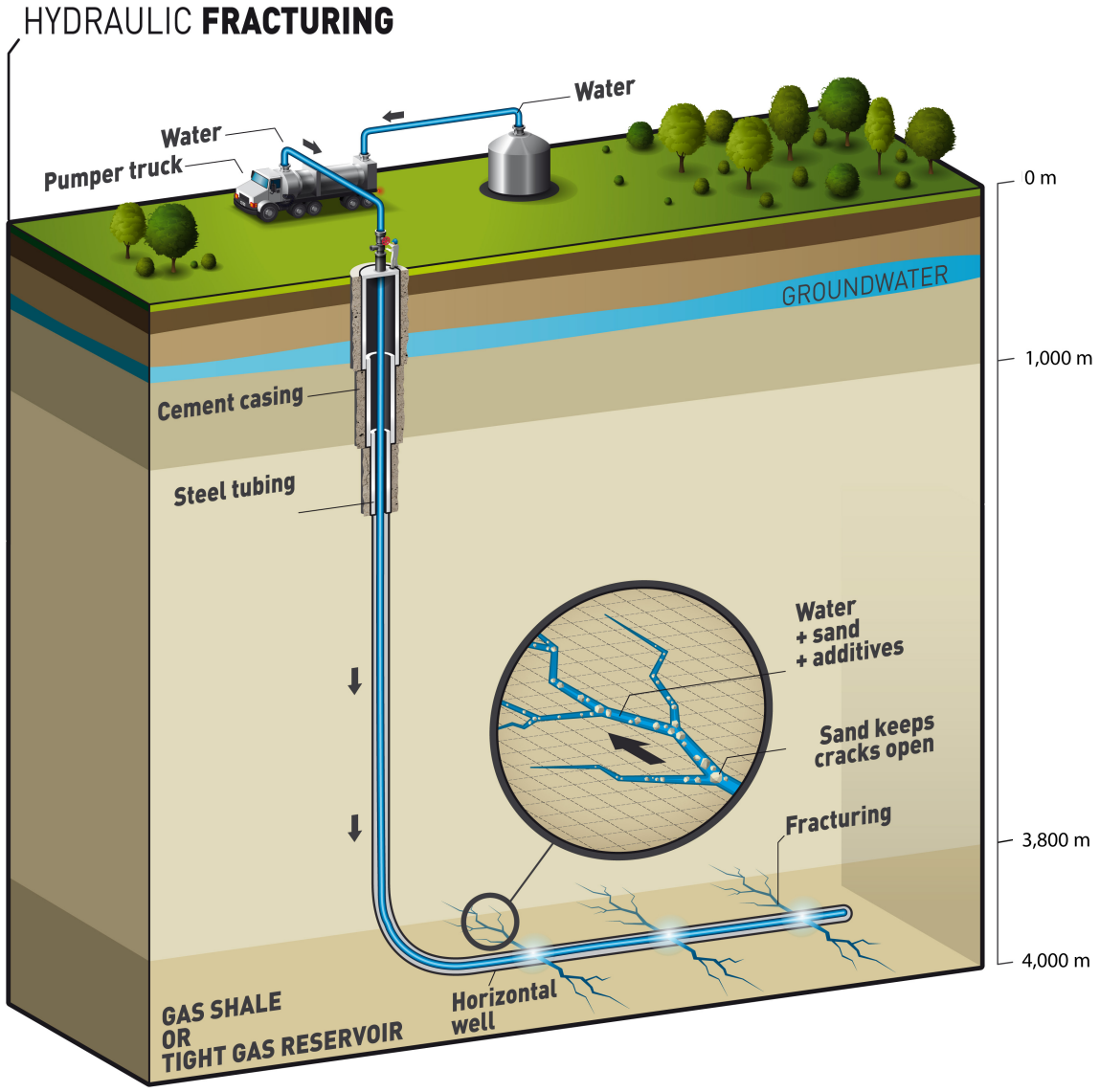

Figure 3.10: *Scheme of hydraulic fracturation.*

3.4.2. Nanometric deformation of a dead cow

Because mining and Oil & Gas resources are becoming less and less accessible, their exploitation is more challenging than ever. Therefore, the geodetic monitoring of unconventional reservoirs covers two major issues including (1) the optimization of reservoir

withdrawal and (2) the respect of environmental constraints (*e.g.* hydraulic contamination of aquifer Vengosh et al., 2014; Zou et al., 2018). Even if microseismicity is already used to characterize the fractures during hydraulic fracturation (Wessels et al., 2011; Le Calvez et al., 2016), geodetic network could bring substantial constrain on the evolution of the fluid withdrawal, identifying undrained Stimulated Reservoir Volumes, connections between SRVs or fluids migrations through layers. In order to prevent industrial damage and to minimize the environmental impact of resource extraction, the surface deformation caused by a given production scenario must be accurately monitored and predicted.

The petroleum industry has been motivated since the inception of fracturing to understand and control fracture growth (Zoback, 2007). Exploiting a low permeability reservoirs implies deformation of surrounding rocks up to the surface, producing first uplift when fluids are injected to generate fractures, then subsidence when the hydrocarbons are then extracted. Although tiny, this surface deformation can be measured using arrays of highly sensitive tiltmeters (Warpinski et al., 1997; Fisher and Warpinski, 2011; Warpinski, 2014). Figure 3.11 illustrates the expected tilt deformation for a fracking stage injecting 10 000 m^3 of fluids. Using Okada's model, this synthetic example simulates the opening of 1 m of a vertical fracture with dimensions of 100x100 m located at 3000 m deep and centered at (5 km,5 km) in the domain (blue line exaggeration x5 on Figure 3.11). Figure 3.11 does not display real data from the creation of a Stimulated Reservoir Volume. The vertical displacement and the x-component of the tilt along the profile A-B (grey line on Figure 3.11a) is displayed on Figure 3.11. The maximum vertical displacement is 0.2 mm, which is smaller than the resolution of GPS, InSAR and levelling techniques, while tilt values range from 0 to 0.25 μrad, about 50 times greater than the resolution of tiltmeters.

Because the entire process of fracking (from used tools and instruments to injected fluids) is expensive, optimizing the number of stages during the fracking is essential. Overlapping fractures networks do not increase productivity, but companies expect no gap between stages. To do so, a typical configuration considers one stage every 100 m, with fractures spreading over 50 m high and 200 m away from the well and characterized by microseismicity (Lin and Zhang, 2016; Wu et al., 2017). The surface deformation induced by hydraulic fracturing is function of fracture azimuth, dip, depth, and total fracture volume. Estimating those parameters is mandatory in unconventional reservoir exploitation if one wants to know whether the fractures are covering at best the reservoir volume. Also, uncontrolled fracking may reach adjacent aquifers and create communication pathways for fracking fluids or hydrocarbons to pollute surface layers and water. Multiple studies use tilt data (Castillo et al., 1997; Fisher and Warpinski, 2011; Astakhov et al., 2012; Zhou et al., 2015) and few using InSAR data (Vasco et al., 2008) to retrieve the fractures parameters defined by Okada's analytical model. For instance, Fisher and Warpinski (2011) showed that heights of most stimulated fractures are well-contained in the reservoir layer. In addition, Astakhov et al. (2012) presented a new method to retrieve characteristics of complex network of fractures and Zhou et al. (2015) illustrated the importance of an appropriate tilt fracture mapping to characterize multi-stages fracturing of cluster of wells. The principle of tiltmeter fracture mapping is to determine hydraulic fracture geometry and Stimulated Reservoir Volume strain, by measuring this fracture-induced rock deformation. Pinnacle-Halliburton company (specialized in fracture mapping and reservoir monitoring services) provides services combing microseismicity and microdeformation analysis to evaluate SRV changes during hydraulic stimulation.

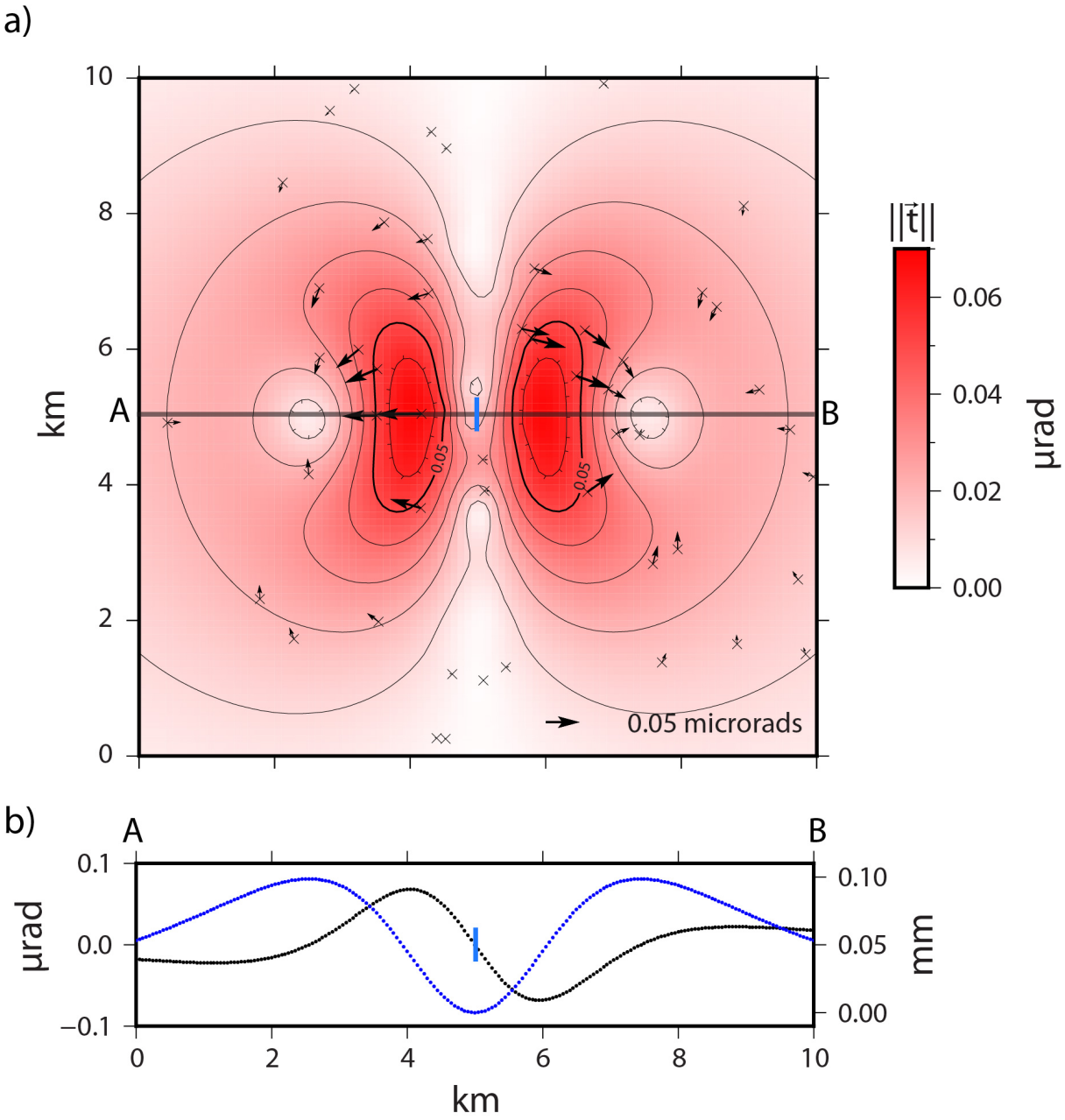

Figure 3.11: *Simulation of the microdeformation induced by a vertical fracture (blue line exaggeration ×5). a) Spatial distribution of the tilt norm and tilt vectors at potential instruments locations. b) Horizontal profile (A-B on a) for the x-component of the tilt (black dots) and associated vertical displacement (blue dots).*

Because of confidentiality clauses, results of these analysis are rarely published or shared (Astakhov et al., 2012), restricting the potential of such databases.

Therefore, as part of the MIRZA[1] project, our working group aims at building a pilot project on the unconventional field, Vaca Muerta, exploited by the French company Total S.A in Argentina. Indeed, Total S.A is particularly interested in developing a new moni-

[1]Not to be confused with the song Mirza from Nino Ferrer (1965).

toring method of the ground displacement for unconventional exploitations. As tiltmeters are extremely sensitive instruments, they would be appropriate instruments to measure ground displacements induced by hydraulic fracturation and resource extraction. However, to cover the entire time of exploitation, the long-term drift of the instruments need to be relatively small (Chawah et al., 2015b) and well constrained. Available instruments (*e.g.* borehole tiltmeters from Halliburton, Lily tiltmeters from Jewell Instruments) display a drift of about $\pm$ 4 μrad/month. Thus a project of building low-drifting tiltmeters has been initiated alongside with the methodology involving drift estimation developed in this manuscript. A first project (ANR Lines 2009-2012) allowed to build a prototype of a low drifting borehole tiltmeter (Chawah, 2012). Then, a more industry-driven project (FUI MIRZA 2015-2018) was initiated. Named *MIRZA* (Monitoring Inclinométrique des Risques dans les Zones Actives, Hazards Monitoring of Active Zones using Tiltmeters), the project is now coordinated by the French company Aquitaine Electronique in collaboration with two research laboratories, Géosciences Montpellier and the LAAS in Toulouse (Laboratoire d'Analyse et d'Architecture des Systèmes, Laboratory for Analysis and Architecture of Systems). Its main goal is to develop commercially available low drifting tiltmeters.

The Vaca Muerta deposit is located at 3000 m deep and is several hundreds of meters thick. Because of the reservoir's depth, ground deformations are small. Total S.A operates several blocks listed on Figure 3.12: Aguada Pichana Est, San Roque, Rincon La Ceniza and La Escalonada. This project involves an optimized deformation survey using low drifting tiltmeters currently built by Aquitaine Electronique, in order to monitor all steps of extracting gas from unconventional reservoir using the methodology developed in this thesis. Located at Neuquén Basin in Argentina, the Vaca Muerta is a sedimentary formation of Jurassic and Cretaceous, hosting possibly one of the currently largest reservoir of hydrocarbons in the world (Romero-Sarmiento et al., 2017). Because the deposit has highest porosity than common non-conventional reservoirs in North-America and the pre-existing fractures network is significant, it makes it suitable to hydraulic fracturing.

We aim at designing an optimized tilt fracture mapping in the particular case of Vaca Muerta exploitation for Total. Contrarily to most of geodetic studies that are only devoted to monitor the fracking stage, Total S.A. aims at monitoring all successive phases of production over the time of exploitation. In this work, we attempt to demonstrate by our modelling that this goal is feasible by combining low drifting tiltmeters and the methodology of optimization developed hereafter. The combination of tilt monitoring and adapted inversion technique would permit to follow the evolution of extracted volumes with an estimation of drift parameters.

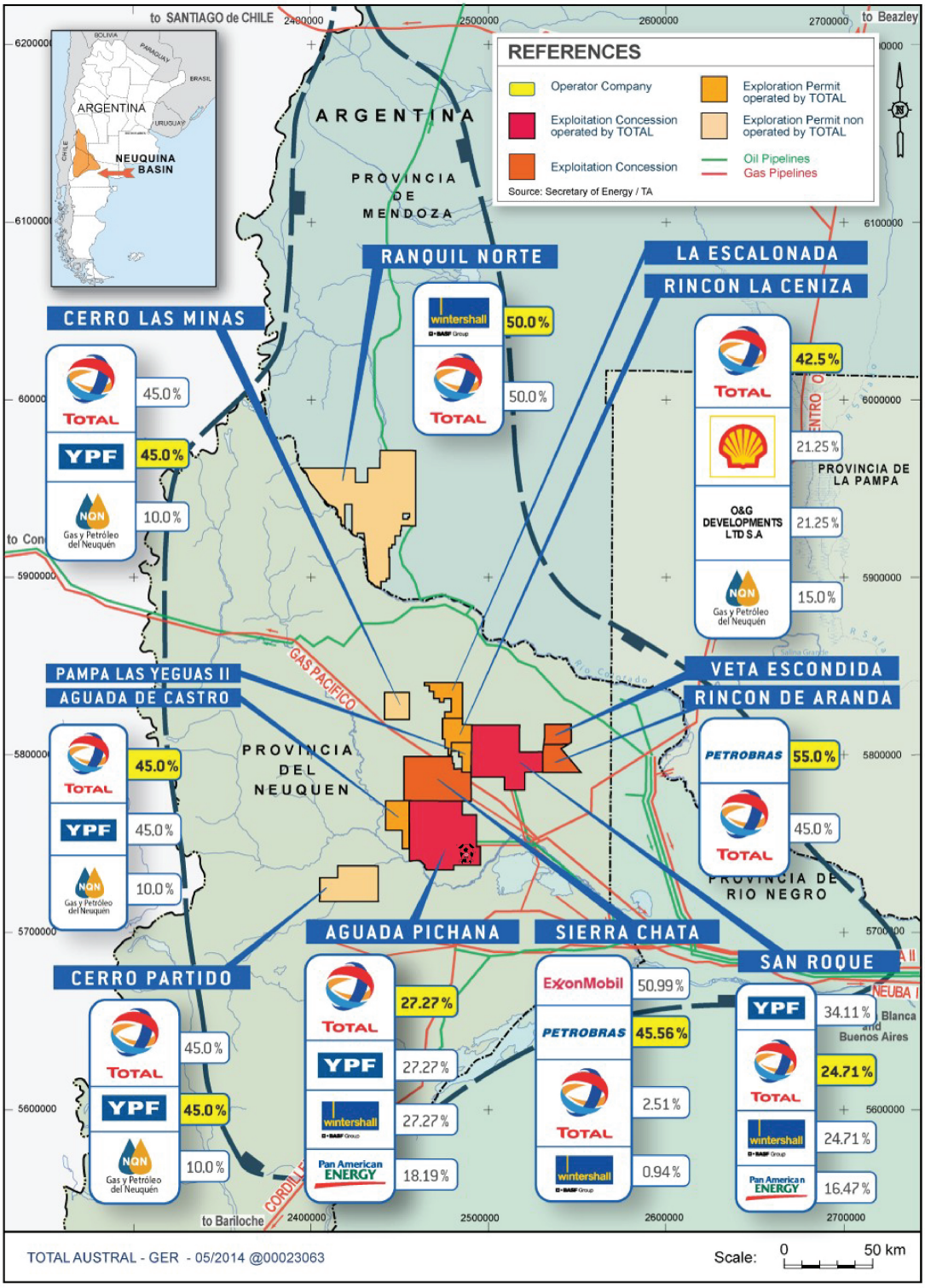

Figure 3.12: *Distribution of companies possessions on the blocks of Vaca Muerta.*

3.5 A common methodology

The aim of this chapter was to get the reader familiar with challenges associated to the 3 types of reservoirs (volcanic, salt and hydrocarbons) in term of geodetic monitoring and modelling. The tackled challenge remains the long term reservoir monitoring for hazard assessment, though reservoirs optimization is highly requested by Oil & Gas companies. We saw that surface displacements produced by different processes modifying those reservoirs ranges from several micrometers (hydraulic fracturation) to several decimeters (strong volcanic events).

However, those 3 reservoirs share common features that motivate us to build a common methodology of inversion. We make the following remarks and hypothesis:

1. modelling the source of deformation is critical for economic, societal and environmental reasons;

2. the induced surface deformation can be accurately monitored and studied using extensive geodetic network;

3. a linear relation can be reasonably assumed between the strain source at depth and the surface deformation, because strain remains small;

4. a small group of analytical sources (Mogi, McTigue or Okada's model) may be used as constitutive strain-stress models.

These reasons encouraged us to develop a global methodology, common to these three kinds of geological systems, in order to jointly invert geodetic datasets. This methodology is described in the following chapter (Chapter 4) and synthetic applications are provided in Chapters 5, 6 and 7.

Chapter 4

Global optimization for geodetic data

Résumé

Nous avons présenté dans le chapitre précédent l'intérêt de développer une méthodologie d'inversion de données géodésiques commune aux trois systèmes géologiques considérés (réservoirs magmatique, salifère et pétrolier). Nous utilisons dans ce chapitre les différentes notions présentées dans le Chapitre 2 afin de décrire les principes techniques de notre méthode d'optimisation.

Les données géodésiques observées contiennent de multiples informations sur tous les mouvements environnants. Dès lors, pour les utiliser en modélisation, nous supposons que le signal enregistré peut s'écrire comme la somme de différents signaux tels que celui produit par la source de déformation, du bruit et des décalages ou dérives. Selon la technique géodésique considérée, le signal sera plus ou moins continu dans le temps et l'espace. Il est donc nécessaire de déterminer une paramétrisation des données (dans l'espace et/ou le temps) afin que l'espace des paramètres à optimiser soit adapté aux objectifs de l'étude.

L'inversion des données géodésiques pour retrouver les caractéristiques des phénomènes profonds consiste à minimiser une fonction coût. Cette dernière n'étant pas forcément convexe (elle peut présenter plusieurs minima), il est nécessaire de choisir une méthode d'optimisation qui permet de converger vers une solution optimale pour tout l'espace des paramètres. Dans cette thèse, la recherche de ce minimum global de la fonction coût parmi tous ses minima locaux est fait grâce à un algorithme de minimisation globale. Cette fonction coût est construite pour tenir compte à la fois de la dimension spatiale des données mais aussi de leur évolution temporelle.

Dans ce chapitre, le processus d'optimisation global (Mohammadi and Saïac, 2003; Ivorra, 2006) est d'abord détaillé avant de présenter la paramétrisation des données. Nous aborderons ensuite la construction de la fonction coût et la non-unicité de la solution.

4.1 Introduction

In Chapter 2, I introduced the various concepts used in the present chapter. Because geodetic data are witnesses of the subsurface deformation, they need to be inverted to retrieve the parameters of the physical model causing the deformation. In order to find the best parameters explaining such phenomenon, one can find the global minimum of a cost function by measuring the distance between the observations and the model. In general, cost functions can have several local minima, meaning that it exists several sets of parameters for which the difference between modelled data and observations is locally minimized. It may be assumed that only one of those parameter sets reproduces the best the data, which is the global minimum. We aim at escaping from local minima and to do so, we use a global optimization approach developed by Mohammadi and Saïac (2003) which allows to find the optimal solution at little extra-computational cost.

Inverting a single dataset might be relatively straightforward and easy to implement, but the resulting parameters are often not sufficiently constrained. This may be due to the simplicity of the forward model, the magnitude of the data uncertainties, the quality of the geodetic network (number, location of instruments) and the type of measurement to be inverted. Because instruments record different deformation data (ground displacement, tilt, strain), they provide a wide range of information concerning the subsurface and its internal strain. In most cases, data are interpreted individually trying to explain a specific event. Indeed, joint inversion is reduced to specific sites where there are enough trustworthy data from different instruments available at a similar time period. In order to use geodetic data in modelling, one can separate the recorded signal with respect to the different signal sources. From a modelling point of view, data are composed by several signals including the source signal, the noise and potentially offsets or trends. For example, tiltmeters are drifting in an unconstrained way, intrinsically to each instrument. Therefore, if looking at long time periods (more than few days), inversion of geodetic data should be able to separate source, drift and noise components.

In this chapter, I give a complete description of the methodology developed in this thesis based on previous works (Mohammadi and Saïac, 2003; Ivorra, 2006; Chéry et al., 2011) before illustrating the specific aspects in applications (Chapters 5, 6 and 7). To do so, I first describe the machinery of the global optimization strategy, then I explain the parametrization of the geodetic data before providing the features of the functional and some strategies to evaluate the uncertainty propagation. Finally, I briefly present the computational code that I developed in order to treat the geodetic problems of the next Chapters.

4.2 Minimizing general cost functions

4.2.1. A step-by-step description

Geophysical inverse problems resume in finding an optimal model that fits best the modelled data to observations. In the search for this optimal solution, we are seeking

the global minimum of a cost function that must be provided by the user. Despite of its explicit definition, the topology of this cost function is generally unknown and it is not necessarily convergent, *i.e.* convex: the surface may be quite bumpy which means that the functional can accept several local minima.

So how to find the global minimum? Our inversion process is based on the gradient method: from initial value of parameters, we search the minimum of the cost function in the direction defined by the gradient of this function. Thus, we are dependent of the initial guess of the parameters. An obvious strategy would be to test several initial guesses.

Therefore the methodology described in this section is based on a recursive algorithm, varying not only the parameters of the model, but also the initial guesses for a user defined 'core' minimization algorithm (Ivorra, 2006). The core denotes the algorithm which allows to improve the initialization of a given local minimization algorithm (e.g. conjugate gradient). This allows to ensure that a given set of optimal model parameters realizes the global minimum of the cost function.

4.2.1.1. Core minimization and first layer

The method is illustrated on Figure 4.1 (1)-(4) and detailed below. Consider a functional J whose behaviour is unknown (grey curve on the different plot of Figure 4.1) and x a parameter ranging from x_{min} to x_{max}.

1. We initialize this parameter arbitrarily choosing x_1^1 and we estimate the associated functional J_1. A conjugate gradient method is applied starting from x_1^1 giving x_{1m}^1. We consider this point as a local minimum where $J = J_{1m}$.

2. A second set of initial parameters x_2^1 is then chosen such as $x_2^1 = x_1^1 + \alpha$ with α a non-zero random vector in the parameter space from which the conjugate gradient method gives J_{2m} at x_{2m}^1. If the functional is convex, we should find the same optimal value at $x_{1m}^1 = x_{2m}^1$.

3. if $x_{1m}^1 \neq x_{2m}^1$ and $J_{2m} \neq J_{1m}$ a new value x_3^1 is determined using a linesearch method (e.g. the secant method):

$$x_3^1 = x_2^1 - J_{2m}\frac{x_2^1 - x_1^1}{J_{2m} - J_{1m}}, \tag{4.1}$$

   x_3^1 is projected in the admissible space and in particular has its components bounded by those of x_{min} and x_{max}. If $J_{1m} \approx J_{2m}$ we introduce an admissible x_3^1 with the components randomly chosen in order to escape the plateau. Once more, the functional is estimated from this new point x_3^1 and the conjugate gradient method leads to a new parameter x_{3m}^1.

4. We call h_1 (orange curve on Figure 4.1) the function defined by the optimal values of the functional J_{km} for each of the initialization of the conjugate gradient method. The process is repeated as long as a user defined total number of functional evaluations is not reached. A stopping criteria based on the value of the functional can also be introduced if one has an indication on the infimum of the functional.

In Figure 4.1 h_1 is made of plateaus and has a unique minimum level J_{3m}.

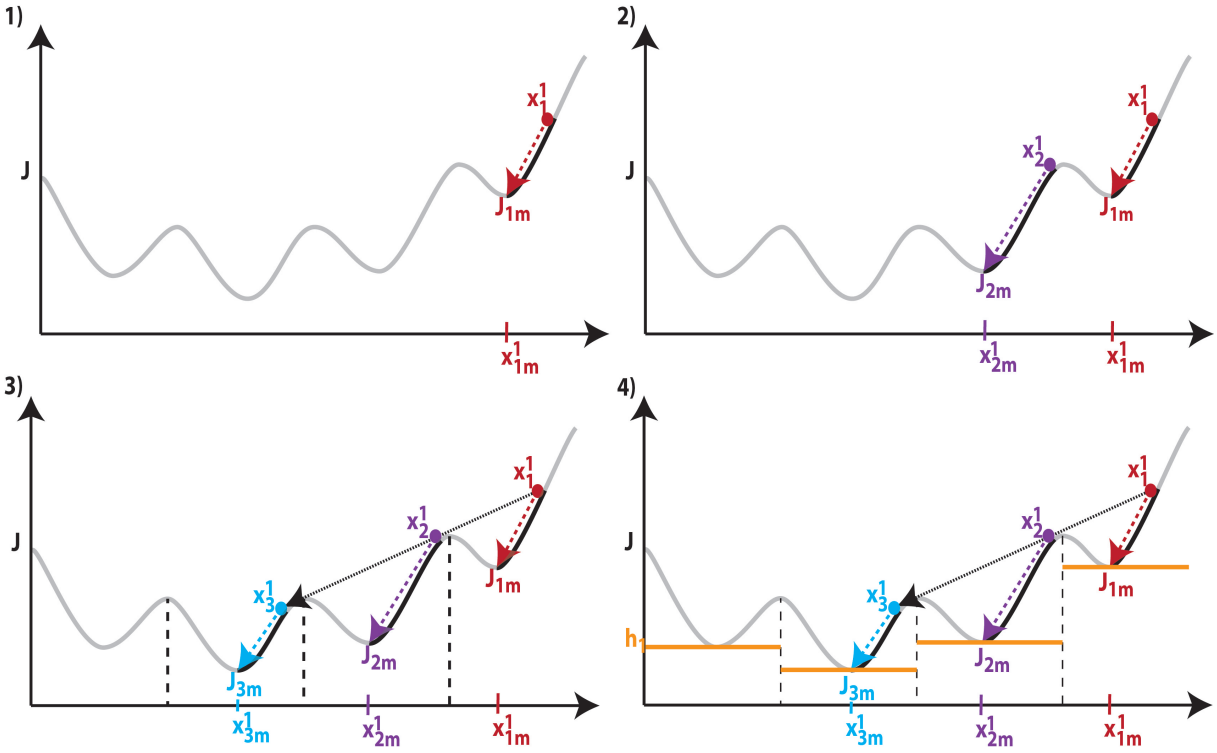

Figure 4.1: *Graphical sketch of how the functional h_1 is built (adapted from Ivorra (2006)).1) Initialization of the parameter set with x_1^1 and estimation of J_{1m}. 2) x_2^1 is randomly chosen to estimate J_{2m}. 3) Using a linesearch method, a third parameter set x_3^1 is selected to deduce the value of J_{3m} . 4) h_1 is the function defined by the optimal values of the functional J_{km}.*

4.2.1.2. Second layer and more

The functional can be more complex than in the above illustration (grey curve on Figure 4.2). h_1 increases the convexity of J, but, unlike in Figure 4.1, it does not have a unique minimum level. In such cases, it is necessary to add a new layer following the same procedure, but this time applied to the function h_1 instead of J with the aim of improving the initialization of the linesearch method Eq. (4.1). This construction leads to the definition of a new functional h_2 as shown in Figure 4.2 (green dashed line). Here h_2 has only three plateaus. The procedure can again be repeated building a constant function h_3 (red dashed curve in Figure 4.2). The algorithm ends when this situation is reached. Hence, initializing the higher level (here level 3) with any admissible couple of points, the outcome of the algorithm will be the same point and will correspond to the optimal inital state for all lower levels processes, eventually leading to the global optimum, if it is unique.

In the following section, more details are given on the mathematical framework behind this approach.

4.2.2. The mathematical approach

We consider the minimization of a functional $J(x), x \in \mathcal{O}_{ad}$, where x is the optimization variable and belongs to the admissible space $\mathcal{O}_{ad}$.

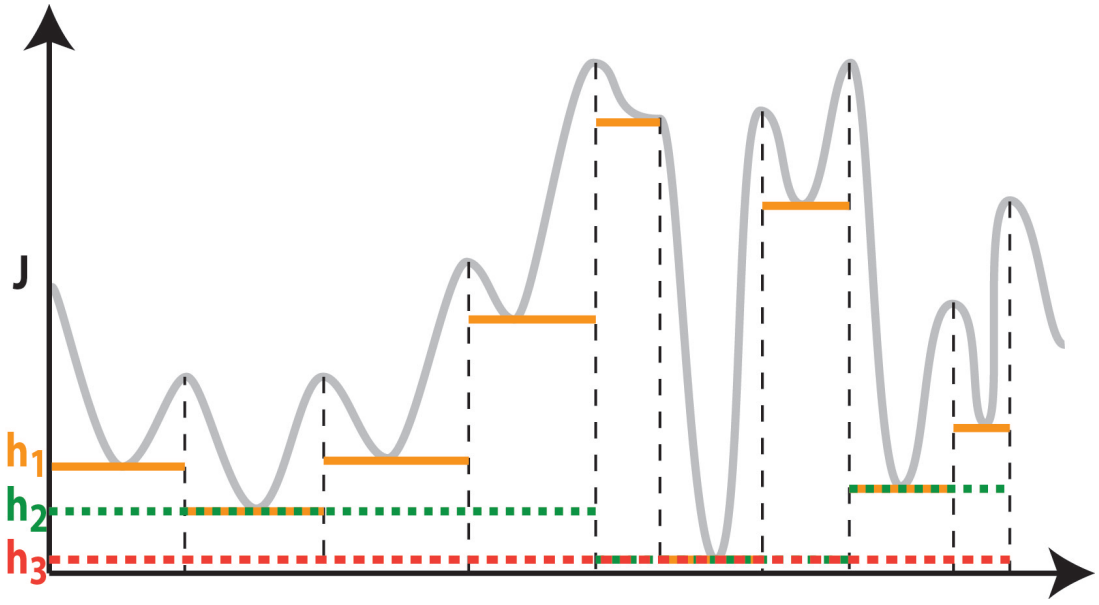

Figure 4.2: *Geometrical interpretation of h_1 (orange), h_2 (green dashed) and h_3 (red dashed) considering a function J (grey) non-convex with several minima close to each other (adapted from Ivorra, 2006).*

Global solution of such general minimization problems is of great importance in applications. However, it is usually stated that evolutionary algorithms are needed (Goldberg, 1989; Fonseca and Fleming, 1995). Such algorithms use mechanisms inspired by biological evolution, such as reproduction, mutation, recombination, and selection. Unfortunately, the complexity of these algorithms makes them difficult to use.

The algorithm briefly presented here enables to improve the global search features of a user-defined local minimization algorithm (e.g. a gradient based algorithm, for more details, see Section 2.4) and this with relatively small extra computational effort (Mohammadi and Pironneau, 2009; Mohammadi and Saïac, 2003; Ivorra and Mohammadi, 2007).

4.2.2.1. Parameters initialization

The algorithm aims at improving the initialization of a given local minimization algorithm (e.g. conjugate gradient). In the sequel, we call this algorithm the core. Any such local search algorithm requires an initialization. If this initialization belongs to the attraction basin of the global infimum, the core has a good chance to succeed in finding the global solution. So the question is how to provide a good initialization for the core.

Let us consider the initialization not anymore as something given but as a variable itself. This new variable has to be found solving a new optimization problem for a functional defined by the best value found by the core for the different initializations. Hence, solving this new optimization problem will improve the solution given by the core.

But then this new problem needs initialization too. And, a new optimization problem can be introduced looking for the right initialization for this new problem.

This recursive construction can be pursued indefinitely adding new optimization layers each providing an initial condition for the layer below. The algorithm stops when the

functional is eventually convex.

In what follows, we suppose that :

- the functional has a unique global minimum J_m,
- the problem is feasible in the sense that there exists a unique point x_m where $J(x_m) = J_m$,
- the functional is coercive (i.e. $J(x) \to \infty$ when $\|x\| \to \infty$),
- the functional has enough regularity.

In practice, one does not know J_m. In such cases, the algorithm stops either when a maximum computational effort (e.g. number of functional evaluations) or when a given target reduction in the functional value is achieved. Also, for the construction to be efficient, one needs to solve the extra-optimization problems with simple and cheap algorithms. In the sequel we use simple secant method.

4.2.2.2. Minimization algorithms and boundary value problems

Starting from an initial guess x_0, a minimizing sequence can be built as:

$$\left\{ \begin{array}{l} x^{n+1} = x^n - \tau^n_{opt} M^n \nabla J^n, \\ x^0 = x_0, \\ \tau^n_{opt} = \text{argmin}_\tau (J(x^n - \tau M^n \nabla J^n)) > 0 \end{array} \right. \tag{4.2}$$

where M^n are positive definite matrices. This sequence converges to a local minimum of J. The case $M^n = Id$ corresponds to the classical steepest descent method. If M^n is the inverse of the Hessian $(\nabla^2 J)^n$ of the functional we recover the Newton (resp. quasi-Newton) method. For simplicity, we consider $M^n = Id$.

The iteration above corresponds to a discretization of $(\dot{x} = -\nabla J, \quad x(0) = x_0)$. If the optimization problem has a solution, solving the global minimization problem consists in finding $x(T)$ solution of the following over-determined problem for a finite time T:

$$\left\{ \begin{array}{l} \dot{x} = -\nabla J, \\ x(0) = x_0, \\ J(x(T)) = J_m. \end{array} \right. \tag{4.3}$$

In practice, we choose an a priori finite number of iteration N of Eq. (4.2), rather than T and $T = \sum_{n=0}^{N-1} \tau^n_{opt}$ is a positive and finite quantity.

4.2.2.3. Removing the over-determination

The over-determination can be removed by considering the initial condition as a variable to be found by shooting for the minimization of $h(v) = J(x_v) - J_m$ where x_v is the solution found after N iterations of Eq. (4.3) starting from v. The algorithm reads the first initial values v^1_1, $v^1_2 = v^1_1 + \alpha$, the threshold value ε and P the number of iterations to find the best v.

Compute $h(v^1_1) = J(x_{v^1_1}) - J_m$ and $h(v^1_2) = J(x_{v^1_2}) - J_m$,

For $p = 2, .., P$ **Do**

If $h(v_p^1) = J(x_{v_p^1}) - J_m > \varepsilon$ and $||v_p^1 - v_{p-1}^1|| > \varepsilon$, **Then**

$v_{p+1}^1 = v_p^1 - h(v_p^1)\frac{(v_p^1 - v_{p-1}^1)}{h(v_p^1) - h(v_{p-1}^1)}$,

Find $x_{v_{p+1}^1}$ after N iterations of Eq. (4.3) starting from v_{p+1}^1.

Else Stop

EndIf

EndFor (p)

α indicates an admissible variation around the initial guess such that $h(v_1^1) \neq h(v_2^1)$. Eq. (4.1) is the secant method to find a zero of $h(v^1)$ along the direction defined by (v_1^1, v_2^1).

4.2.2.4. Multi-level shooting method

As shown through our illustrations above, the algorithm above may not converge to an initial state that guarantees the convergence to the global minimum. Indeed, the application of the algorithm above leads to a piece-wise constant, non-convex functional h. The idea is then to add an external loop to the algorithm above, minimizing the new functional h. This leads to the following two-level algorithm:

v_1^2, $v_2^2 = v_1^2 + \beta$, ε_1, K, given

For $k = 2, .., K$ **Do**

Compute $h^2(v_1^2)$ **and** $h^2(v_2^2)$,

If $h^2(v_k^2) > \varepsilon_1$ and $||v_k^2 - v_{k-1}^2|| > \varepsilon_1$, **Then**

$v_1^1 = v_k^2$, $v_2^1 = v_k^2 + \alpha_k$, ε_2, P given,

Compute $h^1(v_1^1)$ and $h^1(v_2^1)$,

For $p = 2, .., P$ **Do**

If $h^1(v_p^1) > \varepsilon_2$ and $||v_p^1 - v_{p-1}^1|| > \varepsilon_2$, **Then**

$v_{p+1}^1 = v_p^1 - h^1(v_p^1)\frac{(v_p^1 - v_{p-1}^1)}{h^1(v_p) - h^1(v_{p-1}^1)}$,

Find $x_{v_{p+1}^1}$ after N iterations of Eq. (4.3) starting from v_{p+1}^1,

Else (p) Stop

EndIf (p)

EndFor (p)

$h^2(v_k^2) = h^1(v_p^1)$ **and** $v_k^2 = v_p^1$,

$v_{k+1}^2 = v_k^2 - h^2(v_k^2)\frac{v_k^2 - v_{k-1}^2}{h_k^2(v_k^2) - h_k^2(v_{k-1}^2)}$,

Else (k) Stop

EndIf (k)

EndFor (k)

Above, we denote $h^i(v)$ the successive generated functionals, with $h^1(v) = J(x_v) - J_m$, i denotes the level of the external loop. α_k should be linearly independent together and with β.

The construction above can be pursued adding other new external loops. More details on the development of this algorithm can be found in Mohammadi and Pironneau (2009); Mohammadi and Saïac (2003); Ivorra and Mohammadi (2007).

4.3 Geodetic data parametrization

4.3.1. Mapping a continuous function

Geodetic data are complex signals from which we are trying to extract information about the ground deformation and source strain. Depending on the recording instruments, data display various levels of continuity in time and space. For this study, encompassing both time and space aspects of the deformation is performed choosing an adapted parametrization (in time and/or space). Therefore, the parametrization consists in linking physical observations to parameters of a model that needs to be optimized. If one attempts to reproduce a continuous signal (*e.g.* Figure 4.3) using as much parameters as data points, the optimization would not converge in a reasonable amount of time. Therefore, a discretization of the data permits to sample both data and parameter spaces in order to produce a tractable optimization problem. Also the sampling procedure should reflect the required level of precision. For instance, one month of data sampled every second (Figure 4.3) can be downsampled to 1 data every hour or day depending on the type of event to model (*e.g.* high frequency events such as Deflation-Inflation event, see Chapter 3 or low frequency events like volcanic eruptions).

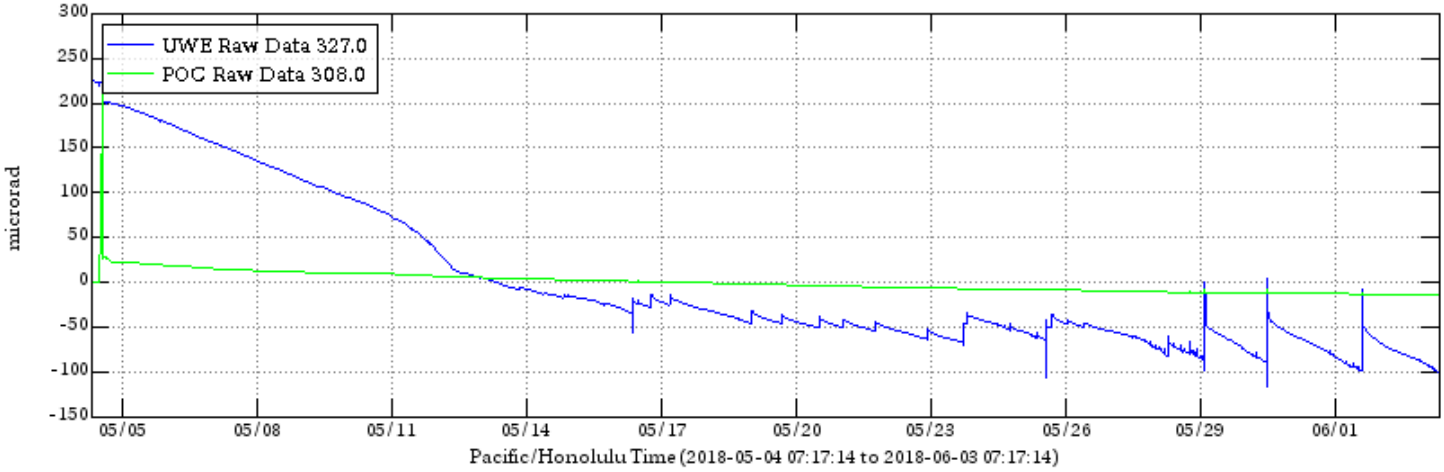

Figure 4.3: *One month of electronic tilt recordings at Kīlauea Volcano starting 5^{th} of May. The blue line shows the radial tilt at Uwēkahuna (UWE), on the northwest rim of Kīlauea's caldera. The green line is radial tilt at Pu'u 'Ō'ō (POC), on the north flank of Pu'u 'Ō'ō cone (from USGS).*

In the following manuscript, we do not discretize the interseismic GPS velocities when infering the lateral variations of the lithosphere (Chapter 5). Instead, we discretize the spatial domain of the model and its parameters using finite elements to approximate deformation. As for the study associated to reservoir deformation (Chapter 6), we use a linear relation between tilt data and volume variations to parametrize tilt data. In the later (Furst et al., submitted), we discretize by down-sampling the time-continuous distribution of 1440 tilt measurements for one tiltmeter (1 tilt measure every 6 hours) to monthly data. Thus, the considered signal for one tiltmeter is composed by 12 measure-

ments that are used to estimate the volume variation ΔV. To get back to the continuous time domain, we interpolate the volume variations using a time-linear relation between two adjacent samples of ΔV.

In the following sections, all data referring to the observations, that are real observations or synthetic observations, are noted as d_o, while data from the modelling are mentioned as d_m.

4.3.2. Absolute vs relative measurements

The measure of surface deformation can be either absolute, which means that the real deformation is known without ambiguity at any given time in a fixed reference frame. But it can also be given relatively to a reference state, station or time. For instance, the displacements measured by GPS or levelling are often relative to a reference point where zero displacement is arbitrarily assumed. Also, InSAR and tiltmeters give a difference of deformation relatively to the onset of the measure which is not necessarily the start of the deformation. By contrast, absolute gravity measurements provide the full measure of gravitational attraction. This implies a potential translation of a dataset if its reference frame is different from the zero-deformation assumption.

For these studies, we consider here that all datasets are expressed in the same geometric and time frames.

4.3.3. Power-law noise in geodetic data

We assume that deformations observed at the surface are the results of some deep physical process that we seek to understand. But the signal measured by instrument contains a lot more information than just the contribution of the studied physical process. In this perspective, we call noise all signals that are measured in addition to the source signal. This noise can be deterministic or random. Deterministic noises include physical processes (*e.g.* tides) or drift (*e.g.* due to the instrument construction, the installation process, the coupling with the medium). These noises can sometimes be removed from the signal when their origins are constrained by physical relations (tides). For noises whose origins are more complex to apprehend (drift, brutal rupture in recordings), they can be cleared from the signal by detrending the data during the processing. Also, as we present in Chapter 6, we can consider this drift as unknown of the inverse problem to estimate it. Non-deterministic noise can be approached using the power-law noise $1/f^{\beta}$, also named colored noise (ref). The color of noise is defined by the power $0 \leq \beta \leq 2.0$ associated to the frequency f of the noise signal. The noise signal is produced by a stochastic process intrinsic to the physics of the measurements (due to electronic, optical, mechanical problems). For instance, building white noise $\alpha = 0$ consists in randomly choosing values within a specific standard deviation: the power spectrum of such signal is flat. On the contrary, a Brownian noise $\alpha = 2$, also known as "random walk" or "drunkard's walk", is built by cumulating random values with a time interval associated to a physical process. For this kind of noise, the power spectrum decreases with increasing frequency.

Random noise can strongly alter the recorded signal and its associated uncertainties. For instance Figure 4.4 illustrates the evolution of white noise (grey dots bounded by

dark grey dashed lines) and Brownian noise (brown dots bounded by dark brown dashed lines) for 1 year. From the same initial standard deviation, the Brownian noise tends to increase the standard deviation leading to wider uncertainties on the data as time is going on. Furthermore, one can identify a linear trend in the Brownian noise which can be surimposed to the deterministic linear signal.

Because of the characteristics of the different noise models (*e.g.* white or Brownian), it can strongly influence the observed signal and the associated uncertainty when adding some noise to the source signal (Figure 4.4).

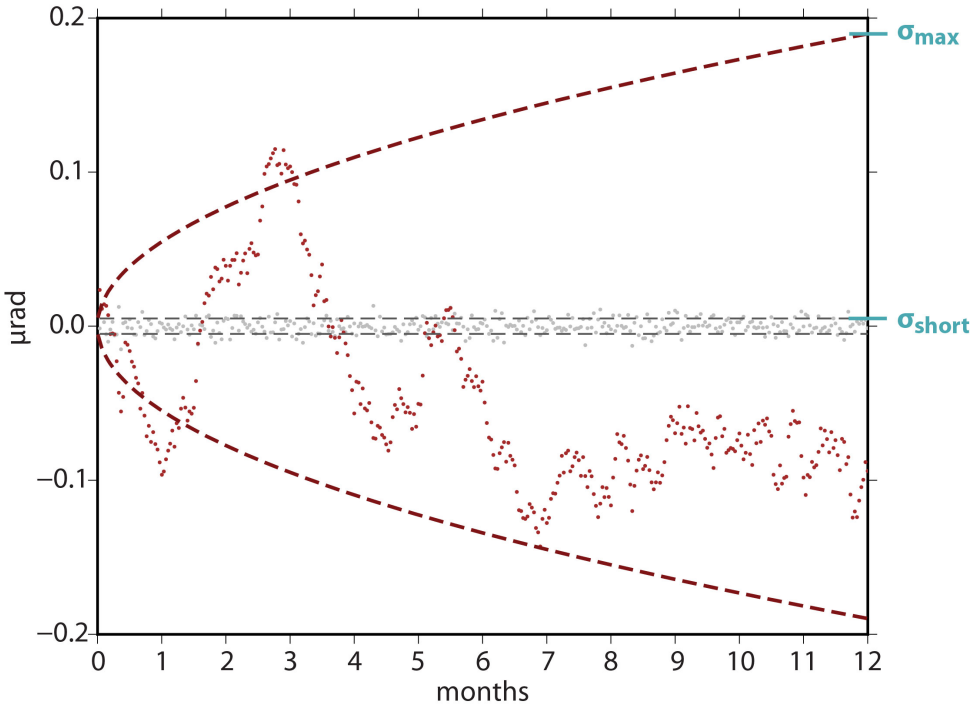

Figure 4.4: *White noise (grey dots) and Brownian noise (brown dots) over 1 year. The dashed lines represent the standard deviation as function of time for the white noise (dark grey) and for the Brownian noise (dark brown).*

4.3.4. Long-term tilt drift

This work has been motivated by the goal of finding a new monitoring method of the ground displacement for unconventional reservoirs using tiltmeters (see Chapter 3). In this objective, I explicitly focus on the uncommon parametrization of tilt data which is detailed hereafter.

Although borehole tiltmeters are sensitive to very small deformations, they are drifting with time in a largely unconstrained way, intrinsic to each instrument and depending on the installation setup (see Chapter 2). Indeed, a "good" instrument (presenting desired characteristics in laboratory conditions) may display strong drift noise if not properly installed on the field. Which means that the instrumental drift is increased by an imperfect installation (*e.g.* poor coupling between instrument and the medium, not perfectly vertical). If correctly installed trying to reproduce the optimal conditions (as in the laboratory), the drift stays as expected.

It is convenient to assume that the actual tilt signal of ground deformation $\vec{d_o}(t)$ is the sum of the signal produced by the source $\vec{d_s}(t)$, a linear instrumental drift $\vec{d_d}(t)$ and some colored noise $\vec{n}(t)$ (Figure 4.5, Eq. (4.4)).

$$\vec{d_o}(t) = \vec{d_s}(t) + \vec{d_d}(t) + \vec{n}(t) \tag{4.4}$$

We assume for each instrument that the drift is linear in time such as $\vec{d_d}(t) = \vec{a}t$ with t the length time series and $\vec{a} = (a_x, a_y)$ is a constant drift rate vector. Because drift and noise are cumulative, they are largely influencing the tilt signal when time increases, thus preventing the use of large tilt time series. Therefore, we aim at estimating those parameters through the global optimization method.

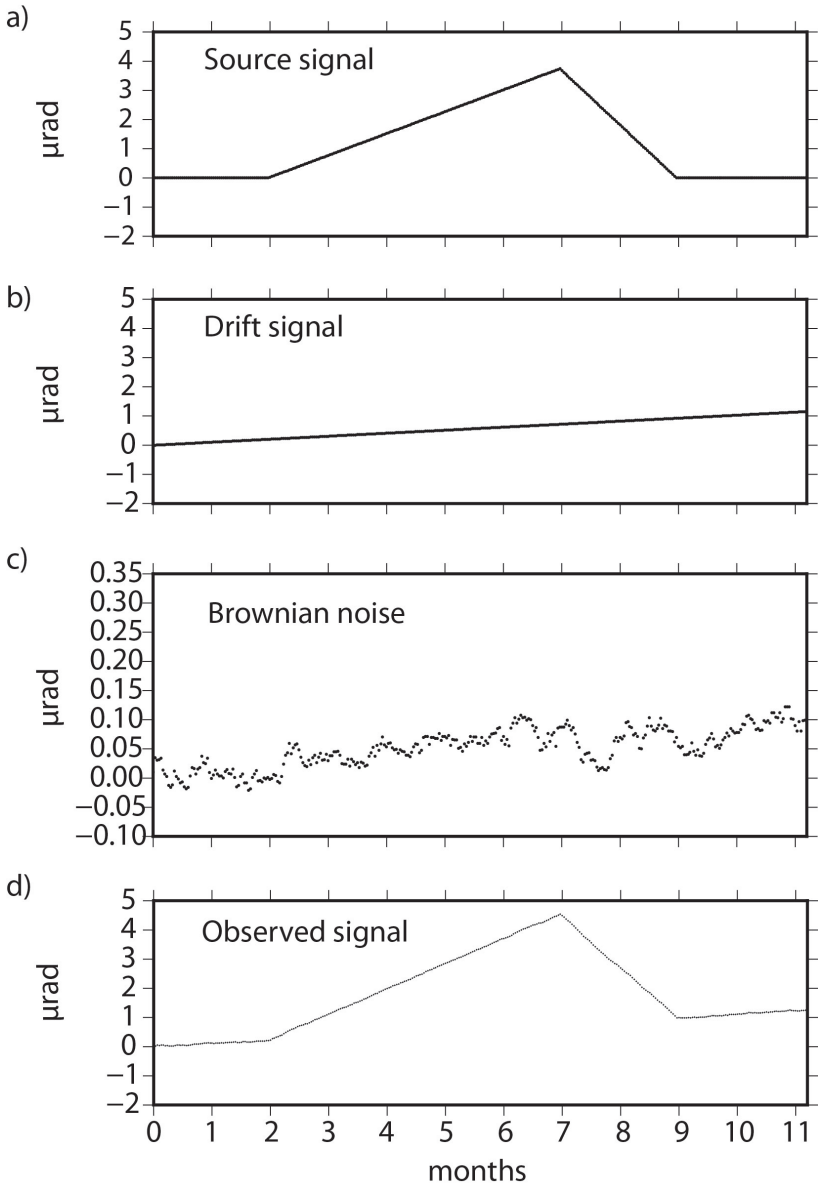

Figure 4.5: *Construction of a tilt signal for one component (t) of one instrument with a) the signal of the source $d_s(t)$, b) the linear drift $d_d(t)$, c) the Brownian noise $n(t)$ and d) the observed tilt $d_o(t)$.*

4.4 Definition of the functional

Because numerous instruments are disposed on the field with various geometrical deformations and record deformation over time, the functional must consistently assemble this spatio-temporal information. This study considers not only 4 data types but also several time series and instrumental parameters. Our goal is to build a single functional considering all those aspects at once. We previously introduced the instrumental parameters. Below we describe our data fusion strategy and time integration procedures.

For a given data type (e.g. GPS, tiltmeters, interferograms), the difference between modelled ($\vec{d}_m(p)$) and observed ($\vec{d}_o$) data of dimension M is expressed through a residual vector:

$$\vec{D} = \vec{d}(p) - \vec{d}_o \tag{4.5}$$

where p denotes the optimization variables (model parameters) associated to one source. To this vector, we need to associate information about the quality of the data. This is done using the covariance matrix for the given data, Σ, that represents the uncertainties on the measurements. Because instruments do not have equivalent accuracy, the covariance matrix can be different at each point of the dataset. The functional associated to this data type is defined as:

$$J_M = \frac{1}{M}\sum_{i=1}^{M} \|\vec{D}_i\|^2_{\Sigma_i^{-1}} = \frac{1}{M}\sum_{i=1}^{M} \vec{D}_i^T \ \Sigma_i^{-1} \ \vec{D}_i, \tag{4.6}$$

where M is the number of data points at a given time and ^{T} denotes the transpose of the vetor.

With this instantaneous quantity in hand, the cumulative expression of the functional over time can be obtained by a discrete time integration. If we suppose a linear evolution of the modelled data between two successive times t_i and t_{i+1} we can use the trapezoidal rule:

$$J_{MN} = \frac{1}{t_{N+1} - t_1} \sum_{i=1}^{N-1} \frac{(J_M)_i + (J_M)_{i+1}}{2}[t_{i+1} - t_i] \tag{4.7}$$

with N the number of time intervals, t_1 and t_N the initial and final times (Figure 4.6). Thus, we minimize J_{MN} which consists in minimizing the green surface on Figure 4.6a. At the end of the optimization (Figure 4.6b), the value of J_M for each time interval has reached a minimum. As J_M is built using weighted Euclidian norms, it is dimensionless. Thus, we assume that the optimization is complete when $J_M \leq 1$.

The previous construction holds for one type of data. If P different data types are present, we consider the following cumulative functional J:

$$J = \sum_{i=1}^{P} \omega_i (J_{MN})_i, \quad \text{with} \quad \sum_{i=1}^{P} \omega_i = 1. \tag{4.8}$$

By introducing weighting factors ω_i we can adapt the contribution of one type of data in the analysis. Unlike the covariance matrix that considers the uncertainties on the

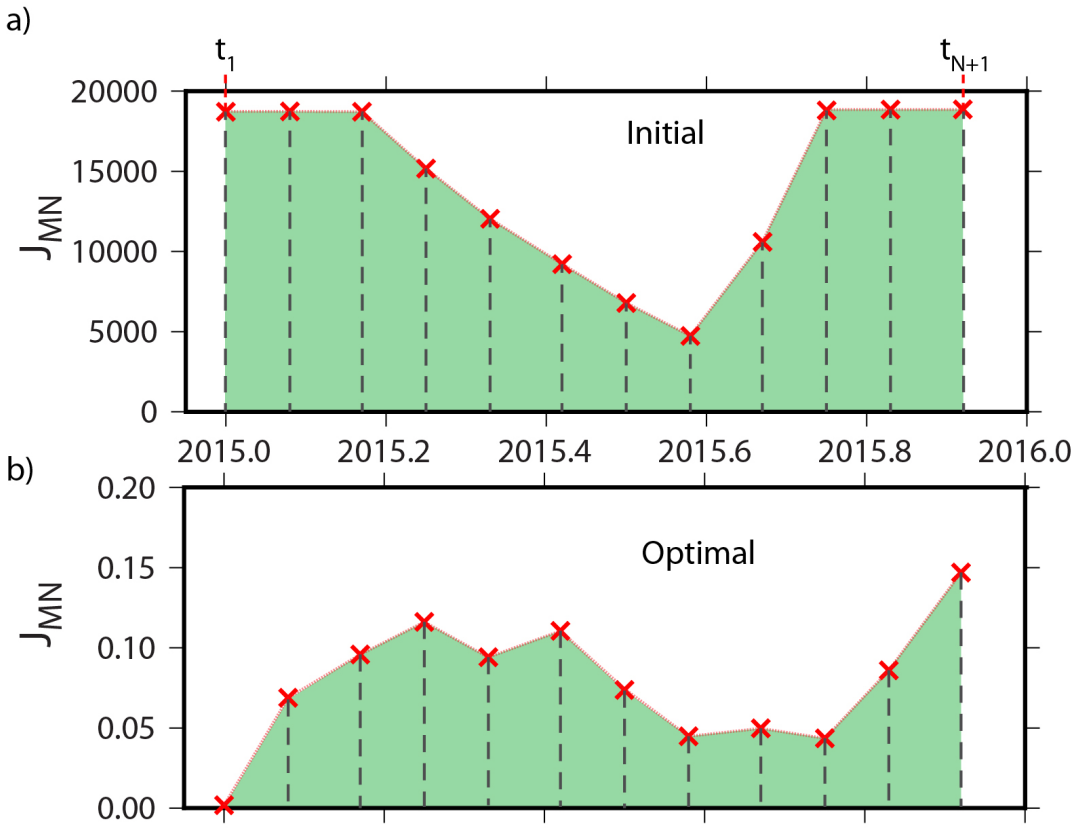

Figure 4.6: *Construction of J_{MN} for one type of data and $N = 12$ time series, a) from the first iteration of the optimization to b) the optimal state. Note the difference in the vertical scale between a) and b).*

data, the weighting coefficients need to be user defined. If no rule can be chosen to set the weighting coefficient, one way could be to study the Pareto front (Vassilvitskii and Yannakakis, 2005) and determine each ω_i needed to minimize the functional J. A Pareto front is defined by a given set of solutions of J as a function of ω_i.

In this study, we consider individual functional j for each data type, normalized by the associated number of data and the inverse of their covariance matrix (Eq. (4.6)). At this stage, we (1) include the resolution of the geodetic technique through the covariance matrix and also (2) we get cleared from the number of points associated to each dataset. Indeed, for highly uncertain data, their covariance matrix is large compared to the data values, leading to small values of J_M for the considered dataset. Also, we weight J_M by the number of data to get an average value for all points in the dataset. By doing that, we equally consider large datasets (several hundreds of points) and small datasets (up to tens of points). Thus when building the cumulative functional J, we actually compare similar values to the data uncertainties.

Throughout this work, we set $\omega_i = \frac{1}{P}$ with P the number of considered data type in the inversion. Optimizing this functional using the global optimization method leads to one set of parameters explaining the observation along with data residuals. These residuals are defined by the difference between observed and modelled data Eq. (4.5) and can be due to the noise inherent to the data, to the ill-chosen model or model parametrization or to the lack of convergence of the optimization procedure.

4.5 On the uniqueness of the solution

From the previous definition of the functional, we can either consider a whole dataset of several data types during the inversion process or each data type can also be individually inverted. Let's then concentrate on tilt data used into a linear forward model.

The observations $\vec{d_o}(t)$ are made of the signals induced by the source, the instrumental drift and some noise (see Section 4.3.4., Eq. (4.4)). During the inversion process, these data are compared to various sets of modelled tilt, $\vec{d_m}(t)$. The latter is expressed as the sum of the source signal $\vec{d_s}(t)$ and the linear drift $\vec{d_d}(t) = \vec{a}t$. We assume that the ground deformation component $\vec{d_s}(t)$ is a linear combination of strain source parameters at depth. This linear relation is valid if we consider Mogi or McTigue models (Mogi, 1958; McTigue, 1987), which involve an elastic medium (homogeneous or heterogeneous) equipped by observation points and submitted to strain sources at depth. For small deformations of the medium, the source signal induced by one source can be written as,

$$\vec{d_s}(t) = \vec{\alpha}p(t) \tag{4.9}$$

where $\vec{\alpha}$ represents the contribution of a source unit strain to each instrument measurement. For instruments close to the source, their corresponding $\vec{\alpha}$ component display large values, indicating a higher sensitivity to source parameters $p(t)$ changes. This leads to the definition of the modelled tilt,

$$\vec{d_m}(t) = \vec{\alpha}p(t) + \vec{a}t \tag{4.10}$$

The noise $\vec{n}(t)$ is fully contained in the observations $\vec{d_o}(t)$ as we are not estimating it through the inversion. When looking for source parameters and drift parameters, the optimization algorithm converges towards an admissible parameter set $(p_a(t), \vec{a}_a)$ which also contains the linear trend included in the observation noises. In Table 4.1, I sum up all the variables and their meanings.

Because of the relation given by Eq. (4.10), inverting tilt data clearly leads to infinite sets of parameters $(p(t), \vec{a})$. Instead of converging towards a global minimum with one set of parameters, the functional tends to a family of admissible combinations of parameters, all explaining the data equally well. Therefore the optimization procedure finds one of the infinite scenarios that are similarly close to the data, without being able to discriminate the targeted one.

Thus, from Eq. (4.10) we can write the following relation,

$$\vec{\alpha}p^*(t) + \vec{a}^*t = \vec{\alpha}p_a(t) + \vec{a}_a t \tag{4.11}$$

where the true scenario is denoted by the exponent * and the subscript $_a$ expresses any of all the admissible scenarios given by the optimization. Can we restore the uniqueness of the solution? To answer these questions, let's look at the results of the optimization. It produces one set of admissible parameters (p_a) inducing tilt data $(\vec{d_a})$ explaining our synthetic data $(\vec{d_o})$ to some residuals from the inversion. Starting from the admissible solution $(p_a(t)\ ;\ \vec{a}_a)$ and Eq. (4.11), the desired solution $(p^*(t)\ ;\ \vec{a}^*)$ must simultaneously satisfy:

$$\vec{a}^* = \vec{a}_a - R\vec{\alpha} \tag{4.12}$$

$$p^*(t) = p_a(t) + Rt \tag{4.13}$$

Variables	Definitions
$\vec{d_o}(t) = \vec{d_s}(t) + \vec{d_d}(t) + \vec{n}(t)$	observation
$\vec{d_s}(t) = \vec{\alpha}p(t)$	strain source signal
$\vec{d_d}(t)$	tilt drift
$\vec{d_m}(t) = \vec{\alpha}p(t) + \vec{a}t$	modelled data
$\vec{n}(t)$	noise
p_a and p^*	admissible and desired source parameters
$\vec{a}_a$ and $\vec{a}^*$	admissible and desired drift parameters
$\vec{\alpha}$	strain source unit for each instrument
R	flow rate coefficient

Table 4.1: *Reminder of all variables used in this section.*

where R is a correction coefficient to be estimated, hereafter named the *flow rate coefficient*. This means that considering the same tilt residuals from the optimization, we are exploring, by varying R, the whole range of admissible solutions for $(p(t)\ ;\ \vec{a})$. Nevertheless, only one set of parameter is requested. Thus, we need to estimate the flow rate coefficient in order to discriminate between all the possibilities.

Due to the lack of knowledge about the structure of $p(t)$, we use *a priori* information concerning the source model (through $\vec{\alpha}$ of dimension N) and the drift parameters (through $\vec{a}$ of dimension N). Indeed, the drift of an instrument does not depend on the position of this instrument regarding the source position. This implies that there should be no correlation between $\vec{a}^*$ and $\vec{\alpha}$. From the definition of the correlation between two vectors of same dimension, $corr(\vec{a}^*, \vec{\alpha}) = 0$ leads to

$$\frac{\mathbb{E}(\vec{a}^*\vec{\alpha}^T) - \mathbb{E}(\vec{a}^*)\mathbb{E}(\vec{\alpha})^T}{\sigma_{\vec{a}^*}\sigma_\alpha} = 0 \tag{4.14}$$

where $\mathbb{E}$ and σ are respectively the expected value and the standard deviation of the distribution ($\vec{a}^*$ or $\vec{\alpha}$) and $\mathbb{E}(\vec{a}^*\vec{\alpha}) - \mathbb{E}(\vec{a}^*)\mathbb{E}(\vec{\alpha}) = cov(\vec{a}^*, \vec{\alpha})$. Thus, the absence of correlation between the two variables $\vec{a}^*$ and $\vec{\alpha}$ is only verified when,

$$cov(\vec{a}^*, \vec{\alpha}) = 0 \tag{4.15}$$

and replacing $\vec{a}^*$ in Eq. (4.15) using Eq. (4.12),

$$\begin{aligned} cov(\vec{a}_a - R\vec{\alpha}, \vec{\alpha}) &= 0 \\ cov(\vec{a}_a, \vec{\alpha}) - Rcov(\vec{\alpha}, \vec{\alpha}) &= 0 \end{aligned}$$

with $cov(\vec{\alpha}, \vec{\alpha}) = var(\vec{\alpha})$ the equation of the flow coefficient can eventually be deduced like,

$$R = \frac{cov(\vec{a}_a, \vec{\alpha})}{var(\vec{\alpha})} \tag{4.16}$$

This reasoning allows us to find the desired solution from the infinite possibilities of admissible solutions given by inverting only tilt data. If the strain source signal is significant enough to be measured by other geodetic techniques, inverting tilt data together with GPS, InSAR and/or levelling data could reduce the number of admissible solutions. In Chapter 6, I illustrate how our methodology leads to recover both drift rates and volumetric source history using an example of the time inflation of a buried volumetric source at depth.

4.6 Uncertainties

The predicted values cannot, in general, be identical to the observed values for two reasons: data uncertainties and model imperfections. As we use a weighted Euclidian norm to build the functional J (see Section 4.4), we account for data uncertainties. Considering these uncertainties in the functional induces a propagation of uncertainties through the inversion process from the data to the parameters. But propagating data uncertainty leads to a fraction of uncertainty about the physical system value. Indeed, it does not take into account model discrepancy (and other sources of uncertainty) (Tarantola and Valette, 1982; Brynjarsdóttir and Ohagan, 2014). This source of uncertainty was firstly introduced by (Kennedy and O'Hagan, 2001). They considered the problem of using observations of the real physical system to learn about uncertain input parameters (the process of calibration) and showed how to account for model discrepancy in calibration and in subsequent predictions of the physical system. In this study, we only account for the data uncertainties in the inversion process, but we acknowledge the existence of model inadequacy.

It is generally not possible to set inverse problems properly without a careful analysis of parameter uncertainties which consists in estimating a range of confidence of the optimized parameters. One way to determine the model parameters uncertainties is to link the covariance matrices of the parameters ($\Sigma_{\vec{p}}$) and data ($\Sigma_{\vec{d}}$) with assuming a linear relation:

$$\Sigma_{\vec{d}} = A \Sigma_{\vec{p}} A^T \tag{4.17}$$

where the matrix A is a linear operator between parameters and data. Through this relation we are seeking the parameters sensibility $\Sigma_{\vec{p}}$ according to data uncertainties $\Sigma_{\vec{d}}$. Because A is not necessarily invertible, analytically calculating this matrix can be numerically unstable (Furst et al., 2017). Thus, finite differences can be used to simulate perturbations on the data induced by small perturbations on the parameters. This is done by perturbing the selected parameter around its optimum and then by running the optimization again, the new solution displaying the results accounting for the perturbation. Although more robust, it is computationally time-consuming.

In Furst et al. (2017) we assume $A = \nabla_p d$ which is the Jacobian matrix made of the derivatives of the velocities at geodetic measurement locations with respect to the model parameters.

4.7 About the computation code

The methodology described in this chapter allows for the optimization of various inverse problems. Its implementation is achieved using Fortran 77 and 95 and can be divided into 3 blocks featuring the global optimization in the master program, a user interface for the parametrization of the model and a collection of routines including the forward models and the construction of the functional.

- The optimization process is implemented in the main program named **BMO**. Developed in previous studies (Ivorra, 2006; Ivorra and Mohammadi, 2007), it contains the different layers of the semi-deterministic approach described in Section 4.2. A well detailed user-guide is presented in Ivorra (2006).
- The main program calls the interface, **BMO_user**, from which the user can provide information about the data, the functional or the calculation of the gradient (*e.g.* for adjoint calculation). It permits to connect the optimization process to the user-defined parametrization.
- The final block acts as a library of additional routines required to generate modelled data from various forward models and to calculate the functional previously described. I implemented the functional as well as two forward models already described (Mogi and McTigue) and adjoined the routines for Okada's model (Okada, 1992).

The flow chart of this optimization presented in Figure 4.7 summarizes our strategy and the main functional relations. Our optimization parameters p are picked between sources and instrumental parameters depending on the selected forward model (Mogi, McTigue or Okada's model). The free parameters are set to an initial guess in their admissible variation domains. No a priori knowledge of these initial values is needed, but when available providing shorter range of searching values accelerates the calculation. This initial set of parameters includes the first model from which synthetic data are produced using the constitutive equations of the chosen forward model (Figure 4.7). Model predictions are then compared to the observations through the specific functional.

The stopping criteria is based either on a user-defined target value of the functional J or on a prescribed maximum number of functional evaluations. Also, one could consider that continuing the inversion is useless if individual functionals $(J_{MN})_i$ are below the corresponding data uncertainty.

4.8 Three levels of complexity

In the following Chapters (5, 6 and 7) I present direct applications of the methodology, using different kinds of observations and forward problems. The code that has been implemented is able to treat three levels of complexity. To describe these levels of complexity, I either vary the number of data types in the linear problem or consider time-independent or time-dependent parameters in the optimization (Table 4.2).

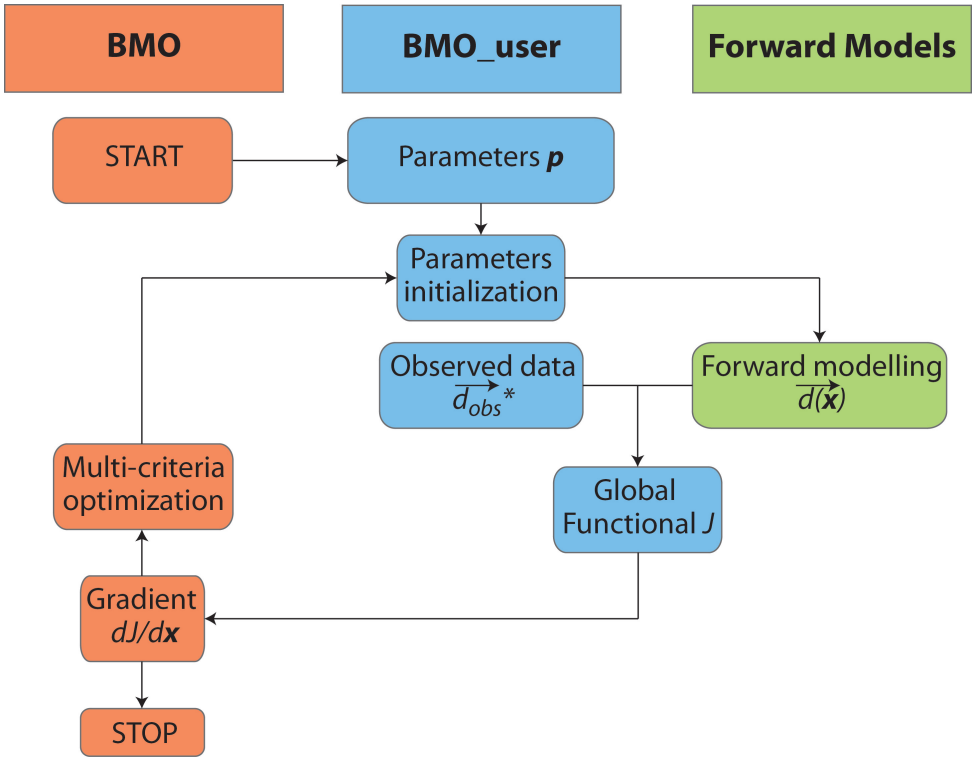

Figure 4.7: *Workflow of the methodology with the three blocks of code: BMO, BMO_user and Forward Models.*

The I-level of complexity considers one data type with no time-dependent parameter. As an illustration of this first level, we used interseismic velocity measured by GPS to infer the shear rigidity of plate with an application to the San Andreas Fault. The II-level includes time-dependent parameters in the optimization process. For this case, we invert tilt time-series to retrieve both volume variations of a point source and the drift parameters of the tiltmeters. Eventually, the III-level jointly inverts several data types (GPS, tilt, InSAR and levelling) with time-dependent parameters. A synthetic example is shown in Chapter 7.

Complexity level	Data type	Time dependency	Forward model linearity	Application
I	1	no	yes	GPS data inversion Furst et al. (2017)
II	1	yes	yes	Tilt time series inversion Furst et al 2018 (submitted)
III	>1	yes	yes	Time-dependent geodetic data fusion

Table 4.2: *Review of the three levels of complexity used hereafter for the applications of the methodology.*

Chapter 5

Large scale interseismic GPS dataset inversion

Résumé

Ce chapitre propose une première application de la méthodologie d'optimisation décrite dans le Chapitre 4. En ne considérant qu'un type de données géodésiques, les mesures GPS, nous tentons de retrouver un paramètre de la croûte continentale, la rigidité au cisaillement . L'article "Lithosphere rigidity by adjoint-based inversion of interseismic GPS data, application to the Western United States" *(Furst et al., 2017) est un prolongement du travail effectué par Chéry et al. (2011) basé sur la même méthodologie mais en y apportant des perfectionnement qui permettent d'avoir des résultats plus robustes et fiables et mieux résolus (l'adjoint a permis l'augmentation du nombre de paramètres considérés).*

Le principe est le suivant: les variations latérales de vitesses intersismiques horizontales peuvent s'expliquer par une variation latérale de rigidité que nous appellerons rigidité cisaillante. Les vitesses intersismiques enregistrées par les GPS sont supposées représenter les mouvements lents et continus induits par la tectonique des plaques. Tout mouvement dû à des événements sismiques (co- et post-sismique) est supprimé (autant que possible) des données GPS pour ne conserver que le signal intersismique. C'est à partir de ces données corrigées que nous pouvons retrouver certaines propriétés des plaques. En inversant les données géodésiques, nous cherchons à les reproduire en faisant varier les paramètres de notre modèle direct. En l'occurrence, nous avons choisi de considérer un problème élastique linéaire avec une discrétisation de l'espace en élements finis pour créer notre modèle numérique. Dans un premier temps, nous avons créé des données synthétiques pour valider la méthode d'optimisation, puis nous l'avons appliquée à un jeu de données réelles. Nous nous sommes intéressés à l'Ouest américain dans la partie Sud de la faille de San Andreas. Ici, des zones à fort taux de déformation (le réseau de failles de San Andreas) cotoient des zones où le taux de déformation est extrêmement faible (la Sierra Nevada par exemple).

L'inversion des données intersismiques repose sur la minimisation de la somme des écarts quadratiques entre les données modélisées et observées. L'objectif est de retrouver

les paramètres du modèle qui prédisent au mieux les données observées. Ces paramètres sont la rigidité cisaillante de la croûte, pour laquelle nous n'avons pas d'évaluation géophysique alternative, et les vitesses de déplacement au bord du domaine qui peuvent être ajustées grâce aux conditions aux limites de Dirichlet (vitesses) du modèle. Un terme de régularisation de type Tikhonov a été introduit dans la fonctionnelle. Il permet de lisser ces conditions aux bords pour éviter des changements trop important du gradient de vitesse. Le gradient de la fonctionnelle est ensuite calculé en utilisant la formulation adjointe du problème direct, ce qui nous permet de considérer un nombre important de paramètres d'optimisation tout en conservant un coup de calcul raisonnable. A l'issue de l'optimisation, nous obtenons une distribution de la rigidité cisaillante accompagnée d'une distribution des résidus en vitesse GPS ainsi qu'une distribution des incertitudes associées aux paramètres de rigidité. Les résultats de taux de déformation associés à ce modèle sont discutés et comparés aux études précédentes sur cette zone de l'Ouest Américain.

5.1 Introduction

In a first stage of development of the methodology described in Chapter 4, we attempted to infer the rigidity of continental plates using horizontal velocities measured by GPS. This interseismic strain is a small fraction of millions years of continuous accumulation of anelastic processes in the lithosphere due to plate motions. Although the flexure of the lithosphere may be well constrained using a simple secular cooling model in the ocean (Stewart and Watts, 1997), it remains challenging to determine this mechanical parameter in the continents. In the case of flexure, plates submitted to topographic and other internal loads display vertical motions controlled by plate rigidity (Watts, 2001). One commonly estimates the flexural rigidity, expressed through the effective elastic thickness (EET) of the lithosphere, by studying the lithosphere's vertical motion resulting from long-term geological loads. However, plate can also be subjected to shear stress, inducing horizontal motions. We imagine that the variations in horizontal displacements observed in these conditions are due to lateral variations of lithosphere elastic properties, hereafter named shear rigidity. In the following paper, we present an approach of inversion using the horizontal velocities to evaluate lateral rigidity variations.

Because the present day strain of the Western United States has been thoroughly investigated using GPS geodesy, this area is quite adapted to illustrate our methodology. Similarly to Chéry et al. (2011), we choose this area where weakly strained areas (e.g., the Sierra Nevada) are connected with areas of large strain rate (e.g. San Andreas Fault system). We add some improvements to the optimization process: the adjoint formulation of the gradient of the functional allows to consider huge number of optimization variables, the boundary conditions are free parameters as well as rigidity and a Tikhonov regularization is applied to the boundary conditions. Finally, we associate uncertainties to the optimal rigidity distribution. We created synthetic cases first, in order to validate the approach and then consider a homogeneous set of geodetic data: 615 GPS velocities during interseismic period (Southern California Earthquake Center Crustal Motion Map Version 3.0, SCEC CMM3). As this dataset is based on decades of GPS measurement, the signal induced by significant seismic events is removed (Kreemer and Hammond, 2007).

The forward model considers a finite element model (CAMEF code, courtesy of R. Hassani) of an area of several hundreds of kilometers which can deform according to linear and isotropic elasticity on plane stress. A uniform 2-D Delaunay mesh composed by triangles is generated for a given spatial domain (for synthetic tests and application) leading to 2284 individual elements for the application to Western United States (394 elements for synthetic cases). Along the boundary of our domain, we apply Dirichlet boundary conditions allowing us to compare to the observations. The boundary velocities are therefore free parameters intrinsic to each node of the mesh boundary. Besides, associated to each element we also define the free parameter D (shear rigidity) which is linked to the elastic parameters and interseismic velocities using the stress equilibrium of the model. This constitutive equation links the strain rate to the stress rate and boundary conditions.

As it is exposed in Chapter 4 this method involves the minimization of a cost function J defined as the quadratic measure of the differences between measured and predicted velocity fields on a discrete set of points. Because our inverse problem is ill-posed, we include regularization terms to control local fluctuations of the parameters (Tarantola, 2004; Tikhonov, 1943). By doing so, our goal is to adjust the predicted data to the observed data, while preserving some degree of regularity on the velocities along the boundaries. As the result of the finite element discretization of the domain, the number of free parameters can reach several thousands. Although optimization becomes time consuming in such conditions, one can reduce the optimization time and complete the inversion using an adjoint formulation of the gradient of the functional with respect to the independent parameters of the model. With no information about the convexity of the cost function and its potential local minima, we apply the global optimization approach for one type of data in order to converge towards the smallest admissible value of the functional.

The inversion of interseismic data produces a map of effective rigidity distribution associated with velocity residuals and corresponding uncertainties for the rigidity. We present and discuss these results, focusing on the sensitivity of the model with respect to the data. We also compare our deformation model to previous studies of strain rate and rigidity distribution in the Western United States and California. We finally propose future applications of this method in different classes of tectonic or geodynamic problems.

5.2 Lithosphere rigidity by adjoint based inversion of interseismic GPS data, Application to the western United States

ARTICLE IN PRESS
TECTO-127432; No of Pages 20

Tectonophysics xxx (2017) xxx–xxx

Contents lists available at ScienceDirect

Tectonophysics

journal homepage: www.elsevier.com/locate/tecto

Lithosphere rigidity by adjoint-based inversion of interseismic GPS data, application to the Western United States

Severine Furst [a,*], Michel Peyret [a], Jean Chéry [a], Bijan Mohammadi [b]

[a] Géosciences Montpellier, Université de Montpellier, CNRS UMR-5243, 34095 Montpellier, France
[b] Institut Montpelliérain Alexander Grothendieck, CNRS, Université de Montpellier

ARTICLE INFO

Article history:
Received 18 July 2016
Received in revised form 10 March 2017
Accepted 21 March 2017
Available online xxxx

Keywords:
GPS
Interseismic velocity
Effective rigidity
Global optimization
San Andreas Fault system
Uncertainties

ABSTRACT

While vertical motion induced by long-term geological loads is often used to estimate the flexural rigidity of the lithosphere, we intend to evaluate the shear rigidity of the lithosphere using horizontal motion. Our approach considers that the rigidity of the lithosphere may be defined as its resistance to horizontal tectonic lateral forces. In this case, a spatial distribution of an effective shear rigidity can be estimated from the analysis of the interseismic velocity fields. We consider the Western United States zone where weakly strained areas (e.g., the Sierra Nevada) are connected with areas of large strain rate (e.g. San Andreas Fault system). By inverting interseismic strain distribution measured by geodetic methods, we infer the effective shear rigidity of the lithosphere. The forward problem is defined using the equations of linear elasticity. The inversion relies on the minimization of the sum of a quadratic measure of the differences between measured and modelled velocity fields. The functional also includes regularization terms for the parameters of the model. The gradient of the functional with respect to the minimization parameters is computed using an adjoint formulation. This permits the treatment of large dimensional minimization problems. Finally, a measure of the uncertainty of our inversion is illustrated through the covariance matrix of the parameters at the optimum. The optimization chart is validated on two synthetic velocity distributions. Then, the effective shear rigidity variations of the Western United States are estimated using the CMM3 interseismic velocities. The inversion displays low effective rigidities along the San Andreas Fault system, the Mojave Desert and in the Eastern California Shear Zone, while rigid areas are found in the Sierra Nevada and in the South Basin and Range. Finally, we discuss the differences between our strain rate and rigidity maps with previously published results for the Western United States.

1. Introduction

Geological strain occurring over millions of years results from the continuous accumulation of anelastic processes in the crust and in the lithosphere in response to plate motion. Active deformation areas are identified by seismicity and geodetic deformation. In active deformation area, the comparison of plates motion from geology and geodesy, at these two different time scales, provides a fair agreement in term of horizontal velocities (Sella et al., 2002). Geologic and geodetic comparisons can also be made across active faults using standard models for interseismic strain (McCaffrey, 2005; Meade and Hager, 2005; Savage and Burford, 1973). It appears that most of the documented faults display a close agreement between geodetic and geologic strain rates (Vernant, 2015).

From a mechanical viewpoint, the close agreement between short and long-term strain rates (i.e. time scales from 10 yrs to 1 Myrs) probably reflects the stability of the stress balance in the lithosphere under the action of slowly evolving remote forces associated to subduction, basal drag and, more generally, the plate system gravitational potential energy. Under the action of these forces, strain distribution is mostly controlled by the lithospheric strength. By strength we mean the maximum force sustainable by the lithosphere. Like lithospheric stress, lithospheric strength cannot be determined precisely with depth, unless with crude rheological yield strength envelope models (Tesauro et al., 2011). Indeed, a precise strength estimate with depth would require a detailed knowledge of the temperature profile with depth, lithology and water contents, as well as friction law in the brittle domain and temperature dependent viscous laws in the ductile crust and mantle. Therefore, the lithospheric strength can only be approached through its integral measure along depth, with numerical models of the lithosphere. These solve stress equilibrium using elasto-visco-plastic laws with prescribed boundary conditions (Bird and Kong, 1994; Chéry et al., 2001). However, a simplified version of lithospheric strength is embedded in the concept of effective elastic thickness (EET) applied to plate flexure. Indeed, it has been shown that plates submitted to topographic and other internal loads display vertical motions controlled by plate rigidity (Watts, 2001). Combined analysis of topographic and gravimetric signals allows

* Corresponding author.
E-mail address: severine.furst@gm.univ-montp2.fr (S. Furst).

http://dx.doi.org/10.1016/j.tecto.2017.03.015
0040-1951/

for computing effective elastic thickness and its variation at continental scale (Lowry and Smith, 1994; Pérez-Gussinyé et al., 2009). A fair agreement is generally found between heat flow and EET where small values of EET correspond to high heat flow zones.

Both lithospheric strength and effective elastic thickness are commonly associated with the long-term behaviour of the lithosphere. However, these concepts can be adapted in order to interpret interseismic geodetic measurements (Chéry, 2008). For a typical time of 10 years of geodetic observation and in the absence of large earthquakes, a linear evolution of GPS motion is often observed. Therefore, a collection of GPS velocities may be used in order to compute strain rate maps at plate scale (Kreemer et al., 2014). Even if this latter analysis is purely kinematic, the resulting geodetic strain rate must satisfy stress equilibrium over the time of observation. In such a problem, the unknown is the incremental lithospheric strength. One example is the spatial variation of the stress change integrated over the depth over the time of GPS observation. The problem can be simplified assuming that lateral strength variation is modulated by geodetic plate thickness (Chéry, 2008). The integrated value of the shear-stress at depth is what we call the effective shear rigidity. It is conceptually similar to the flexural rigidity: the effective shear rigidity expresses the resistance of the lithosphere to lateral forces (unit is N), while the effective flexural rigidity is related to the resistance of the lithosphere to vertical bending (unit is N·m).

In Chéry et al. (2011), we proposed a global optimization approach to estimate effective plate rigidity maps by the inversion of a GPS velocity field. The inversion provides a rigidity field realizing a RMS between the observed and modelled velocity fields close to 2 mm/yr for a dataset in southern California. However, we faced difficulties to properly fit high velocity gradients in the vicinity of the San Andreas Fault system. This is because the method did not allow the consideration of large inversion problem and therefore the local spatial density of our model parameters was too low. Moreover, a priori velocity boundary conditions were necessary and no uncertainties estimated.

In this paper, we present an enhanced version of the method to address the previous issues:

- the number of optimization variables can now be arbitrary thanks to the use of an adjoint formulation of the forward problem. This permits high spatial resolution for the rigidity.
- boundary conditions are not anymore prescribed but now treated as optimization variables as well.
- uncertainties are calculated for optimal rigidity value.

The paper is organized as follows: (1) we describe the new features of the method and we state the differences with respect to Chéry et al. (2011), (2) we demonstrate the efficiency of our new approach on a synthetic dataset that mimics a strike slip fault locked at depth, (3) we propose a refined rigidity map of southern California and we study the sensitivity of the solution of the inversion problem with respect to the location of domain boundaries. Finally, (4) we compare and discuss our results with those already published, both in terms of strain rate maps and effective elastic thickness.

2. Governing equations and forward modelling

Geophysical laws provide the mathematical framework to compute the outcome of some physical processes: this is called the forward problem. In other words, the model and its inputs are known and specific data (e.g. seismic, geodetic, or magnetic) are sought thanks to the equations linking the physical parameters to the solution at the observation location. Most of the time, we only have access to the consequences of a physical process (e.g. the geodetic measurements). These consequences need to be inverted to determine the physical properties of the Earth interior (Tomography: e.g. Montelli et al., 2004; Tanaka et al., 2009. Volcanoes and geothermal zones: e.g.; Anderson and Segall, 2013; Dzurisin, 2003; Mossop and Segall, 1999. Application to reservoirs: e.g. Hesse and Stadler, 2014). In some cases, there are analytical theories dictating the distribution of model's parameters that accurately reproduces the observations. For most geophysical problems, the limited amount of data used to reconstruct a model with infinite degrees of freedom leads to the non-uniqueness of the solution. Consequently, the inverse problem only provides one of the many models that explain the data and has uncertainty because the real data are subject to uncertainties and errors.

The effective elastic thickness of the lithosphere can vary laterally due to both elastic properties and the rheological failure properties that limit elastic strength. Flow strength depends on other factors than the temperature. Also, part of the variation imaged by the geodetic technique is probably due to the limits of frictional strength on faults (Bird and Kong, 1994). The thermal plate regime probably exerts a large influence due to the sensitivity of the effective plate rigidity with respect to its temperature profile (Watts, 2001). Here, we model these rigidity variations as lateral variations of the elastic properties of a plate with constant thickness. Thus, our forward model is made of a domain (Ω) symbolizing a 2-D plate, which can deform according to linear and isotropic elasticity (Fig. 1). Along the boundary of the domain $\partial\Omega$, we apply Dirichlet conditions (i.e., in-plane velocities u_{BC}) and assume free normal traction at the surface of the plate (plane stress assumption). This hypothesis means that strain perpendicular to the plane can occur. The forward model is therefore composed of three equations, the stress equilibrium (Eq. (1)), a constitutive equation linking the strain rate to the stress rate for a 2-D plate (Eq. (2)) and boundary conditions (Eq. (3)):

$$div(\dot{\sigma}) = 0 \quad \text{on } \Omega \tag{1}$$

$$\dot{\sigma}_{i,j} = \frac{E(x,y)}{1+\nu}\left(\dot{\varepsilon}_{ij} + \frac{\nu}{1-2\nu}\dot{\varepsilon}_{kk}\delta_{ij}\right) \quad \text{on } \Omega \tag{2}$$

$$u = u_{BC} \quad \text{on} \partial\Omega \tag{3}$$

where $\dot{\varepsilon}$ and $\dot{\sigma}$ are the strain- and stress-rate tensors, δ is the Kronecker delta function, i,j and $k = 1,2$. Because of the relatively small variation of the Poisson's ratio for the lithosphere, ν is assumed to be constant and equal to 0.25. The Young modulus E remains the only free mechanical parameter in this equation. Since the model is driven by a velocity condition, only the relative variation of the Young's modulus matters for strain computation. This means that any distribution of the form $C \times E(x,y)$ provides the same velocity field u regardless the value of the constant C. For this reason, we define the non-dimensional effective rigidity distribution $D(x,y)$ as $\frac{E(x,y)}{E_{min}}$ where E_{min} is the minimum value of $E(x,y)$ over the domain. So, all distributions of D presented in this paper range from 1 to some maximum values.

For a given spatial domain, we generate a uniform 2-D Delaunay mesh composed by triangles. In order to estimate the velocity field u at geodetic measurement locations we use the academic 2-dimensional finite element code CAMEF. The code does not incorporate the value of the plate thickness. Therefore, we cannot discriminate plate thickness and elastic properties of the lithosphere from the rigidity values. Hence, fixing an absolute value to the rigidity remains an open problem. Finally, the velocity field u produced by the forward model depends on two input parameter sets: the velocity boundary conditions u_{BC} and the distribution of $D(x,y)$ (Fig. 1). Eventually, we try to fit u with the observations u^*.

3. Inversion method

Running the direct problem requires the prescription of the velocity on the boundary nodes and the rigidity for each mesh element. Contrary to the approach proposed in Chéry et al. (2011), the boundary conditions are not imposed anymore in the inverse problem and are treated

Please cite this article as: Furst, S., et al., Lithosphere rigidity by adjoint-based inversion of interseismic GPS data, application to the Western United States, Tectonophysics (2017), http://dx.doi.org/10.1016/j.tecto.2017.03.015

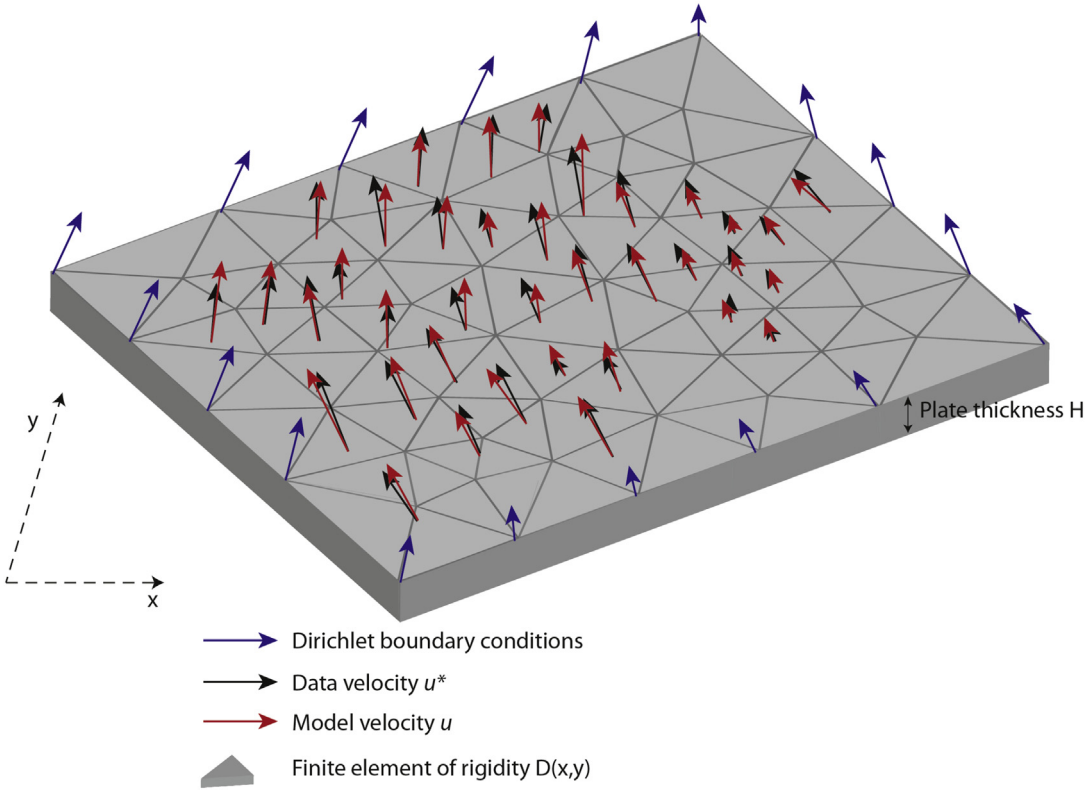

Fig. 1. Schematic representation of the optimization problem: the domain Ω is meshed with elements of constant rigidity $D(x,y)$ and submitted to Dirichlet boundary conditions along the boundary $\partial\Omega$. The black arrows symbolize the geodetic measurements u^* within the domain, the blue ones the Dirichlet conditions which are part of the optimization variables and the red ones are the solution of the model. (For interpretation of the references to color in this figure legend, the reader is referred to the web version of this article.)

as optimization parameters. We associate one rigidity parameter to each mesh element leading to a very large optimization problem. Our global optimization algorithm requires the gradient of the functional. We consider an adjoint formulation of the forward model to access this gradient with respect to all the model parameters simultaneously.

3.1. Cost function

We want to invert observed data u^* and determine the model parameters $p(D, u_{BC})$ minimizing the distance (here L_2-norm) between the observed data u^* and the predicted field $u(p)$ inside the domain Ω:

$$J(p) = \|u^* - u(p)\|^2_{\sigma^{-1}} \tag{4}$$

where J is the cost function to minimize, and subscript σ^{-1} means that the L_2-norm is weighted by the inverse of the covariance matrix of the geodetic measurements.

Geophysical inverse problems are usually ill-posed and need to include a subjective degree of regularization to achieve relevant geophysical solutions (e.g. Zaroli et al., 2013). We therefore introduce to the cost function two Tikhonov regularization terms to control local fluctuations of the parameter vector (Tarantola, 2004; Tikhonov, 1943). We separate the regularization of the parameters along the boundaries u_{BC} and those associated to the rigidity D inside the domain:

$$J(p) = \|u^* - u(p)\|^2_{\sigma^{-1}} + \lambda_1 R_1(D) + \lambda_2 R_2(u_{BC}) \tag{5}$$

where $R_1(D)$ and $R_2(u_{BC})$ are regularization operators. The former acts over the domain and controls the regularity of the rigidity distribution, while the latter monitors the regularity of the boundary conditions. Both are particular forms of non-linear Laplace-Beltrami operators with a local control of the level of regularization (Mohammadi and Pironneau, 2009). The weights λ_i have to be chosen by the user. Series of different optimizations have been run to highlight the effect of λ_i on the inversion. By doing so, our goal is to adjust $u(p)$ to the data u^*, while preserving some degree of regularity on both the rigidity inside the domain and the velocities along the boundaries. However, for each simulation, we only have the values of the velocities (and not rigidity) to compare with. Hence, adjusting the regularity of the rigidity is largely subjective and we found that using no regularization ($\lambda_1 = 0$) for rigidity leads to acceptable spatial rigidity gradients. Hence, in this study, we only consider the regularization term of the boundary conditions.

In order to choose λ_2, we explore the *trade-off* between the residual data misfit $Res(p) = \|u^* - u(p)\|^2$ and the regularization term $R_2(u_{BC})$. This is featured in a *trade-off* or Pareto curve, which gathers all feasible solutions that cannot be improved in any of the objectives without degrading the other objectives (e.g. Vassilvitskii and Yannakakis, 2005). The selection of an optimally regularized solution depends upon the requirements of a particular study. We will illustrate the impact of the regularization over the boundary conditions for the rigidity inversion in Southern California.

3.2. Global optimization

We apply a global optimization algorithm (Ivorra et al., 2013) to iteratively invert interseismic geodetic data. Global optimization is necessary as we have no information on the convexity of the cost function and several local minima can be present. The global optimization strategy is meant to improve the initial condition for classical gradient-based methods looking for an initialization in the attraction basin of the global optimum (Mohammadi and Pironneau, 2009).

In addition to the Tikhonov regularization mentioned above, the gradient of the functional is smoothed (Mohammadi and Pironneau, 2004, 2009) in order to control the regularity of the parameters. The optimization algorithm ends when the functional or the variations of the

Please cite this article as: Furst, S., et al., Lithosphere rigidity by adjoint-based inversion of interseismic GPS data, application to the Western United States, Tectonophysics (2017), http://dx.doi.org/10.1016/j.tecto.2017.03.015

gradient are smaller than some user-defined thresholds. A synthetic flow chart of the inverse problem is given in Fig. 2.

Functional derivatives computation is done using an adjoint formulation of the forward model (e.g. Plessix, 2006). In most of the inverse problems in geophysics, the cost function cannot be analytically linearized. If a finite difference approach is adopted, the number of forward computations for assessing the gradient of the functional is proportional to the number of parameters. Let us briefly recall the adjoint technique. The gradient of the functional with respect to the model parameters can be expressed as follows:

$$\nabla_p J = \frac{\partial J}{\partial p} + \left(\frac{\partial J^t}{\partial u}\frac{\partial u}{\partial p}\right)^t \tag{6}$$

where J is the functional, p the parameters and u the velocity calculated at each node of the mesh. From the equilibrium equation $\boldsymbol{K}u = f$, we incorporate the rigidity matrix $\boldsymbol{K}$ and the stress vector f in (Eq. (6)):

$$\nabla_p J = \frac{\partial J}{\partial p} + \left(\frac{\partial J^t}{\partial u}\cdot \boldsymbol{K}^{-1}\cdot\left(\frac{\partial f}{\partial p} - \frac{\partial \boldsymbol{K}}{\partial p}u\right)\right)^t \tag{7}$$

Defining the adjoint variable V as the solution of the system $\boldsymbol{K}^t \cdot V = \boldsymbol{K}\cdot V = \frac{\partial J}{\partial u}$ (because $\boldsymbol{K}$ is self-adjoint in our case), we obtain:

$$\nabla_p J = \frac{\partial J}{\partial p} + \left(V^t\cdot\left(\frac{\partial f}{\partial p} - \frac{\partial \boldsymbol{K}}{\partial p}\cdot u\right)\right)^t \tag{8}$$

Consequently, the amount of computation needed to obtain the gradient of the functional mostly corresponds to the solution of one forward model, by opposition to a finite difference scheme which needs a number of forward model solutions equal to the number of parameters.

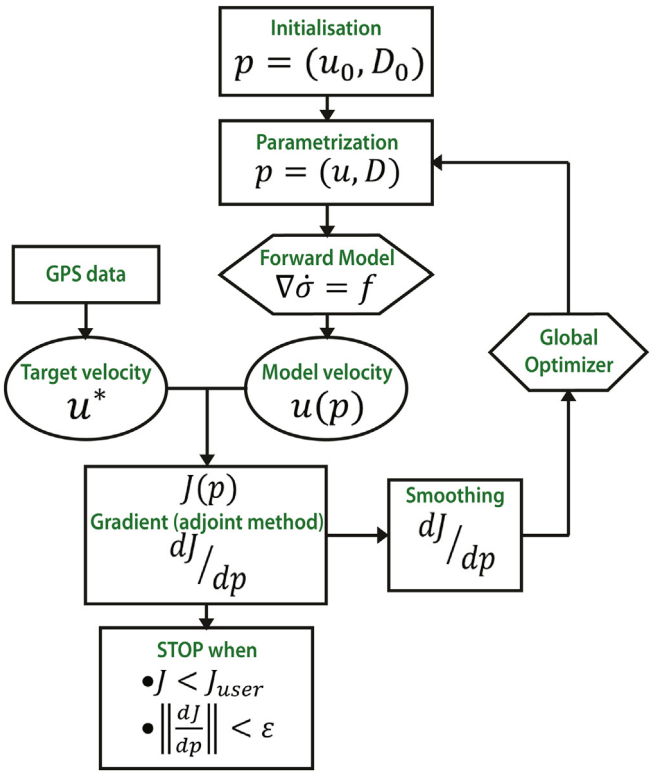

Fig. 2. Sketch of optimization algorithm applied to plate rigidity inversion. For each iteration we optimize both the rigidity within the domain and the velocity along the boundaries.

3.3. Model parameters initialization

Real GPS datasets present large spatial variations of density measurements. GPS stations are usually set to observe the velocity gradient around fault zones. Therefore, we usually expect null strain in geographical areas where measurements are sparse. This information can be used to define the initial guess for the lithosphere rigidity in the optimization procedure. This is similar to what is done in topological optimization (e.g. Allaire et al., 2004) where the initial structural rigidity is set to the maximum admissible value. Optimization then aims at making the structure softer and softer. A common problem in mechanical structure design is to optimize the topology of an elastic structure given certain boundary conditions. Optimality implies to minimize the weight, but at the same time, the structure needs to be as strong and rigid as possible. The rigidity of each element is hence reduced at each iteration of optimization when requested.

Synthetic and real cases presented in this paper involve rigidity reaching very large values in areas that exhibit little internal deformation. Thus, the rigidity amplitude ranges from a given minimum to infinity in no-deformation zones. This semi-open variation domain is not suitable for numerical search. Consequently, we choose a parameterization design using the compliance, $C = \frac{1}{D}$, of the material instead of the rigidity. The compliance is defined over the interval $[\varepsilon, 1]$, the lower bound corresponding to a quasi-rigid body. We have considered different values of ε. It appears that a value of $\varepsilon = 0.01$ which corresponds to two order of magnitude admissible variation for the rigidity is sufficient to fully capture the range of most strain-rates observed at the Earth's surface (see discussion in Appendix B). This use of compliance insures greater stability of the inversion process. For ease of understanding and interpretation, we express our results in terms of rigidity D after the inversion is completed.

3.4. Model parameters uncertainty

GPS observations are plagued with uncertainty due to various factors: instrumental noise, field measurement procedure, the skill of the operator and local environmental motions. These uncertainties affect in a complex way the GPS time series and generate a colored noise on positions (Mao et al., 1999). But, these also induce uncertainties on the model parameters determined through our optimization process. For that reason, it is essential to quantify the impact of data uncertainty

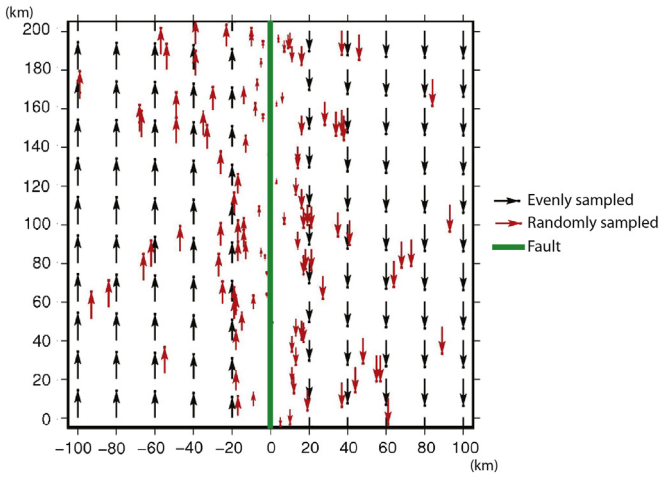

Fig. 3. Distribution of the synthetic velocities considering an evenly sampled domain (black arrows) and a randomly sampled domain whose density decreases with the distance to the fault (red arrows). The fault (green line) is a dextral strike slip fault locked during the interseismic motion. (For interpretation of the references to color in this figure legend, the reader is referred to the web version of this article.)

Please cite this article as: Furst, S., et al., Lithosphere rigidity by adjoint-based inversion of interseismic GPS data, application to the Western United States, Tectonophysics (2017), http://dx.doi.org/10.1016/j.tecto.2017.03.015

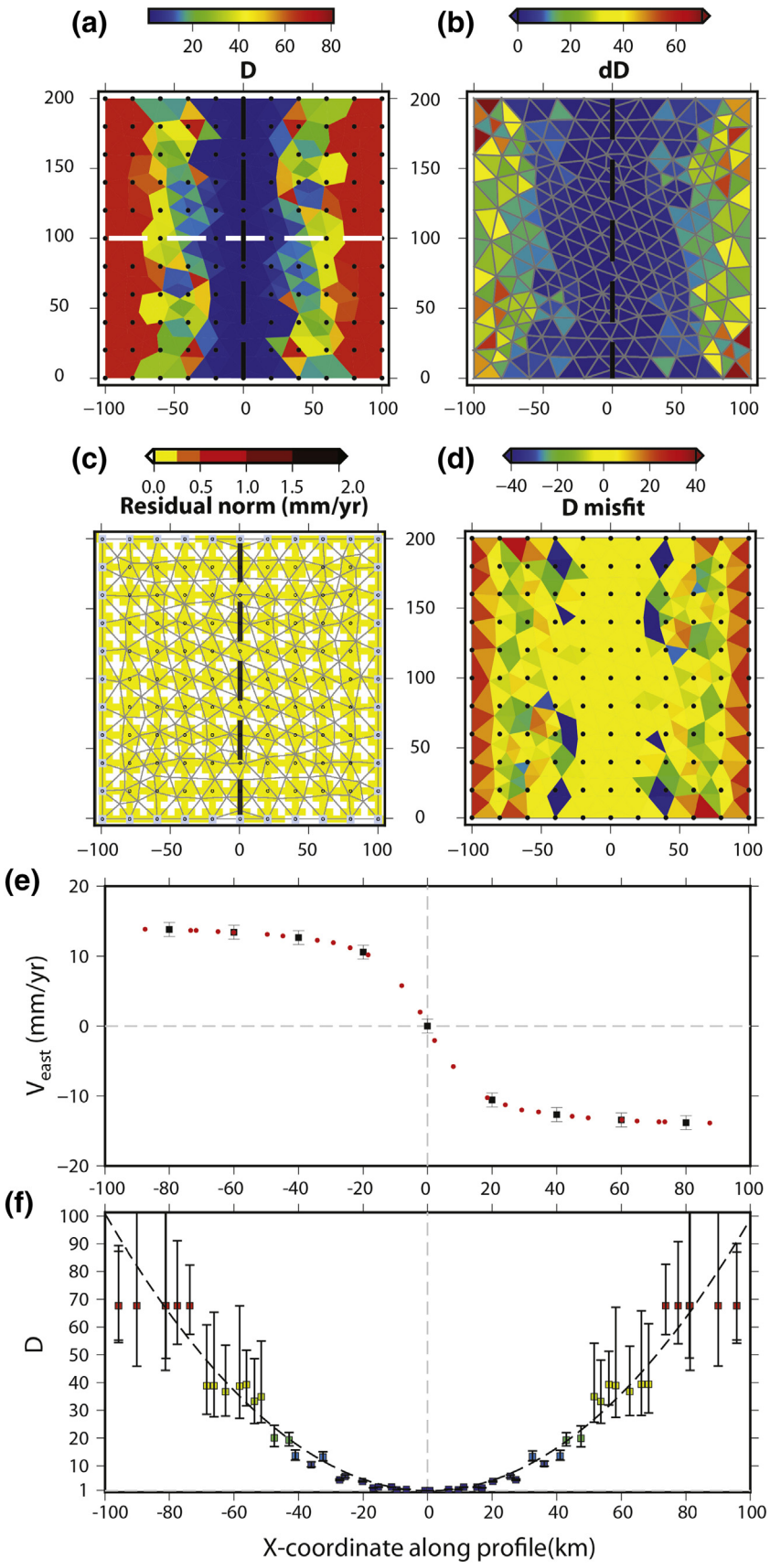

Fig. 4. Results of the inversion for the synthetic case with a geodetic spatial sampling (black dots on (a), (c) and (d)) whose density is constant whatever the distance to the fault (black line at coordinate 0 along the Y-axis). (a) rigidity distribution determined by the optimization; (b) associated uncertainty; (c) norm of residual velocities; (d) misfit between predicted D and theoretical D^*; (e) velocity measurements (black squares with uncertainty bars) and velocities predicted by our model (red circles) along the profile shown in white dotted line on (a); (f) rigidity values and their associated uncertainties along the same profile. The plotted values are estimated at the barycentre of the elements of the mesh in a 30-km wide bandwidth centred on the profile. The color code is the same as in (a). (For interpretation of the references to color in this figure legend, the reader is referred to the web version of this article.)

Please cite this article as: Furst, S., et al., Lithosphere rigidity by adjoint-based inversion of interseismic GPS data, application to the Western United States, Tectonophysics (2017), http://dx.doi.org/10.1016/j.tecto.2017.03.015

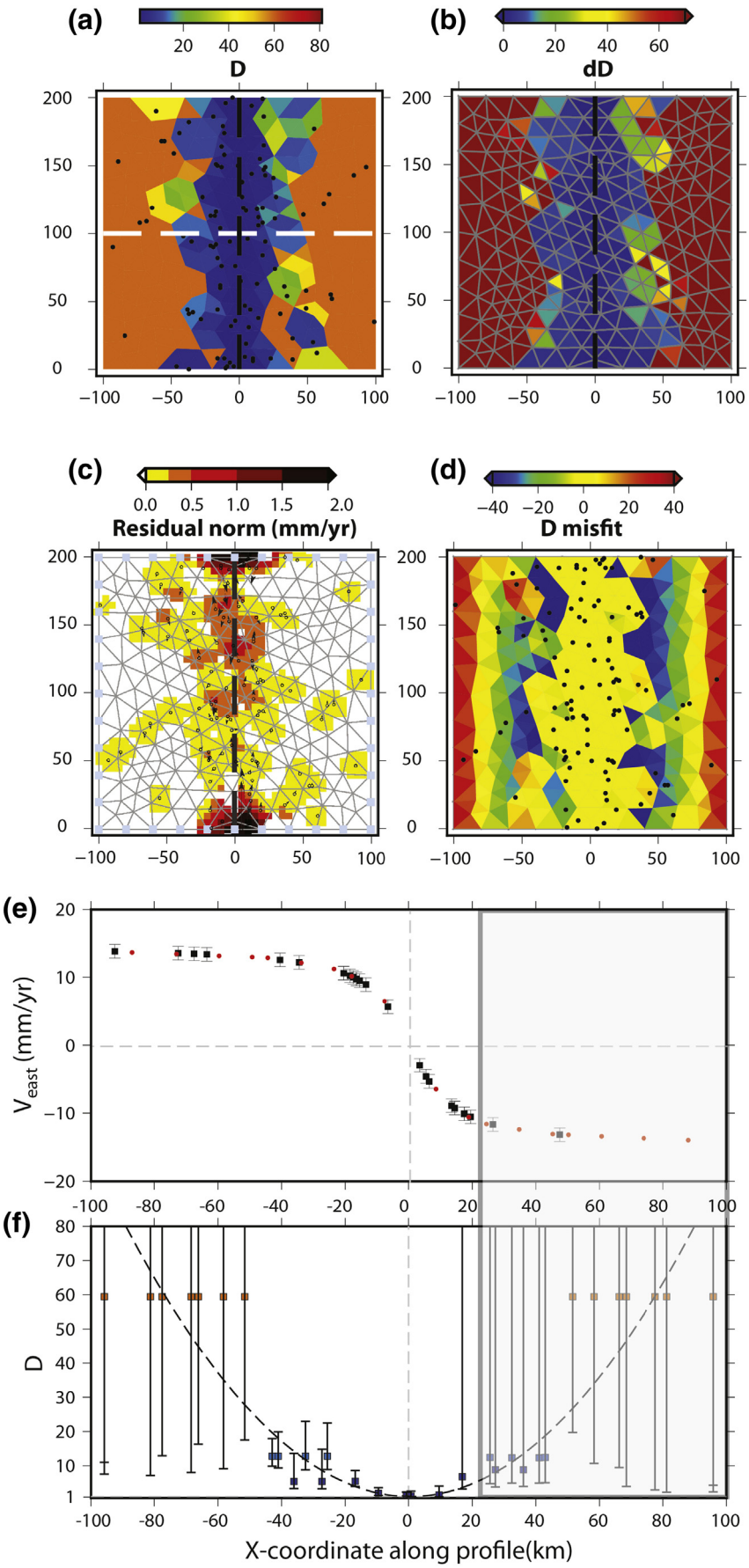

Please cite this article as: Furst, S., et al., Lithosphere rigidity by adjoint-based inversion of interseismic GPS data, application to the Western United States, Tectonophysics (2017), http://dx.doi.org/10.1016/j.tecto.2017.03.015

propagating through the inversion. Hence, the resulting rigidity distribution is complemented with a sensitivity map.

To determine the model parameters uncertainties, we link the covariance matrices of the parameters and data. Let us consider the observation u^* (geodetic velocities) as a sum of a 'true and noise-free' value u_r with zero variance (i.e. $\mathrm{cov}(u_r)=0$) and an uncertain quantity δu: $u^*=u_r+\delta u$. For this sum, the covariance matrix is given by:

$$cov(u^*) = cov(u_r) + cov(\delta u) + 2\, cov(u_r, \delta u) \tag{9}$$

Because u_r is deterministic, u_r and δu are independent (i.e. $\mathrm{cov}(u_r, \delta u)=0$). Therefore, the covariance matrix reduces to:

$$cov(u^*) = cov(\delta u) \tag{10}$$

We consider a linear relationship between δp and δu:

$$\delta u = (\nabla_p u)\cdot \delta p \tag{11}$$

which leads to:

$$cov(u^*) = \mathcal{I}\cdot\ cov(\delta p)\cdot \mathcal{I}^t \tag{12}$$

where $\mathcal{I}=\nabla_p u$ is the Jacobian matrix made of the derivatives of the velocities at geodetic measurement locations with respect to the model parameters. Similarly to (Eq. (9)), we define the covariance matrix of the predicted parameters $\mathrm{cov}(p_{obs})$ as:

$$cov(p_{obs}) = cov(p_r) + cov(\delta p) + 2\, cov(p_r, \delta p) \tag{13}$$

where p_r (the actual values of the parameters) is assumed deterministic. Again, p_r and δp are assumed independent, and therefore:

$$cov(p_{obs}) = cov(\delta p) \tag{14}$$

Finally, equation (Eq. (12)) becomes:

$$cov(u^*) = \mathcal{I}\cdot\ cov(p_{obs})\cdot \mathcal{I}^t \tag{15}$$

$$cov(p_{obs}) = \mathcal{I}^{-1}\cdot\ cov(u^*)\cdot \mathcal{I}^{-t} \tag{16}$$

So, this equation formulates the uncertainty propagation from geodetic measurements to the model parameters via the Jacobian matrix $\mathcal{I}$. The construction of this matrix can be performed in two different ways. The simplest approach consists in expressing it analytically as a function of the gradients that have been evaluated during the resolution of the adjoint problem. Indeed, $\mathcal{I}$ can be explicitly deduced from the equation $\nabla_p J = \frac{\partial J}{\partial p} + \left(\left(\frac{\partial J}{\partial u}\right)^t \mathcal{I}\right)^t$. This approach is straightforward and theoretically correct, but it is numerically unstable since it involves the inversion of singular matrices. Consequently, it is more robust to build $\mathcal{I}$ from finite difference computations. This consists in perturbating one parameter around its optimum (typically by 10%), and then computing the perturbation of the predicted velocity at all geodetic measurement locations. This approach is numerically robust because it involves no matrix inversion. With the second member of Eq. (16) in hand, we can now provide an estimation of the variance (diagonal of the covariance matrix) of the optimization variables.

In this study the parameter is the compliance C with its standard deviation $dC=(\mathrm{diag}(\mathrm{cov}(C))^{1/2}$. We define dissymmetric upper and lower bounds around the optimum for the rigidity parameter $D=\frac{1}{C}\in[\frac{1}{C+dC}, \frac{1}{\max(C-dC,10^{-4})}]$. To represent the uncertainty on the rigidity (dD) we use the fact that D is the inverse of the compliance and therefore:

$$dD = D^2\cdot dC \tag{17}$$

4. Determination of effective rigidity for a synthetic case

Before running our optimization scheme on real cases, we evaluate its efficiency to recover a given rigidity distribution D^* (target rigidity) associated with a specific 2-D velocity field u^*.

Surface strain across a locked fault zone can be interpreted either using the concept of a slipping fault zone beneath a locking depth (Savage and Burford, 1973) or by assuming a shear-rigidity variation perpendicular to the fault (Chéry, 2008). Differences and similarities between these models are discussed in this latter paper. According to the variable rigidity hypothesis, we define a target given by:

$$D^*(x) = 1 + \left(\frac{x}{d}\right)^2 \tag{18}$$

where D^* is a non-dimensional rigidity, x is the distance to the fault and d is a characteristic dimension. Solving force balance within such a plate leads to the following fault-parallel velocity field:

$$u^* = \frac{s}{\pi}\ arctan\left(\frac{x}{d}\right) \tag{19}$$

Therefore, such a velocity distribution is the solution of the spatially variable function of Eq. (18) but can also be associated to a screw dislocation at depth (e.g., Savage and Burford, 1973). In the case of active fault systems, d is generally associated to a physical locking depth which can be estimated using geodesy and seismology. In the case of the San Andreas Fault system, values of d range from 6 to 22 km depending on the location along the fault and the method of determination (e.g. Smith-Konter et al., 2011).

We conduct two tests to verify the ability of the method to retrieve the rigidity distribution given by Eq. (18) for different GPS data sets. We also test different values of d (from 2 km to 17 km) in order to generate velocity fields commonly observed on the San Andreas Fault. The specific case of fully-creeping faults (d ~ 0 km) is discussed in Appendix A, with application to the SAF segment located North of Parkfield. We focus here on the consequences of processing two different spatial distributions of GPS data: (1) evenly spatially distributed and (2) concentrated near highly strained zones. This corresponds to on site situations (Fig. 3). Both distributions are made of about 120 GPS velocities vectors.

Several experiments have been conducted to define an optimal mesh size. On the one hand, the computational time is related to the mesh size. The finer is the grid, the longer will be the optimization (about 60 times longer for a mesh 3.6 times finer). On the other hand, the grid needs to be fine enough to capture the variations of the velocity field, notably close to high velocity gradient areas such as the creep zones of the Parkfield segment. Eventually, a spatially adaptive mesh should be implemented. We choose to work with a mean constant spacing of 20 km. This configuration is generally a good compromise between the number of available geodetic measurements, the number of parameters that need to be adjusted and the size of the object we want to study.

For the first case, GPS measurements (black arrows on Fig. 3) are uniformly distributed over the domain, with a constant spacing of

Fig. 5. Results of the inversion for the synthetic case that mimics a real geodetic spatial sampling (black dots on (a) (c) and (d)) whose density decreases with the distance to the fault (black line at coordinate 0 along the Y-axis). (a) rigidity distribution from the optimization; (b) associated uncertainty; (c) norm of residual velocities; (d) misfit between predicted D and theoretical D^*; (e) velocity measurements (black squares with uncertainty bars) and velocities predicted by our model (red circles) along the South to North profile shown in white dotted line on (a); (f) rigidity values and their associated uncertainties along the same profile. The opaque rectangle over the northern termination of rigidity and velocity profile (e) and (f) highlights a zone where the density of measurements is low, leading to high rigidity uncertainties. (For interpretation of the references to color in this figure legend, the reader is referred to the web version of this article.)

Please cite this article as: Furst, S., et al., Lithosphere rigidity by adjoint-based inversion of interseismic GPS data, application to the Western United States, Tectonophysics (2017), http://dx.doi.org/10.1016/j.tecto.2017.03.015

20 km. For the second distribution, we mimic a "real" GPS network by producing a velocity field whose spatial density decreases with the distance to the fault. In both cases, the domain is a 200-km square with a 20-km mesh size (394 elements). The dextral strike-slip fault (green line on Fig. 3) has a slip rate s of 30 mm/yr and is locked at 10 km depth. The admissible values for the non-dimensional relative rigidity range from 1 to 100 (see Appendices A and B for a discussion of such a choice).

We apply our optimization algorithm to invert the two velocity fields (Figs. 4 and 5). In the case of the uniform dataset (Fig. 4a–f), we first compare the synthetic velocities (red dots on Fig. 4e) to the modelled ones (grey dots on Fig. 4e) along a profile (white dashed line on Fig. 4a) perpendicular to the fault (black dashed line on Fig. 4a–c). The dataset from the inversion almost perfectly matches the characteristic shape of a 2-D arctangent velocity field given by Eq. (19) (Fig. 4e). The misfit between predicted D and theoretical D^* (Fig. 4d) permits to estimate the tendency in over or under estimating D in our inversions. Besides, the difference between synthetic and modelled velocities, hereafter called residual velocities, is lower than 0.25 mm/yr over the whole domain (Fig. 4c).

Contrary to real cases where the true effective rigidity distribution is unknown, synthetic cases allow for testing the efficiency of our inversion method to retrieve the quadratic rigidity field given by Eq. (18). Fig. 4a shows the rigidity distribution over the whole domain of analysis, while Fig. 4b shows the uncertainty distribution map and Fig. 4f focuses along one transect across the fault. We can notice that, as expected, the code predicts a low rigidity zone (90% of the elements ranging between 1 and 3) along a 40 km-wide area centred on the fault. Also, D increases rapidly with the distance to the fault to reach high values (>30) 60 km from the fault. Associated with these rigidity values, we find uncertainties that are very small where rigidity is small but quite high when the opposite occurs (Fig. 4b). This mainly comes from the predominance of the (squared) rigidity term in Eq. (17). This expresses the fact that, in areas that do not deform significantly, very large values of rigidity are admissible (up to infinity) without modifying significantly the local velocity field. Since our search interval for rigidity is bounded, our optimal solutions tend to underestimate the real rigidity in non-deforming areas. This can be seen far from the fault in all the synthetic cases presented in this study (Figs. 4, 5, A.1 and A.2). Finally, we find that, within the uncertainties estimated by our method (Section 3.4), our predicted rigidity distribution fits its theoretical value. This is clearly true along the transect crossing the fault on Fig. 4f.

For a data set whose density decreases with distance to the fault (Fig. 5a–f), we observe the same ability for the optimization algorithm to retrieve an arctangent-shaped velocity field (Fig. 5f) and this despite sparse data away from the fault. In this synthetic case, some elements of the grid contain more than one velocity, making the capture of very local velocity gradients difficult if not impossible using one single rigidity parameter over each mesh element. Therefore, residual velocities (Fig. 5c) are generally higher for case 2 than for case 1, with 10% of residual vectors >1 mm/yr (the 1σ uncertainty associated with the data being 2 mm/yr) mainly located in the vicinity of the fault where each element of the grid contains several GPS measurements. As a result, local gradients are more difficult to estimate than for case 1 and this could explain the distribution of residual we observe in Fig. 5c. Despite these moderate residuals, the mean residual velocity over the whole dataset is as low as 0.85 mm/yr which is lower than the 1σ uncertainty of the data. This situation is typical of real dataset with a high density of GPS installed in highly deformed areas.

Finally, as for the uniform case, we find that our inversion leads to a distribution of rigidity that fits well its theoretical model within the predicted uncertainties (Fig. 5f). Indeed, considering the 40-km band width around the fault, (Fig. 5a) shows that 66% of the elements show low rigidities (between 1 and 3) while 29% present moderate ones (between 3 and 10). As described above, in very few deforming areas, the optimal solution underestimates the real rigidity but the uncertainty associated with these high values of rigidity tends to be quite high. Moreover, the uncertainty values also depend on the local density of geodetic measurements. Consequently, even when the optimization leads to fairly correct values of low-to-moderate rigidity close to the fault, their uncertainties may be large (Fig. 5b) as one can see along the transect between 20 and 100 km especially if the data distribution is random (Fig. 5f). Again, we present the misfit between D and D^*.

Overall, the satisfactory results of this experience lead us to keep this dimensioning of the grid (triangles with about 20 km edges) for the real case application below.

5. Effective rigidity of Western USA

5.1. Tectonic context and GPS data

The tectonic of the Western United States mostly occurs in response to the relative motion between the Pacific plate and the North American plate. Two main zones accommodating the deformation are the San Andreas Fault system zone and the Basin and Range. In northern California, the relative motion between the Pacific plate and the Sierra Nevada reaches a differential rate of 30 mm/yr and results in large earthquakes. East of the Sierra Nevada, a significant part of the deformation (~10 mm/yr) occurs within the Basin and Range over a broad fault system. To the south, most of the strain is accommodated by the San Andreas Fault system while the southern Basin and Range is relatively inactive (Kreemer and Hammond, 2007). Although significant vertical deformation can occur during seismic events (Landers 1992, Northridge 1994 or Hector Mine 1999 earthquakes, red stars on Fig. 6), vertical motion observed in the area are nearly 10 times smaller than the horizontal velocities during interseismic periods (Smith-Konter et al., 2014). Consequently, we chose to analyse only horizontal motion.

We focus our study on the southern part of the San Andreas Fault system (SAFS) where high-quality spatially dense GPS measurements are available. We use the CMM3 (Southern California Earthquake Center Crustal Motion Map Version 3.0, SCEC CMM3) velocity field as it was published by Kreemer and Hammond (2007). It is supposed to represent the interseismic motion that affects our region of interest. This means that all transient motions induced by the seismic events of Landers, Northridge and Hector Mine have been modelled and removed. These data are associated with relatively homogeneous uncertainties of 1.2 mm/yr in average.

A Lambert conformal conic projection is used to project the GPS velocity field on a Cartesian frame. To evaluate the effect of the choice of the domain, we analyse two overlapping areas shown in Fig. 6. We aim at checking that effective rigidity values remain invariant regardless of the chosen borders. The first area of interest, hereafter named Zone 1, is limited by a red dashed line on Fig. 6 and is identical to the one used by Chéry et al. (2011). Then, a translation moves Zone 1 by 100 km towards the Northeast to obtain the second region called Zone 2 (blue dashed lines on Fig. 6). Both areas include the central San Andreas Fault system (SAFS) segment, the Eastern California Shear Zone (ECSZ), the south Sierra Nevada (SN) to the North, the Mojave Desert (MD) in the centre, the Salton Sea (SS) and the south Basin and Range (SBR) to the East. The western part of Zone 1 contains a part of the Pacific Plate along the Californian coast whereas Zone 2 is directly bounded by the San Andreas fault to the West.

5.2. Model parameterization and regularization coefficients

According to the synthetic experiments presented above, we choose a uniform grid spacing of 20 km. This configuration leads to meshes of 2284 elements.

At first, we attempt to evaluate the Tikhonov parameter λ_2. To do so, we analyse the *trade-off* between the normalized regularization member of the functional along the domain boundaries, $M(u_{BC}) = \frac{R_2(u_{BC})}{\max(R_2(u_{BC}))}$, and

Please cite this article as: Furst, S., et al., Lithosphere rigidity by adjoint-based inversion of interseismic GPS data, application to the Western United States, Tectonophysics (2017), http://dx.doi.org/10.1016/j.tecto.2017.03.015

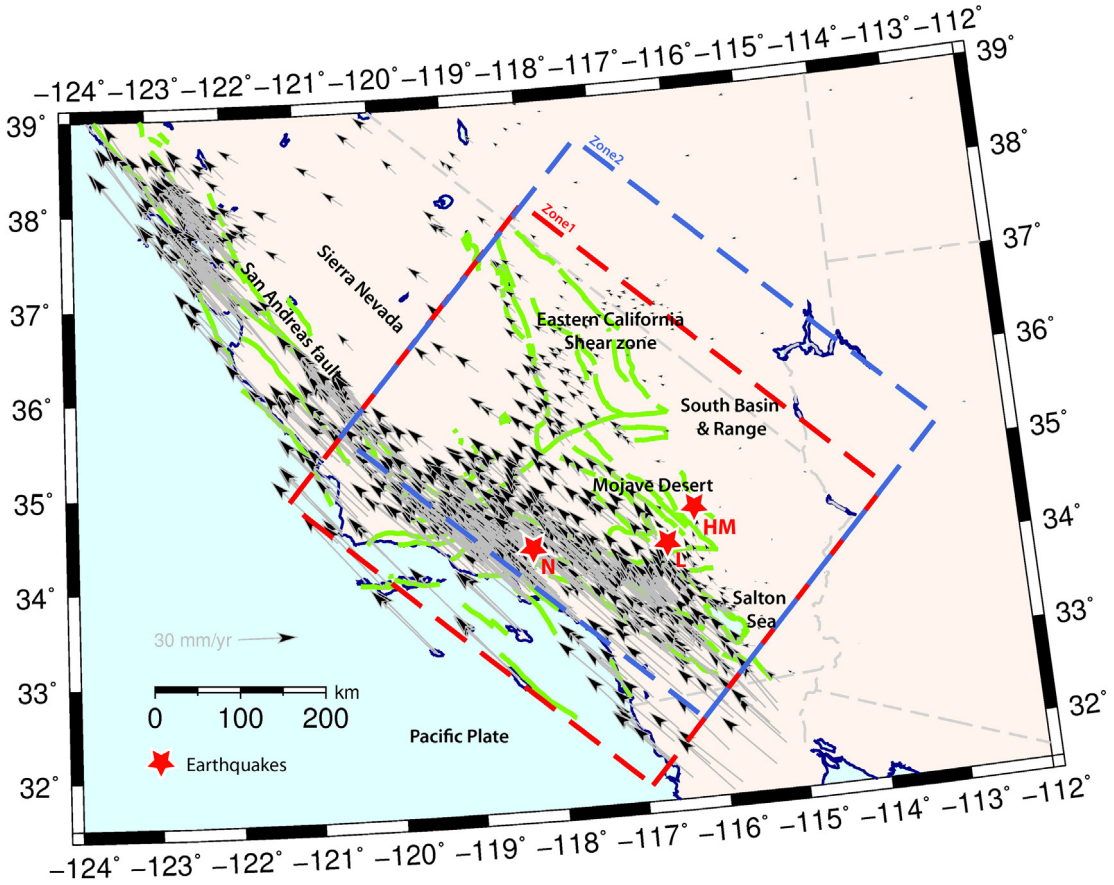

Fig. 6. Spatial distribution of the geodetic measurements on the SAF system used for the inversion. The black arrows show the velocity field in the North American reference frame. Our main domain of analysis is shown in the red rectangle (Zone 1 – 615 GPS velocities) while the blue one (Zone 2 – 530 GPS velocities) represents a translation of the area of interest. The red stars indicate the location of Landers (L), Northridge (N) and Hector Mine (HM) earthquakes. (For interpretation of the references to color in this figure legend, the reader is referred to the web version of this article.)

the residual data misfit $Res(p)$ at all geodetic measurements within the domain (Fig. 7a). Each point of the curve represents an optimization for a given value of the regularization parameter λ_2. A decrease of M corresponds to an increase of the regularization of the velocity field along the domain boundary, meaning that high gradient changes of u_{BC} are smoothed. This would confer some degree of smoothness to the solution. On the contrary, a reduction of regularization enables a better fit to high velocity gradient changes along the domain boundary. These particularly occur at the transition between highly deforming fault zones and rigid far fields. Nevertheless, this may induce undesirable velocity gradient variations where the velocity field is smooth. Hence, in order to find the appropriate balance between the regularity of the boundary conditions and velocity residual, we compare observed and modelled velocity distributions along the boundary (Fig. 7b–c–d). When the damping parameter is small (Fig. 7b), we allow the regularization term of the functional to be high. This in turn permits to better fit the observed velocities close to the boundaries and consequently within the domain. Nevertheless, the boundary solution may show in some places a degree of sharpness that is not supported by any data. Increasing the damping parameter used in Fig. 7c increases the regularity of the boundary conditions while still fitting properly the data along the border. We observe that this is done without significantly altering the fit between modelled and observed velocities. Finally, increasing the damping parameter, which means that extremely smooth boundary conditions become admissible, leads to incompatibility between modelled and observed velocities along the border (Fig. 7d). From this analysis, we set the regularization parameter λ_2 to 10^{-3} for which the balance between the regularization of the boundary conditions and the fit to observed velocities within the domain appears to be optimal.

5.3. Results of the inversion

Considering the model geometry and parameterization previously described, we perform the inversion of the GPS velocities for the two selected zones (Zone 1 and Zone 2) of the Western United States.

5.3.1. Estimated relative rigidity and corresponding uncertainty distributions

The inversion of the interseismic velocities leads to the distribution of effective rigidity illustrated by Fig. 8a–b. In the case of Zone 1 (Fig. 8a), the lowest values of D (1–1.5) are centred on the Mojave Desert, whereas slightly higher rigidities (1.5–4) are observed along the San Andreas Fault system and in the extreme South of the Eastern California Shear Zone. However, lower values of rigidity (associated with higher deformation rates) are expected along the San Andreas Fault system rather than in the Mojave Desert. We expect that this artefact is likely due to an over-correction of the post-seismic motion of the seismic events of 1992 (Landers), 1994 (Northridge) and 1999 (Hector Mine) within the CMM3 velocity field (Liu et al., 2015). When the GPS data are processed to only keep the interseismic velocity, the post-seismic answer of the earthquakes is estimated at its best. This artefact in our results could help identify the residual post-seismic motion left in the data. As for the high rigidities (>12), they are associated to the South Basin and Range and the South Sierra Nevada where no significant deformation needs to be accommodated. As an extension of Zone 1, the

Please cite this article as: Furst, S., et al., Lithosphere rigidity by adjoint-based inversion of interseismic GPS data, application to the Western United States, Tectonophysics (2017), http://dx.doi.org/10.1016/j.tecto.2017.03.015

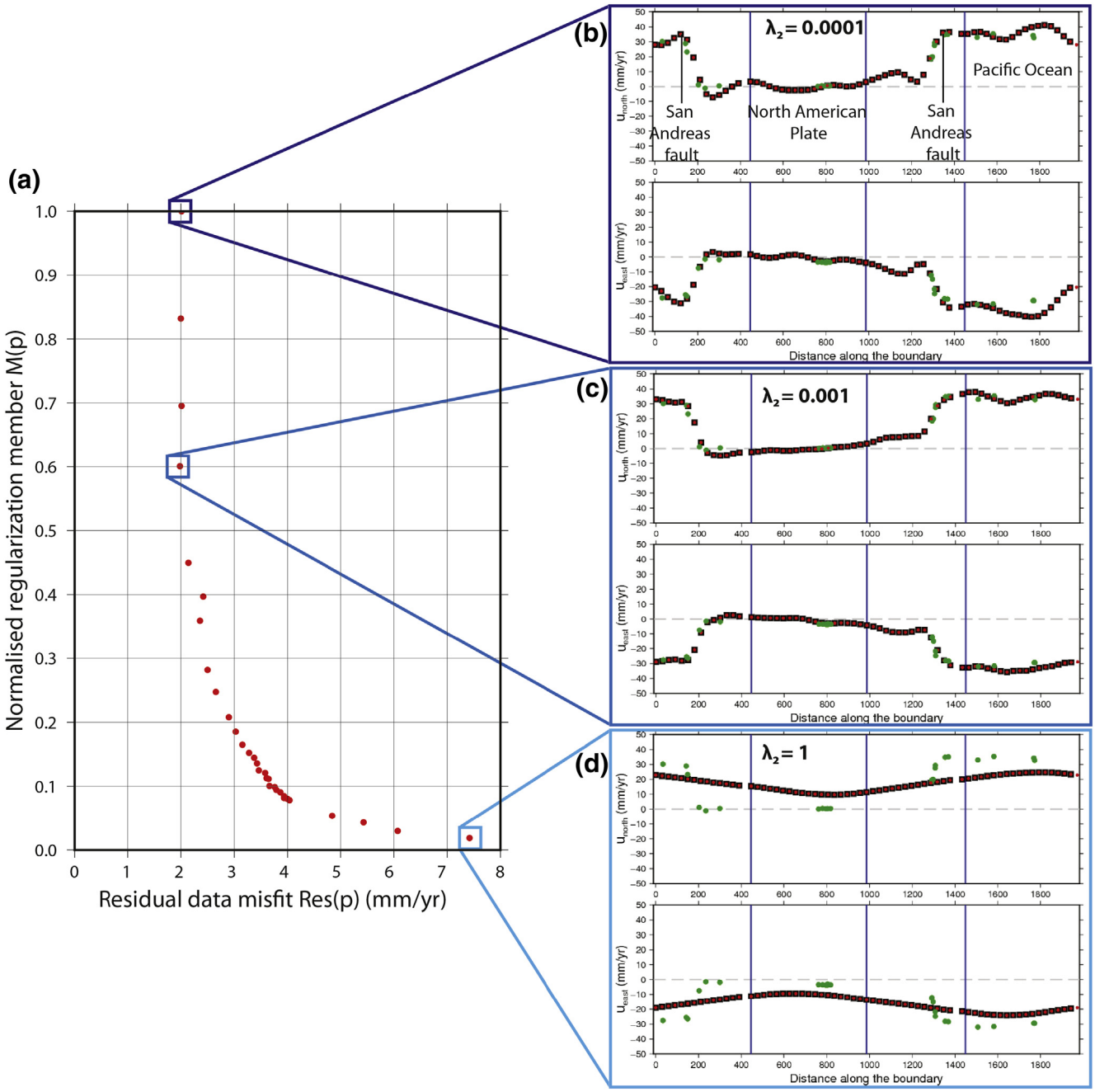

Fig. 7. Pareto curve for different regularization parameters used in the optimization algorithm applied to the southern California. (a) Plot of the normalized velocity variations norm as a function of the residual data misfit as damping λ_2 varies. (b), (c) and (d) represent the velocities observed within a 10-km distance of the domain boundary (green) and calculated on the boundaries (red) for different damping parameter λ_2. (For interpretation of the references to color in this figure legend, the reader is referred to the web version of this article.)

inversion in Zone 2 (Fig. 8b) produces similar rigidity distribution along the SAF and the extreme South of the ECSZ (1.5–4), with, again a surprisingly low rigidity (<1.5) in the Mojave Desert. However, one main difference can be underlined as a zone with rigidity ranging from 6 to 12 is found in the eastern part of the South Basin and Range.

As described in Section 3.4, we determine the uncertainties associated with our rigidity estimation which essentially result both from the local measurement density and the uncertainties associated with the data themselves. For each mesh element, we estimate the lower and upper admissible value for rigidity (Fig. 9a–b). First, along all the active fault systems, identified rigidity values are quite low as the amplitude between the upper and lower bounds are lower than 3. The reliability of our solution in deforming zones comes from the local high density of measurements and from large amplitude of the deformation. Conversely, when entering rigid zones, where only few measurements are available, the uncertainties increase very much reaching values that typically range from 2.5 to above 16 by several orders of magnitude. This is notably the case East of the ECSZ. Although the distribution of rigidity shown in Fig. 8a suggests an optimal value of 6–12, uncertainties in this area (Fig. 9) indicate that a much larger rigidity value (higher than 16 by several orders of magnitude) is also valid. This can be noted in the inversion over the shifted domain (Fig. 8b).

5.3.2. Associated residual velocities

Alongside with the distribution of the rigidity, we evaluate the difference between GPS and the modelled velocities to produce the

Please cite this article as: Furst, S., et al., Lithosphere rigidity by adjoint-based inversion of interseismic GPS data, application to the Western United States, Tectonophysics (2017), http://dx.doi.org/10.1016/j.tecto.2017.03.015

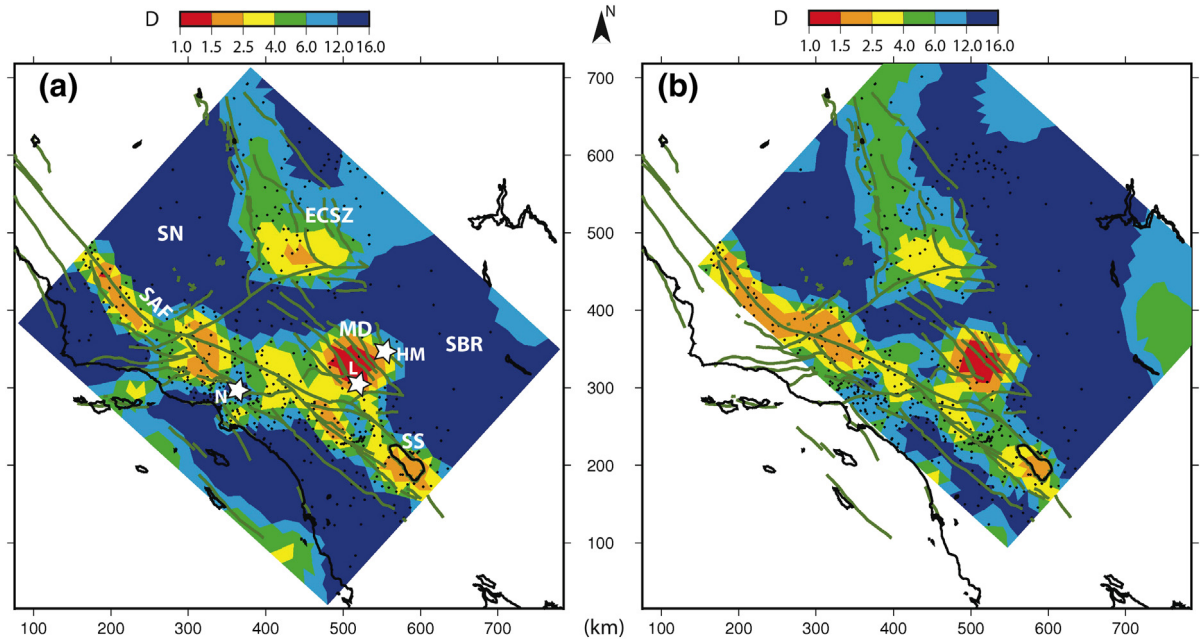

Fig. 8. Distributions of the relative rigidity D represented for Zone 1 (a) and for Zone 2 (b). According to Eq. (23), the elastic thickness T_g is proportional to D. The GPS data are represented by black dots, the faults by green lines and the Landers (L), Northridge (N) and Hector Mines (HM) earthquakes by white stars. SAF, SN, ECSZ, SBR, MD and SS stand for San Andreas Fault, Sierra Nevada, Eastern California Shear Zone, South Basin and Range, Mojave Desert and Salton Sea respectively. (For interpretation of the references to color in this figure legend, the reader is referred to the web version of this article.)

residual map (Fig. 10a–b). The fit between observed and modelled data is estimated using the normalized root mean square (*NRMS*) (McCaffrey, 2005),

$$NRMS = \left[0.5N^{-1}\left(\sum_{i=1}^{N}\left(\frac{r_i^e}{\sigma_i^e}\right)^2 + \left(\frac{r_i^n}{\sigma_i^n}\right)^2\right)\right]^{1/2} \quad (20)$$

where e and n stand for the eastern and northern directions respectively, r is the residual velocity, σ the data standard error and N the number of data. In addition to the *NRMS*, the weighted root mean square (*WRMS*) gives a measure of the a posteriori weighted scatter in the fits (McCaffrey, 2005),

$$WRMS = \left[\left(\sum_{i=1}^{N}\left(\frac{r_i^e}{\sigma_i^e}\right)^2 + \left(\frac{r_i^n}{\sigma_i^n}\right)^2\right) \Big/ \left(\sum_{i=1}^{N}\left(\frac{1}{\sigma_i^e}\right)^2 + \left(\frac{1}{\sigma_i^n}\right)^2\right)\right]^{1/2} \quad (21)$$

For Zone 1 (Fig. 10a), we get a *NRMS* of 1.26, with a *WRMS* of 1.10 mm/yr that can be compared with the uncertainty of 1.20 mm/yr

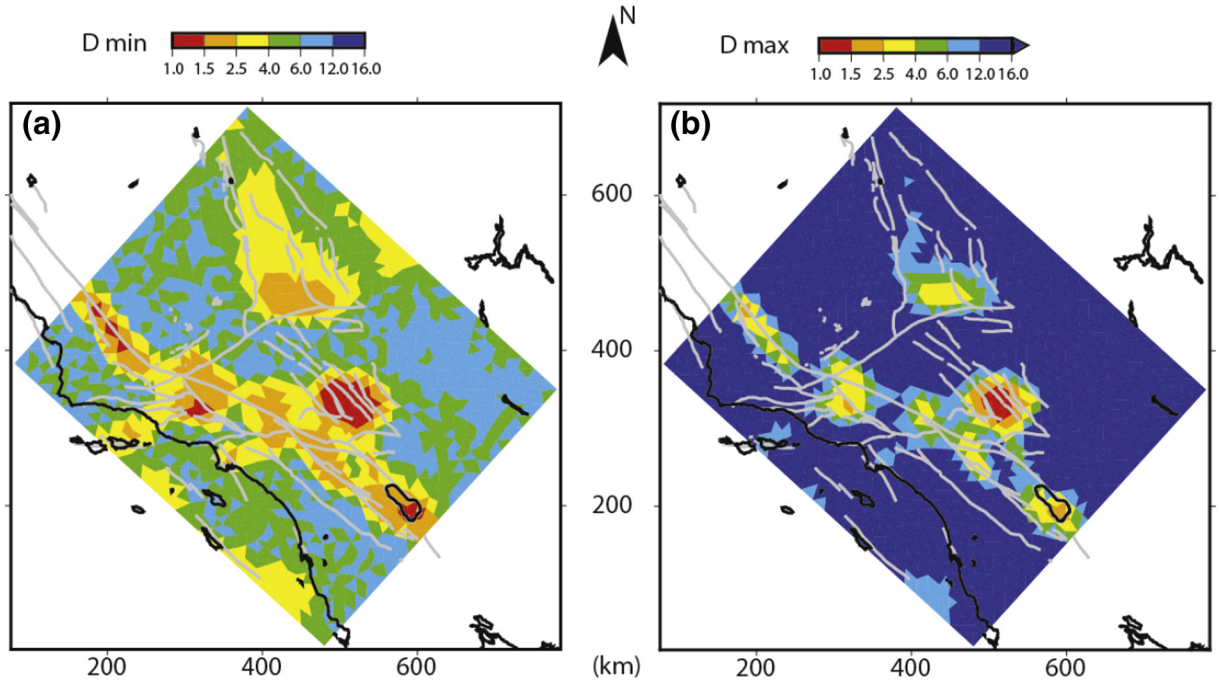

Fig. 9. (a) Lower and (b) upper bounds for the rigidity values around the optimal distribution displayed on Fig. 8a for Zone 1. In very few (or non-) deforming areas, D_{max} reach values that are several orders of magnitude higher than the optimal solution.

Please cite this article as: Furst, S., et al., Lithosphere rigidity by adjoint-based inversion of interseismic GPS data, application to the Western United States, Tectonophysics (2017), http://dx.doi.org/10.1016/j.tecto.2017.03.015

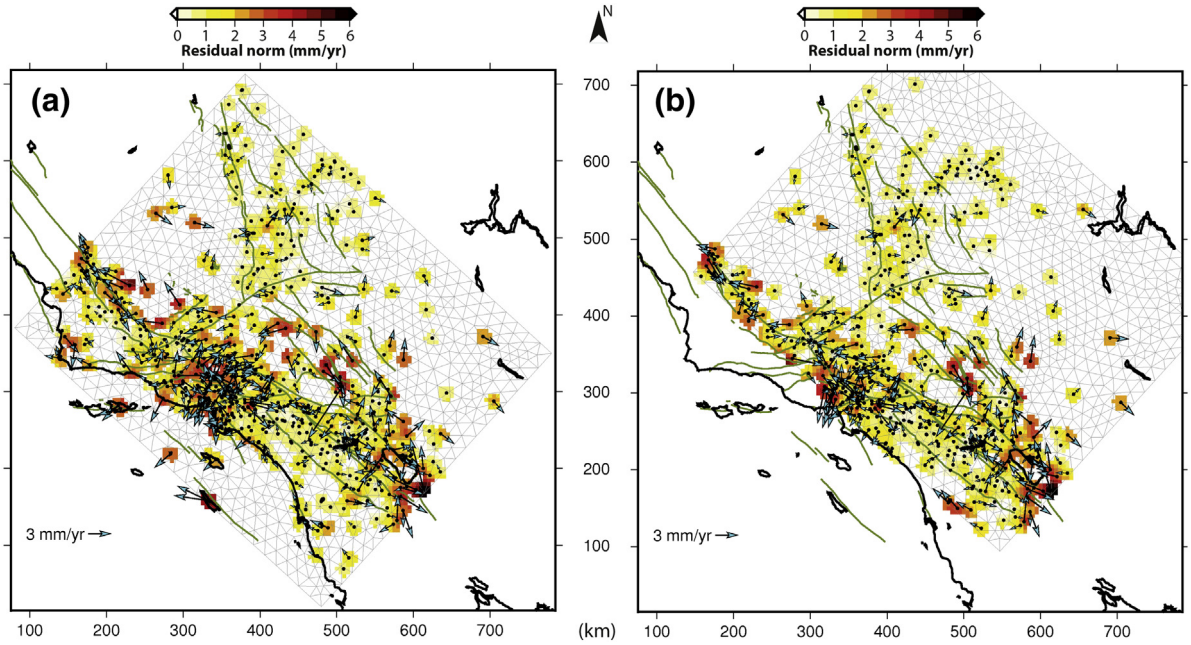

Fig. 10. Norm of residual velocities between GPS and modelled velocities associated with the rigidity distribution determined for a) Zone 1 (*NRMS* = 1.26) and b) Zone 2 (*NRMS* = 1.25).

associated with the data. The highest residuals (>4.5 mm/yr) occur on the southern segments of the SAF, while intermediate residuals (2.5–4.5 mm/yr) are unevenly distributed between high and low data density zones.

A similar analysis for Zone 2 gives a *NRMS* of 1.25 (Fig. 10b) with a *WRMS* of 0.93 mm/yr. The difference observed in the values of both zones can be explained by the data distribution. Indeed, the second zone excludes some of the velocities that are poorly estimated by the optimization (notably on the Pacific plate) and includes few vectors that are better recovered.

6. Discussion

Based on the hypothesis that interseismic strain mostly reflects rheological contrasts across the lithosphere, the solved inverse problem entirely depends on the quality of the CMM3 velocity field. Therefore, we first discuss the sensitivity of the model result with respect to the data. Then, we discuss our results (strain rate and rigidity distributions) in the light of the ones provided by previous studies on western US and California. We finally discuss the future use of our method for tectonic and geodynamic purposes.

6.1. Robustness of the inversion

In this study, we use the entire dataset of the Southern California Crustal Motion Map Version 3.0, involving 615 vectors for Zone 1 and 530 vectors for Zone 2. In order to evaluate the impact of data selection on rigidity distribution, we perform complementary inversions using identical parameterization, but removing GPS vectors whose residual norms *r* are greater than a given threshold value. These residuals can be due to three different factors:

1) GPS uncertainty. Data uncertainties range from 0.16 mm/yr to 3.71 mm/yr for the horizontal components with a *RMS* value of 1.20 mm/yr. The maximum data uncertainties are observed in the South of Mojave Desert, along the Los Angeles Bay and for a few isolated points in the Sierra Nevada and ECSZ.
2) Local motions. Besides interseismic plate motions, some sites may be affected by gravitational collapse, geothermal activity (e.g. Vasco et al., 2002) or the exploitation of aquifer systems (e.g. Galloway et al., 1998; Hoffmann et al., 2001). Many different processes can locally obscure the GPS interseismic velocity component, such as unravelled postseismic motions.
3) Modelling. The optimization algorithm and the forward model can also be at the origin of the residual velocities. Indeed, a poor estimation of the velocity along the boundaries could be the reason why high residual velocities are observed at the junction between the fault and the boundaries of the domain for both synthetic and real data cases. Furthermore, our forward model includes several assumptions such as an absence of body forces. Also, the data are assumed free of post-seismic effects which can be inexact if all post-seismic effects due to the Landers, Northridge and Hector Mine earthquakes, for instance, have not been fully removed.

We choose to withdraw from 0.3% (r > 6 mm/yr) up to 50% (r > 1.3 mm/yr) of the data in order to analyse the stability of the solution of our inversion. The corresponding *NRMS*, *WRMS* and the correlation of the rigidity distribution with respect to the one obtained by the previously described inversion are gathered in Table 1. We choose experiment 1 as the reference solution to estimate the rigidity correlation. Removing up to 10% of the GPS measurements exhibiting significant residuals in our initial inversion (experiences 3 to 6 in Table 1) neither enhance the *NRMS* or the *WRMS*, nor significantly modify the rigidity distribution. But considering only 50% of the data (experience 7 in Table 1) improves the *NRMS* to 0.67 and the *WRMS* to 0.54 mm/yr and leads to a rigidity correlation of 0.831 with the main features preserved.

Table 1
List of the experiments, the *NRMS*/*WRMS* values of the residual velocities and the correlation of the rigidity distribution relatively to experiment 1.

Experiment	Zone	Grid Size	Number of GPS vectors	*NRMS* of the residual velocities	*WRMS* (mm/yr)	Rigidity correlation
1	1	20	615	1.26	1.10	1
2	2	20	530	1.25	0.93	0.831
3	1	20	613 (99.7%)	1.25	1.08	0.995
4	1	20	600 (97.5%)	1.21	1.04	0.986
5	1	20	583 (94.7%)	1.16	1.00	0.987
6	1	20	553 (90%)	1.10	0.93	0.958
7	1	20	307 (50%)	0.67	0.54	0.831

Please cite this article as: Furst, S., et al., Lithosphere rigidity by adjoint-based inversion of interseismic GPS data, application to the Western United States, Tectonophysics (2017), http://dx.doi.org/10.1016/j.tecto.2017.03.015

This approach echoes the strategy Meade and Hager (2005) developed to reduce the number of stations and therefore to minimize the uncertainty magnitude. While based on different quality criteria, they remove about 50% of the initial dataset (CMM3) to compute their inversions. Our results illustrate that selecting the data with the lowest residuals does not significantly influence the modelled rigidity (see correlation in Table 1). However, in areas where data density is poor, a reduction of 50% can lead to a completely different interpretation. Therefore, keeping the whole dataset seems preferable.

6.2. Strain rate: comparison with other approaches

Most of strain rate computations derived from GPS velocity measurements stand on a continuous approximation of a model velocity field. A simple way to compute the strain rate is to design a triangulation of the GPS points collection and then assume that the velocity field inside each triangle evolves linearly. However, this method generates a non-smooth strain map due to a linear interpolation of measured GPS velocities. This method can be adapted to areas covered by sparse GPS networks (Masson et al., 2005) but generates erroneous strain rates when applied to dense networks such as the ones installed in California. In this case, a smooth approximation of the velocity field needs to be performed in order to avoid spurious strain rate modelling. Consequently, a suitable method must also account for high strain gradient occurring around fault zones. A large variety of mathematical approaches can be used to deduce a strain rate map, often leading to relatively large differences (Feigl et al., 1993; McCaffrey, 2005; Shen et al., 1996; Tape et al., 2009).

Our optimal solution of rigidity distribution can be used for the determination of strain rates over the whole study area. But, we have shown above that our models systematically underestimate rigidity in very few deforming areas, typically far from the active fault systems. This bias is partly counterbalanced by the information provided by the upper bound of the admissible rigidity values. These latter are very close to the optimal solution in deforming zones, while they suggest that a purely rigid behaviour may be considered when the deformation is very small, even though a slight deformation remains admissible just considering geodetic measurements. Therefore, using this "strongest" admissible solution is a way to conform to geological considerations and block-model assumptions that state that, in most cases, far from the faults, the blocks are rigid. So, we used the upper bound rigidity distribution (Fig. 9b) for creating our strain rate map (Fig. 11a).

We compare in Fig. 11 our strain rate map (through the 2nd invariant of the strain tensor) with the one obtained by a method originally proposed by Haines and Holt (1993) and later revised in the framework of the strain map global project (Kreemer et al., 2014). Although both methods depend on distinct assumptions, they produce similar intensities (>64 nanostrain/yr) located near faulted areas along the SAF and the ECSZ. This overall similarity is probably due to the fact that both approaches are able to produce a low residual between the discrete and the continuous velocity fields. Using our strongest admissible rigidity solution leads to low strain estimates in weakly deforming areas that are similar to the ones obtained by the global strain map project. This can be noticed in the Great Valley between the SAF and the Sierra Nevada and along the Pacific coast.

A significant difference between the two strain rate maps can be found only on two limited areas: offshore the Pacific coast and east of the ECSZ. Because these two areas display low residuals (Fig. 10), we guess that our model is likely not able to locally estimate the strain rate precisely. This could be due on the one hand, to an improper estimate of the boundary conditions notably within the Pacific plate, and on the other hand, to a very low local data density. Indeed, whereas Kreemer et al. (2014) only interpolate the strain rate dataset to best fit the data, our solution aims at doing the same, but under the constraint of the stress equilibrium equation (Eq. (1)). As demonstrated by the synthetic benchmarks presented in Section 3.4, evenly distributed data lead to a better estimation of the rigidity. Therefore, a future use of our methodology could be to invert interpolated GPS velocities (such as the ones provided by the Global Strain Rate Project) instead of the original GPS data to compute effective rigidity distribution at a continental scale.

Lastly, we compare the spatial distribution of our dilatational strain rate solution with the one obtained by Kreemer et al. (2014) (Fig. 12).

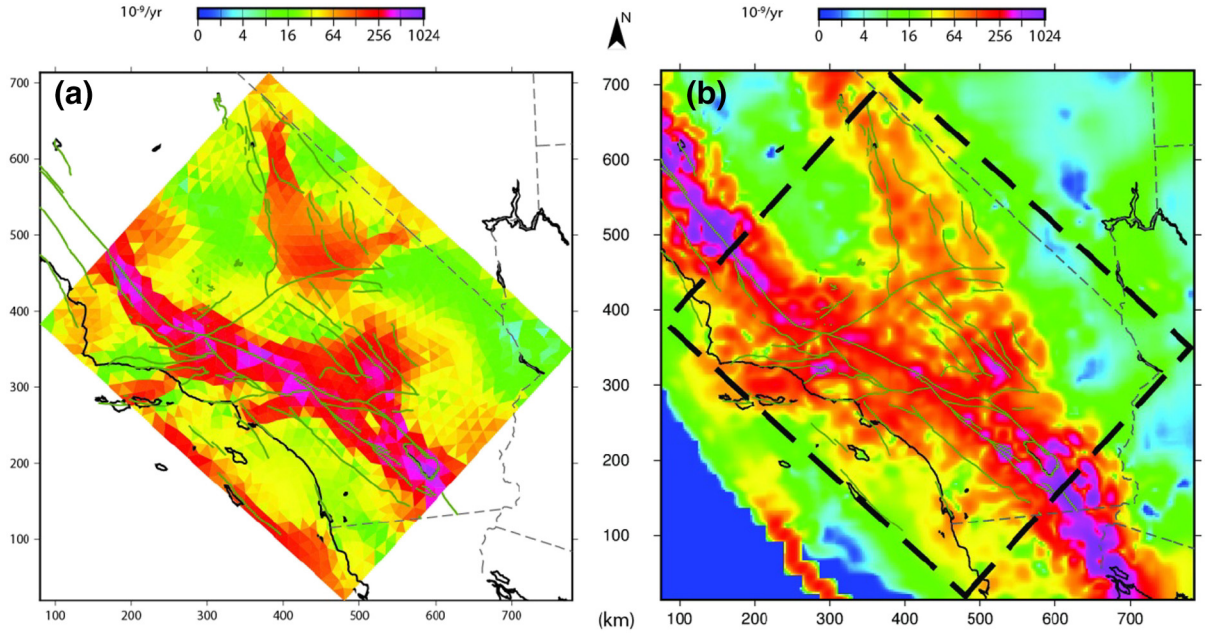

Fig. 11. Distribution of the strain rate for Zone 1. Second invariant of the strain rate tensor from (a) the upper (strongest) admissible values of our rigidity optimization and (b) the global strain map of Kreemer et al. (2014).

Please cite this article as: Furst, S., et al., Lithosphere rigidity by adjoint-based inversion of interseismic GPS data, application to the Western United States, Tectonophysics (2017), http://dx.doi.org/10.1016/j.tecto.2017.03.015

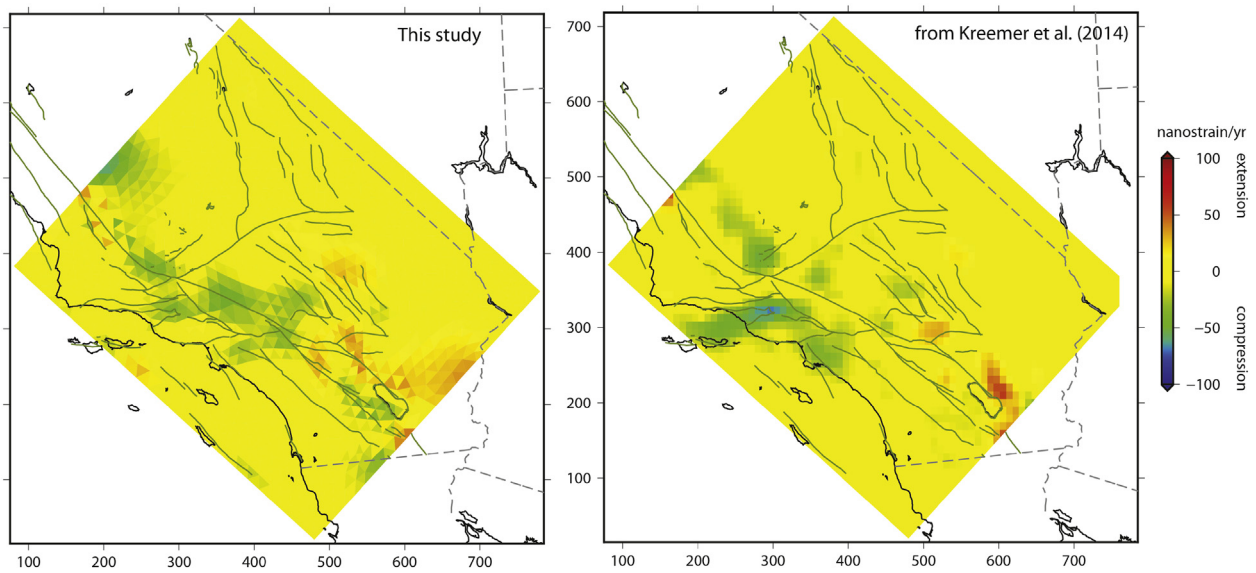

Fig. 12. Distribution of the first invariant of the strain rate tensor for Zone 1 from (a) our optimization and (b) the global strain map of Kreemer et al. (2014).

We use the first invariant of the strain rate tensor (mean of its trace) as a first-order approximation of the dilatational strain rate.

Neither the strain compatibility approach used by Kreemer et al. (2014) nor our study, take vertical velocity measurements into account. Nevertheless, the plane stress formalism of our modelling leads to the prediction of vertical strain rates, which is not the case in Kreemer et al. (2014) analysis. Yet, recent analyses (e.g., Becker et al., 2015) suggest that the rate-change of vertical loading of the lithosphere may play a dominant role in defining the distributions of seismicity and therefore strain.

Despite the difference in their estimation, both spatial distributions of the dilatation strain rate from Kreemer et al. (2014) and us are very similar. They notably highlight the compressive context of the SAF system along the central bend. The only noticeable difference can be found along the fault system located north of Los Angeles where vertical motion is known to occur along active thrust faults (e.g. Northridge or Compton faults).

6.3. Rigidity of the lithosphere and effective elastic thickness

In the following, we study the relation between in-plane rigidity associated with geodetic strain (this work) and the flexural rigidity deduced from gravity and topographic data analysis (Audet and Bürgmann, 2011; Lowry and Pérez-Gussinyé, 2011; Tesauro et al., 2011). In the case of a thin curved elastic plate, the relation between the bending moment M and the flexural rigidity D_f is given by:

$$M = -D_f \frac{d^2 w}{dx^2} = \frac{D_f}{R(x)} \tag{22}$$

where w is the vertical displacement of the plate and $R(x)$ its local curvature radius (e.g. Turcotte and Schubert, 2002). Using Eq. (2), a horizontal force per unit area applied to a vertical section of the lithosphere can be defined as:

$$F = D_g \left(\varepsilon_{ij} + \frac{\nu}{1-2\nu} \varepsilon_{kk} \delta_{ij} \right) \tag{23}$$

where D_g is the stiffness of the lithosphere to horizontal strain. D_g is equal to $2GT_g$ where G is the shear modulus (Pa) and T_g the plate thickness (m). Therefore, in-plane rigidity D_g is expressed in N while the flexural rigidity D_f is given in Nm, precluding a direct comparison between these two fields. In order to compare our relative rigidity map with the flexural rigidity deduced from gravity and topographic data analysis (Audet and Bürgmann, 2011; Lowry and Pérez-Gussinyé, 2011; Tesauro et al., 2011), we use the elastic thickness associated to these two formalisms.

The study of Lowry and Pérez-Gussinyé (2011) provides a map of the flexural elastic thickness (T_e) for the entire western US. We assume that a linear relationship exists between the in-plane plate rigidity and its corresponding thickness (Chéry, 2008 and present work). Therefore, our map of T_g is directly proportional to the distribution of D shown in Fig. 8a. Although such a linear relationship is valid only if elastic parameters do not vary with depth, it provides a simple way to estimate the effective elastic thickness for our modelling. For the purpose of comparison with Lowry and Pérez-Gussinyé (2011), we display their value of T_e over Zone 1 (Fig. 13). Flexural and geodetic elastic thicknesses displayed in Fig. 13 show a very limited degree of agreement. For example, the flexural thickness map predicts a thick plate for most of the SAF, while a low geodetic elastic thickness is deduced using the interseismic velocity field. The only area suggesting some resemblance corresponds to the Basin and Range around the ECSZ and the SAF around the Salton Trough for which both methods display low elastic thickness. In order to find some justifications about the large discrepancies between T_e and T_g at least two lines of arguments could be investigated.

First, despite the formal similarity between flexural plate and shear plate theories (Chéry et al., 2011), they may reflect two distinct lithospheric behaviours. For example, as stated by Thatcher and Pollitz (2008), plate flexure is the result of a long term loading over millions of years, implying that the strain rate in most of the lithosphere is close to zero. T_e is a measure of stress that is supported dynamically over very long timescales by a lithosphere that is in a state of frictional failure and viscoelastic flow, meaning the strain rate is virtually zero. However, given the shorter timescale of geodetic observation and the clear evidence for seismic release of significant elastic strain potential accumulated on century timescales, T_g likely does predominantly reflects the elastic behaviour of a thicker domain associated to interseismic deformation. Another difference may come from the lithospheric loading. Vertical loads modify distinct components of the strain tensor. Indeed, those induce flexure and plate motions and therefore horizontal shear. Hence, distinct behaviours may emerge from these kinds of load.

Please cite this article as: Furst, S., et al., Lithosphere rigidity by adjoint-based inversion of interseismic GPS data, application to the Western United States, Tectonophysics (2017), http://dx.doi.org/10.1016/j.tecto.2017.03.015

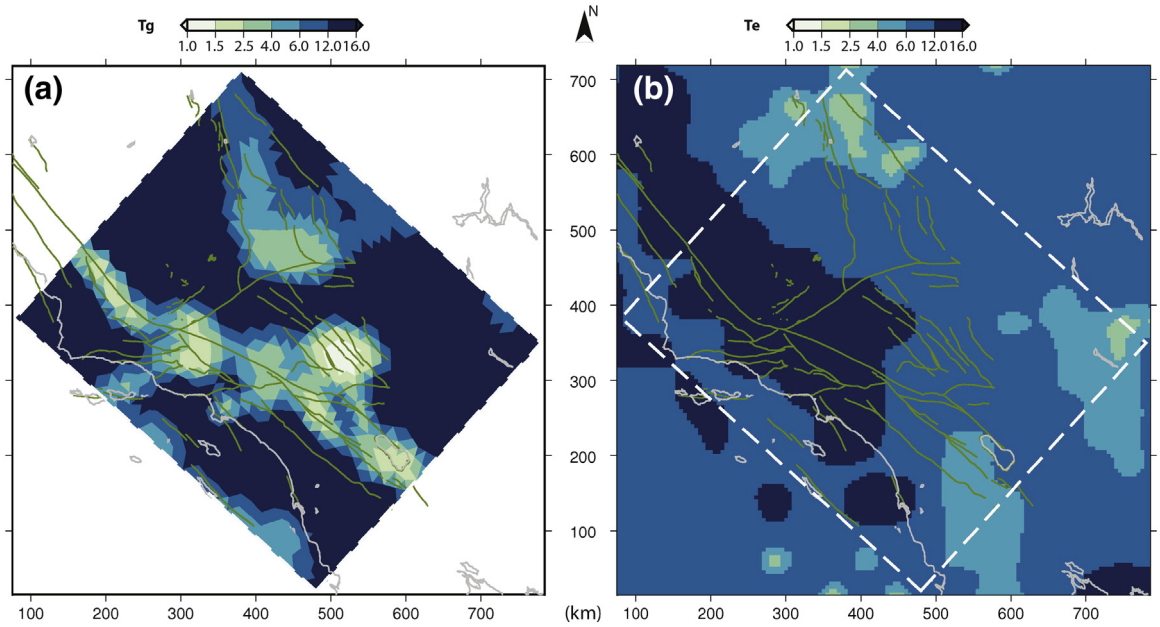

Fig. 13. (a) Geodetic elastic thickness T_g associated to our study; (b) flexural elastic thickness T_e given by Lowry and Pérez-Gussinyé (2011).

In the brittle part of the crust, background seismicity is likely to reflect the loading of interseismic motion, therefore introducing an anelastic component into the analysed shear motion. Beneath the crust and especially under a shear zone like the San Andreas Fault system, the upper mantle presents a laterally variable and strong anisotropy (Hartog and Schwartz, 2001). If such anisotropic behaviours occur at both crustal and mantle levels, flexural and horizontal loading may activate two different rheological systems that could result into significant differences in terms of effective elastic thickness.

A second way to investigate is to assume that flexural and geodetic thicknesses represent the same mechanical concept. However, they could be differently revealed by the data because of the formal differences between the two inverse problems. In the case of flexural thickness, the determination of T_e is based on the correlation between topographic and gravimetric signal. Among other factors, erosion can smooth or sharpen the topographic signal. Even if its influence can be accounted for in modelling approaches (e.g. Forsyth, 1985), the impact of erosion on the determination of T_e seems difficult to quantify due to large uncertainty associated to past erosion. In addition, a geodynamical setting mostly involving shear motion may not be adapted at all for a flexural plate analysis because such a motion is not likely to produce neither topographic nor gravimetric signals. Last but not least, inverse theory of plate flexure requires that flexural thickness cannot be determined for resolutions smaller than the characteristic flexural wavelength (Watts, 2001). This also may explain why a sharp rigidity variation across the SAF cannot be resolved by this method. Even if our methodology has never been used prior to Chéry et al. (2001), the direct relation between shear strain and shear rigidity is likely to produce high resolution estimate of geodetic thickness for zones where the geodetic strain is well defined. Conversely, we acknowledge that our uncertainty analysis predicts inaccurate rigidity determination in zones of low strain-rate like the Sierra Nevada. Also, lithospheric loads like body forces and basal stress coming from mantle motion can impact the strain-rate field and therefore altering the determination of the shear rigidity. The identification of the importance of such effects must be tackled by future studies.

In order to better understand the discrepancy between flexural and shear analysis, a tractable way would be to design a complete mechanical model of western US as it was done for example by Pollitz et al. (2010). Such a model could be used to predict synthetic topographic, gravimetric and deformation datasets obeying to momentum and constitutive equations. Then these "data" could be inverted using the methodologies associated to flexural and shear lithospheric deformation and compared to the rheological input of the forward model.

7. Conclusion

A global inversion strategy has been proposed for the identification of effective rigidity maps using GPS velocity fields under minimum a priori assumptions. Taking advantage of the self-adjoint nature of the governing equations, large dimensional problems coming from necessary high resolution distribution of the rigidity have been considered. Compared to the previous study carried out by Chéry et al. (2011), the results are now backed by uncertainty analysis which suggests that the effective rigidity can only be accurately determined in moderate or highly strained areas.

This is a high-resolution methodology which can be seen as a mechanical model to link shear rigidity to interseismic strain with no prior knowledge of fault locations. The main limitation of this approach relies to the plane stress hypothesis used in the forward model. Therefore, no strain variation occurs with depth for a given horizontal location over the plate. This behaviour is probably over simplified around active faults acting like screw dislocations as proposed by Savage and Burford (1973). To complete what is presented here, the following directions can be considered:

1) The 2D–effective rigidity model can be replaced by a 3D model of Western United States including the effective elastic thickness as the main geophysical parameter. Because this approach would include the full 3D strain rate tensor, it would provide a more realistic approximation of the plate behaviour of the lithosphere especially around faults.
2) The 2D approach can be used over wide areas, for instance at the continental plate scale, after a splitting in patches. This would permit to determine large scale rigidity maps in the framework of the global strain map project of (Kreemer et al., 2014).
3) The strong spatial correlation between low rigidity areas and active fault zones also suggests that our methodology could be applied for deciphering active faults in tectonically poorly known areas.

Please cite this article as: Furst, S., et al., Lithosphere rigidity by adjoint-based inversion of interseismic GPS data, application to the Western United States, Tectonophysics (2017), http://dx.doi.org/10.1016/j.tecto.2017.03.015

Acknowledgements

We thank Prof. Riad Hassani from Nice-Sophia Antipolis University for making available to us his plane stress Finite Element code CAMEF. We also acknowledge Tony Lowry and an anonymous reviewer for their constructive remarks and suggestions. The PhD of S. Furst is supported by the Total Company and the LabEx NUMEV project (n° ANR-10-LABX-20) funded by the "Investissements d'Avenir" French Government program, managed by the French National Research Agency (ANR).

Appendix A. Application to shallow creeping faults

In this appendix, we briefly discuss the way our approach deals with very high strain rates and what this implies in term of prior search interval for the relative shear-rigidity values.

Three terms contribute to the spatial regularization (smoothing) of the modelled distribution of relative rigidity and, consequently, the modelled velocity field. The first one simply comes from mesh size and, therefore, from the spatial resolution of our model. Then, a Tikhonov regularization term can be activated in the cost function (Eq. (5)). Finally, a spatial smoothing process is performed on the gradient of the functional (Fig. 2).

All these components of our approach are likely to limit the range of strain rates that can be properly modelled. In particular, active faults exhibiting very shallow creep are supposed to lead to local under-estimation of rigidity gradients.

In practice, the mesh size is a few kilometres (20 km in the case of this study over South California), the Tikhonov regularization term is not active, and the smoothing process over the gradient of the functional can have a very limited spatial extent. Despite the limitations of the effects of these regularization components, we see that the whole range of the expected strain rates (about 4 orders of magnitude) can hardly be captured by our approach. Nevertheless, we demonstrate, hereafter, that (1) if the spatial sampling is high, then using a 4-order of magnitude search interval allows for a good fit to sharp velocity changes. (2) Using a 2-order of magnitude search interval is sufficient in most cases, small but significant local residues being present only in the case of extremely shallow creeping behaviour.

First, we run our inversion on synthetic cases that are similar to those presented in Section 3, but for which the locking depth is much shallower: 2 km (Fig. A.1) and 0 km (Fig. A.2). For these experiments, the mesh size is set to 3 km.

In the case of a 2-km locking depth, we find that exploring a 2-order of magnitude interval for rigidity is sufficient to perfectly model the velocity field (Fig. A.1). The only significant difference between the modelled and the theoretical values of the relative rigidity appears on non-significantly deforming zones at distances higher than about 20 km from the fault. Indeed, in these areas, we know that changing the relative rigidity by several orders of magnitude has very small influence on the velocity prediction. So, again, we show that our approach underestimates rigidity far from the active faults. Exploring a 4-order of magnitude rigidity interval does not improve the fit to ground velocities. It only pushes a little bit away the limit where the real rigidity is underestimated.

If we consider, now, the extreme case of a fault experiencing creep up to the ground surface, then the strain rate across the fault is infinite. A similar analysis to the preceding case shows that significant residues remain close to the fault (Fig. A.2). Yet, their amplitudes are very small (no >2 mm/yr) except exactly on the fault itself. In such an extreme case, indeed, extending the search interval of rigidity from 2- to 4-order of magnitude allows for the proper modelling of the velocity field everywhere. Nevertheless, this better fit has been obtained at the cost of the regularity of the rigidity distribution which is slightly altered in non-deforming zones (upper and lower central areas).

Let's move now to the case of the SAF fault segment that is located north of Parkfield. This segment is known to be experiencing very shallow creep (e.g. Rosen et al., 1998). We use a 10-km mesh size and run inversions varying the range of the admissible rigidity values and the smoothing factors for the gradient of the cost function. All lead to the same solution that is presented on Fig. A.3. Using a 4-order of magnitude search interval does not provide additional information that would not have been captured by a 2-order of magnitude search interval. This may be due to the 10-km resolution of our mesh, as well as the relatively low density of GPS measurements in the CMM3 database, notably with respect to other high-resolution measurements like InSAR.

In order to illustrate the efficiency of our modelling, we compare the modelled velocity field with the CMM3 measurements along two profiles across the SAF system, one (A–B) just south of the city of San Juan Bautista (Fig. A.3b), and the other (C–D) close to the city of Parkfield (Fig. A.3c). It can be noticed that no significant pattern of the deformation, as gathered by the CMM3 database, is missed by our modelling. Moreover, this good fit has been obtained with a limited range for the admissible rigidity values, which, in turn, guarantees some degree of regularity of the rigidity distribution, even on very few deforming areas.

Appendix B. Processing the SAF zone using a 4-orders of magnitude range for admissible rigidity

In the main body of this paper, we determine the relative rigidity distribution (both for synthetic and real cases) from the exploration of a 2-orders of magnitude range of rigidity values. Appendix A shows that, unless we need to deal with sharp velocity gradients that are typically found on very shallow creeping fault segments, this rigidity range is sufficient to properly fit the interseismic velocity field within their uncertainties. In this appendix, we show that using a wider range of admissible rigidity value (4 orders of magnitude instead of 2) in the inversion process applied to Southern California leads to a very similar solution.

As noticed in Appendix A, the inversion becomes now longer and less steady. Nevertheless, it converges to a solution which differs only in places where ground deformation is very small. Indeed, setting the lowest relative rigidity value to 1, then most of the significantly deforming areas exhibit relative rigidity values that are below 20 (Fig. B1a). Only quasi non-deforming areas require relative rigidity values on the order of 100 or above. But we know that, in very weakly deforming zones, large changes of high rigidity values only lead to small changes in strain prediction. Fig. B1b shows that, as expected, using a wider search domain leads to a similar solution where ground deformation is significant, and to a larger ratio between rigidity in non-deforming zones relatively to deforming areas. However, both solutions (using a 2-fold or 4-fold range of magnitude) fit the data globally in the same way. This confirms the fact that a very large range of rigidity is admissible far from the active fault systems. This statement is illustrated again by the lower and upper bound solutions (Fig. B1b–c). The rigidity distribution is well constrained in significantly deforming zones, lower and upper bounds being close to the optimal solution, but badly constrained elsewhere. Typically, any value of rigidity higher than 10 is an admissible solution for rigid areas.

In conclusion, we see that almost all the significant ground deformation is captured using a 2-orders of magnitude range for relative rigidity. Increasing this range allows either a better modelling of ground deformation induced by shallow surface creeping segments, or the assignment of higher rigidity values in non-deforming zones. But, in this latter case, the fit to the velocity field is very little improved and we know that the uncertainties associated with these rigidity values remain very high.

Please cite this article as: Furst, S., et al., Lithosphere rigidity by adjoint-based inversion of interseismic GPS data, application to the Western United States, Tectonophysics (2017), http://dx.doi.org/10.1016/j.tecto.2017.03.015

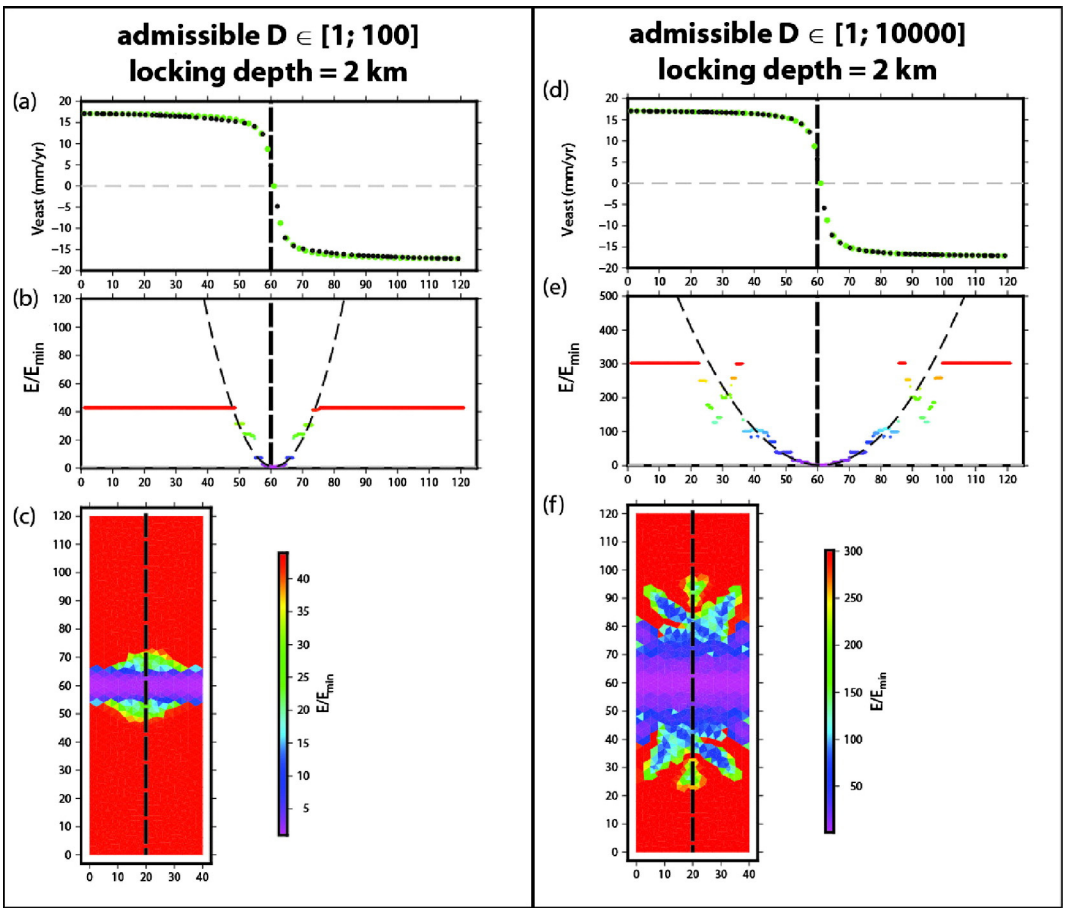

Fig. A.1. Velocity and relative rigidity distributions for synthetic cases mimicking shallow creep on strike-slip faults. The locking depth is set to 2 km. The search interval for the relative rigidity has 2 orders (left) or 4 orders (right) of magnitude. (a and d) Theoretical velocities (green dots) and modelled velocities (black dots) at measurement locations along the profile (dotted black line) indicated in (c). (b and e) Theoretical (dashed curve) and modelled relative rigidity (colored dashes using same color palette as in (c) and (f) respectively) along the same profile. (c and f) Spatial distribution of relative rigidity determined by our inversion. (For interpretation of the references to color in this figure legend, the reader is referred to the web version of this article.)

Please cite this article as: Furst, S., et al., Lithosphere rigidity by adjoint-based inversion of interseismic GPS data, application to the Western United States, Tectonophysics (2017), http://dx.doi.org/10.1016/j.tecto.2017.03.015

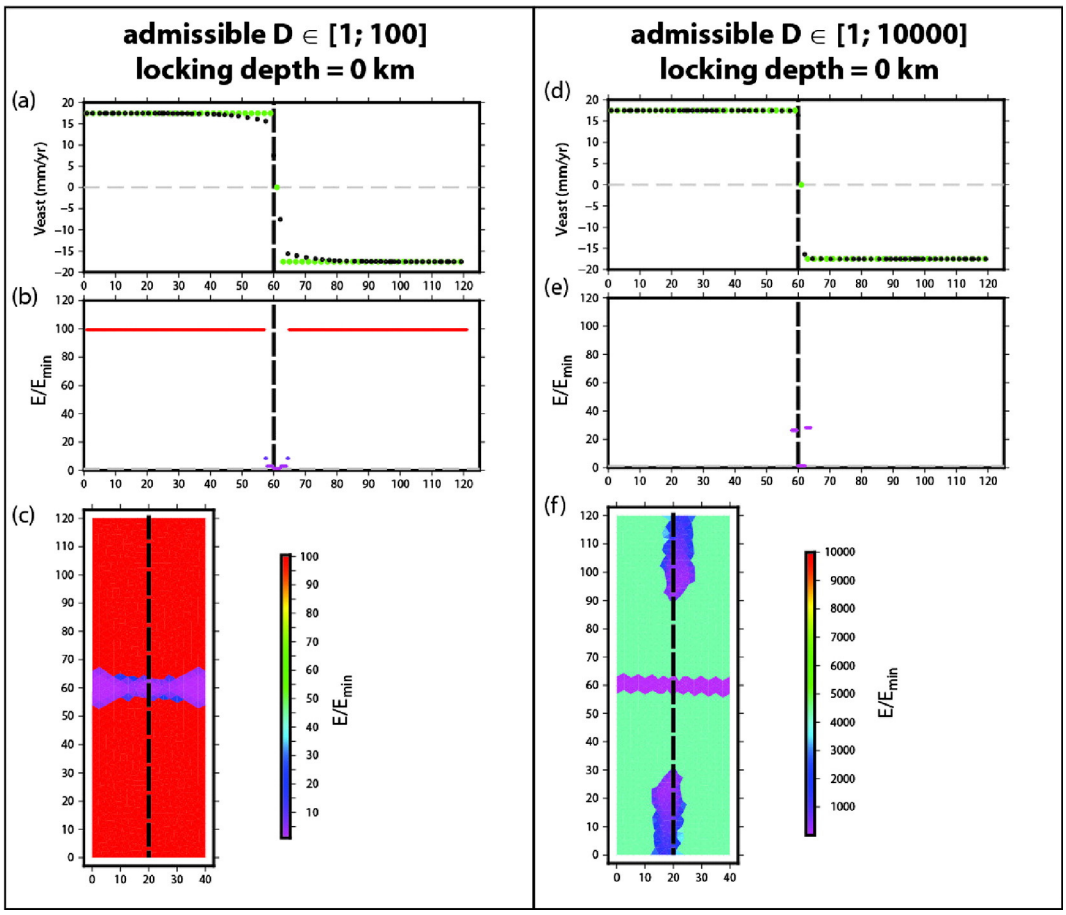

Fig. A.2. Same as Fig. A.1 but the locking depth is now set to 0 km.

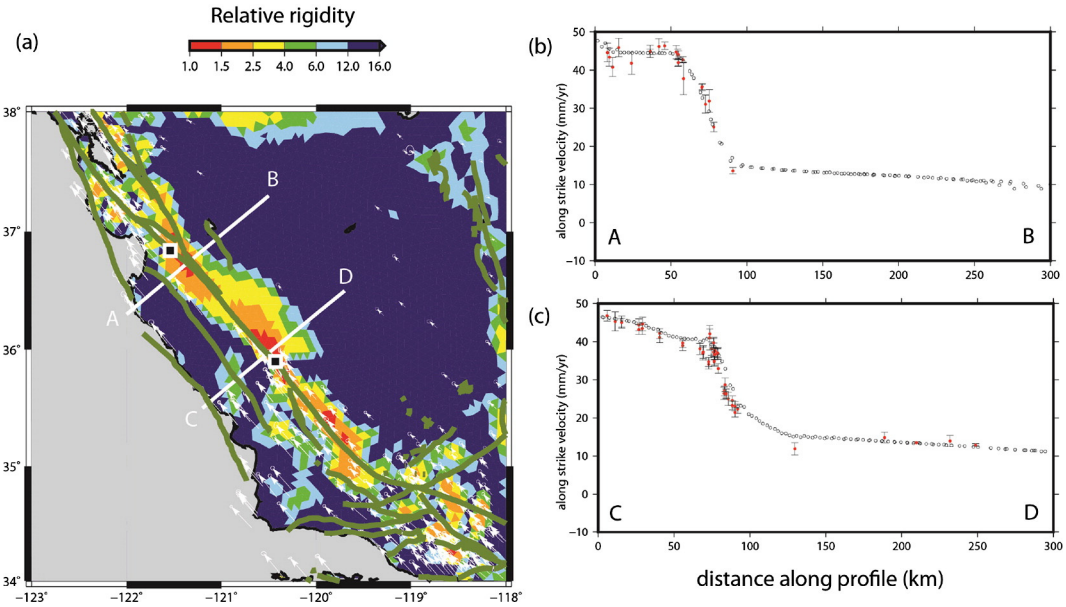

Fig. A.3. (a) Relative rigidity distribution over the Parkfield segment of the SAF. Black squares indicate the location of the cities of San Juan Bautista (north) and Parkfield (south). White arrows are the velocities of the CMM3 database. Measured (red circles) and modelled (black circles) along-strike velocities along (b) A–B and (c) C–D profiles shown in (a). (For interpretation of the references to color in this figure legend, the reader is referred to the web version of this article.)

Please cite this article as: Furst, S., et al., Lithosphere rigidity by adjoint-based inversion of interseismic GPS data, application to the Western United States, Tectonophysics (2017), http://dx.doi.org/10.1016/j.tecto.2017.03.015

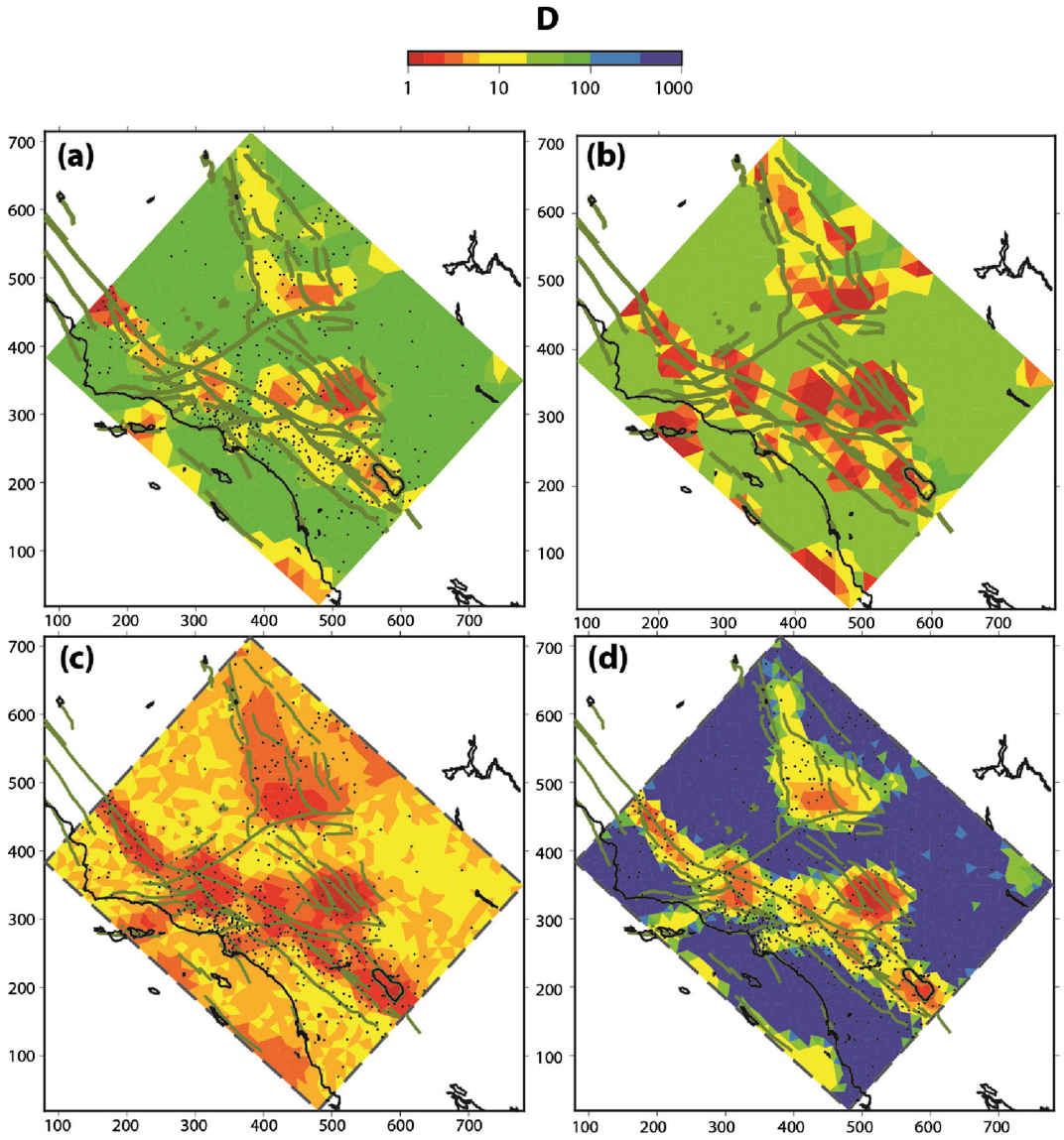

Fig. B1. Rigidity distribution over Southern California as determined using a 4-order of magnitude range of admissible relative rigidity (from 1 to 10,000). (a) Optimal solution, (b) difference with respect to the optimal solution using a 2-order magnitude range (Fig. 8a) (c) lower bound solution and (d) upper bound solution. To be compared with Figs. 8 and 9.

References

Allaire, G., Jouve, F., Toader, A.M., 2004. Structural optimization using sensitivity analysis and a level-set method. J. Comput. Phys. 194:363–393. http://dx.doi.org/10.1016/j.jcp.2003.09.032.

Anderson, K., Segall, P., 2013. Bayesian inversion of data from effusive volcanic eruptions using physics-based models: application to Mount St. Helens 2004–2008. J. Geophys. Res. Solid Earth 118:2017–2037. http://dx.doi.org/10.1002/jgrb.50169.

Audet, P., Bürgmann, R., 2011. Dominant role of tectonic inheritance in supercontinent cycles. Nat. Geosci. 4:184–187. http://dx.doi.org/10.1038/ngeo1080.

Becker, T.W., Lowry, A.R., Faccenna, C., Schmandt, B., Borsa, A., Yu, C., 2015. Western US intermountain seismicity caused by changes in upper mantle flow. Nature 524:458–461. http://dx.doi.org/10.1038/nature14867.

Bird, P., Kong, X., 1994. Computer simulations of California tectonics confirm very low strength of major faults. Geol. Soc. Am. Bull. http://dx.doi.org/10.1130/0016-7606(1994)106<0159:CSOCTC>2.3.CO;2.

Chéry, J., 2008. Geodetic strain across the San Andreas fault reflects elastic plate thickness variations (rather than fault slip rate). Earth Planet. Sci. Lett. 269:351–364. http://dx.doi.org/10.1016/j.epsl.2008.01.046.

Chéry, J., Zoback, M.D., Hassani, R., 2001. An integrated mechanical model of the San Andreas Fault in central and northern California. J. Geophys. Res. 106:22051. http://dx.doi.org/10.1029/2001JB000382.

Chéry, J., Mohammadi, B., Peyret, M., Joulain, C., 2011. Plate rigidity inversion in southern California using interseismic GPS velocity field. Geophys. J. Int. 187:783–796. http://dx.doi.org/10.1111/j.1365-246X.2011.05192.x.

Dzurisin, D., 2003. A comprehensive approach to monitoring volcano deformation as a window on the eruption cycle. Rev. Geophys. 41:1001. http://dx.doi.org/10.1029/2001RG000107.

Feigl, K.L., Agnew, C., Dong, D., Hager, H., Herring, A., Jackson, D.D., Jordan, T.H., King, W., Larson, M., Murray, M.H., Webb, F.H., 1993. Space geodetic measurement of crustal deformation in Central and Southern California, 1984–1992. J. Geophys. Res. 98, 1984–1992.

Forsyth, W., 1985. Subsurface loading and estimates of the flexural rigidity of continental lithosphere. J. Geophys. Res. 90, 12623–12632.

Galloway, D.L., Hudnut, K.W., Ingebritsen, S.E., Phillips, S.P., Peltzer, G., Rogez, F., Rosen, P.a., 1998. Detection of aquifer system compaction and land subsidence using interferometric synthetic aperture radar, Antelope Valley, Mojave Desert, California. Water Resour. Res. 34:2573. http://dx.doi.org/10.1029/98WR01285.

Haines, A.J., Holt, W.E., 1993. A procedure for obtaining the complete horizontal motions within zones deformation of strain rate data. J. Geophys. Res. 98:12057–12082. http://dx.doi.org/10.1029/93jb00892.

Hartog, R., Schwartz, S.Y., 2001. Depth-dependent mantle anisotropy below the San Andreas fault system: apparent splitting parameters and waveforms. J. Geophys. Res. 106:4155. http://dx.doi.org/10.1029/2000JB900382.

Hesse, M.a., Stadler, G., 2014. Joint inversion in coupled quasi-static poroelasticity. J. Geophys. Res. Solid Earth 119:1425–1445. http://dx.doi.org/10.1002/2013JB010272.

Hoffmann, J., Zebker, H.A., Galloway, D.L., Amelung, F., 2001. Seasonal subsidence and rebound in Las Vegas Valley, Nevada, observed by synthetic aperture radar interferometry. Water Resour. Res. 37:1551–1566. http://dx.doi.org/10.1029/2000WR900404.

Please cite this article as: Furst, S., et al., Lithosphere rigidity by adjoint-based inversion of interseismic GPS data, application to the Western United States, Tectonophysics (2017), http://dx.doi.org/10.1016/j.tecto.2017.03.015

Ivorra, B., Mohammadi, B., Ramos, A.M., 2013. Design of code division multiple access filters based on sampled fiber Bragg grating by using global optimization algorithms. Optim. Eng.:1–19 http://dx.doi.org/10.1007/s11081-013-9212-z.

Kreemer, C., Hammond, W.C., 2007. Geodetic constraints on areal changes in the Pacific–North America plate boundary zone: what controls basin and range extension? Geology 35:943. http://dx.doi.org/10.1130/G23868A.1.

Kreemer, C., Klein, E., Shen, Z.-K., Wang, M., Estey, L., Wier, S., Boler, F., 2014. A geodetic platemotion and global strain rate model. Geochem. Geophys. Geosyst.:130 http://dx.doi.org/10.1002/2014GC005407 (Received).

Liu, S., Shen, Z.-K., Bürgmann, R., 2015. Recovery of secular deformation field of Mojave shear zone in southern California from historical terrestrial and GPS measurements. J. Geophys. Res. Solid Earth 120, 3965–3990.

Lowry, A.R., Pérez-Gussinyé, M., 2011. The role of crustal quartz in controlling cordilleran deformation. Nature 471:353–357. http://dx.doi.org/10.1038/nature09912.

Lowry, A.R., Smith, R.B., 1994. Flexural rigidity of the basin and range-Colorado Plateau-Rocky Mountain transition from coherence analysis of gravity and topography. J. Geophys. Res. 99, 20123–20140.

Mao, A., Harrison, C.G.A., Dixon, T.H., 1999. Noise in GPS coordinate time series. J. Geophys. Res. 104:2797. http://dx.doi.org/10.1029/1998JB900033.

Masson, F., Chéry, J., Hatzfeld, D., Martinod, J., Vernant, P., Tavakoli, F., Ghafory-Ashtiani, M., 2005. Seismic versus aseismic deformation in Iran inferred from earthquakes and geodetic data. Geophys. J. Int. 160:217–226. http://dx.doi.org/10.1111/j.1365-246X.2004.02465.x.

McCaffrey, R., 2005. Block kinematics of the Pacific-North America plate boundary in the southwestern United States from inversion of GPS, seismological, and geologic data. J. Geophys. Res. Solid Earth 110:1–27. http://dx.doi.org/10.1029/2004JB003307.

Meade, B.J., Hager, B.H., 2005. Block models of crustal motion in southern California constrained by GPS measurements. J. Geophys. Res. B: Solid Earth 110:1–19. http://dx.doi.org/10.1029/2004JB003209.

Mohammadi, B., Pironneau, O., 2004. Shape optimization in fluid mechanics. Annu. Rev. Fluid Mech. 36:255–279. http://dx.doi.org/10.1146/annurev.fluid.36.050802.121926.

Mohammadi, B., Pironneau, O., 2009. Applied Shape Optimization for Fluids. second ed. Oxford University Press, Oxford.

Montelli, R., Nolet, G., Masters, G., Dahlen, F.A., Hung, S.-H., 2004. Global *P* and *PP* traveltime tomography: rays versus waves. Geophys. J. Int. 158:637–654. http://dx.doi.org/10.1111/j.1365-246X.2004.02346.x.

Mossop, A., Segall, P., 1999. Volume strain within The Geysers geothermal field. J. Geophys. Res. 104:29113–29131. http://dx.doi.org/10.1029/1999JB900284.

Pérez-Gussinyé, M., Swain, C.J., Kirby, J.F., Lowry, A.R., 2009. Spatial variations of the effective elastic thickness, Te, using multitaper spectral estimation and wavelet methods: examples from synthetic data and application to South America. Geochem. Geophys. Geosyst.:10 http://dx.doi.org/10.1029/2008GC002229.

Plessix, R.E., 2006. A review of the adjoint-state method for computing the gradient of a functional with geophysical applications. Geophys. J. Int. 167:495–503. http://dx.doi.org/10.1111/j.1365-246X.2006.02978.x.

Pollitz, F.F., McCrory, P., Wilson, D., Svarc, J., Puskas, C., Smith, R.B., 2010. Viscoelastic-cycle model of interseismic deformation in the northwestern United States. Geophys. J. Int. 181:665–696. http://dx.doi.org/10.1111/j.1365-246X.2010.04546.x.

Rosen, P., Werner, C., Fieldind, E., Hensley, S., Buckley, S., Vincent, P., 1998. Aseismic creep along the San Andreas Fault northwest of Parkfield, Ca measured by radar interferometry. Geophys. Res. Lett. 25:825–828. http://dx.doi.org/10.1029/JB078i005p00832.

Savage, J.C., Burford, R.O., 1973. Geodetic determination of relative plate motion in central California. J. Geophys. Res. 78:832. http://dx.doi.org/10.1029/JB078i005p00832.

Sella, G.F., Dixon, T.H., Mao, A., 2002. REVEL: a model for recent plate velocities from space geodesy. J. Geophys. Res. 107:2081. http://dx.doi.org/10.1029/2000JB000033.

Shen, Z.K., Jackson, D.D., Ge, B.X., Bob, X.G., 1996. Crustal deformation across and beyond the Los Angeles basin from geodetic measurements. J. Geophys. Res. 101: 27927–27957. http://dx.doi.org/10.1029/96JB02544.

Smith-Konter, B.R., Sandwell, D.T., Shearer, P., 2011. Locking depths estimated from geodesy and seismology along the San Andreas Fault System: implications for seismic moment release. J. Geophys. Res. 116, B06401. http://dx.doi.org/10.1029/2010JB008117.

Smith-Konter, B.R., Thornton, G.M., Sandwell, D.T., 2014. Vertical crustal displacement due to interseismic deformation along San Andreas fault: contraints from tide gauges. Geophys. Res. Lett. 41:3793–3801. http://dx.doi.org/10.1002/2014GL060091.

Tanaka, S., Obayashi, M., Suetsugu, D., Shiobara, H., Sugioka, H., Yoshimitsu, J., Kanazawa, T., Fukao, Y., Barruol, G., 2009. P-wave tomography of the mantle beneath the South Pacific Superswell revealed by joint ocean floor and islands broadband seismic experiments. Phys. Earth Planet. Inter. 172:268–277. http://dx.doi.org/10.1016/j.pepi.2008.10.016.

Tape, C., Liu, Q., Maggi, A., Tromp, J., 2009. Adjoint tomography of the southern California crust. Science 325:988–992. http://dx.doi.org/10.1126/science.1175298.

Tarantola, A., 2004. Inverse problem theory and methods for model parameter estimation. Book http://dx.doi.org/10.1137/1.9780898717921.

Tesauro, M., Burov, E.B., Kaban, M.K., Cloetingh, S.A.P.L., 2011. Ductile crustal flow in Europe's lithosphere. Earth Planet. Sci. Lett. 312:254–265. http://dx.doi.org/10.1016/j.epsl.2011.09.055.

Thatcher, W., Pollitz, F.F., 2008. Temporal evolution of continental lithospheric strength in actively deforming regions. GSA Today 18:4–11. http://dx.doi.org/10.1130/GSAT01804-5A.1.

Tikhonov, A.N., 1943. On the stability of inverse problems. Dokl. Akad. Nauk SSSR 39, 195–198.

Turcotte, D.L., Schubert, G., 2002. Geodynamics. Cambridge University Press.

Vasco, D., Wicks, C., Karasaki, K., 2002. Geodetic imaging: high resolution reservoir monitoring using satellite interferometry. Geophys. J. Int. 555–571 (in press).

Vassilvitskii, S., Yannakakis, M., 2005. Efficiently computing succinct trade-off curves. Theor. Comput. Sci. 348:334–356. http://dx.doi.org/10.1016/j.tcs.2005.09.022.

Vernant, P., 2015. What can we learn from 20 years of interseismic GPS measurements across strike-slip faults? Tectonophysics 644–645:22–39. http://dx.doi.org/10.1016/j.tecto.2015.01.013.

Watts, A.B., 2001. Isostasy and Flexure of the Lithosphere. Cambridge University Press, Cambridge.

Zaroli, C., Sambridge, M., Lévêque, J.J., Debayle, E., Nolet, G., 2013. An objective rationale for the choice of regularisation parameter with application to global multiple-frequency S-wave tomography. Solid Earth 4:357–371. http://dx.doi.org/10.5194/se-4-357-2013.

Please cite this article as: Furst, S., et al., Lithosphere rigidity by adjoint-based inversion of interseismic GPS data, application to the Western United States, Tectonophysics (2017), http://dx.doi.org/10.1016/j.tecto.2017.03.015

5.3 Discussion and future directions

This first application of global optimization algorithm described in Chapter 4 allows us to show how to solve a low complexity problem for geodetic inverse problems. The term low complexity refers here to a single data type (GPS velocities) considered invariant with time. In this case, we checked the efficiency of the methodology for the first level of complexity, I-level (one data type, time-independent variables). The work presented in this paper is an extension of a previously published paper (Chéry et al., 2011) with significant methodological enhancements: (1) the use of the adjoint to include larger parameters set at low computational cost, (2) the optimization of the boundary conditions and (3) the generation of an uncertainty map to complete the distribution of the rigidity from the inversion.

Alternatively to the elastic flexural theory, we focus in this paper on linking the shear rigidity to the horizontal motion through the stress equilibrium equation. The adjoint formulation of our forward problem allowed us to consider a high number of parameters and therefore to produce a high resolution map of the rigidity. The application to the western United-States using CMM3 interseismic velocities provides low effective rigidities in regions presenting high deformations (San Andreas Fault system, Mojave Desert, Eastern California Shear Zone) while high rigidities are found in areas displaying little deformations (South Basin and Range, Sierra Nevada). These rigidity variations are associated to low residual velocities ($NRMS = 1.2$) and effective rigidity are accurately determined in moderately and highly strained areas. Furthermore, except in few places (offshore the Pacific Coast and East of the East Californian Shear Zone), we are able to retrieve most of the kinematic strain rate of the Global Strain Rate Map (Kreemer et al., 2014), simply by taking into account the mechanical constraint of the stress equilibrium equation.

As part of further applications of this study, we can imagine extending the 2D effective model to a 3D model representation of the western US. As a result, the effective elastic thickness deduced from the shear rigidity will become one of the free geophysical parameter of the inversion, leading to a more realistic approximation of the plate characteristics and behavior. Another possibility would be to use this 2D approach over wider areas such as continental or even global scale. This could be achieved along with the global strain map project of Kreemer et al. (2014). Finally, because of the strong spatial correlation between low rigidity areas and active fault zones, our methodology could be applied for deciphering active faults behaviour in tectonically poorly known areas or identifying post-seismic residuals in the velocity fields. All these suggestions are only proposals to extend our work and are not developed in this manuscript.

Nevertheless, this paper can be considered as a prelude of the central development of my thesis which consists in jointly inverting various types of geodetic data. From this I-level of complexity, I adapted and expanded the algorithm for time-varying problems (several time intervals) described by a single data type displaying time-dependent component, tilt data (second level of complexity, II-level). A III-level of complexity can be defined if more than one kind of data is considered. This level combines several geodetic data types (GPS, InSAR, levelling and tilt data) with time-dependent parameters.

Chapter 6

Tilt time-series inversion and drift modelling

Résumé

Dans ce chapitre, nous nous intéressons à un deuxième type de problèmes faisant intervenir des paramètres de modèle de source dépendant du temps ainsi que des paramètres instrumentaux inconnus. En effet, les jeux de données géodésiques sont bien souvent quasi-continus dans le temps et forment des séries temporelles qui peuvent couvrir plusieurs années ou décennies. Dans le cas des données de tilt, l'extension de la couverture temporelle peut se faire au détriment de la qualité du signal enregistré. En effet, le bruit coloré ou Brownien contenu dans les données de tilt est dépendant du temps et propre à chaque instrument. En outre, la dérive associée à chaque composante d'un instrument augmente l'incertitude de la mesure et de ce fait, sa capacité à enregistrer le signal produit par la source de déformation.

Nous proposons ainsi une nouvelle approche, dont les principes sont décrits dans le Chapitre 4 qui permet d'estimer à la fois les paramètres de la source de déformation et les paramètres de dérive des inclinomètres. Pour cela, nous faisons l'hypothèse d'une linéarité entre la déformation de la surface et celle de la source. Nous considérons les variations volumétriques subies par 1) une source sphérique (modèle de Mogi) et 2) une fracture en ouverture (modèle d'Okada). Des jeux de données synthétiques associés à ces 2 types de modèles sont créés pour illustrer et éprouver la méthodologie. Ce chapitre présente dans un premier temps les détails de la méthodologie et son application avec une source de type Mogi. Ces travaux ont fait l'objet d'un article soumis au journal Journal of Geodesy. Les résultats obtenus pour le modèle de type Okada sont détaillés dans la deuxième partie du chapitre.

6.1 Introduction

The methodology developed in Chapter 4 has previously been applied to a single type of data with time-independent parameters (I-level of complexity). However, geodetic datasets are generally made of long time series which can therefore be more difficult to interpret due to the time-dependent noise and/or drift. For this reason, we extended the methodology to time-varying problems. I present here the application of the approach on a second level of complexity which still considers a single data type (tilt), but also time-dependent instrumental parameters (long-term drift).

Although borehole tiltmeters are widely used to survey deformation in nearly real-time, these high-resolution instruments are not suitable for long term monitoring due to their poorly known linear drift. In volcano geodesy or reservoir monitoring, surface deformation can be induced by the filling or draining of magmatic chambers, dike propagation, hydraulic fracturation and fracture draining when oil and/or gas are extracted from unconventional reservoirs (see Chapter 3). When switching to modelling these phenomena, analytical models such as point source Mogi (1958) and planar dislocation (Okada, 1992) are widely used. For both models, ground deformation can be linearly expressed as a function of volume variations. Therefore, when inverting tilt data to retrieve volume variations of the source and drift rates, the inversion converges towards an infinity of admissible parameters.

In this chapter, I present a new approach to estimate strain source variations and linear tiltmeters drift using our optimization scheme. By assuming linear dependence between source strain and source parameters, we demonstrate the potential of the methodology to infer the drift parameters of tiltmeters and the volume changes of 2 types of sources: Mogi (1958) and Okada (1992). Firstly, the approach is described and evaluated on synthetic tilt data generated using a Mogi model. This study has been submitted to the journal *Solid Earth*. Secondly, I consider the deformation induced by the opening of a fracture using Okada's model to demonstrate the robustness of our approach to recover the desired parameters.

6.2 How to use tilt series to estimate long-term instrumental drift?

Article to be submitted to *Journal of Geodesy*.

Joint estimation of tiltmeters drift and volume variation during reservoir monitoring

S. Furst[1], J. Chéry[1], B. Mohammadi[2], and M. Peyret[1]

[1]GM, Univ Montpellier, CNRS, Univ Antilles, Montpellier, France
[2]IMAG, Univ Montpellier, CNRS, Montpellier, France.

Correspondence to: Severine Furst (severine.furst@gm.univ-montp2.fr)

Abstract. Borehole tiltmeters are widely used to continuously record small surface deformation of reservoirs and volcanoes. Because these instruments display unknown long-term drift, only short-term tilt signal can be used for monitoring purpose. We propose a method to invert long-term time series of tilt data induced by strain variations at depth. Assuming that tiltmeters drift linearly with time does not yield to uniqueness of volume variation. To overcome this problem, we first invert the data with no constrain on the drift to obtain one particular solution among all admissible. Then, using the linearity of the forward model, we use the statistical properties of the drift distributions to restore the uniqueness of the solution. We illustrate our approach with four synthetic cases simulating volume changes of a reservoir. We demonstrate the efficiency of our method and show that the accuracy of estimated volume variation dramatically improves if low drift tiltmeters are used.

1 Introduction

The deformation of the Earth's surface reflects anthropogenic, tectonic and volcanic processes at depth (e.g., fault slip and/or mass transport) transmitted to the surface through the mechanical properties of the crust. To capture this ground deformation different geodetic instruments and techniques can be used. For instance, Global Navigation Satellite System (GNSS), Interferometric synthetic-aperture radar (InSAR) and levelling surveys commonly monitor millimetric motions of the ground. Complementary to this, tiltmeters locally measure the horizontal derivative of the vertical motion (hereafter denoted as tilt measurement) in one or two directions. These sensitive instruments are suitable for recording small deformations (Goulty, 1976; Agnew, 1986) that would be beyond the resolution limit of other techniques. Unfortunately, these instruments are drifting with time, with drift rate amplitudes depending on instrument type, making these instruments often unusable for revealing slow deformation processes.

Water-tube tiltmeters (10-500m) are intrinsically stable due to the length of the sensor. To minimize subsurface effects, they are usually installed in deep tunnels therefore displaying residual drifts as low as $0.1\ \mu$rad/yr (e.g. Boudin et al., 2008). By contrast, short-base tiltmeters are usually installed in boreholes and display higher drift rates of 1-100 μrad/y (Jahr et al., 2006, Chawah et al., 2015). Despite borehole tiltmeters are deployed as networks in volcanoes and geological reservoirs (e.g.

Gambino et al. 2014), their potential is far from being fully exploited partly because such tiltmeters are drifting in a completely unconstrained way, intrinsically to each instrument. In addition to drift, tiltmeters also display a time dependent noise that can be of various nature, such as environmental (e.g. Gambino et al., 2014; Goulty, 1976) or instrumental (Wu et al., 2015). The environmental noise is mostly induced by hydraulic loading, temperature effect or pressure gradient. These unwanted signals can be lowered when tiltmeters are installed in deep boreholes, to attenuate the amplitude of the noise.

Although the resolution of borehole tiltmeters is as high as 1-5 nrad, tilt data are generally considered only during a short period of time due to the long-term drift and the noise. Indeed, to monitor long term reservoir extraction or magmatic chamber inflation/deflation, tilt time series with low drift and signal-to-noise ratio are essential (Wyatt et al. 1982; Kohl and Levine 1993). Thus, the objective of this study is to infer instrumental drift through the solution of an inverse problem. To overcome the non-uniqueness of the solution, we developed a methodology to simultaneously estimate tiltmeters drift as well as strain source parameters from tilt series. We illustrate our approach with synthetic cases simulating ground deformation induced by a Mogi-type source (Mogi, 1958) whose volume varies over 11 months.

2. Tilt data parametrization

We consider a ground deformation signal recorded by N tiltmeters in both x and y directions directions. For each instrument, the observed tilt $\overrightarrow{d_o}(t)$ is the sum of the signal produced by the source $\overrightarrow{d_s}(t)$, an instrumental drift $\overrightarrow{d_d}(t)$ and a cumulative noise $\overrightarrow{cn}(t)$ as defined by Eq. (1):

$$\overrightarrow{d_o}(t) = \overrightarrow{d_s}(t) + \overrightarrow{d_d}(t) + \overrightarrow{cn}(t) , \quad (1)$$

We assume for each instrument that the drift is linear in time such as $\overrightarrow{d_d}(t) = \vec{a} \cdot t$ with $\vec{a}$ a constant drift rate vector (a_x, a_y) representing the slope of the drift and t is the time elapsed since the beginning of recording. Because the tilt measurement is relative, we assume that the drift is zero at the beginning of observation. The number of unknown drift parameters associated to the problem is therefore 2N.

In the following, we consider that the source strain $\overrightarrow{d_s}(t)$ depends linearly of the source parameter at depth. Strictly speaking, this is obviously not valid in most cases. Nevertheless, such an approximation is considered as reasonable and is widely used in many geophysical domains. For instance, the use of Green functions is widespread for modeling ground deformation induced by dislocation at depth (Okada's model) or volume changes of a deep reservoir (Mogi or McTigue models). For one source, the time varying deformation captured by the tiltmeters can be written as a product of a known coefficient vector $\vec{\alpha}$ and a continuous time function corresponding to a strain source parameter $p(t)$ defined by Eq. (2):

$$\overrightarrow{d_s}(t) = \vec{\alpha} \cdot p(t) , \quad (2)$$

where $\vec{\alpha}$ is called the deformation model parameter and represent the contribution of a unit source parameter to the signal recorded by each tiltmeter. Therefore, larger components in $\vec{\alpha}$ hold for instruments close to the source indicating a higher sensitivity with respect to the source. Combining Eqs.1 and 2, it becomes obvious that an infinite number of pairs involving $p(t)$ and N drift rate vectors $\vec{a}$ produce the same signal $\overrightarrow{d_o}(t)$. Therefore, inverting the tilt data yields to a non-unique solution. Instead of converging towards a single global minimum with one set of parameters, the inversion process tends to a family of admissible combinations of parameters, all explaining the data equally well. Eventually, Eq. (3) provides an *admissible* solution :

$$\overrightarrow{d_a}(t) = \vec{\alpha}\, p_a(t) + \overrightarrow{a_a}\, t = \vec{\alpha}\ p^*(t) + \overrightarrow{a^*}\ t\ , \tag{3}$$

where the subscript $_a$ expresses any of all admissible scenarios provided by the optimization, one of them being the *desired* scenario denoted by the exponent *. We use the statistical properties of the tilt parameters to recover the desired scenario, that is the closest admissible solution to the target.

3. Optimization problem

3.1 Global optimization

We discretized the strain source parameter function $p(t)$ over M time steps, leading to a vector of length M. The total number of unknowns is therefore 2N + M, while the number of observations is 2N · M . We follow a classical scheme of optimization to invert our tilt data to find an admissible set of both p_a and $\overrightarrow{a_a}$. The free parameters are set to an admissible initial guess with no other a-priori knowledge. This initial set of parameters provides a first model $\overrightarrow{d_m}$ using the constitutive Eqs. 1 and 2. Then, they are compared to the observations $\overrightarrow{d_o}$ through a functional denoted J. The stopping criteria is based on a target minimum value for the functional to be reached within given maximum number of iterations. Global optimization is necessary since we have no information on the convexity of the cost function and several local minima may be present.We apply a multi-criteria global optimization algorithm (Ivorra et al., 2013) which aims at improving the initial condition for classical gradient-based methods (Mohammadi & Pironneau, 2009).

To build the global functional, we first compare for the N tiltmeters the model prediction $\overrightarrow{d_m}$ to the observations $\overrightarrow{d_o}$ at a given time t_i . We use a weighted Euclidian norm as defined by Eq. (4):

$$F_i = \overrightarrow{D_i}^t \Sigma_i^{-1} \overrightarrow{D_i}\ , \tag{4}$$

where Σ_i is the covariance error matrix of each measurement and $\overrightarrow{D_i} = \overrightarrow{d_o}(t_i) - \overrightarrow{d_m}(t_i)$. In order to construct a fuctionnal assembling the M time steps, we integrate F_i over time using a piecewise linear approximation between t_i and t_{i+1}. Therefore, the global functionnal gathering all observations and the corresponding models can be written as Eq. (5):

$$J = \frac{1}{t_{M+1}-t_1}\sum_{i=1}^{M-1} \frac{1}{2}\,[F_i + F_{i+1}][t_{i+1} - t_i]\,, \tag{5}$$

The optimization is assumed to be successful whenever this functional is lower than the data uncertainties or while reaching the target minimum value, providing one optimal set (among an inifinite number of others) of p and $\vec{a}$ fitting at best the measurements.

3.2 The non-uniqueness problem

At the end of the optimization, we obtain one set of admissible parameters p_a and $\overrightarrow{a_a}$ that predicts tilt measurements $\overrightarrow{d_a}$ close to our observations $\overrightarrow{d_o}$. The residual tilt is defined by the difference between the admissible dataset and the observations over the M time steps:

$$RMS_{tilt} = \left(\frac{\sum_{i=1}^{M}\|\vec{D}_i\|^2}{M}\right)^{1/2}, \tag{6}$$

This residual can be due to the noise $\overrightarrow{cn}$ embedded in the observations but also to some lack of convergence of the minimization process. Due to non-uniqueness, this admissible set of parameters provides a strain source history and a set of drift rates that can greatly differ from the target solution. Starting from the admissible solution (p_a ; $\overrightarrow{a_a}$) and equation 3, the desired solution (p^*; $\overrightarrow{a^*}$) must satisfy:

$$\overrightarrow{a^*} = \overrightarrow{a_a} - R\,\vec{\alpha}\,, \tag{7a}$$

$$p^* = p_a + R^*\,t\,, \tag{7b}$$

where $R = \frac{p^*-p_a}{t}$ is a correction coefficient to be estimated. When varying R, we get admissible distributions of $\vec{a}$ and p. Having no indication on the strain source history $p(t)$, we cannot use equation 7b to infer a suitable value for R. By constrast, equation 7a contains a-priori information concerning the source model (N components of $\vec{\alpha}$) and the drift parameters (N values of $\vec{a}$). Because $\vec{\alpha}$ and $\vec{a}$ datasets represent respectively the source effect (dependant to the instrument position with respect to source position) and the instrument properties, they must be statistically independant. Therefore, the value of R in equation 7b must be chosen to provide a desired solution $\overrightarrow{a^*}$ displaying a lack of correlation with $\vec{\alpha}$. Hence, the enforcement of $cov(\overrightarrow{a^*}, \vec{\alpha}) = 0$ leads to the following solution:

$$R = \frac{cov(\overrightarrow{a_a}, \vec{\alpha})}{var(\vec{\alpha})}, \tag{8}$$

meaning that R is the coefficient of the linear regression adusting $\overrightarrow{a_a}$ as a function of $\vec{\alpha}$. Using an example of the time inflation of a buried volumetric source at depth, we show how our methodology leads to recover both the actual drift rates and volumetric source history.

4. Application to reservoir modeling

4.1 Forward model

The above optimization problem requires a linear relation between the source parameters and the observation. Therefore, this class of problem covers numerous elastic solutions (either analytical or numerical) used for reservoir modeling (Segall, 2010). Among them, the so-called *Mogi model* is the simplest and probably the most widely used analytical solution for a pressurized point source in a homogeneous elastic half-space (Mogi, 1958). The Mogi source is defined by its radius R, centered at a depth z_s beneath the free surface at $z = 0$, z being counted positive upwards. A uniform internal pressure P is applied to the boundary of the spherical source. The volumetric change associated with the deformation is given by $\Delta V = \frac{\pi}{\mu} PR^3$ with μ being the shear modulus. The system is described by four variables, including the cartesian coordinates of the point source $\overrightarrow{x_s} = (x_s, y_s, z_s)$ and the volumetric change (ΔV) that plays the role of the parameter p in the optimization problem (section 3 above). The Mogi model predicts 3-D surface deformation $\vec{u} = (u_x, u_y, u_z)$ at a given observation point $\vec{x} = (x, y, 0)$. The ground tilt vector is given by the horizontal derivatives of the vertical displacement $u_z = (x, y)$. The tilt $\overrightarrow{d_s}$ is therefore the slope of u_z, considering that tilt vectors are pointing in direction of decreasing vertical displacements. Therefore, $\overrightarrow{d_s} = -\nabla\vec{U}_z$ (U_z being the vector made of the u_z of all the tiltmeters at the time considered) and the tilt vector associated to a source is expressed by the following expressions:

$$\vec{d}_s = \vec{\alpha}\,\Delta V\,, \tag{9a}$$

$$\vec{\alpha} = \frac{3(1-\nu)}{\pi}\frac{-z_s \cdot r}{(z_s^2+r^2)^{3/2}}\,\vec{n}\,, \tag{9b}$$

where ν is the Poisson ratio (chosen to be 0.25), r the horizontal distance $\sqrt{(x_s - x)^2 + (y_s - y)^2}$ between the source point and the observation point and $\vec{n}$ the unit vector pointing from the source to the observation point. Even if all four variables $(x_s, y_s, z_s, \Delta V)$ can be considered as optimization parameters, we choose to fix the position of the source and to only seek for the volumetric changes over time.

4.2 Synthetic data

In addition to the tilt component induced by the source (Eq. 9a-b), we add to the synthetic signal some random tiltmeter drift and tiltmeter noise to generate 11 months of observations. We present hereafter the results of four different synthetic configurations involving different levels of drift and noise. Each tiltmeter is assumed to have a randomly chosen drift rate for both components using a uniform probability density function. The range of probability is chosen according to known average values for low drift ($\pm$ 2.4 μrad/yr) and moderate drift ($\pm$ 48 μrad/yr). Besides drift, we either consider no noise in the data (Cases 1a and 2a, see table 1) or, to be more realistic, we introduce Brownian noise in tilt data (Cases 1b and 2b). We assign a standard deviation of the short term tilt measurements of $\sigma_{short} = 5$ nrads and assume that a Brownian noise is leading to a maximum standard deviation σ_{max} at the end of the experiment. Given the lack of knowledge about noise for the borehole

tiltmeters cited above, we arbitrarily set the maximum standard deviation to 180 nrads after one year of experiment. The tilt covariance matrix is therefore built using the maximum standard deviation for both components of each tiltmeters (Kasdin, 1995):

$$\sigma = \sigma_{short} T^{A/4} , \quad (10)$$

where T is the number of iterations for each data sample required to reach σ_{max} after 11 months and A is the type of noise (i.e. $A = 0$ for White noise and $A = 2$ for Brownian noise). We estimate T to 1440 using Eq. (10) for the specified values of σ_{short} and σ_{max}. The deformation is produced by a spherical source embedded in an elastic medium at 1500 m deep and centered in a 10x10 km observation domain. The induced deformation is recorded by 50 tiltmeters randomly distributed (Fig. 1a). Synthetic data are monthly down-sampled values to decrease the time size of the problem (M=12), corresponding to monthly time-intervals volume variations (Fig. 1b). The volume change is set to zero during the first 2 months, then increases linearly to 250 000 m^3 the next 5 months and finally goes back to zero after 2 months. The vertical deformation induced by a the volume variation of the source is therefore maximum at $t = 7$ months. The corresponding synthetic ground deformation signal at this time is shown for case 1b (low drift instrument and noise of 180 nrad, Fig. 1c). An example of daily time series for x-component of the tilt is shown Fig. 1d for the instrument marked with a green cross on Fig. 1a.

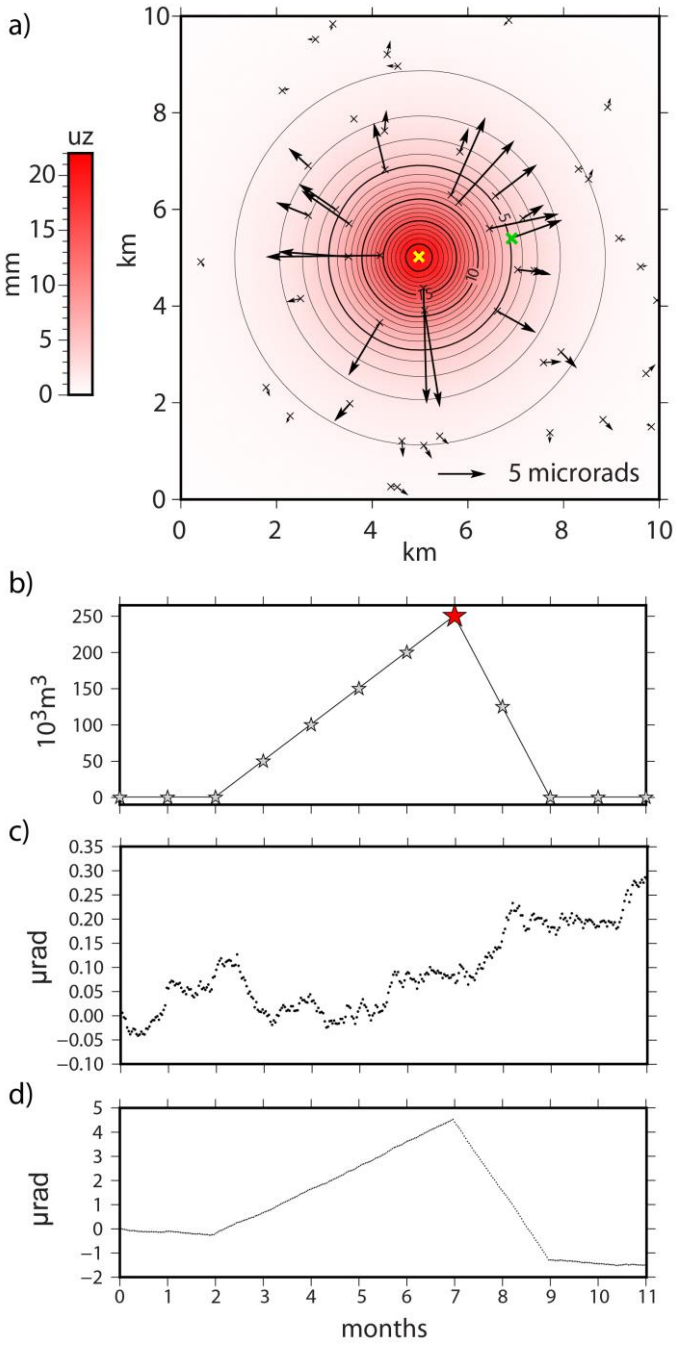

Fig. 1: Synthetic tilt produced by volumetric changes of a spherical source with an added drift of 2.4 μrad/yr and a Brownian noise, during 11 months of the experiment. a) Screenshot of the vertical displacement u_z (color scale) and tilt signal (black arrows) induced by a volumetric variation at t=7 ($\Delta V = 250\,000$ m^3, red star on b) of a spherical source (yellow cross). b) Evolution of the targeted volumetric changes over one year c) Typical random walk noise associated to the tilt over 11 months d) Synthetic tilt signal with drift and noise in x-direction for one tiltmeter (green cross on Fig. 1a).

4.3 Results

The configurations and results of the four experiments previously described are summarized in Table 1. After the optimization process, we converge towards an admissible solution with a set of parameters, ΔV_a and $\overrightarrow{a_a}$ giving the lowest residual between synthetic and modelled data, as provided by the RMS value that integrates time series over the whole time period. Table 1 shows a coherent relation between instrumental properties (drift and level of noise) and RMS_{tilt}. Indeed, the tilt residual only increases when adding noise to the data (cases 1b and 2b) but not when the level of drift increases (cases 2a and 2b). The inversion process provides a fairly homogeneous tilt residual over time for the whole set of tiltmeters (Fig. 2a). Also, the spatial distribution of the residual values between synthetic and modelled tilt vectors shows a lack of spatial trend for both amplitude and azimuth (Fig. 2b).

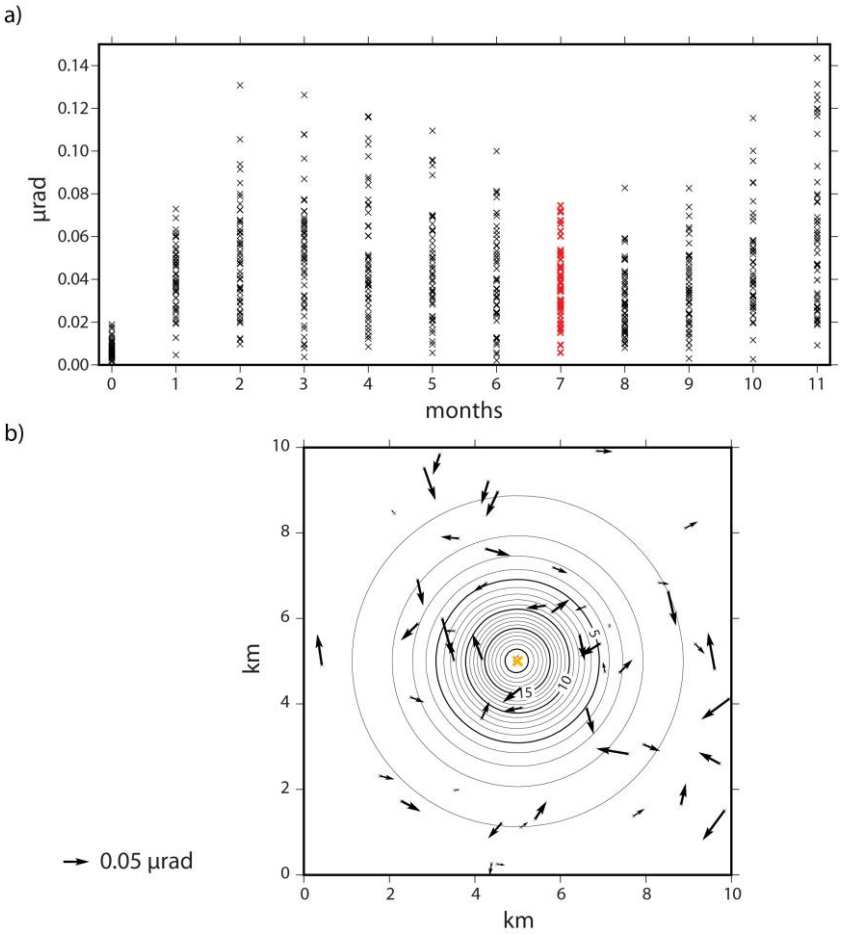

Fig. 2: Residual tilt provided by global optimization for case 1b a) Time evolution of the norm of the residual tilt vectors for all instruments. Red crosses correspond to residual shown in b) Tilt residual pattern at t=7 month (black arrows) superimposed to the uplift model (solid isovalues). The position of the spherical source is represented by a yellow cross.

This admissible optimal solution is only one particular solution of the family associated to Eq. 3. Because no constrain is applied at this stage on the relation between $\vec{\alpha}$ (which expresses the dependency of ground measurements on their relative spatial distribution with respect to source location) and drift parameters $\overrightarrow{a_a}$, a clear correlation pattern occurs between these two quantities (Fig. 3 showing case 1b). In order to cancel this trend which is caused by the non-uniqueness of the inverse problem, we enforce the lack of correlation between the deformation model parameters $\vec{\alpha}$ and the desired drift parameters $\overrightarrow{a^*}$ by inserting the result of Eq. (8) in Eq. (7a). As a result, the components of $\overrightarrow{a^*}$ display a variance similar to the one associated to the target drift coefficients (Fig. 3). In addition, there is an excellent agreement between the desired and target drift values with a residual value equal or smaller to 0.1 μrad/yr for case 1b. Because this value is markedly smaller than the trend of the synthetic Brownian noise for case 1b (that is in average equal to 0.2 μrad/yr, see Eq. (10) and Fig. 1c), we can conclude that the optimization process retrieves the sum of both deterministic and stochastic linear trends. Once the correction factor R is determined, it can be used in Eq. (7b) to obtain the desired volume change ΔV^*. Because the target volume change after 11 months is zero, the flow trend rate $\dot{V}_0$ between initial and final values of ΔV^* should be zero. Therefore, the modelled value of $\dot{V}_0$ in Table 1 provides some insight about the precision of instrumental drift determination. Unsurprisingly, low drift tiltmeters retrieve precisely the final target volume (Table 1 and Fig. 4a). Similar values of $\dot{V}_0$ provided by experiments 1a and 1b (respectively 2a and 2b) are due to identical set of the drift coefficients used for these experiments. Beyond these particular solutions, one needs to provide a statistical bound of the solution uncertainty. Two kinds of estimates are needed (1) the volumetric flow rate resolution $\delta\dot{V}$ (i.e. the accuracy of the linear component of the solution along time) (2) the instantaneous volume resolution δV. The former quantity is associated to the Eq. 7a and to the precision of determination of R. The latter term δV is linked to Eq. 9a and to the precision of the determination of $\vec{\mathrm{d}}_\mathrm{s}$ that depends in turn from $\mathrm{RMS}_{\mathrm{tilt}}$. Because of the linear character of these equations, uncertainties on $\delta\dot{V}$ and δV associated respectively to R and ΔV are given by the following relations:

$$\delta\dot{V} = RMS_{a^*}/(\alpha_{max} - \alpha_{min}) , \quad (11a)$$

$$\delta V = RMS_{tilt}/(\alpha_{max} - \alpha_{min}) , \quad (11b)$$

where RMS_{a^*} is the residual drift rate computed over all components of $\overrightarrow{a^*}$, α_{min} and α_{max} being the minimum and maximum values over all components of $\vec{\alpha}$. The computation of these values in Table 1 indicates that the target volume solution is adequately covered by this *a-posteriori* uncertainty computation of δR. Finally we check by removing the trend associated to targeted and modelled evolutions that the residual volume of the solution over time is bounded by *a-posteriori* uncertainty δV, that is of 490m^3 for case 1b (Fig. 4b).

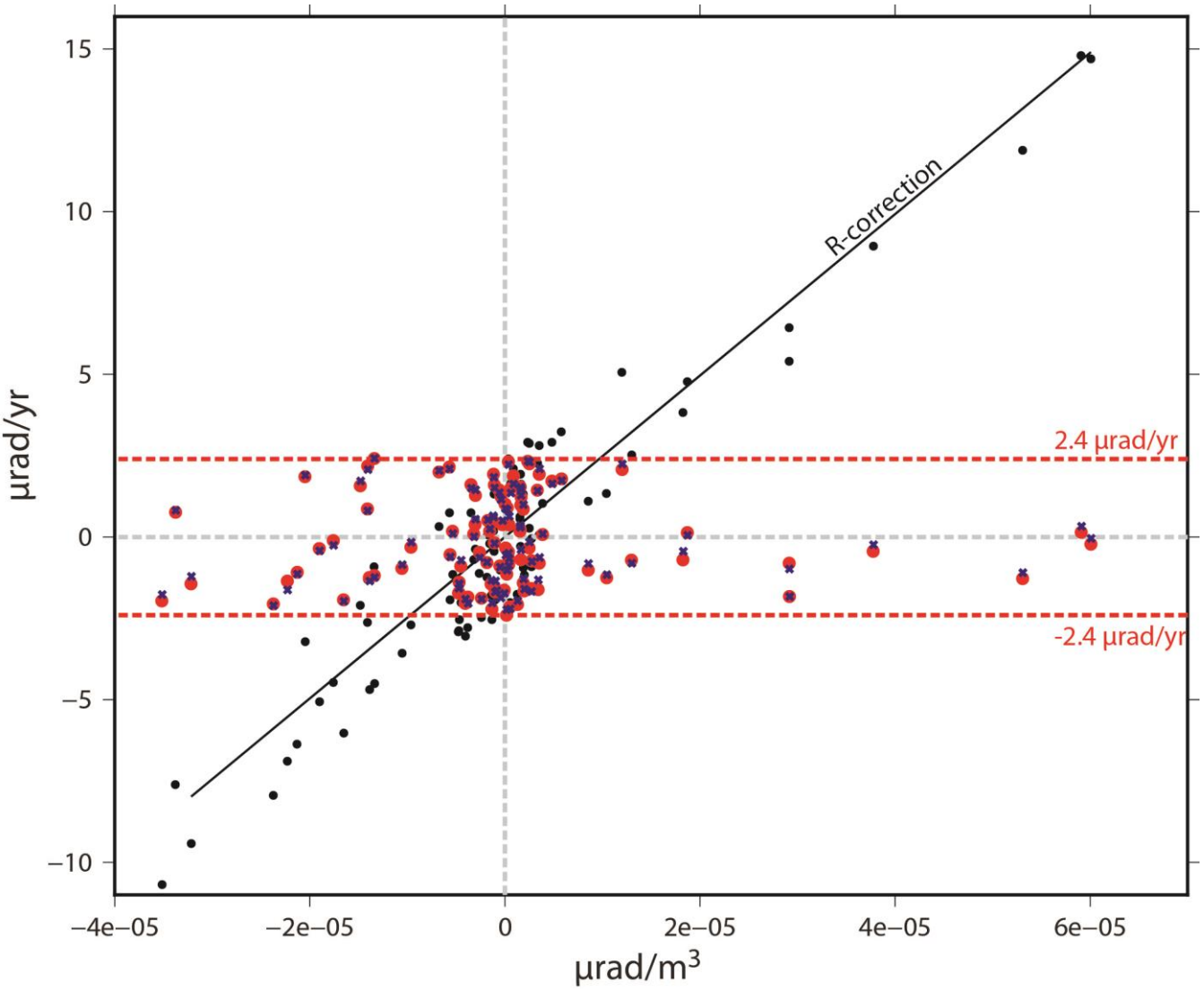

Fig. 3: Relation between all components (x-y) of drift rate $\vec{\alpha_a}$ and model coefficients $\vec{\alpha}$ for case 1b of Table 1. Black dots refer to the components of $\vec{\alpha_a}$ that display a clear correlation with $\vec{\alpha}$ components. After a linear correction using the value of R provided by Eq. 8, the components of $\vec{\alpha^*}$ are fully decorrelated with $\vec{\alpha}$ components. Target coefficients (blue crosses) are retrieved with a precision of 0.1 µrad/yr.

	Test	1a	1b	2a	2b
Configuration	Drift (μrad/y)	$\pm$2.4	$\pm$2.4	$\pm$48	$\pm$48
	Noise (μrad/y)	0	0.18	0	0.18
Optimization	RMS_{tilt} (nrad)	0.59	46.7	3.05	48.2
	Flow rate trend $\dot{V}_0$ (10^3 m^3/yr)	2.14	2.03	-181	-182
	Flow rate uncertainty $\delta\dot{V}$ (10^3 m^3/yr)	14.1	14.2	280	281
	Volume resolution δV (m^3)	6	490	32	506

Table 1: Configurations and results of the combination of global optimization and flow correction for four synthetic cases (1a-b and 2a-b). The RMS_{tilt} describes the mean residual in tilt measurements for all instruments over time. The flow rate trend $\dot{V}_0$ represents the average slope of ΔV over the two first months and the two last months. The flow rate uncertainty $\delta\dot{V}$ and the volume resolution δV are provided according Eqs. (11a-b).

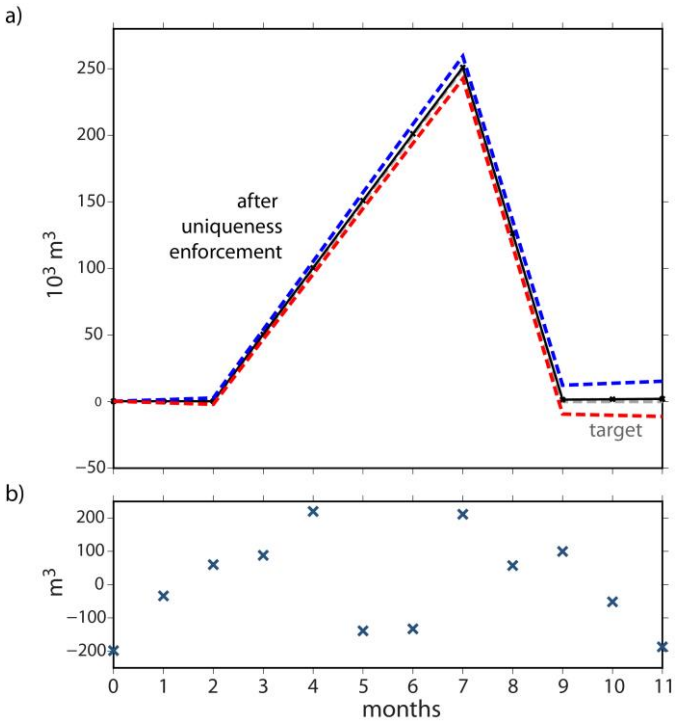

Fig. 4: Evolution of volume variation ΔV along time for case 1b a) comparison of target volume variation (grey dotted line), modeled volume variation after flow correction (black plain line), upper and lower modeled volume variation at 2-σ uncertainties (blue and red dashed lines); b) residual volume equal to the difference between target and modeled volume with the linear trend removed for both solutions.

5. Discussion

This two-step optimization approach allows for estimating the strain source change in a reservoir monitored by subsurface tiltmeters displaying a compound of linear drift but also colored noise. First, the resolution of the inverse problem with no constrain imposed on the drift rate leads to a family of solutions displaying an even adjustment to the data. The quality of the adjustment is directly linked to the amount of non-linear noise generated (or recorded) by the tiltmeters and does not involve the drift rate. Afterwards, the uniqueness of the solution (volume change and drift rate) is enforced by minimizing the correlation between deformation model parameters $\vec{\alpha}$ (that represents the sensitivity of the tiltmeters to volumetric change at depth) and drift parameters $\vec{a}$ (that should be independent from source parameters). For this second step, the precision of volumetric change retrieval is directly linked to the average magnitude of drift. For the amount of deformation considered here (a maximum tilt of 15 μrad) over a 11-months duration, low drift tiltmeters (2.4 μrad/yr) allow for precise recovery of the trend of the volumetric solution with an uncertainty rate of 14 000 m^3/yr for a depth source of 1500m. By contrast, the target solution is poorly retrieved if moderate drift tiltmeters are considered. We also show that the instantaneous volume uncertainty is linked to the amplitude of Brownian noise associated to the tiltmeters but does not depend on average drift rate amplitude. Therefore, our approach provides a relation between the quality of the tiltmeters (in term of linear drift and noise) and the precision of strain source retrieval for a given network configuration. As far as long term monitoring is concerned, the value of the short-term standard deviation of the tiltmeter (σ_{short} in Eq. 10) presents little interest and must be completed by a quantification about the linear drift rate of the sensor as well as the magnitude of its time-dependent noise.

To our knowledge, no method was previously available to mathematically separate tiltmeters drift from the surface deformation associated to a deep strain source over a monitoring time ranging from months to years. We overcome two difficulties: (1) the relatively large number of free parameters associated to both tiltmeters drift rates and a long strain source history and (2) the lack of a-priori knowledge on drift rates parameters distribution. At this stage, we found that splitting the minimisation step in the inversion problem and the retrieval of the drift parameters enforcing uniqueness makes the problem easy to adapt to different optimization strategies. We noticed however that this two-step method could be replaced by a global formulation. Indeed, removing the correlation between source and drift parameters inside the global minimization algorithm can also be achieved by looking for drift parameters having the lowest variance. This multi-criteria problem can be solved introducing, for instance, a weighted functional linear combination of the model-data misfit and the drift parameters variance.

6. Conclusion

Our inverse methodology paves the way for long-term tilt monitoring of concentrated or distributed sources of strain at depth, notably for geothermal areas, oil & gas reservoirs and volcanoes. The generic key features can be retained:

1. The approach is usable for any forward model involving a linear relation between source parameter (typically volume change) and surface deformation (tilt or strain). Therefore, all small strain elastic formulations involving non-spherical sources (Segall, 2010), opening dislocations (Okada, 1992), or even inhomogeneous distributions of the medium properties (Masterlark et al. 2016) are suitable.

2. Our methodology relies on the assumption of the independence between source parameters and drift parameters. The enforcement of this statistical property provides a way for determining confidence intervals of parameters. This first study suggests that only low drift tiltmeters (ie, lower than a few μrad/yr) are useful for long term geodetic monitoring without additional geodetic measurements like GNSS or InSAR.

3. Instrumental drift and noise can be extracted from the residual signal of a network of tiltmeters. Although we have chosen a low level of noise compared to instrumental drift, this study demonstrates that tilt residual critically depends on the non-linear instrumental behaviour. In addition, the analysis of tilt network residual using approaches developed for GNSS time analysis (Williams, 2003) may bring insight on long-term correlated noise of borehole tiltmeters that is poorly known so far.

4. The methodology could be extended to account for other geodetic measurement like GNSS times series, InSAR and leveling in order to perform a model-data fusion (e.g. Gregg & Pettijohn, 2016). In this case, a multi-criteria functional would combine all geodetic measurements with their relative weights and error covariance as well as an estimation of the correlation between drift and source parameters.

Acknowledgments

The PhD of S. Furst is supported by the Total Company and the LabEx NUMEV project (n° ANR-10-LABX-20) funded by the "Investissements d'Avenir" French Government program, managed by the French National Research Agency(ANR).

References

Agnew, D. C. Strainmeters and tiltmeters. *Reviews of Geophysics*, *24*(3), 579-624, 1986.

Boudin, F., Bernard, P., Longuevergne, L., Florsch, N., Larmat, C., Courteille, et al. A silica long base tiltmeter with high stability and resolution. *Review of Scientific Instruments*, *79*(3), 1–11. https://doi.org/10.1063/1.2829989, 2008.

Chawah, P., Chéry, J., Boudin, F., Cattoen, M., Seat, H. C., Plantier, G., & Gaffet, S. A simple pendulum borehole tiltmeter based on a triaxial optical-fibre displacement sensor. *Geophysical Journal International*, *203*(2), 1026–1038. https://doi.org/10.1093/gji/ggv358, 2015.

Gambino, S., Falzone, G., Ferro, A., & Laudani, G. Volcanic processes detected by tiltmeters: A review of experience on Sicilian volcanoes. *Journal of Volcanology and Geothermal Research*, *271*, 43–54. https://doi.org/10.1016/j.jvolgeores.2013.11.007, 2014.

Goulty, N. R. Strainmeters and tiltmeters in geophysics, *34*(2687), 245–256, 1976.

Ivorra, B., Mohammadi, B., & Ramos, A. M. Design of code division multiple access filters based on sampled fiber Bragg grating by using global optimization algorithms. *Optimization and Engineering*, 1–19. https://doi.org/10.1007/s11081-013-9212-z, 2013.

Gregg, P. M., & Pettijohn, J. C. A multi-data stream assimilation framework for the assessment of volcanic unrest. *Journal of*

Volcanology and Geothermal Research, *309*, 63-77, 2016.

Jahr, T., Letz, H., & Jentzsch, G. Monitoring fluid induced deformation of the earth's crust: A large scale experiment at the KTB location/Germany. *Journal of Geodynamics, 41*(1–3), 190–197. https://doi.org/10.1016/j.jog.2005.08.003, 2006.

Kasdin, N. J. Discrete Simulation of Colored Noise and Stochastic Processes and 1/fα Power Law Noise Generation. *Proceedings of the IEEE, 83*(5), 802–827. https://doi.org/10.1109/5.381848, 1995.

Masterlark, T., Donovan, T., Feigl, K. L., Haney, M., Thurber, C. H., & Tung, S. Volcano deformation source parameters estimated from InSAR: Sensitivities to uncertainties in seismic tomography. *Journal of Geophysical Research: Solid Earth*, *121*(4), 3002-3016, 2016.

McTigue, D. F. Elastic stress and deformation near a finite spherical magma body: Resolution of the point source paradox. *Journal of Geophysical Research, 92*(B12), 12931–12940. https://doi.org/10.1029/JB092iB12p12931, 1987.

Mogi, K. Relations between the eruptions of various volcanoes and the deformations of the ground surfaces around them. *Bulletin of the Earthquake Research Institute*. https://doi.org/10.1016/j.epsl.2004.04.016, 1958.

Mohammadi, B., & Pironneau, O. *Applied Shape Optimization for fluids* (2nd Edition). Oxford: Oxford University Press, 2009.

Okada, Y. Internal deformation due to shear and tensile faults in a half-space. *Bulletin of the Seismological Society of America*, *82*(2), 1018–1040, 1992.

Segall, P. *Earthquake and volcano deformation*. Princeton University Press, 2010.

Williams, S.D.P. The effect of coloured noise on the uncertainties of rates estimated from geodetic time series. *Journal of Geodesy*, *76*(9-10), 483-494, 2003.

Wu, L., Li, T., Chen, Z., & Li, H. A new capacitive borehole tiltmeter for crustal deformation measurement and its performance analysis. *International Journal of Mining Science and Technology*, *25*(2), 285–290, https://doi.org/10.1016/j.ijmst.2015.02.018, 2015.

Wyatt, F., Cabaniss, G., & Agnew, D.C. A comparison of tiltmeters at tidal frequencies. *Geophysical Research Letters*, *9*(7), 743-746, 1982.

6.3 Determination associated to fracture opening

The mathematical formalism described in Section 6.2 and tested using synthetics data and a Mogi's model shows how to retrieve both drift parameters and strain source parameters over a long period of time. This could permit the use of tilt time series for reservoir and volcano monitoring.

Because our approach only requires the linearity of the forward model between the data and the volume variations, it is applicable to a broad range of deformation models used in volcano geodesy and geomechanical reservoir modeling. For instance, volume variations can be induced when dikes open under the pressure of ascending magma. Besides, in unconventional reservoirs the process of hydraulic fracturation produces volumetric strain when creating or draining a Stimulated Reservoir Volume. Planar dislocations (Okada, 1992) can be used to model both processes and their associated ground deformation. Thus, as a complement to the previous experiment, I present here the application of the methodology using synthetic data generated using Okada's model.

6.3.1. Forward model

The modelling of fracture opening is often done using planar dislocation which analytical expression is given by Okada (1992) (see Chapter 2). In such case, the problem can be described by 9 parameters including the cartesian coordinates of the center of the fracture, $\vec{x}_s$=(x_s,y_s,z_s), the azimuth ϕ (with respect to the East, trigonometric rotation) and dip δ (with respect to the horizontal) of the plane, and the length L, width W and 3-D dislocation Δu_i (dip ζ_1, rake ζ_2, opening ζ_3) of the fracture. In our case of fracture opening (also called tensile case), $\Delta u_i = \zeta_3$, limiting the parameters number to 8. For such tensile case, the equation of the vertical displacement u_3 resumes to (Okada, 1992):

$$u_3 = \zeta_3 \times F(\phi, \delta, W, L, \vec{x_s}, \vec{x}) \tag{6.1}$$

where F is a function including all parameters except for the dislocation. Thus the vertical displacement is proportional to ζ_3. As the tilt vector is numerically calculated using $\vec{d_s} = -\nabla u_3$ (Eq. (2.9) in Chapter 4), the tilt signal $\vec{d_s}$ is also proportional to ζ_3. This allows us to assume once more a linear relation between observations and volume variations ($\Delta V = \zeta_3\ W\ L$). Similarly to Eq.9a from Section 6.2, we can write:

$$\vec{\alpha} = \frac{\vec{d_s}}{\Delta V} \tag{6.2}$$

In order to compare with Mogi's model results, we keep a level of complexity similar to the previous section in order to jointly invert volume history and tiltmeters drift. Therefore we choose to fix all source parameters except the opening dislocation ζ_3 which is then the only free parameter of Okada's model in the optimization.

6.3.2. Synthetics

As previously done, we consider the observed tilt signal $\vec{d_o}(t)$ as the sum of the source signal $\vec{d_s}(t)$, the instrumental drift $\vec{d_d}(t)$ and some Brownian noise $c\vec{n}(t)$ (see Chapters 4 and 6). We use the same values of the 2 components of the long-term drift as in case 1b of the example generated in previous section (Section 6.2). The Brownian noise is built similarly to the one considered in previous section: from the standard deviation of the short term tilt measurement σ_{short}= 5 nrads, the standard deviation of the noise reaches a maximum σ_{max} of 180 nrads at the end of the experiment.

We simulate the ground deformation induced by 2 models involving a fracture of dimensions 100x100 m at 2000 m depth whose associated volume changes ΔV are equivalent to previous study (Figure 6.1a). Therefore, the history of fracture opening in meters ζ_3 evolves with time from 0 to 25 m. The corresponding volume can be computed by multiplying the fracture area (10^4 m^2) by the amount of opening (Figure 6.1). Such variations in ζ_3 are obviously not representative of the real physical model, but allow us to create a numerical approximation of the volume.

The 2 models of fractures differ from their azimuth ϕ and dip δ such as:

- Case 3a involves a low dipping fracture ($\phi = 61°$, $\delta = 37°$) which produces comparable deformation as the Mogi source of the paper (Figure 6.1b).
- Case 3b corresponds to a near-vertical fracture ($\phi = 22°$, $\delta = 79°$, Figure 6.1c).

The same network of tiltmeters as for Mogi's modelling is used to monitor the deformation.

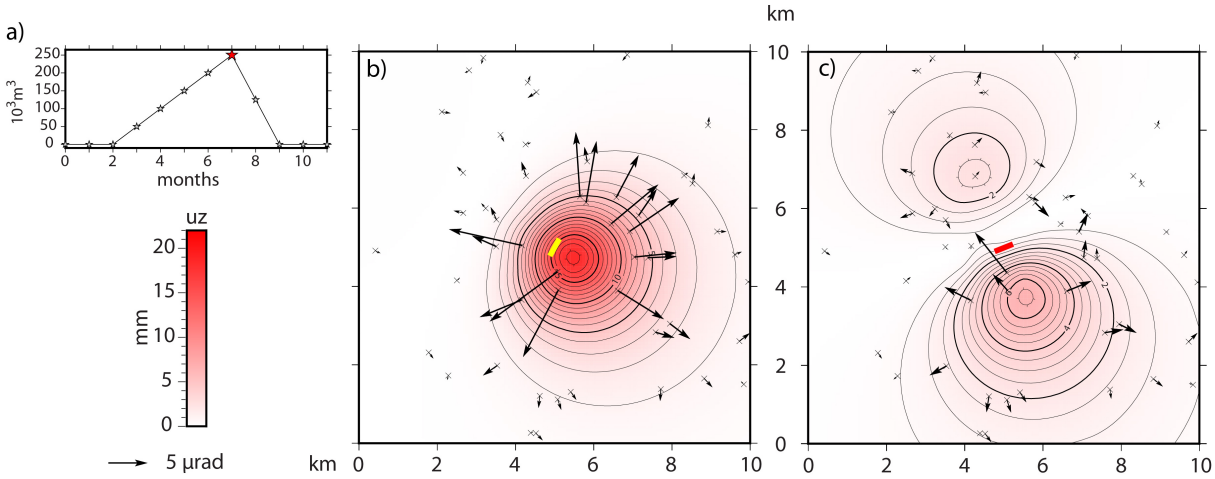

Figure 6.1: *Synthetic tilt and uplift produced by the opening of 2 fractures with different azimuth ϕ and dip δ. a) Evolution of the volume variation during the 11 months of experiment duration. The red star indicates the time and volume values for building ground deformation presented on b) and c). b) Deformation induced by a low dipping fracture (upper limit shown by a yellow marker, ×5 exaggerated) : azimuth $\phi = 61°$, dip $\delta = 37°$. c) Deformation induced by a quasi-vertical fracture (upper limit shown by a red marker, ×5 exaggerated) : azimuth $\phi = 22°$, dip $\delta = 79°$.*

6.3.3. Results

Following the methodology described in Chapter 4 and illustrated in the previous section, we performed a global optimization in order to retrieve volume variations and drift parameters associated to the synthetic data. Table 6.1 summarizes the results of the 2-step optimization, from the inversion to the flow rate correction. After the first part of the inversion process, values of RMS_{tilt} (49.8 nrads and 50.3 nrads for cases 3a and 3b respectively) are similar to the ones for cases 1b and 2b associated to Mogi's Model (Table 6.1 and Section 6.2 Table 1).

For case 3a, the parameters values of the flow rate correction, the flow rate trend $\dot{V}_0$=3.56 m^3/yr, the flow rate uncertainty $\delta\dot{V}$=15 m^3/yr and the volume correction δV=570 m^3 are also very similar to those of cases 1b and 2b (Table 6.1). Comparing cases 3a and 3b, a factor 2.4 can be noticed for the flow rate trend $\dot{V}_0$=8.47 m^3/yr ($\dot{V}_0$=3.56 m^3/yr for Case 3a). Concerning flow rate uncertainty, this ratio is 2 (case 3a $\delta\dot{V}$=15.00 m^3/yr and case 3b $\delta\dot{V}$=30.48 m^3/yr). The same ratio is observed for the volume resolution (case 3a δV= 570 m^3 and case 3b δV= 1151 m^3). This proportionality can be understood as $\delta\dot{V}$ and δV are built according to Eq.11a and Eq.11b (Section 6.2) and are proportional to $\frac{1}{\alpha_{max}-\alpha_{min}}$. For case 3b, this value is 8.9 10^{-5} μrad/m^3, which is 2 times larger than the value of 4.4 10^{-5} μrad/m^3 for case 3a.

Test	3a	3b
$RMS_{tilt}(nrad)$	49.8	50.3
Flow rate trend $\dot{V}_0$ (10^3m^3/yr)	3.56	8.47
Flow rate uncertainty $\delta\dot{V}$ (10^3m^3/yr)	15.00	30.48
Volume resolution δV m^3	570	1151

Table 6.1: *Configurations and results of the combination of global optimization and flow correction for the two synthetic cases (3a and 3b). The RMS_{tilt} describes the mean residual in tilt measurements for all instruments over time. The flow rate trend $\dot{V}_0$ represents the average slope of ΔV over the two first months and the two last months. The flow rate uncertainty $\delta\dot{V}$ and the volume resolution δV are provided according Eq.11a and Eq.11b from Section 6.2*

Figure 6.2 represents the relation between all components of the drift rate $\vec{a}$ and model coefficients $\vec{\alpha}$. The drift rates obtained after the inversion are defined by the black dots. For the case 3a, the values found by the inversion process are almost completely uncorrelated from the model coefficient (Figure 6.2a). Because the parameter domain is explored randomly following the optimization steps described in Chapter 4, the inversion can converge to an admissible solution which is close to the target one. The linear relation (Eq. 7a Section 6.2) links the drift to the model coefficients, this trend being more obvious on Figure 6.2b. The estimation of the flow rate correction R is calculated using Eq. 8 of Section 6.2 Then, by correcting the drift rate, a new set of uncorrelated drift to model coefficient is given by the red dots on Figure 6.2. Because these results are produced from a synthetic dataset, we can compare the corrected drift rates (red dots) to the target drift rates (blue crosses).

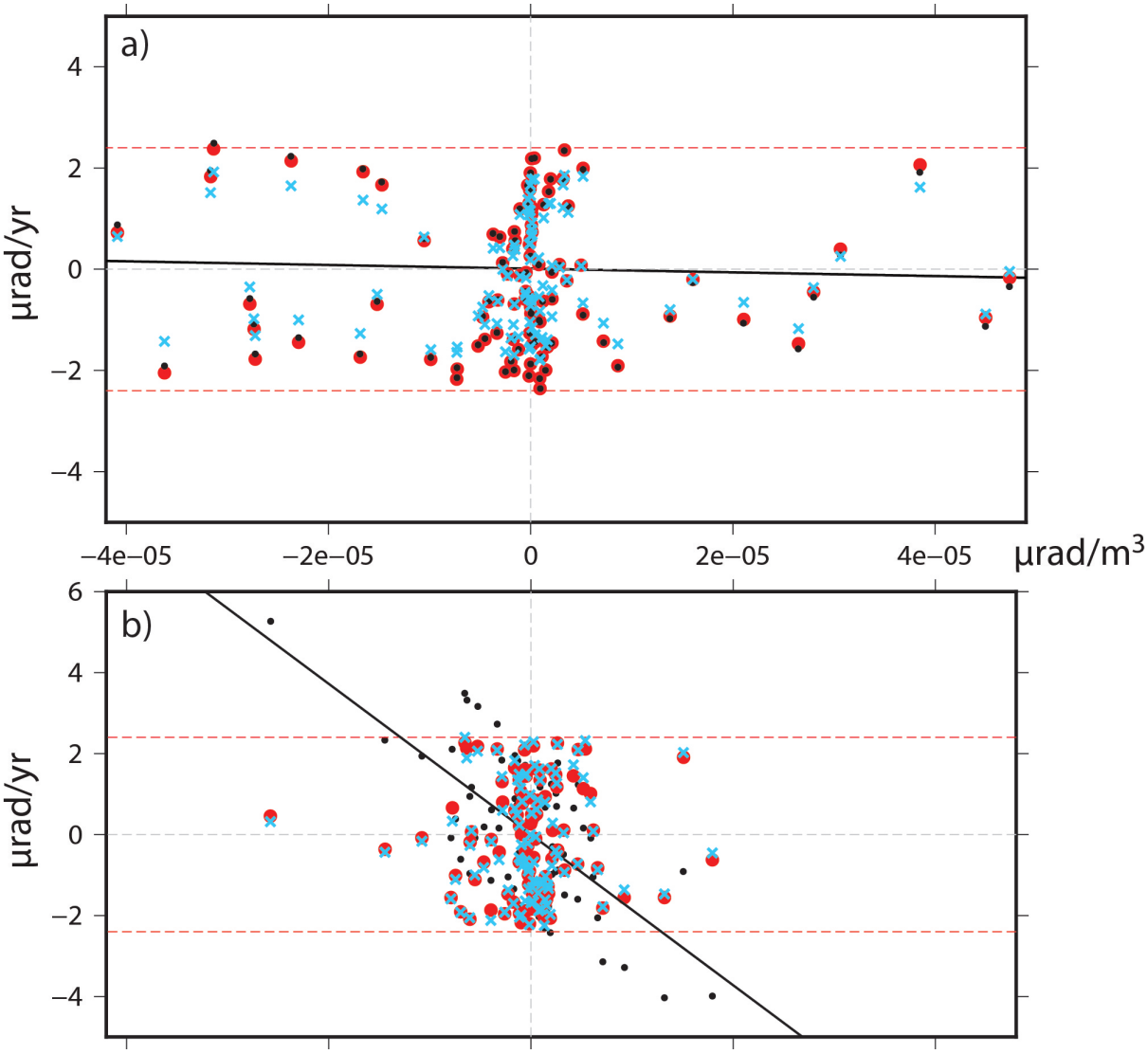

Figure 6.2: *Relation between all components (x-y) the model coefficients $\vec{\alpha}$ and the drift rates $\vec{a_a}$ before (black dots) and after (red dots) correction along with target drift rates (blue crosses) for cases a) 3a and b) 3b. The dashed lines define the limits of the uniform distribution used to create synthetic models.*

Once R is estimated, the volume variations can be deduced from Eq.7b. Because the correction does not fully retrieve the target drift, one can observe a remaining linear trend, the flow rate trend. This trend is estimated to 3.56 10^3 ± 15.00 10^3 m^3/yr for case 3a, to be compared to 8.47 10^3 ± 30.48 10^3 m^3/yr for case 3b. Figure 6.3 illustrates the efficiency of the flow rate correction for cases 3a and b respectively by representing the targeted evolution (grey dashed line), the evolution after flow rate correction (black plain line) bounded by the *a-posteriori* 2-σ uncertainty $2\delta\dot{V}$. The resolution of the volume variation is calculated from Eq.11b and is given by δV in Table 6.1 (570 m^3 and 1151 m^3 for cases 3a and b respectively). It allows to bound the instantaneous volume variation at a given time. It can be noticed that the difference between target and corrected volume is always within the bounds given by δV.

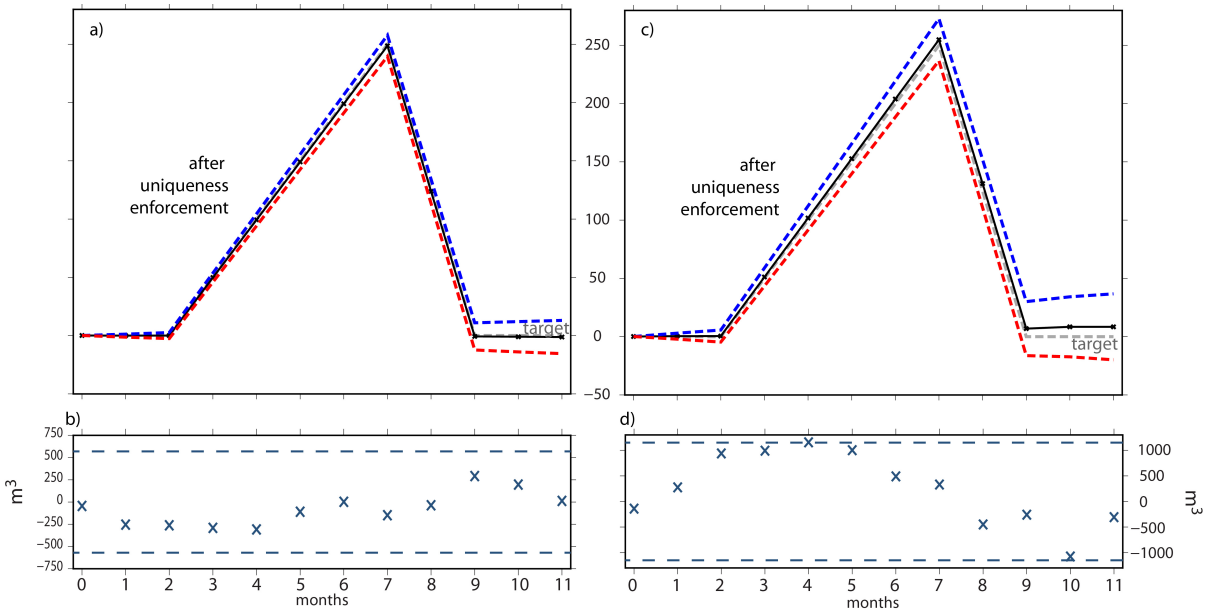

Figure 6.3: *a) Comparison of target volume variations (grey dashed line), modeled volume variations after flow correction (black plain line), upper and lower modeled volume variations at 2-σ uncertainties (colored dashed lines); b) residual volume showing the difference between target and modeled volumes with the linear trend removed for both solutions. Blue dashed lines represent the volume resolutions δV estimated from Eq.11b.*

6.4 Discussion

In this chapter, we have considered geodetic problems combining time-dependent parameters, the volume variation of a source at depth, and instrumental parameters, *i.e.* the long-term drift rates of tiltmeters. These problems correspond to the II-level of complexity described in Chapter 4 and allowed us to check the efficiency of our methodology. Synthetic tilt data are built using 2 types of forward models, 1) a spherical source based on Mogi (1958) and 2) a fracture opening described by Okada model (Okada, 1992).

The inversion of tilt data leads to non-unique solutions. Therefore, we developed a two-step optimization approach to first resolve the inverse problem with no constraint on the drift rate. In the second step, we enforce the uniqueness of the solution by minimizing the correlation between the model coefficients $\vec{\alpha}$ and the drift parameters $\vec{a}$.

These 2 synthetic examples using different forward models (Mogi and Okada models) illustrate the ability of the optimization process to jointly retrieve the volume history and drift rates of tiltmeters for a given set of fixed model parameters. To do so, we set all fixed parameters to their true value. But what happens if one of the fixed parameters has a false value? Let's take the case 3a from previous section (Okada's model for a fracture dipping at 37°) to study this question. I introduce some changes in the initial values of the fixed model parameters (x_s, y_s, z_s, ϕ or δ) that are summarized in Table 6.2.

Parameters	Case 3a	Case 3a[1]	Case 3a[2]	Case 3a[3]	Case 3a[4]
x_s	5000 m	5000 m	5000 m	5000 m	4000 m
y_s	5000 m	5000 m	5000 m	5000 m	4000 m
z_s	2000 m	2000 m	2000 m	1000 m	2000 m
ϕ	61 °	0 °	61 °	61 °	61 °
δ	37 °	37 °	90 °	37 °	37 °
Optimization					
J	6.3 10^{-2}	37.5	33.5	43.8	87.1
RMS_{tilt}	0.05 μrads	0.93 μrads	1.7 μrads	1.0 μrads	1.4 μrads
RMS_a	1.4 μrads/yr	1.9 μrads/yr	2.3 μrads/yr	1.9 μrads/yr	2.3 μrads/yr

Table 6.2: *Table summarizing the different modifications introduced in the model parameters (in red) and the associated residuals in terms of tilt and drift rates.*

Results discussed below are obtained after the inversion of tilt data. From these new experiments, some remarks can be made:

- In all those 4 experiments, the inversion process converges towards a value of the functional J largely higher than 1 (from 33.5 to 87.1). Hence, we did not perform any flow rate correction as the functional J has not converged.

- Modifying the azimuth (ϕ=0°, case 3a[1]) of the fracture influences the tilt residuals (RMS_{tilt} = 933 nrads), but only moderately changes the standard deviation of the drift rates (RMS_a=1.9 μrads/yr). Despite the false azimuth, the inversion find volume variations not too far from the expected ones (Figure 6.4). One can conjecture some explanations: 1) an azimuth change produces a rotation of the modelled deformation pattern but same amplitude of surface deformation and 2) the induced deformation is nearly symmetrical hence, the azimuth does not change the determination of the volume variations. Indeed, for the case of a near-horizontal fracture, the predicted ground displacement is almost one of a Mogi source which is perfectly spherical. Thus rotating the fracture does not introduce much difference in the signal measured by the network of tiltmeters. The difference resides in the source signal measured by each tiltmeter: changing the azimuth induces a change in the tiltmeters that are the most sensitive to the deformation (*i.e.* whose associated α are the largest).

- Changing the dip, the depth or the horizontal position of the source also introduce high residuals on the tilt data and on the standard deviation of the drift rates. However, the largest error is occurring on the volume change retrieval (Figure 6.4).

These additional simulations open the discussion to future work that would focus on the effects induced by uncertainties or errors associated with different forward models, on the model coefficients $\vec{\alpha}$, *i.e.* comparing the coefficients $\vec{\alpha}$ associated to Mogi's model with the ones of Okada's model.

We completed these optimization experiments in order to study the behaviour of the functional, data residual and parameters resolution for the purpose of optimizing more source parameters (*e.g.* position, dip and azimuth of the source). Indeed, while position of

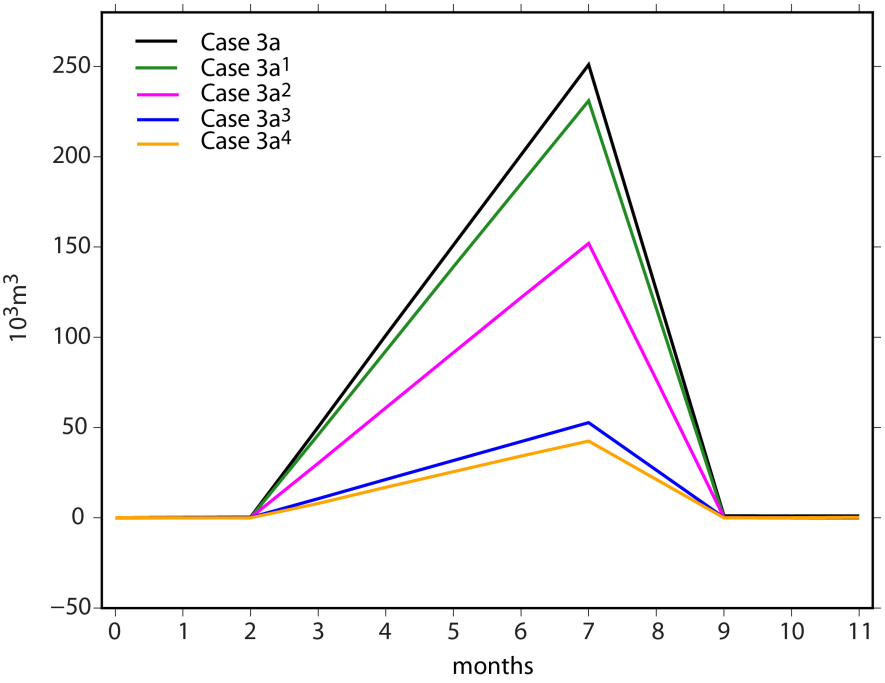

Figure 6.4: *Comparison of optimized volume variations for the 5 inversions: case 3a (black line), case 3a^1 (green line), case 3a^2 (magenta line), case 3a^3 (blue line) and case 3a^4 (orange line). The target volume history can be assimilated to the one of case 3a.*

the source can be fairly constrained in mining and oil & gas reservoirs, magmatic sources are generally poorly located. Therefore, additional simulations setting the position of the source as part of the parameters to be optimized could complement our collection of demonstrating tests before being able to consider real cases.

One way to improve this optimization approach would be to resolve the inverse problem including a constraint on the drift rate minimization. To do so, a new term in the global functional J could be added to minimize the variance of the drift rates. Indeed, the variance of the desired solution in term of drift rates $\vec{a}^*$ can be developed using Eq.9a:

$$var(\vec{a}^*) = var(\vec{a}_a - R\vec{\alpha}) \tag{6.3}$$

Assuming $\vec{a}_a$ and $\vec{\alpha}$ are independent, this leads to,

$$var(\vec{a}^*) = var(\vec{a}_a) + R^2 var(\vec{\alpha}) - 2\ R\ cov(\vec{a}_a, \vec{\alpha}) \tag{6.4}$$

Finally, using the definition of $R = cov(\vec{a}_a, \vec{\alpha}))/var(\vec{\alpha})$ from previous section (Eq.8), the variance of $\vec{a}^*$ resumes to:

$$var(\vec{a}^*) = var(\vec{a}_a) - \frac{cov(\vec{a}_a, \vec{\alpha})^2}{var(\vec{\alpha})} \tag{6.5}$$

Consequently, the variance of the desired solution is lower than the one of the admissible solution, whatever this latter is.

The desired solution is given by the solution of the minimum of variance $var(\vec{a}_a)$. This would enforce the uniqueness of the solution directly during the inversion process. Such modification of the functional could be necessary for solving more complex problems, as we will see and discuss in the next chapter.

Chapter 7

Geodetic joint inversion

Résumé

Dans les Chapitres 5 et 6, nous avons éprouvé notre méthodologie sur des problèmes de complexités croissantes. Ainsi, nous avons démontré l'intérêt et l'utilité d'appliquer une approche d'optimisation globale pour un type de données et des paramètres d'optimisation indépendants du temps (complexité de niveau I, Chapitre 5) ou dépendants du temps (complexité de niveau II, Chapitre 6). Dans ce chapitre, nous nous intéressons au niveau III de complexité qui comprend l'inversion de plusieurs types de données géodésiques avec des paramètres d'inversion qui peuvent aussi dépendre du temps.

En effet, dans le cas des systèmes volcaniques, les jeux de données géodésiques intègrent souvent différents types de mesures de déformation du sol. Parmi les instruments et techniques qui mesurent ces déplacements, nous considérons les GPS, les inclinomètres, les images InSAR et les profils de nivellement. Ces mesures de déformation étant complémentaires, avec des précisions et des résolutions variées, nous pouvons probablement améliorer l'estimation des paramètres du modèle en les inversant conjointement.

Pour ce faire, je présente dans une première partie le modèle de source qui m'a servi à créer les données synthéthiques enregistrées par un réseau géodésique fictif comprenant des GPS, des inclinomètres, des interférogrammes InSAR et des profils de nivellement. Dans une seconde partie, je décris les résultats obtenus à l'issue de l'inversion de ces données synthétiques en terme de variations de volume, de dérive instrumentale et de résidus associés aux données.

7.1 Introduction

In the two previous Chapters (5 and 6), we demonstrate the efficiency of our methodology for the two first levels of complexity described in Chapter 4: the I-level considers a single type of data with time-independent parameters and the II-level also assumes a single data type but with time-dependent parameters. In this chapter, we are presenting the implementation of the approach for the III-level of complexity which involves several data types and time-dependent parameters.

From the 3 types of reservoirs considered in this manuscript, the most diversified geodetic networks are certainly those installed on volcanic systems, including GPS, tiltmeters, levelling lines and InSAR images. Such networks not only contain various types of data, but they can also cover long time series lasting up to several decades (Gambino et al., 2014; Derrien et al., 2015; Bonforte et al., 2017; Narváez Medina et al., 2017). Because these considered geodetic techniques are complementary and present different spatial and/or temporal resolutions, jointly inverting all of them could improve model parameters estimation and resolution.

In the following chapter, we apply the optimization process to a synthetic case simulating the inflation of a spherical source (Mogi, 1958). The induced ground deformation is monitored by GPS, tiltmeters, levelling surveys and InSAR images. The chapter is structured as follow: I first describe the source of deformation before focusing on the geodetic network and associated data. Once the model parametrization is stated, I describe the results in terms of volume variations, drift rates and data residuals.

7.2 Creation of a synthetic dataset

7.2.1. Forward model

The expansion or contraction of geological reservoirs can be modeled at first order by a dilatation source in an elastic half space. In order to create our synthetic dataset, we assume that surface displacements are produced by a spherical source embedded in a homogeneous, isotropic, elastic half space (Mogi, 1958). The Mogi source is located 1500 m beneath the free surface (Figure 7.1a) in a medium with a shear modulus μ=30 GPa and a Poisson's ratio ν=0.25.

In this experiment, we consider an increase of internal volume strain of the source similarly to studies in Chapter 6. Therefore, the history of volume variation is monitored during 11 months and is described in Figure 7.1b. The pressure involved to create such volume variations can be derived using Eq. (2.2) (see Chapter 2) such as:

$$\Delta V = \frac{\pi a^3}{\mu} P \tag{7.1}$$

where $\frac{\pi a^3}{\mu}$ can be seen as a linear coefficient that is independent of the volume variations.

Indeed, starting from a lithostatic initial state of the spherical source (*i.e.* a reservoir), we consider the variations of the associated volume due to an increase or decrease of the pressure P. Assuming 2 spheres with radius $a_1 < a_2$, the pressure involved to produce equivalent volume variations ΔV are such as $P_1 > P_2$. Which means that it is easier (in terms of applied pressure) to increase the volume of a large reservoir than a smaller one.

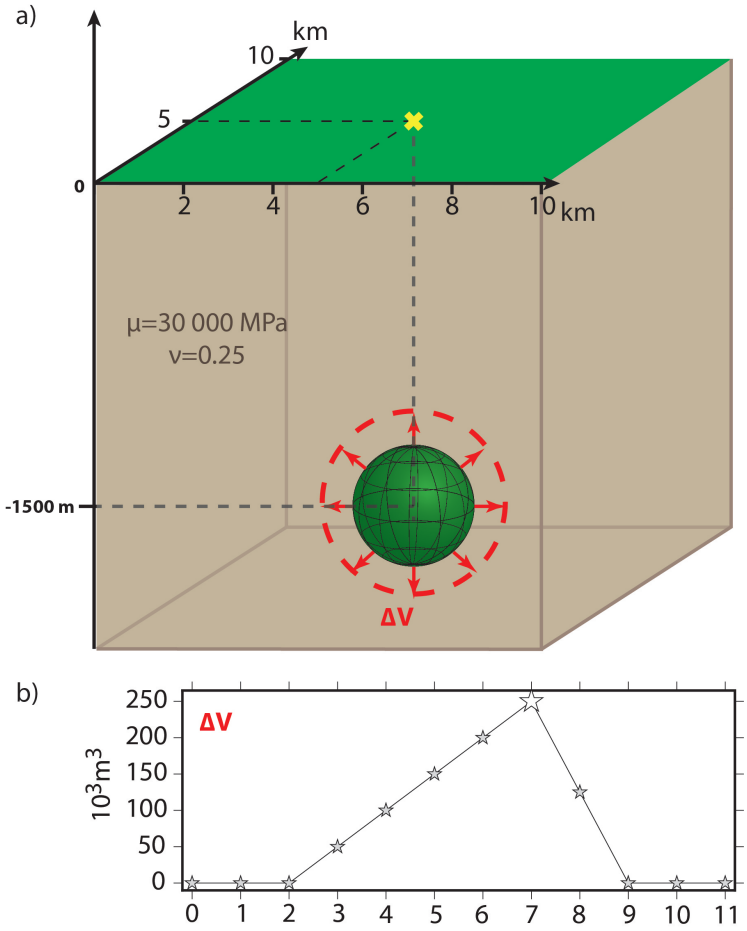

Figure 7.1: *a) Configuration of the Mogi model with the source centered in a 10 km by 10 km domain. The sphere is embedded in a homogeneous, isotropic, elastic flat half space characterized by a shear modulus μ=30 000 MPa and a Poisson's coefficient ν=0.25. b) History of volume variations of the source over 11 months of experiment.*

7.2.2. Geodetic network

Let's assume that the synthetic deformation induced by the volume variations of the sphere is monitored using multiple geodetic instruments and techniques. In an attempt to build a realistic geodetic network recording surface deformation above geological reservoirs, our synthetic network includes 10 GPS stations, 5 borehole tiltmeters, 19 levelling markers and 400 InSAR points distributed over the studied domain (Figure 7.2). InSAR points are supposed to sample a denser grid. For the sake of consistency with real networks, the number of each geodetic instruments and the spatial distribution of each type have been carefully assigned.

GPS stations and tiltmeters are commonly installed above a known or supposed source of deformation while levelling lines are crossing the deformation zone and InSAR interferograms are more able to cover the entire area. Our geodetic network may been one of the three types of geological reservoirs presented in Chapter 3. Because position of the source of volcanic event is generally unknown, GPS and tiltmeters are commonly placed all over the volcanic edifice depending on the accessibility (*e.g.* on the flanks of the volcano, near active or not fissures or craters) to capture the maximum information about ground deformation. To the contrary, in salt mining and hydraulic fracturation, instrument positions are well defined on the base of microseismicity (see Chapter 3). In all cases, geodetic instruments are optimally deployed to capture the deep source deformation.

Our synthetic network is built based on these realistic conditions with a known position of the source (red point on Figure 7.2). The 5 tiltmeters are in a 2 km radius from the source (magenta crosses on Figure 7.2). Seven GPS are located in the vicinity of the source and they are backed up by 3 stations further away from the source (blue inverted triangles on Figure 7.2). The levelling profile starts from the South-West and ends Est of the domain (profile from A to B on Figure 7.2). Finally, we use a uniform spatial discretization of the InSAR data (black dots on Figure 7.2). By doing this, we obtain 400 points instead of several thousands that could be found on domains of such dimensions under propitious conditions (stability of the reflectors throughout the year).

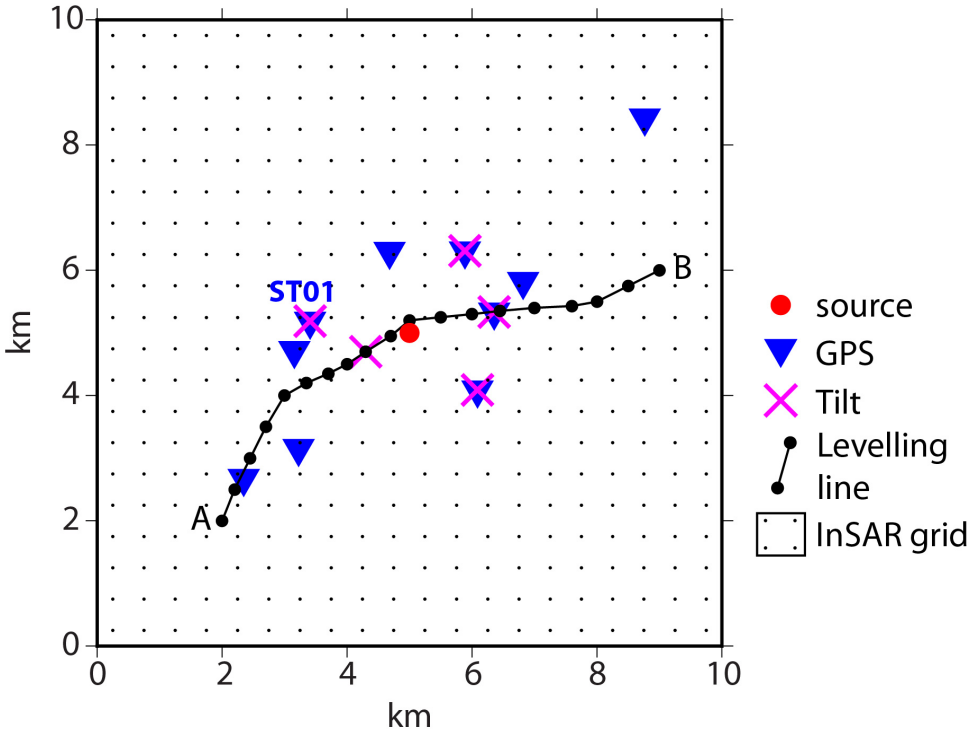

Figure 7.2: *Distribution of the synthetic geodetic network. The source location is known and is represented by a red circle. Locations of GPS and tiltmeters stations are indicated by blue inverted triangles and magenta crosses respectively. The levelling line starts from point A and ends at point B, with 19 markers shown by the black points. Finally the background grid indicates the points of InSAR data. The station ST01 is chosen for representing GPS and tilt data on Figure 7.3.*

7.2.3. Data generation

This synthetic network monitors the deformation induced by the volume strain of the source described in Section 7.2.1. (Figure 7.3a). We generate data $\vec{d}_o$ as the sum of the source $\vec{d}_s$, drift $\vec{d}_d$ and/or noise $c\vec{n}$ signals. Hereafter, I detail the construction of each data type.

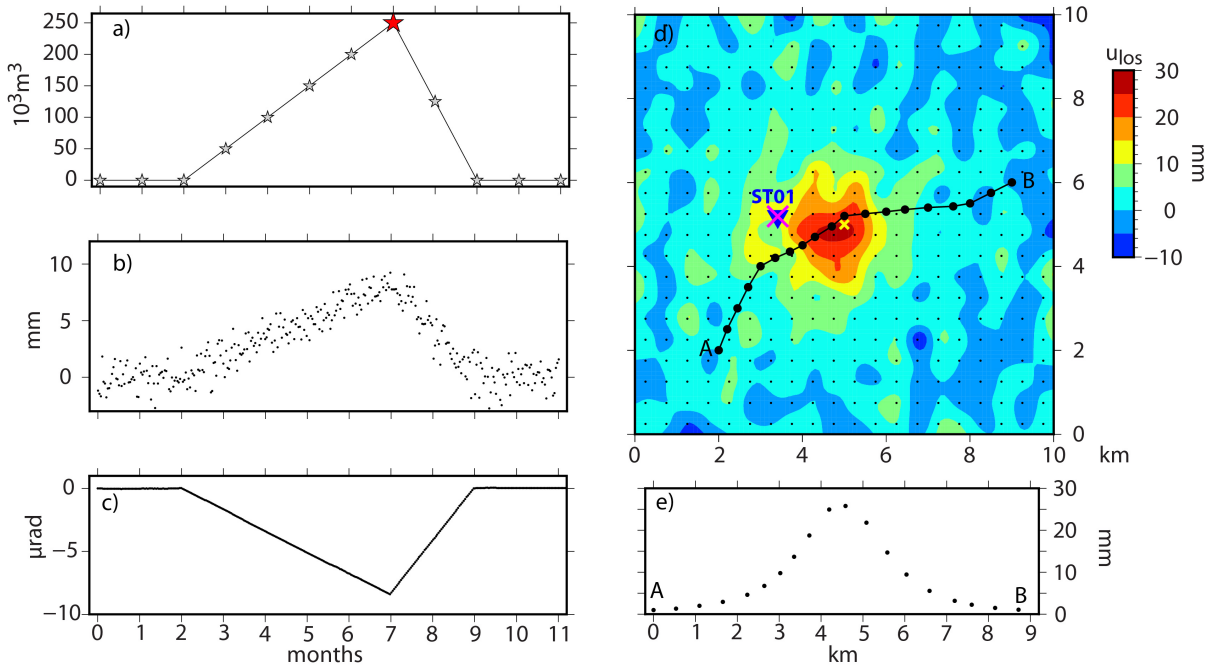

Figure 7.3: *Representation of geodetic data associated to the synthetic model. a) Volume variation of the spherical source over 11 months of the experiments. The red star indicates the time for which InSAR data and levelling data are represented (d and e respectively): ΔV=250 000 m^3 at t=7. b) Vertical displacement of the GPS station located at ST01 on d and Figure 7.2. c) x-component of the tilt measured by the tiltmeter of station ST01 as well. d) Displacement along the line of sight of the satellite produced by the volume variation . The yellow cross stands for the location of the source. Station ST01 indicates the emplacement of the GPS and tiltmeter producing data on b and c. The levelling line is also represented. e) Vertical displacement of levelling along the profile A-B (see Figure 7.2) at t=7.*

1. *GPS data.* The signal recorded by the GPS's is considered to be the sum of the source signal along with some noise: $(\vec{d}_o)_{gps} = \vec{d}_s + \vec{n}_{gps}$. Mao et al. (1999) suggest that noise of all three components of GPS data can be approximated using a combination of white ($\alpha = 0$) and pink ($\alpha = 1$) noise (also named flicker noise). Because the purpose of this study is not to analyze the influence of the type of noise in the determination of the parameters, we generate only white noise for all 3 components of the displacement. This noise is randomly chosen within a standard deviation of σ=1 mm (see Chapter 4). Therefore, the GPS covariance matrix is built using the standard deviation and using Eq.10 of Chapter 6: $\sigma_{gps} = \sigma T^{A/4}$. With A=0 for white noise, the uncertainties associated to the three components of the GPS data are therefore σ_{gps}=1 mm. Figure 7.3b shows the vertical displacement

of station ST01 (Figure 7.2). Starting from a daily measure of GPS, we choose to down-sample the signal to have 12 time intervals.

2. *Tilt data.* Similarly as in Chapter 6, we build the observed tilt by adding to the source signal, a time-dependent linear drift and a Brownian noise: $(\vec{d_o})_{tilt} = \vec{d_s} + \vec{d_d} + \vec{n}_{tilt}$. The drift components are randomly chosen using a uniform probability function ranging from -2.4 μrad/yr to +2.4 μrad/year. The Brownian noise is generated by accumulating random values within a standard deviation depending on the time of experiment. We use the standard deviation of the short term measurement σ_{short}=5 nrads. After one year, we assume a standard deviation of 180 nrads. This leads to a number of iterations T=1440 (from Eq.10 of Chapter 6) which hence corresponds to the total number of synthetic tilt data (Figure 7.3c). The covariance matrix is set using final value, σ_{tilt}=0.18 μrads, of Eq.6 (Chapter 6).

3. *InSAR data.* InSAR interferograms measure the 1-D displacement along the Line Of Sight (LOS) of the satellite. The LOS is defined here by the heading angle of 15° and by the incidence angle of 19.5 °. Interferograms are generated considering the source signal and some time-dependent noise: $(d_o)_{insar} = d_s + n_{insar}$. The noise associated to InSAR data is induced by several factors including geometrical decorrelation (difference in the orbital position of the satellite between 2 acquisitions), temporal decorrelation (difference in time between 2 images) and all spatially correlated noise (atmospheric bias). This implies that the uncertainties associated to InSAR data should vary in time and space. Because we generate synthetic data, we do not proceed to the geometrical and temporal decorrelation nor correct the images from any correlated noise. As a result, we choose a common value of uncertainty for all data points. Similarly to GPS data, we consider white noise. The white noise associated to InSAR data is randomly chosen for each point within a standard deviation σ=3 mm, leading to uncertainty of σ_{insar} =3 mm. A synthetic interferogram is shown on Figure 7.3d imaging the displacement along the line of sight of the satellite at t=7 of the experiment. The displacement does not reflect the real vertical displacement due to the obliquity of the LOS. The LOS displacement is significantly different from the measure of the vertical displacement of GPS or levelling.

4. *Levelling data.* When measuring surface heights along a levelling profile, a reference point is chosen implying that levelling measurements are relative to this point. To account for the relative character of this measurement, an offset parameter can be set up in the model. Besides, the ground deformation is measured with respect to a cumulative error proportional to $e\sqrt{d}$ where e is a nominal error and d the distance between 2 markers of the levelling line (see Chapter 2). Associated to the data an error model need to be defined in order to consider this measurement error. At this time of the thesis development, we have not yet implemented these features of levelling measures (offset, spatial noise). Consequently, we set the reference point far enough from the deformation such as there is no surface displacement. Therefore, this choice is equivalent to a parameter offset with a zero value. Although our synthetic data are free from noise, we must choose an error model to normalize the residuals associated to the levelling data in the functional (Eq. (4.6)). Therefore,

we consider a maximal error such as $\sigma_{level} = e\sqrt{d_{max}}$ with d_{max} the total distance between the first and last marker of the line (Mossop and Segall, 1999). We choose e=2 mm (see Chapter 2) and compute the associated error with d_{max}=8.71 km (Figure 7.3). Thus, the uncertainty associated to the levelling measurement is σ_{level}=5.9 mm. The levelling profile at t=7 is represented on Figure 7.3e.

7.2.4. Model parametrization

Once the forward model and the geodetic data have been defined, we can look at the parameters of the optimization. Although we can set the location of the source and the volume variation as free parameters, we choose to optimize only volume variation along with the drift parameters (as in Chapter 6). This configuration matches the goal of modelling salt mining and hydraulic fracturation that often have a fairly precise source position. Thus the inversion assumes a spatially fixed source and 22 free parameters (12 values of ΔV and 10 values of drift coefficient).

7.3 Results

7.3.1. Some insights of the optimization

To retrieve the parameters of the forward model, we jointly invert the 4 types of data using the methodology described in Chapter 4. Let's remind the formulation of the global functional J (Eq. (7.2) in Chapter 4):

$$J = \sum_{i=1}^{P} \omega_i J_{MNi}, \quad \text{with} \quad \sum_{i=1}^{P} \omega_i = 1. \tag{7.2}$$

where J_{MNi} are functionals associated to each data type and integrate over the time. In this study, the weighting coefficient ω_i are set to $1/P$=0.25. After checking the convergence of the inversion with 1 and 2 layers in the process (see Chapter 4), it appears that global optimization is unnecessary in such case; meaning that the global minimum is simply found by a steepest gradient descent.

In Figure 7.4, I represent the evolution of J with respect to J_{MNi} (i=1,2,3,4 stand for GPS, tilt, InSAR of levelling data respectively). The values of J_{MNi} and therefore J are dimensionless because of the normalization of the residuals (square of the difference between modelled and observed data) by the covariance matrix of each data type. One can notice that J_{MN1} and J_{MN3} do not decrease below 1. All J_{MNi} are converging towards an optimal state except for J_{MN4}. It reaches its optimal value at the 12^{th} iteration (J_{MN4}=10^{-5}) and then increases (J_{MN4}=2.10^{-4}) again while the others J_{MNi} keep decreasing slightly (not visible on Figure 7.4 due to the vertical log scale). Nevertheless, J_{MN4} has very little influence in the functional J compared to J_{MN1} or J_{MN2}. At the end of the inversion, J=0.95 and reflects the optimal state of our parameter set.

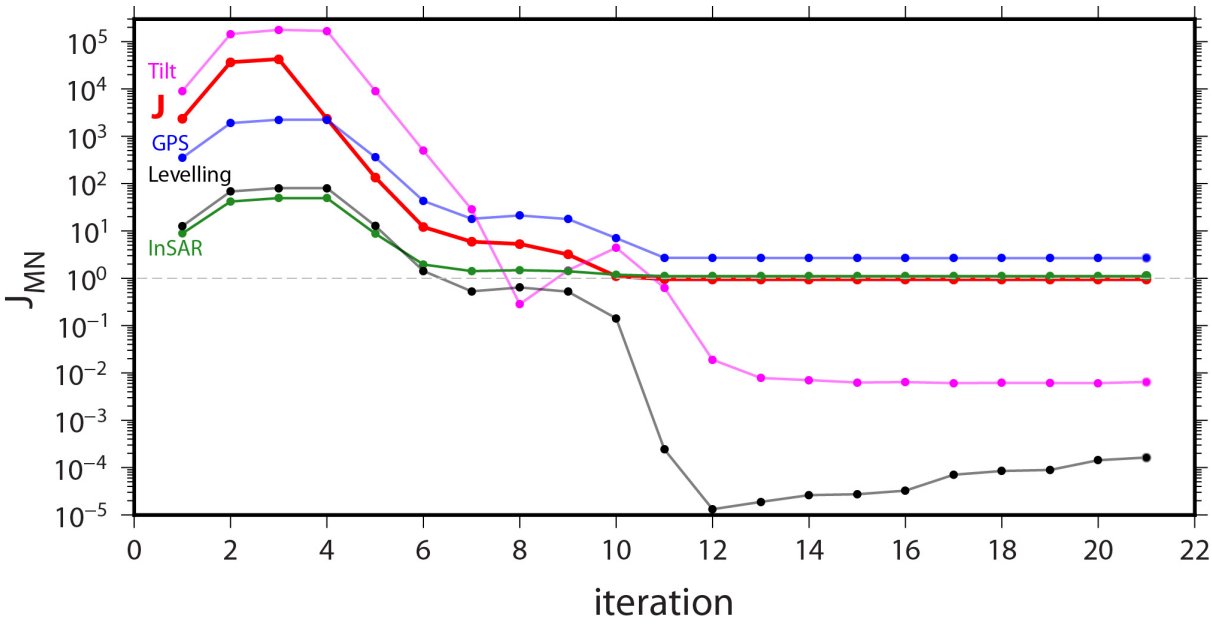

Figure 7.4: *Convergence of individual J_{MNi} (blue curve for GPS, pink curve for tilt, green curve for InSAR and black curve for levelling) and global J (red curve) functionals. The global functional is built using the individual functionals, each one weighted by 0.25. The global minimum is reached at iteration 15.*

7.3.2. Residual data

In addition to the evaluation of each functional (GPS, tilt, InSAR, levelling) we comment the difference between modelled and observed geodetic data, that are associated to residual data distributions in space and time (Figure 7.5a-h). The fit between modelled and observed data is estimated using the root mean square value.

We can describe the RMS at 3 different scales for each data type:

- **Data point scale**: For each data points k, we determine the difference between modelled and observed data (black crosses on Figure 7.5b,d,f,h). Figure 7.5a,c,e,g represent this spatial distribution of data residuals at time t=7.
- **Time point scale**: Summing the residuals of all data points at a given time leads to an averaged residual for the considered time j (red crosses on Figure 7.5b,d,f,h).
- **Experiment scale**: Finally, in Table 7.1 we indicated the average residuals over the entire time of the experiment.

Hereafter, we detail the residuals associated to each data type.

7.3.2.1. GPS data

GPS residuals associated to each data points are systematically lower than 4 mm (black crosses on Figure 7.5b). By looking at Figure 7.5a, one can check that the residuals at t=7 are uncorrelated to the spatial locations of GPS stations. Moreover, this is true for all time series. The average residual per time series varies between 0.7 to 2 mm for an

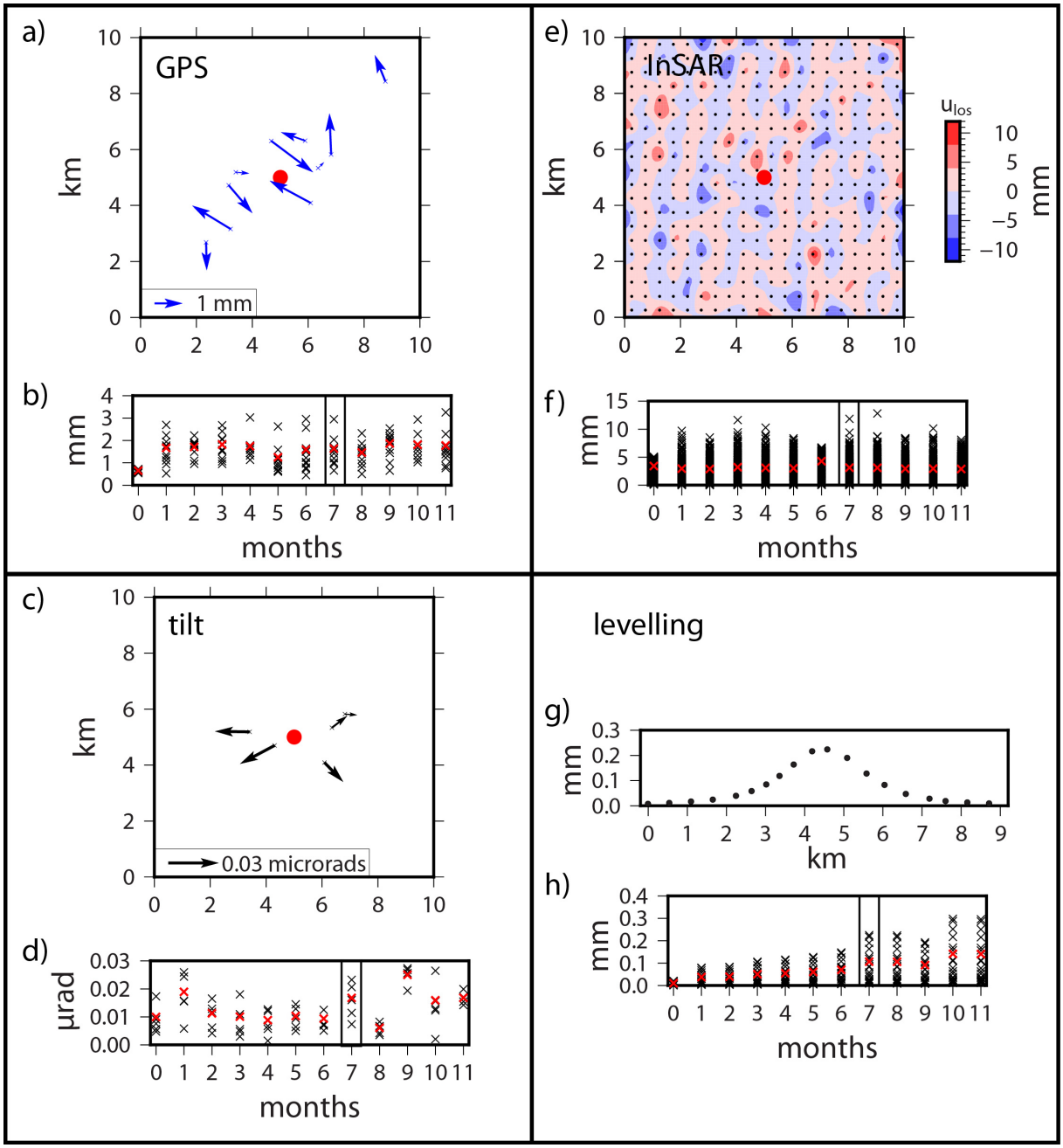

Figure 7.5: *Spatial and temporal distributions of GPS (upper left), tilt (lower left), InSAR (upper right) and levelling (lower right) residuals. The source of deformation is indicated by a red dot on a), c) and e). a) Spatial distribution of the GPS residuals at time t=7 (rectangle on b). b) Temporal distribution of the GPS residuals and mean residual for each time series (red crosses). c) and d), e) and f), g) and h) represent the same as a) and b) for tilt, InSAR and levelling data respectively.*

average value for the entire experiment of 1.58 mm (Table 7.1). This value is greater than the data uncertainty σ_{gps}=1 mm, that could be due to the coarse spatial distribution of the stations and the noise distribution. As detailed in Section 7.2.3., some white noise is added to the source signal, with a time constant standard deviation of 1 mm. For stations close to each other, there are some redundancy in the measured signal with different noise signal. As a result, the signal measured by those 2 stations can diverge and the model cannot explain both signals.

7.3.2.2. Tilt data

Tilt residuals at each point are smaller than 0.03 μrad (black crosses on Figure 7.5d) and they are correlated to the spatial distribution (red crosses on Figure 7.5c). Indeed, because the inversion finds admissible values $\vec{a}_a$ but fails in recovering the true values $\vec{a}^*$, the tilt residuals remain correlated to $\vec{\alpha}$ components. Although this correlation is clear on Figure 7.5c, we apply the linear regression between $\vec{\alpha}$ and $\vec{a}$ to quantify the correlation, leading to a value of -0.1. Comparing to a correlation of 0.9 when inverting only tilt data, we can assume that GPS, InSAR and levelling data significantly contribute for removing the ambiguity of the solution (Figure 7.6). Because the correlation is not equal to zero, this results in some correlation between tilt residuals and their associated $\vec{\alpha}$. We could expect that with no correlation between those parameters, the tilt residual would also be uncorrelated to the spatial distribution of the instruments. At this stage of development, from the relation $\vec{d_d} + \vec{a}_a t = \vec{d^*} + \vec{a}^* t$, we can only provide for the admissible values and not the desired ones yet. For each time series, the average value of residuals fluctuates between 0.005 and 0.025 μrad for an average residual over whole experiment of 0.013 μrad (Table 7.1). This residual value is largely lower than the tilt uncertainty of 0.18 μrad and currently, we can only give conjectures about this result. These low residuals could be explained by the parametrization of the tilt data. Indeed, tilt data are built like the sum of the source signal, a linear trend and some Brownian noise displaying some linear trend too. But in the optimization process, we parametrize the tilt data as the sum of the source signal and a linear drift. Therefore, when inverting tilt data, the optimization tries to explain the total linear trend present in the data, which is the sum of the drift rates and the linear trend from the Brownian noise.

7.3.2.3. InSAR data

InSAR data present residuals lower than 15 mm (black crosses on Figure 7.5f) that are again spatially uncorrelated. The average value per time series appears to be fairly constant, certainly due to the number of data point (red crosses on Figure 7.5e). The associated average RMS for the experiment is 3.14 mm which is about the same as the data uncertainty (3 mm, Table 7.1), meaning that the inversion has converged to an optimal solution. Similarly to GPS data, I would assume that this value of residuals is due to the redundancy of the information.

7.3.2.4. Levelling data

The residuals associated to levelling points are very low, with values ranging from 0 to 0.3 mm (black crosses on Figure 7.5h). This can be explained by the absence of

time-dependent noise in levelling data. However, the average residual per time series increases with time (red crosses on Figure 7.5g). We suppose this is linked to the retrieval of the volume variations. Indeed, with no errors in the levelling data, the measured signal is directly the source signal. As we recover the volume variations with respect to some residuals (Figure 7.6b), it implies the same pattern in the average levelling residual per time series. Although the residuals increase with time, the average residual (0.076 mm) over the experiment remains largely lower than the data uncertainties (5.9 mm).

7.3.3. Optimal parameters and associated uncertainties

Once the joint inversion of GPS, tilt, InSAR and levelling data has converged, we obtain a set of optimal parameters including volume strain and drift rates. Figure 7.6a represents the history of the volume variations given by the inversion process (red dots and line) compared to the target volume history (black line). In order to display the difference between modelled and target volume variations, Figure 7.6b shows only this difference (the volume residuals). The volume variations are retrieved with a maximum residual of $\dot{V}_0$=2884 m^3 at t=10.

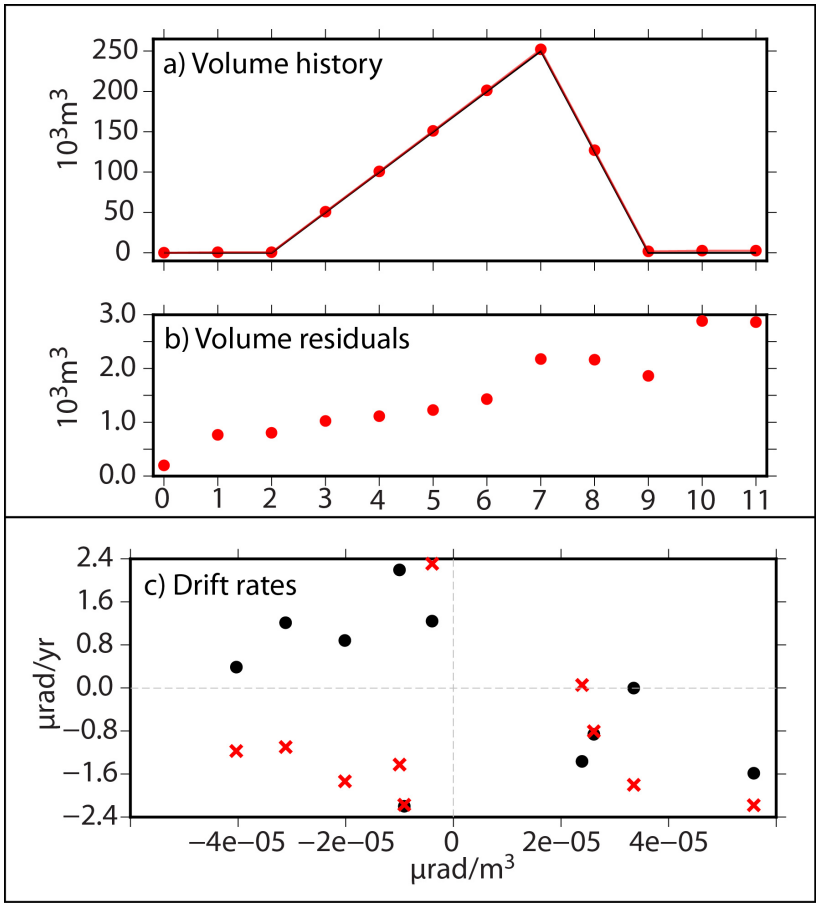

Figure 7.6: *a) Optimal history of volume variations from the inversion process (red dots and line) compared to the target history (black line). b) Difference between the modelled volume variations and the target values. c) Drift rates from the inversion (red crosses) compared to the target drift rates (black dots).*

Comparing the modelled values of drift rates (red crosses on Figure 7.6) to the target ones (black dots on Figure 7.6) reveals more obvious differences. This discrepancy can be explained by the fact that the optimization algorithm explains all linear trends contained in the data, which means that in addition to the linear drift, it also finds the linear trend of the Brownian noise. For this reason, we observe such difference between observed and target drift rates, while keeping such low value of $(J_{MN})_{tilt}$ (Figure 7.4).

Associated to the volume variations, we attempt to estimate the instantaneous volume resolution δV. To do so, let's recall our main modelling assumption: the ground displacement for each instrument is linearly linked to the volume variations. Therefore, each signal $\vec{d_i}$ measured by the different data types (GPS, tilt, InSAR, levelling) can be written as,

$$\vec{d_i} = \vec{\alpha_i}\ \Delta V \tag{7.3}$$

where α_i are the model coefficient associated to each specific data type. The expression of δV associated to each data type can be deduced from this equation (Eq. (7.3)). This coefficient is a measure of the volume resolution at a given time series which depends on the precision of the determination of $\vec{d_i}$. Thus, this latter does not consider the potential linear trend of the solution with time, but only the measure of the data misfit RMS_i, leading to:

$$\delta V = \frac{RMS_i}{\alpha_{imax} - \alpha_{imin}} \tag{7.4}$$

In the previous chapter, we also characterize the measure of the accuracy of the linear component of the solution with time $\delta\dot{V}$. However, this was possible because we assume a long-term drift in tilt data unlike GPS, levelling or InSAR data. For this reason, we cannot use the same definition of $\delta\dot{V}$ and we have not found the right expression of this coefficient yet.

Table 7.1 present for each data type, the associated uncertainty σ_i, the value of individual functional $(J_{MN})_i$, the difference between modelled and observed data RMS_i and the instantaneous volume resolution δV. The values of $(J_{MN})_i$ are discussed in the previous section while values of RMS_i are the subject of the following section. When looking at data type individually, one can notice that the instantaneous volume resolution is largely better for tilt data δV=142 m^3 and levelling data δV=760 m^3 due very low residuals.

Data type i	σ_i	J_{MNi} optimal	RMS_i	δV
GPS	1 mm	2.67	1.58 mm	19 799 m^3
tilt	0.180 μrad	5.6 10^{-3}	0.013 μrad	142 m^3
InSAR	3 mm	1.11	3.14 mm	31 605 m^3
level	5.9 mm	2.02 10^{-4}	0.076 mm	760 m^3

Table 7.1: *Data uncertainties σ_i and results of the joint inversion of GPS, tilt, InSAR and levelling data, including the $(J_{MN})_i$ at the end of the inversion, the associated residual RMS_i, the flow rate uncertainty $\delta\dot{V}$ and the volume resolution δV.*

7.4 Discussion

The global optimization approach has been finally tested for the III-level of complexity which considers 4 types of geodetic data along with time-dependent model parameters. We choose to monitor the inflation of a Mogi source by a realistic geodetic network composed of 10 GPS stations daily sampled, 5 tiltmeters with one measure every 6 h, 12 InSAR images (made of 400 reflectors) and 12 levelling profiles (made of 19 markers). Once more, the optimization process succeeded in retrieving the model parameters. But this time, no global optimization is needed to converge towards the solution, certainly due to the correct location of the source initially set.

Indeed, when optimizing the horizontal position of the source, x_s and y_s, along with the volume variations and the drift rates needs the activation of the second layer in the global optimization approach. We initialize the position of the source at x_s=4000 and y_s=4000. The search interval associated to the horizontal position of the source is a square of 3 by 3 kilometers. By doing so, we are able to retrieve nearly the same set of volume variations and drift rates (Figure 7.7), but we also recover the horizontal position of the source, with x_s^*=5002.6 m and y_s^*=5001.7 m. When increasing the search interval (square of 10 by 10 kilometers) of the horizontal position, the inversion does not converge towards the solution.

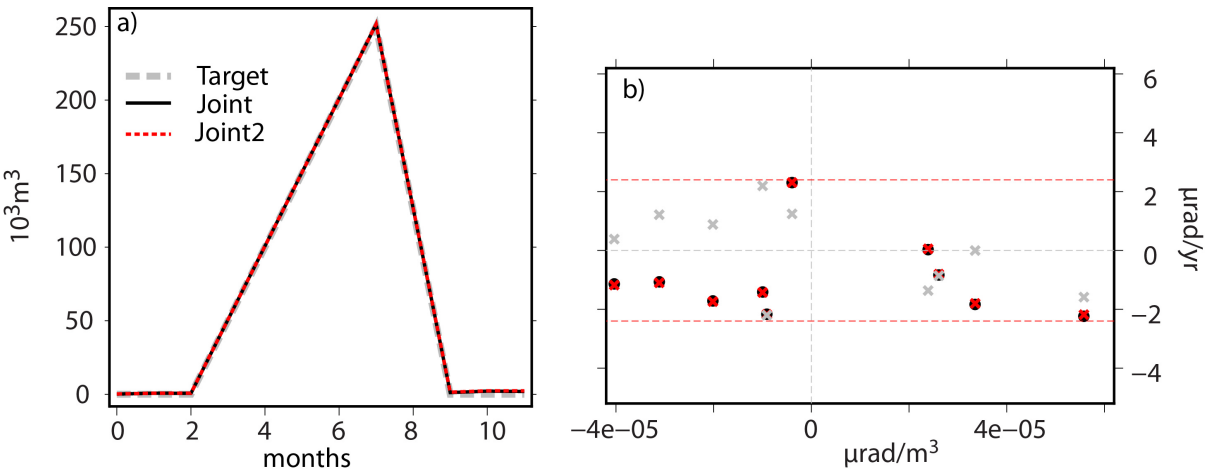

Figure 7.7: *a) Representation of the volume variations. The results from the first joint inversion (only ΔV) are represented by the black line. The results from the second joint inversion (looking for ΔV and horizontal position of the source x_s and y_s) correspond to the red dashed line. They are both compared to the target volume history (grey dashed line). b) Comparison of the optimal drift rates from the second inversion (red crosses) with the first inversion (black dots) and the target drift rates (grey crosses).*

What is the contribution of the joint inversion to the parameters estimation? Inverting individually GPS, tilt and InSAR data leads to very similar values of J_{MN} (hence, $J_{MN} = J$ for the inversion of a single type) summarized in Table 7.2 and Figure 7.8. How-

ever in the case of tilt inversion, the flow rate correction needs to be applied to recover the volume variation (Figure 7.8). This suggests that considering 5 tiltmeters strategically installed is sufficient to retrieve both volume variations and drift coefficient. The only difference lies in the inversion of levelling data (J_{MNi}=2.02 10^{-4} instead of 2.7 10^{-8}). Whereas the three first data type considers some noise, the levelling data are assumed to have space-dependent error (as a function of the square root of the distance in kilometers). This implies to perfectly converge towards the exact solution for volume variations whereas volumes remain less constrained when only GPS or InSAR are inverted. Although we invert signals that can be individually optimized, the joint inversion improves the determination of the optimization parameters.

Data type i	J_{MNi} joint inversion	J_{MNi} single inversion
GPS	2.67	2.60
tilt	5.6 10^{-3}	2.4 10^{-3}
InSAR	1.11	1.11
level	2.02 10^{-4}	2.7 10^{-8}

Table 7.2: *Comparison of J_{MNi} from the joint inversion and from the inversion of individual data type.*

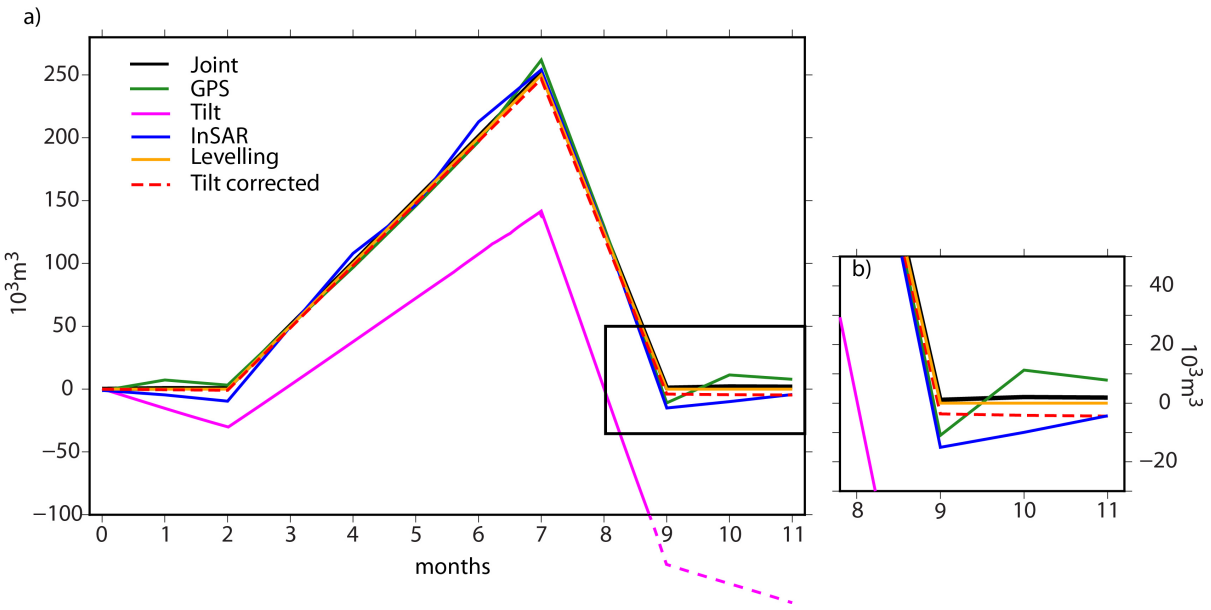

Figure 7.8: *Representation of the volume variations from the joint and individual inversions of GPS, tilt, InSAR and levelling for a) the whole experiment and b) focusing at the 3 last time steps. The black line corresponds to the results of the joint inversion, the green line to the inversion of GPS data, the magenta to tilt data, the blue to InSAR data, the orange to levelling data and the dashed red line to the corrected drift. The target volume variations match the volume variations from the inversion of levelling data.*

One may find surprisingly that each individual inversion leads to a correct estimations of the volume variations. This is due to our choice to model volume variations that are

significant enough to be solved by each instrument separately. This is the reason why we can invert the data separately. However, the volume variations may not always be of such intensity (*e.g.* in salt mining or oil & gas reservoirs), requiring then, a joint inversion for a precise volume variation estimation.

Although this first experience was successful, many other parameters configurations need to be explored. For instance, one could attempt to optimize not only the volume variations, but also the position of the source or its characteristics (dip, azimuth for Okada's model). For a model configuration similar to the one of this chapter, we should be able to converge to an admissible set of parameters. Nevertheless, with lower values of volume variations, only tilt data are able to detect the induced deformation and thus would influence the functional J. Without the contribution of the other data in the determination of the parameters, the optimal solution would again be one among all admissible and the flow rate correction would be needed to enforce the uniqueness.

Chapter 8

Discussion and future work

8.1 Achievements, weaknesses and upgrades

In this manuscript I present a methodology developed in order to address the challenge of long term reservoir monitoring. The ground deformation is measured by various geodetic means including GPS networks, InSAR images, tiltmeters and levelling routes. They are complementary in characterizing the displacement of the surface: cartesian coordinates for GPS, along the Line Of Sight of the satellite for InSAR, gradient of the vertical displacement for tiltmeters, vertical displacement for levelling and the change in gravity attraction if gravimeters are operating. In order to connect these observations to the origin of the deformation, we developed inverse problems, assuming analytical or numerical mechanical models describing the physical phenomenon. After solving these problems, an optimal set of parameters from the model should produce modelled data that are close to the observations with respect to the associated uncertainties. Because the quest for the best parameters is non-unique and can be computationally slow and filled with obstacles due to the nature of the functional, the optimization approach is based on an algorithm developed by Mohammadi and Saïac (2003) matching the following criteria:

1. it accounts for potential local minima,
2. it considers physical problems of various complexities,
3. it jointly inverts several data types,
4. it is computationally straightforward and fast.

The optimization aims at finding the parameters of the desired model that best reproduce the observations. To do so, the algorithm wisely explores the parameters domain in its whole. It does not only seek for optimal values of the parameters using a steepest gradient descent but it also tries to find the initial condition that leads to the global optimum. We applied this optimization approach to geodetic systems and demonstrated its efficiency and high potential on three levels of complexity considering 1 to 4 types of

data and 3 different models (1 numerical and 2 analytical). The I-level refers to a problem considering 1 type of data (interseismic GPS velocities) and time-independent parameters (lateral rigidities of the lithosphere in the vicinity of the San Andreas Fault system). For this application, we illustrate the methodology on both synthetic and real data (Western United States) leading to a publication in *Tectonophysics* (Furst et al., 2017). The II-level involves 1 type of data (2-D tilt) and includes both time-independent parameters (drift rates associated to both components of the tiltmeters) and time-dependent parameters (volume variations of the source in time). In this case, synthetic data with colored noise have been produced and results will be submitted to the journal *Journal of Geodesy*. Finally, the III-level jointly inverts 4 types of geodetic data (GPS, tilt, InSAR and levelling) in order to recover time-independent parameters (drift rates) and time-dependent parameters (volume variations of the source). Again, only synthetic data are used to illustrate this level of complexity. These 3 applications highlight the potential for the global optimization to treat various geodetic inverse problems under minimum *a priori* assumptions. I would like to emphasize the following points:

- The approach allows to consider a high number of free parameters (cases with more than 2000 parameters to optimize have been tested) using an adjoint formulation of the forward model. This leads to a high resolution exploration of the optimal parameters at reasonable computational cost (3h of simulations using a laptop). For smaller number of parameters (one hundred), the inversion is completed in a matter of a few minutes ($\sim$3 min with a laptop).

- For tilt data inversion, the associated long-term drift can be jointly estimated with source parameters by adding a second step to the optimization. Firstly, the inverse problem is solved with no constraint on the drift rate, leading to one out of all admissible sets of parameters. Uniqueness is then enforced by assuming that source parameters are independent from drift parameters. This 2-step approach stands as long as the considered forward model involves a linear relation between source parameters $\vec{\alpha}$ and drift parameters $\vec{a}$. A paper describing this approach is about to be submitted in Journal of Geodesy. Associated to each application, we attempted to back the optimal set of parameters by a careful uncertainty analysis. Nevertheless, when jointly inverting several data types, we are not able to estimate the uncertainty associated to the long term trend.

- A joint inversion of various geodetic data allows to improve the parameters determination. Adding GPS, InSAR and levelling data to tilt measurements permits to remove the ambiguity of the solution. However, it must be recalled that that the tilt signal is by far the most sensitive to small strain changes. Then, if the source signal is not significant enough to be detected with GPS, InSAR or levelling, the functional would only be affected by the tilt signal. In this case, the 2-step approach could be used to enforce uniqueness of the solution.

- Jointly inverting all geodetic data leads to modelled tilt, whose associated tilt drift are slightly correlated to the source parameters. Unfortunately, this correlation cannot be removed using the 2-step optimization as we defined it. Indeed, the second step changes drift rates associated to tiltmeters and also volume variations. Therefore, these modified volume variations induce in turn different GPS, InSAR and

levelling predictions. As a result, the correction used to decorrelate drift parameters from tilt signal must be implemented in a 1-step inversion process. To do so, I would assume that considering the variance of the drift rates in the functional would help removing this ambiguity between parameters and tilt data (see Chapter 6 for demonstration). This new term would be minimized simultaneously with the residual associated to each data type.

- Most of the geodetic data that we considered are relative measurements, which means that they measure the deformation relatively to some translation. As of today (July 5th 2018), we do not consider any translation factor. Implementing these new parameters could therefore be an improvement of the algorithm for processing real geodetic datasets. This evolution is clearly needed for notorious relative measurements such as levelling or InSAR.

- We develop a single numerical tool separating the inverse problem from the forward models to provide inversion of various geodetic data types considering problems of increasing complexity. Therefore, other forward models can be easily added like more complex physical models including for instance a spherical source with a viscoelastic shell (Dragoni and Magnanensi, 1989) or finite element models (Dieterich and Decker, 1975).

These enhancements would complete the present-day methodology and permit the application to a wide range of geophysical inverse problems. Despite we demonstrate the ability of the method to solve relatively complex synthetic problems, a clear weakness of this work is relative to the lack of using real geodetic data. Therefore, I attempt to reconnect to the challenges associated with the 3 geological reservoirs and discussed future projects involving the salt reservoir of Vauvert (France), the unconventional exploitation of a gas reservoir (Vaca Muerta, Argentina) and Kīlauea volcano (Hawaï).

8.2 Geological reservoirs projects

We have seen in Chapter 3 the characteristics and challenges associated to 3 different geological reservoirs. In this section, I present some ongoing projects that could become relevant for the application of the developed methodology.

Since February 2018, the salt exploitation in Vauvert is equipped with a Halliburton tiltmeter, measuring the deformation induced by the extraction of brine, but also by draining two nearby wells. Data have not yet been processed nor analyzed, but they could be used in a joint inversion, along with GPS, InSAR, levelling and gravimetric data, in order to model the reservoir deformation associated to salt withdrawal. The joint inversion would be appropriate because the ground deformation is significant enough ($\sim$2 mm/yr) to be measured by GPS, levelling (see Figure 3.9), tiltmeters, gravimetry (Eugène, 2016) and InSAR (Raucoules et al., 2003; Maisons and Raucoules, 2006). This particular example could become a benchmark for implementing additional forward models, as fluid pressure and brine flow (injected and extracted) and salt saturation are also monitored

by the company. Besides, as part of the MIRZA project, one prototype of low drifting tiltmeter is planned to be installed in the same hole as Halliburton's tiltmeter. By doing so, we aim at comparing the signal of these 2 tiltmeters during several months to give a first estimation of the long-term drift of each tiltmeter. Once we validate the low-drift characteristic of MIRZA tiltmeter (*i.e.* checking measured signals, level of drift, reliability of the installation process and other potential issues), we plan to set up a pilot on one of Total's field in Argentina to monitor the unconventional exploitation of the Vaca Muerta layer in collaboration between Total S.A and Aquitaine Electronique. Contrary to Vauvert's site, the inversion method would be tested a network of 20 to 30 tiltmeters.

For this project, I aim to apply the methodology developed in my thesis to monitor the different steps of a production well, from the stimulation of the first reservoir volume to the long-term draining of the entire network. Using MIRZA's tiltmeters, we would assume that the volume variations involved during the fracking would be well constrained (as shown by previous studies: Pinnacle Technologies, 2007; Astakhov et al., 2012, Figure 8.1a). With respect to the cited work, a major evolution would be the use of the tiltmeters network to follow the long-term evolution of volume variations (up to 2-3 years) thanks to the low drifting tilmeters and the optimization approach that we developed. Because the deformation induced by one fracking is tens of nanometers (Figure 8.1b), only tilt data could measure it during the first stages. However, when draining the Stimulated Reservoir Volumes, the cumulative deformation should be detectable on InSAR images. The joint inversion of tilt data and InSAR signals would lead to the estimation of these different Stimulated Reservoir Volumes varying in time, highlighting how they are drained and if they are drained.

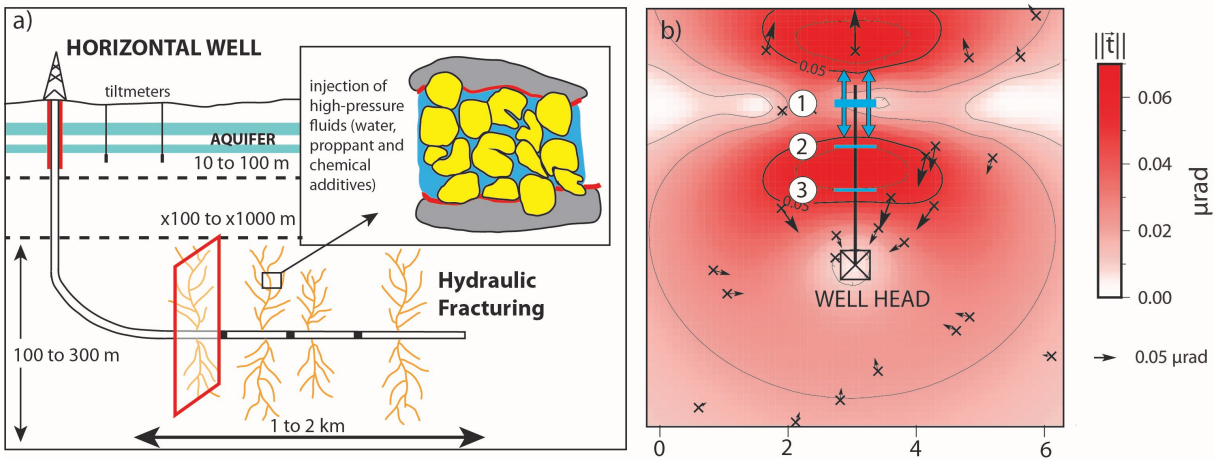

Figure 8.1: *a) Representation of multistages hydraulic fracturing in an unconventional reservoir (note the variable vertical scale). We assimilate the network of fractures produced during one stimulation stage as a planar dislocation (red rectangle). b) Simulation of a fracking stage using an Okada's tensile model. The injected volume is 10 000 m^3 and stimulates a vertical fracture of 100×100 m. The tilt signal distribution informs about the location of maximum deformation. If opening is simulated on fracture 2, the deformation translates with respect to the distance between the 2 vertical fractures.*

Before deploying tiltmeters on the field, the design of the surface tiltmeter network is mandatory to anticipate the quality of the fracture mapping network. To do so, I plan to create a synthetic experiment, simulating the history of volume variations, with several stages of nearly instantaneous hydraulic fracturing and a long-term depletion due to gas extraction. I would assume some pre-existing fracturation in the medium (following *a priori* geologic information) that would be assimilated to a tensile plan opening under the injected fluid. Figure 8.1b illustrates one fracking stage measured by 25 tiltmeters randomly placed above the horizontal well. The continuous distribution of the tilt signal amplitude is displayed by the colored scale of the figure. For such studies, I could vary the geometry of each fracture zone but also the volume variations involved in the extraction to understand how the ground surface is reacting to different deep strain sources. This could help to define the number of necessary tiltmeters and to place them in order to optimize the network that would capture at best the geometry and the deformation of the Stimulated Reservoir Volumes. This first analysis would allow to efficiently deploy a network of tiltmeters on the selected pilot well in Argentina. If the experiment is successful, the methodology could become widely used for long-term geodetic monitoring and data inversion in nearly real time.

Joint inversions have sometimes be performed to better constrain the source of the deformation, for modelling the propagation of a dike or locating the magmatic chamber and its inflation/deflation. Concerning Kīlauea volcano, jointly inverting GPS, tilt and InSAR data during Kamoamoa eruption in 2011 has not yet been tested. Modelling the source of this event could help to better constrain the source of Deflation-Inflation events occurring at the summit crater of the volcano. Moreover, using our approach could help to model the evolution of volume variations during several months, instead of considering isolated events. For such simulation, it would probably be necessary to consider a finite element model to account for a free geometry of the source, the rheological variations of the medium and the topography. This improvement of the forward model should not change the nature of the optimization problem as long as a linear strain-stress relationship is assumed.

These are proposals for applying our methodology to real cases but others could be envisaged and developed.

Chapter 9

Bibliography

Agnew, D. C. (1986). Strainmeters and Tiltmeters. *Review of geophysics*, 24(3):579–624.

Alvarado-Montero, R., Schwanenberg, D., Krahe, P., Helmke, P., and Klein, B. (2017). Multi-parametric variational data assimilation for hydrological forecasting. *Advances in Water Resources*, 110(October):182–192.

Anderson, K., Lisowski, M., and Segall, P. (2010). Cyclic ground tilt associated with the 2004-2008 eruption of Mount St. Helens. *Journal of Geophysical Research: Solid Earth*, 115(11):1–29.

Anderson, K. R. and Poland, M. P. (2016). Bayesian estimation of magma supply, storage, and eruption rates using a multiphysical volcano model: Kilauea Volcano, 2000-2012. *Earth and Planetary Science Letters*, 447:161–171.

Anderson, K. R., Poland, M. P., Johnson, J. H., and Miklius, A. (2015). Episodic Deflation-Inflation Events at Kilauea Volcano and Implications for the Shallow Magma System. In Carey, R., Cayol, V., Poland, M., and Weis, D., editors, *Hawaiian Volcanoes: From Source to Surface*, chapter 11, pages 229–250. John Wiley & Sons, Inc., first edition.

Astakhov, D. K., Roadarmel, W. H., Nanayakkara, a. S., and Service, H. (2012). SPE 151017 A New Method of Characterizing the Stimulated Reservoir Volume Using Tiltmeter-Based Surface Microdeformation Measurements. In *SPE Hydraulic Fracturing Technology Conference*, pages 1–15, The Woodlands, Texas.

Battaglia, M., Cervelli, P. F., and Murray, J. R. (2013a). DMODELS: A MATLAB software package for modeling crustal deformation near active faults and volcanic centers. *Journal of Volcanology and Geothermal Research*, 254:1–4.

Battaglia, M., Cervelli, P. F., and Murray, J. R. (2013b). Modeling crustal deformation near active faults and volcanic centers-a catalog of deformation models. In *US Geological Survey Techniques and Methods, book 13*, chapter B1, page 96. USGS.

Berardino, P., Fornaro, G., Lanari, R., and Sansosti, E. (2002). A new algorithm for surface deformation monitoring based on small baseline differential SAR interferograms. *IEEE Transactions on Geoscience and Remote Sensing*, 40(11):2375–2383.

Bérest, P., Bergues, J., Brouard, B., Durup, J., and Guerber, B. (2001). A salt cavern abandonment test. *International Journal of Rock Mechanics and Mining Sciences*, 38(3):357–368.

Bérest, P. and Brouard, B. (2003). Safety of salt caverns used for underground storage blow out; mechanical instability; seepage; cavern abandonment. *Oil & Gas Science and Technology*, 58(3):361–384.

Berest, P., Djakeun-djizanne, H., Brouard, B., and Hévin, G. (2012). Rapid Depresurizations : Can they lead to irreversible damage ? In *SMRI. SMRI Spring Conference*, pages 63–86, Regina.

Bérest, P., Karimi-jafari, M., Brouard, B., Bazargan, B., Mécanique, L. D., Polytechnique, E., and Consulting, B. (2006). In situ mechanical tests in salt caverns. In *Solution Mining Research Institute*, pages 1–39, Brussels, Belgium.

Bonaccorso, A. and Davis, P. M. (1999). Models of ground deformation from vertical volcanic conduits with application to eruptions of Mount St. Helens and Mount Etna. *Journal of Geophysical Research*, 104:10531.

Bonafede, M. and Ferrari, C. (2009). Analytical models of deformation and residual gravity changes due to a Mogi source in a viscoelastic medium. *Tectonophysics*, 471(1-2):4–13.

Bonforte, A., Fanizza, G., Greco, P., Matera, A., and Sulpizio, R. (2017). Long-termdynamics across a volcanic rift: 21 years of microgravity and GPS observations on the southern flank ofMt. Etna volcano. *Journal of Volcanology and Geothermal Research*.

Bossler, J. D. (1984). Standards and Specifications for Geodetic Control Networks. Technical report, Federal Geodetic Control Committee.

Brynjarsdóttir, J. and Ohagan, A. (2014). Learning about physical parameters: The importance of model discrepancy. *Inverse Problems*, 30(11).

Caffagni, E. and Bokelmann, G. (2016). Geophysical Monitoring of a Hydrocarbon Reservoir. *Energy Procedia*, 97:294–301.

Camacho, A. G., González, P. J., Fernández, J., and Berrino, G. (2011). Simultaneous inversion of surface deformation and gravity changes by means of extended bodies with a free geometry: Application to deforming calderas. *Journal of Geophysical Research: Solid Earth*, 116(10):1–15.

Castillo, D., Hunter, S., Harben, P., Wright, C., Conant, R., and Davis, E. (1997). Deep Hydraulic Fracture Imaging: Recent Advances in Tiltmeter Technologies. *Int. J. Rock Mech. & Min. Sci.*, 34(047):3–4.

Cayol, V. and Cornet, F. H. (1997). 3D Mixed Boundary Elements for Elastostatic Deformation Field Analysis. *Int. J. Rock Mech. & Min. Sci.*, 34(2):275–287.

Cervelli, P. F. (2013). Analytical Expressions for Deformation from an Arbitrarily Oriented Spheroid in a Half-Space. *EOS Trans. AGU*.

Chawah, P. (2012). *Développement d'un capteur de déplacement à fibre optique appliqué à l'inclinométrie et à la sismologie*. PhD thesis, Université de Montpellier II.

Chawah, P., Chéry, J., Boudin, F., Cattoen, M., Seat, H., Plantier, G., Lizion, F., Sourice, A., Bernard, P., Brunet, C., Boyer, D., and Gaffet, S. (2015a). A simple pendulum borehole tiltmeter based on a triaxial optical-fibre displacement sensor. *Geophysical Journal International*, 203(2):1026–1038.

Chawah, P., Chéry, J., Boudin, F., Cattoen, M., Seat, H., Plantier, G., Lizion, F., Sourice, A., Bernard, P., Brunet, C., Boyer, D., and Gaffet, S. (2015b). A simple pendulum borehole tiltmeter based on a triaxial optical-fibre displacement sensor. *Geophysical Journal International*, 203(2):1026–1038.

Chéry, J., Mohammadi, B., Peyret, M., and Joulain, C. (2011). Plate rigidity inversion in southern California using interseismic GPS velocity field. *Geophysical Journal International*, 187(2):783–796.

Cockett, R., Kang, S., Heagy, L. J., Pidlisecky, A., and Oldenburg, D. W. (2015). SimPEG: An open source framework for simulation and gradient based parameter estimation in geophysical applications. *Computers and Geosciences*, 85:142–154.

Colombo, D., Mantovani, M., Stefano, M. D., De Stefano, M., Garrad, D., and Al-Lawati, H. (2007). Simultaneous Joint Inversion of Seismic and Gravity Data for Long Offset Pre-Stack Depth Migration in Northern Oman. *CSPG CSEG Convention*, 41569:191–195.

Davis, P. M. (1986a). Surface Deformation Due to Inflation of an Arbitrarily Oriented Triaxial Ellipsoidal Cavity in an Elastic Half-Space, With Reference to Kilauea Volcano, Hawaii. *Journal of Geophysical Research*, 91:7429–7438.

Davis, P. M. (1986b). Surface deformation due to inflation of an arbitrarily oriented triaxial ellipsoidal cavity in an elastic half-space, with reference to Kilauea volcano, Hawaii. *Journal of Geophysical Research*, 91(B7):7429.

Derrien, A., Villeneuve, N., Peltier, A., and Beauducel, F. (2015). Retrieving 65 years of volcano summit deformation from multitemporal structure from motion: The case of Piton de la Fournaise (La Réunion Island). *Geophysical Research Letters*, 42(17):6959–6966.

Dieterich, J. H. and Decker, R. W. (1975). Finite element modeling of surface deformation associated with volcanism. *Journal of Geophysical Research*, 80(29):4094–4102.

Dragoni, M. and Magnanensi, C. (1989). Displacement and stress produced by a pressurized, spherical magma chamber, surrounded by a viscoelastic shell. *Physics of the Earth and Planetary Interiors*, 56(3-4):316–328.

Eaton, J. P. and Murata, K. J. (1960). How volcaones grow. *Science*, 132(3432):925–938.

Eugène, M. (2016). Application de la géodésie à l'étude d'un site en subsidence : Vauvert. Technical report, Géosciences Montpellier, Montpellier.

Fernández, J., Pepe, A., Poland, M., and Sigmundsson, F. (2017). Volcano Geodesy: Recent developments and future challenges. *Journal of Volcanology and Geothermal Research*, 344:1–12.

Ferretti, A., Prati, C., and Rocca, F. (2000). Nonlinear subsidence rate estimation using permanent scatterers in differential SAR interferometry. *IEEE Transactions on Geoscience and Remote Sensing*, 38(5 I):2202–2212.

Fialko, Y., Khazan, Y., and Simons, M. (2001). Deformation due to a pressurized horizontal circular crack in an elastic half-space, with applications to volcano geodesy. *Geophysical Journal International*, 146:181–190.

Fisher, K. and Warpinski, N. (2011). Hydraulic Fracture-Height Growth: Real Data (SPE 145949). In *SPE Annual Technical Conference and Exhibition*.

Flammarion, C. (1888). *L'atmosphère : météorologie populaire*. Librairie Hachette et Compagnie, Paris.

Fonseca, C. M. and Fleming, P. J. (1995). An Overview of Evolutionary Algorithms in Multiobjective Optimization *. *Evolutionary Computation*, 3(1):1–16.

Fores, B., Champollion, C., Le Moigne, N., Bayer, R., and Chéry, J. (2017). Assessing the precision of the iGrav superconducting gravimeter for hydrological models and karstic hydrological process identification. *Geophysical Journal International*, 208(1):269–280.

Fukushima, Y., Cayol, V., and Durand, P. (2005). Finding realistic dike models from interferometric synthetic aperture radar data: The February 2000 eruption at Piton de la Fournaise. *Journal of Geophysical Research B: Solid Earth*, 110(3):1–15.

Fukushima, Y., Cayol, V., Durand, P., and Massonnet, D. (2000). Evolution of magma conduits during 1998 - 2000 eruptions of Piton de la Fournaise. *October*, pages 1–46.

Furst, S., Peyret, M., Chéry, J., and Mohammadi, B. (2017). Lithosphere rigidity by adjoint-based inversion of interseismic GPS data, application to the Western United States. *Tectonophysics*.

Gambino, S., Falzone, G., Ferro, A., and Laudani, G. (2014). Volcanic processes detected by tiltmeters: A review of experience on Sicilian volcanoes. *Journal of Volcanology and Geothermal Research*, 271:43–54.

Geirsson, H., La Femina, P. C., Sturkell, E., Ofeigsson, B., Arnadottir, T., Hooper, A. J., Lund, B., Schmidt, P., Sigmundsson, F., and Affiliation: (2014). Joint Inversion of GPS, InSAR, Tilt, and Borehole Strain Data from the 2000 Eruption of Hekla Volcano, Iceland. In *AGU 2014*, number 1, pages 1–5.

Godano, M., Bardainne, T., Regnier, M., Deschamps, A., and Valette, M. (2012). Spatial and temporal evolution of a microseismic swarm induced by water injection in the Arkema-Vauvert salt field (southern France). *Geophysical Journal International*, 188(1):274–292.

Goldberg, D. E. (1989). *Genetic Algorithms in Search, Optimization, and Machine Learning*, volume Addison-We. Addison-Wesley Professional.

Got, J. L., Carrier, A., Marsan, D., Jouanne, F., Vogfjörd, K., and Villemin, T. (2017). An analysis of the nonlinear magma-edifice coupling at Grimsvötn volcano (Iceland). *Journal of Geophysical Research: Solid Earth*, 122(2):826–843.

Hadamard, J. (1902). Sur les problèmes aux dérivées partielles et leur signification physique. *Princeton Uni. Bull. (1902)*, 13:49–52.

Hager, B. H., King, R. W., and Murray, M. H. (1991). Measurement of Crustal Deformation Using the Global Positioning System. *Annual Review of Earth and Planetary Sciences*, 19(1):351–382.

Harrison, J. C. and Herbst, K. (1977). Thermoelastic strains and tilts revisited. *Geophysical Research Letters*, 4(11):535–537.

Helmert, F. R. (1880). *Die mathematischen und physikalischen theorieen der höheren geodäsie*. B. G. Teubner, Leipzig.

Hesse, M. a. and Stadler, G. (2014). Joint inversion in coupled quasi-static poroelasticity. *Journal of Geophysical Research: Solid Earth*, 119(2):1425–1445.

Hooper, A., Zebker, H., Segall, P., and Kampes, B. (2004). A new method for measuring deformation on volcanoes and other natural terrains using InSAR persistent scatterers. *Geophysical Research Letters*, 31(23):1–5.

Ivorra, B. (2006). *Optimisation globale semi-déterministe et applications industrielles*. Mathématiques appliquées, Université Montpellier II.

Ivorra, B. and Mohammadi, B. (2007). Semi-deterministic global optimization method. *Journal of Optimization, Theory and Applications*, 135(3):549–561.

Jackson, R. B., Vengosh, A., Carey, J. W., Davies, R. J., Darrah, T. H., O'Sullivan, F., and Pétron, G. (2014). The Environmental Costs and Benefits of Fracking. *Annual Review of Environment and Resources*, 39(1):327–362.

Jacob, T., Bayer, R., Chery, J., Jourde, H., Moigne, N. L., Boy, J. P., Hinderer, J., Luck, B., and Brunet, P. (2008). Absolute gravity monitoring of water storage variation in a karst aquifer on the larzac plateau (Southern France). *Journal of Hydrology*, 359(1-2):105–117.

Jha, B., Bottazzi, F., Wojcik, R., Coccia, M., Bechor, N., McLaughlin, D., Herring, T., Hager, B., Mantica, D., and Juanes, R. (2008). Soil parameter identification using a genetic algorithm. *International Journal for Numerical and Analytical Methods in Geomechanics*, 32(March 2007):189–213.

Jouanne, F., Genaudeau, N., Ménard, G., and Darmendrail, X. (1998). Estimating present-day displacement fields and tectonic deformation in active mountain belts: An example from the Chartreuse Massif and the southern Jura Mountains, western Alps. *Tectonophysics*, 296(3-4):403–419.

Jouanne, F., Ménard, G., and Darmendrail, X. (1995). Present-day vertical displacements in the north-western Alps and southern Jura Mountains: Data from leveling comparisons. *Tectonics*, 14(3):606–616.

Kachanov, L. (1958). Rupture Time Under Creep Conditions. *Izvestia Akademii Nauk SSSR, Otdelenie tekhnicheskich nauk*, 97(8):26–31.

Kennedy, M. C. and O'Hagan, A. (2001). Bayesian calibration of computer models. *Journal of the Royal Statistical Society: Series B (Statistical Methodology)*, 63(3):425–464.

Kreemer, C. and Hammond, W. C. (2007). Geodetic constraints on areal changes in the Pacific-North America plate boundary zone: What controls Basin and Range extension? *Geology*, 35(10):943.

Kreemer, C., Klein, E., Shen, Z.-K., Wang, M., Estey, L., Wier, S., and Boler, F. (2014). A geodetic platemotion and Global Strain Rate Model. *Geochemistry, Geophysics, Geosystems*, page 130.

Le Calvez, J., Malpani, R., Xu, J., Stokes, J., Williams, M., Probert, T., Bradford, I., Cambridge, E., and Zakhour, N. (2016). Hydraulic Fracturing Insights from Microseismic Monitoring. *Oilfield Review*, 28(2):16–33.

Li, Q., Xing, H., Liu, J., and Liu, X. (2015). Review article A review on hydraulic fracturing of unconventional reservoir. *Petroleum*, 1(1):8–15.

Lin, Y. and Zhang, H. (2016). Imaging hydraulic fractures by microseismic migration for downhole monitoring system. *Physics of the Earth and Planetary Interiors*, 261:88–97.

Lingyun, J., Qingliang, W., and Shanlan, Q. (2013). Present-day deformation of Agung volcano, Indonesia, as determined using SBAS-InSAR. *Geodesy and Geodynamics*, 4(3):65–70.

Lundgren, P., Poland, M., Miklius, A., Orr, T., Yun, S. H., Fielding, E., Liu, Z., Tanaka, A., Szeliga, W., Hensley, S., and Owen, S. (2013). Evolution of dike opening during the March 2011 Kamoamoa fissure eruption, KÄ«lauea Volcano, Hawai'i. *Journal of Geophysical Research: Solid Earth*, 118(3):897–914.

Maerten, F. (2010). Adaptive cross-approximation applied to the solution of system of equations and post-processing for 3D elastostatic problems using the boundary element method. *Engineering Analysis with Boundary Elements*, 34(5):483–491.

Maerten, L., Maerten, F., Lejri, M., and Gillespie, P. (2016). Geomechanical paleostress inversion using fracture data. *Journal of Structural Geology*, 89:197–213.

Maisons, C. and Raucoules, D. (2006). Monitoring of slow ground deformation by satellite differential radar-interferometry . A reference case study . In *Solution Mining Research Institute*, Brussels.

Mao, A., Harrison, C. G. A., and Dixon, T. H. (1999). Noise in GPS coordinate time series. *Journal of Geophysical Research*, 104(B2):2797.

Massonnet, D. and Feigl, K. L. (1998). Radar interferometry and its application to changes in the earth's surface. *Reviews of Geophysics*, 36(4):441–500.

Mayer, A. (2016). Risk and benefits in a fracking boom: Evidence from Colorado. *Extractive Industries and Society*, 3(3):744–753.

McTigue, D. F. (1987). Elastic stress and deformation near a finite spherical magma body: Resolution of the point source paradox. *Journal of Geophysical Research*, 92(B12):12931–12940.

Meng, Q. (2017). The impacts of fracking on the environment: A total environmental study paradigm. *Science of the Total Environment*, 580:953–957.

Minson, S. E., Murray, J. R., Langbein, J. O., and Gomberg, J. S. (2014). Real-time inversions for finite fault slip models and rupture geometry based on high-rate GPS data. *Journal of Geophysical Research: Solid Earth*, 119(4):3201–3231.

Mogi, K. (1958). Relations between the eruptions of various volcanoes and the deformations of the ground surfaces around them.

Mohammadi, B. and Pironneau, O. (2009). *Applied Shape Optimization for fluids*. Oxford University Press, Oxford, 2nd editio edition.

Mohammadi, B. and Saïac, J.-H. (2003). *Pratique de la simulation numérique*.

Mossop, A. and Segall, P. (1999). Volume strain within The Geysers geothermal field. *Journal of Geophysical Research*, 104:29113–29131.

Munson, D. and Dawson, P. (1984). Salt constitutive modeling using mechanism maps. In *First Conference on the Mechanical Behavior of the SaltMechanical Behavior of Salt*, Pennsylvania. Trans Tech Pub, Clausthal-Zellerfeld, Germany.

Narváez Medina, L., Arcos, D. F., and Battaglia, M. (2017). Twenty years (1990-2010) of geodetic monitoring of Galeras volcano (Colombia) from continuous tilt measurements. *Journal of Volcanology and Geothermal Research*, 344:232–245.

Nocedal, J. and Wright, S. J. (1999). *Numerical Optimization*. Springer-Verlag New York, 2 edition.

Nocquet, J. M., Sue, C., Walpersdorf, A., Tran, T., Lenôtre, N., Vernant, P., Cushing, M., Jouanne, F., Masson, F., Baize, S., Chéry, J., and Van Der Beek, P. A. (2016). Present-day uplift of the western Alps. *Scientific Reports*, 6(March):1–6.

Norton, F. (1929). *The creep of steel at high temperature*. New York McGraw-Hill book company, inc., Norton, 1st edition.

Nunnari, G., Puglisi, G., and Guglielmino, F. (2005). Inversion of SAR data in active volcanic areas by optimization techniques. *Nonlinear Processes in Geophysics*, 12(6):863–870.

Obrizzo, F., Pingue, F., Troise, C., and De Natale, G. (2004). Bayesian inversion of 1994-1998 vertical displacements at Mt Etna: evidence for magma intrusion. *Geophysical Journal International*, 157(2):935–946.

Okada, Y. (1992). Internal deformation due to shear and tensile faults in a half-space. *Bulletin of the Seismological Society of America*, 82(2):1018–1040.

Olson, J. E., Du, Y., and Du, J. (1997). Tiltmeter data inversion with continuous non-uniform opening distributions: a new method for detecting hydraulic fracture geometry. *International journal of rock mechanics and mining sciences & geomechanics abstracts*, 34(3-4):436.

Ooi, E. T. and Yang, Z. J. (2010). A hybrid finite element-scaled boundary finite element method for crack propagation modelling. *Computer Methods in Applied Mechanics and Engineering*, 199(17-20):1178–1187.

Orr, T., Poland, M., Patrick, M., Thelen, W., Sutton, A., Elias, T., Thornber, C., Parcheta, C., and Wooten, K. (2015). Kilauea's 5-9 March 2011 Kamoamoa fissure eruption and its relation to 30+ years of activity from Pu'u'O'o. In Carey, R., Cayol, V., Poland, M., and Weis, D., editors, *Hawaiian Volcanoes: From Source to Surface*, chapter 18, pages p. 393–420. John Wiley & Sons, Inc., first edition.

Palano, M., Puglisi, G., and Gresta, S. (2008). Ground deformation patterns at Mt. Etna from 1993 to 2000 from joint use of InSAR and GPS techniques. *Journal of Volcanology and Geothermal Research*, 169(3-4):99–120.

Peltier, A., Staudacher, T., and Bachèlery, P. (2007). Constraints on magma transfers and structures involved in the 2003 activity at Piton de La Fournaise from displacement data. *Journal of Geophysical Research: Solid Earth*, 112(3):1–16.

Peltier, A., Staudacher, T., Bachèlery, P., and Cayol, V. (2009). Formation of the April 2007 caldera collapse at Piton de La Fournaise volcano: Insights from GPS data. *Journal of Volcanology and Geothermal Research*, 184(1-2):152–163.

Pinnacle Technologies, I. (2007). Surface Tiltmeter Fracture Mapping Results for the Klatt. Technical Report 1, Pinnacle.

Poland, M., Miklius, A., and Montgomery-Brown, E. (2014). Magma Supply, Storage, and Transport at Shield-Stage Hawaiian Volcanoes. *U.S. Geological Survey Professional Paper 1801*, 2010:1–52.

Poland, M. P. and Carbone, D. (2016). Insights into shallow magmatic processes at KÄ«lauea Volcano, HawaiÊ»i, from a multiyear continuous gravity time series. *Journal of Geophysical Research: Solid Earth*, 121(7):5477–5492.

Qin, P., Huang, D., Yuan, Y., Geng, M., and Liu, J. (2016). Integrated gravity and gravity gradient 3D inversion using the non-linear conjugate gradient. *Journal of Applied Geophysics*, 126:52–73.

Raucoules, D., Maisons, C., and Carnec, C. (2004). Monitoring subsidence on the Vauvert salt mine using radar interferometry. In *Journées Nationales de Géotechnique et de Géologie de l'ingénieur*, pages 413–417, Lille, France.

Raucoules, D., Maisons, C., Carnec, C., Le Mouelic, S., King, C., and Hosford, S. (2003). Monitoring of slow ground deformation by ERS radar interferometry on the Vauvert salt mine (France): Comparison with ground-based measurement. *Remote Sensing of Environment*, 88(4):468–478.

Ricco, C., Aquino, I., Augusti, V., D'Auria, L., Del Gaudio, C., and Scarpato, G. (2018). Improvement and development of the tiltmetric monitoring networks of Neapolitan volcanoes. *Annals of Geophysics*, 61(1).

Richards, M. (2007). A Beginner's Guide to Interferometric SAR Concepts and Signal Processing [AESS Tutorial IV]. *IEEE Aerospace and Electronic Systems Magazine*, 22(9):5–29.

Romero-Sarmiento, M. F., Ramiro-Ramirez, S., Berthe, G., Fleury, M., and Littke, R. (2017). Geochemical and petrophysical source rock characterization of the Vaca Muerta Formation, Argentina: Implications for unconventional petroleum resource estimations. *International Journal of Coal Geology*, 184:27–41.

Ronchin, E., Masterlark, T., Dawson, J., Saunders, S., and Martì Molist, J. (2017). Imaging the complex geometry of a magma reservoir using FEM-based linear inverse modeling of InSAR data: application to Rabaul Caldera, Papua New Guinea. *Geophysical Journal International*, 209(3):1746–1760.

Sambridge, M. and Mosegaard, K. (2002). Monte Carlo Methods in Geophysical Inverse Problems. *Earth*, 40(September):1009.

Sasagawa, G. S., Klopping, F., Niebauer, T. M., Faller, J. E., and Hilt, R. L. (1995). Intracomparison tests of the FG5 absolute gravity meters. *Geophysical Research Letters*, 22(4):461–464.

Segall, P. (2010). *Earthquake and Volcano deformation*. Princeton University Press, Princeton & Oxford.

Segall, P. (2013). Volcano deformation and eruption forecasting. *Geological Society, London, Special Publications*, 380(1):85–106.

Segall, P., Llenos, A. L., Yun, S.-H., Bradley, A. M., and Syracuse, E. M. (2013). Time-dependent dike propagation from joint inversion of seismicity and deformation data. *Journal of Geophysical Research: Solid Earth*, 118(11):5785–5804.

Sinclair, S. and Rockwell, G. (2014). Cirrus.

Stewart, J. and Watts, a. B. (1997). Gravity anomalies and spatial variations of flexural rigidity at mountain ranges.

Sturkell, E., Ágústsson, K., Linde, A. T., Sacks, S. I., Einarsson, P., Sigmundsson, F., Geirsson, H., Pedersen, R., LaFemina, P. C., and Ólafsson, H. (2013). New insights into volcanic activity from strain and other deformation data for the Hekla 2000 eruption. *Journal of Volcanology and Geothermal Research*, 256:78–86.

Tarantola, A. (2004). *Inverse Problem Theory and Methods for Model Parameter Estimation*. SIAM.

Tarantola, A. and Valette, B. (1982). Inverse Problems = Quest for Information. *Journal of Geophysics*, 50(3):159–170.

Tikhonov, A. N. (1943). On the stability of inverse problems. *Doklady Akademii Nauk Sssr*, 39(5):195–198.

Tilling, R., Heliker, C., and Swanson, D. (2010). *Eruptions of Hawaiian volcanoes; past, present, and future*. USGS, second edition.

Tilling, R. I. and Dvorak, J. J. (1993). Anatomy of a basaltic volcano.

Valette, M. (1991). *Etude stracturale du gisement salifère oligocène de Vauvert (Gard)*. PhD thesis, Université de Montpellier.

Valette, M. and Benedicto, A. (1995). Gravity thrust halotectonics in the extensional Camargue basin (Gulf of Lion margin, SE France). *Bulletin de la Société Géologique de France*, 166(2):137–147.

van Keken, P. E., Spiers, C. J., van den Berg, A. P., and Muyzert, E. J. (1993). The effective viscosity of rocksalt: implementation of steady-state creep laws in numerical models of salt diapirism. *Tectonophysics*, 225(4):457–476.

Vasco, D. W., Ferretti, A., and Novali, F. (2008). Reservoir monitoring and characterization using satellite geodetic data: Interferometric synthetic aperture radar observations from the Krechba field, Algeria. *Geophysics*, 73(6):WA113.

Vassilvitskii, S. and Yannakakis, M. (2005). Efficiently computing succinct trade-off curves. *Theoretical Computer Science*, 348(2-3):334–356.

Vengosh, A., Jackson, R. B., Warner, N., Darrah, T. H., and Kondash, A. (2014). A critical review of the risks to water resources from unconventional shale gas development and hydraulic fracturing in the United States.

Vouille, G., Tijani, S., and De Grenier, F. (1984). Experimental determination of the rheological behaviour of Tersanne Rock Slat. In *First Conference on the Mechanical Behavior of the Salt*, pages 407–420, Pennsylvania. Trans Tech Pub, Clausthal-Zellerfeld, Germany.

Warpinski, N. (2014). Surface Tiltmeters : A Proven Tool for New Answers in Unconventional Reservoir Stimulations. Technical report, Pinnacle - Halliburton.

Warpinski, N., Branagan, P., Engler, B., Wilmer, R., and Wolhart, S. (1997). Evaluation of a downhole tiltmeter array for monitoring hydraulic fractures. *Int. J. Rock Mech. & Min. Sci.*, 34(329):3–4.

Watts, A. B. (2001). *Isostasy and flexure of the Lithosphere*. Cambridge University Press, Cambridge.

Weng, X. (2015). Modeling of complex hydraulic fractures in naturally fractured formation. *Journal of Unconventional Oil and Gas Resources*, 9:114–135.

Wessels, S. A., De La Pena, A., Kratz, M., Williams-Stroud, S., and Jbeili, T. (2011). Identifying faults and fractures in unconventional reservoirs through microseismic monitoring. *First Break*, 29(7):99–104.

Wiley, C. a. (1965). Pulsed doppler radar methods and apparatus.

Wilgan, K., Rohm, W., and Bosy, J. (2015). Multi-observation meteorological and GNSS data comparison with Numerical Weather Prediction model. *Atmospheric Research*, 156:29–42.

Wilschut, F., Peters, E., Visser, K., Fokker, P. A., and van Hooff, P. (2011). Joint History Matching of Well Data and Surface Subsidence Observations Using the Ensemble Kalman Filter: A Field Study. *SPE Reservoir Simulation Symposium*.

Wu, F., Yan, Y., and Yin, C. (2017). Real-time microseismic monitoring technology for hydraulic fracturing in shale gas reservoirs: A case study from the Southern Sichuan Basin. *Natural Gas Industry B*, 4(1):68–71.

Wyatt, F., Cabaniss, G., and Agnew, D. C. (1982). A comparison of tiltmeters at tidal frequencies. *Geophysical Research Letters*, 9(7):743–746.

Yabuki, T. and Matsu'ura, M. (1992). Geodetic data inversion using a Bayesian information criterion for spatial distribution of fault slip. *Geophysical Journal International*, 109(2):363–375.

Yang, X.-M., Davis, P. M., and Dieterich, J. H. (1988). Deformation from inflation of a dipping finite prolate spheroid in an elastic half-space as a model for volcanic stressing. *Journal of Geophysical Research*, 93(7):4249.

Yukutake, T. and Tachinaka, H. (1967). Geomagnetic variation associated with stress change wihin a semi infinite elastic earth caused by a cylindrical force source. *Bulletin of the Earthquake Research Institute*, 45:785–798.

Yun, S., Segall, P., and Zebker, H. (2006). Constraints on magma chamber geometry at Sierra Negra Volcano, Galápagos Islands, based on InSAR observations. *Journal of Volcanology and Geothermal Research*, 150(1-3):232–243.

Zhai, G. and Shirzaei, M. (2016). Spatiotemporal model of KÄ«lauea's summit magmatic system inferred from InSAR time series and geometry-free time-dependent source inversion. *Journal of Geophysical Research Solid Earth*, 121:5425–5446.

Zhan, Y. and Gregg, P. M. (2017). Data assimilation strategies for volcano geodesy. *Journal of Volcanology and Geothermal Research*.

Zhaohai, M. (2016). 3D inversion of full gravity gradient tensor data using SL0 sparse recovery. *Journal of Applied Geophysics*, 127:112–128.

Zhou, J., Zeng, Y., Jiang, T., Zhang, B., and Zhang, X. (2015). Tiltmeter Hydraulic Fracturing Mapping on a Cluster of Horizontal Wells in a Tight Gas Reservoir. In *SPE/IATMI Asia Pacific Oil & Gas Conference and Exhibition*, Bali, Indonesia.

Zhou, X., Chang, N.-B., and Li, S. (2009). Applications of SAR Interferometry in Earth and Environmental Science Research. *Sensors*, 9(3):1876–1912.

Zoback, M. D. (2007). *Reservoir Geomechanics*. Cambridge University Press.

Zou, C., Ni, Y., Li, J., Kondash, A., Coyte, R., Lauer, N., Cui, H., Liao, F., and Vengosh, A. (2018). The water footprint of hydraulic fracturing in Sichuan Basin, China. *Science of the Total Environment*, 630.

Zurek, J. (2007). *Characterizing the Plumbing Systems of Active Volcanoes Through Potential Field Studies*. PhD thesis, University of Victoria.

Abstract

The Earth's surface is affected by numerous local processes like volcanic events, landslides or earthquakes. Along with these natural processes, anthropogenic activities including extraction and storage of deep resources (*e.g.* minerals, hydrocarbons) shape the Earth at different space and time scales. These mechanisms produce ground deformation that can be detected by various geodetic instruments like GNSS, InSAR, tiltmeters, for example. The purpose of the thesis is to develop a numerical tool to provide the joint inversion of multiple geodetic data associated to plate deformation or volume strain change at depth. Four kinds of applications are targeted: interseismic plate deformation, volcano deformation, deep mining, and oil & gas extraction. Different inverse model complexities were considered: the I-level considers a single type of geodetic data with a time independent process. An application is made with inverting GPS data across southern California to determine the lateral variations of lithospheric rigidity (Furst et al., 2017). The II-level also accounts for a single type of geodetic data but with a time-dependent process. The joint determination of strain change history and the drift parameters of a tiltmeter network is studied through a synthetic example (Furst et al., submitted). The III-level considers different types of geodetic data and a time-dependent process. A fictitious network made by GNSS, InSAR, tiltmeters and levelling surveys is defined to compute the time dependent volume change of a deep source of strain. We develop a methodology to implement these different levels of complexity in a single software. Because the inverse problem is possibly ill-posed, the functional to minimize may display several minima. Therefore, a global optimization algorithm is used (Mohammadi and Saïac, 2003). The forward part of the problem is treated by using a collection of numerical and analytical elastic models allowing to model the deformation processes at depth. Thanks to these numerical developments, new advances for inverse geodetic problems should be possible like the joint inversion of various types of geodetic data acquired for volcano monitoring. In this perspective, the possibility to determine by inverse problem the tiltmeter drift parameters should allow for a precise determination of deep strain sources. Also, the developed methodology can be used for an accurate monitoring of oil & gas reservoir deformation.

Keywords : Geodesy, Inversion, Geological reservoirs, Optimization, Modelling

Résumé

La surface terrestre est affectée par de nombreux processus locaux tels que des événements volcaniques, des glissements de terrain ou des tremblements de terre. Parallèlement à ces processus naturels, les activités anthropiques, y compris l'extraction et le stockage des ressources profondes (par exemple, les minéraux ou les hydrocarbures) façonnent la Terre à différentes échelles spatiales et temporelles. Ces mécanismes produisent une déformation du sol qui peut être détectée par divers instruments et techniques géodésiques tel que le GNSS, l'InSAR, les inclinomètres. Le but de cette thèse est de développer un outil numérique permettant l'inversion conjointe de multiples données géodésiques associées à la déformation de la plaque ou au changement de contrainte volumique en profondeur. Quatre types d'applications sont ciblés: la déformation intersismiques des plaques, la déformation des volcans, l'exploitation minière profonde et l'extraction de pétrole et de gaz. Différentes complexités du modèle inverse ont été considérées: le niveau I considère un seul type de données géodésiques avec un processus indépendant du temps. Une application est réalisée avec l'inversion des données GPS à travers le sud de la Californie pour déterminer les variations latérales de la rigidité lithosphérique (Furst et al., 2017). Le niveau II représente également un seul type de données géodésiques mais avec un processus dépendant du temps. La détermination conjointe de l'historique des changements de contrainte et des paramètres de dérive d'un réseau d'inclinomètres est étudiée à l'aide d'un exemple synthétique (Furst et al., soumis). Le niveau III considère différents types de données géodésiques et un processus dépendant du temps. Un réseau fictif combinant des données GNSS, InSAR, inclinométriques et de nivellement est défini pour calculer le changement de volume dépendant du temps d'une source profonde de déformation. Une méthodologie pour implémenter ces différents niveaux de complexité est développée dans un seul logiciel. Parce que le problème inverse peut être mal posé, la minimisation de la fonctionnelle peut produire plusieurs minima. Par conséquent, un algorithme d'optimisation global est utilisé (Mohammadi and Saïac, 2003). Le problème direct est traité en utilisant un ensemble de modèles élastiques numériques et analytiques permettant de modéliser les processus de déformation en profondeur. Grâce à ces développements numériques, des avancées concernant les problèmes inverses en géodésie devraient être possibles telle que l'inversion jointe de différents types de données géodésiques acquises lors de la surveillance des volcans. Dans cette perspective, la possibilité de déterminer par inversion les paramètres de dérive des inclinomètres permettrait une détermination précise des sources de déformation profondes. En outre, la méthodologie développée peut être utilisée pour une surveillance précise de la déformation des réservoirs de pétrole et de gaz.

Mots-clefs : Géodésie, Inversion, Réservoirs géologiques, Optimisation, Modélisation